Estimating Point Source Emissions Using CO_2 and CH_4 Lidar Observations

Sebastian Wolff

München 2025

Estimating Point Source Emissions Using CO_2 and CH_4 Lidar Observations

Sebastian Wolff

Dissertation
an der Fakultät für Physik
der Ludwig–Maximilians–Universität
München

vorgelegt von
Sebastian Wolff
aus Mühlacker

München, den 29.10.2025

Erstgutachter: Prof. Dr. Markus Rapp
Zweitgutachter: Prof. Dr. Sander Houweling
Tag der mündlichen Prüfung: 16.12.2025

“If —” by Rudyard Kipling (1865–1936)

If you can keep your head when all about you
    Are losing theirs and blaming it on you,
If you can trust yourself when all men doubt you,
    But make allowance for their doubting too;
If you can wait and not be tired by waiting,
    Or being lied about, don’t deal in lies,
Or being hated, don’t give way to hating,
    And yet don’t look too good, nor talk too wise:

If you can dream — and not make dreams your master;
    If you can think — and not make thoughts your aim;
If you can meet with Triumph and Disaster
    And treat those two impostors just the same;
If you can bear to hear the truth you’ve spoken
    Twisted by knaves to make a trap for fools,
Or watch the things you gave your life to, broken,
    And stoop and build ’em up with worn-out tools:

If you can make one heap of all your winnings
    And risk it on one turn of pitch-and-toss,
And lose, and start again at your beginnings
    And never breathe a word about your loss;
If you can force your heart and nerve and sinew
    To serve your turn long after they are gone,
And so hold on when there is nothing in you
    Except the Will which says to them: ‘Hold on!’

If you can talk with crowds and keep your virtue,
    Or walk with Kings — nor lose the common touch,
If neither foes nor loving friends can hurt you,
    If all men count with you, but none too much;
If you can fill the unforgiving minute
    With sixty seconds’ worth of distance run,
Yours is the Earth and everything that’s in it,
    And — which is more — you’ll be a Man, my son!

Zusammenfassung

Internationale Klimaabkommen zielen darauf ab, die anthropogenen Treibhausgas-Emissionen (THG) in den kommenden Jahrzehnten zu reduzieren. Ein erheblicher Teil dieser Emissionen stammt aus lokalen Punktquellen wie z.B. Kraftwerken und Kohlebergwerken. Mit abnehmenden Emissionen müssen die Quantifizierungsmethoden präziser und belastbarer werden, um Veränderungen zuverlässig zu erfassen. Satellitenbeobachtungen eignen sich aufgrund ihrer globalen Abdeckung gut für diese Aufgabe, stützen sich jedoch meist auf passive Sensoren, die reflektiertes Sonnenlicht messen. Dadurch sind sie bei Bewölkung, über dunklen Oberflächen sowie nachts oder im polaren Winter nur eingeschränkt nutzbar.

Die aktive Fernerkundung mit IPDA-Lidar (Integrietated Path Differential Absorption) unterliegt diesen Einschränkungen nicht. In dieser Dissertation wird das flugzeuggetragene IPDA-Lidar-System CHARM–F verwendet, um CO_2- und CH_4-Emissionen aus Punktquellen anhand von Daten der CoMet-Kampagne 2018 in Europa zu quantifizieren. Zwei Fallstudien mit zunehmender Komplexität demonstrieren seine Fähigkeiten.

Fallstudie I untersucht die isolierte CO_2-Abgasfahne des Kohlekraftwerks Jänschwalde. Unter Verwendung der Querschnittsflussmethode leite ich eine durchschnittliche Emission von 20,3 ± 7,9 $\mathrm{Tg\,a^{-1}}$ ab, die innerhalb der Unsicherheit mit den jährlich gemeldeten Inventardaten übereinstimmt. Die Variabilität zwischen den Überflügen resultiert hauptsächlich aus turbulenzbedingten Inhomogenitäten in der Plumeausbreitung und übersteigt die formale Messunsicherheit. Einzelne Überflüge erzielen Flussabschätzungen mit Unsicherheiten von nur 8 – 10 %. Anhand von Simulationen zeige ich, dass diese turbulenzbedingten Einschränkungen durch Nachtflüge unter stabilen Bedingungen umgangen werden könnten, bei denen selbst eine einzelne instantane Flussmessung eine Genauigkeit von etwa 95 % erreicht.

Fallstudie II befasst sich mit multiplen CH_4-Emissionen aus Lüftungsschächten von Kohlebergwerken im Oberschlesischen Kohlebecken. Um überlappende Plumes zu entflechten, entwickle ich einen neuartigen inversionsbasierten Clustering-Ansatz: Durch die Kombination von automatisierter Diagnostik mit Expertenwissen werden einzelne Schächte zu 13 Emissionsclustern zusammengefasst. Für jeden Cluster werden posteriore Emissionsschätzungen ermittelt, die eine Emissionsschätzung für das gesamte Becken von 570 ± 78 $\mathrm{kt\,a^{-1}}$ ergeben, was 16 % über den offiziell gemeldeten Inventardaten liegt. Diese Ergebnisse stimmen mit unabhängigen, auf Beobachtungen basierenden Studien überein, was die Robustheit der Methodik trotz Transport- und Hintergrundunsicherheiten unterstreicht.

Zusammengenommen zeigen diese Fallstudien, dass das flugzeuggetragene IPDA-Lidar zuverlässige und unabhängige Emissionsschätzungen sowohl für isolierte als auch für gruppierte Punktquellen liefern kann. Die Ergebnisse unterstreichen ihren

Wert für die Validierung von Inventaren, die Verringerung von Unsicherheiten bei der Berichterstattung und die Steuerung der Planung künftiger flugzeug- und satellitengestützter Missionen wie MERLIN, wodurch das globale Gesamtkonzept für die Überwachung von THG gestärkt wird.

Abstract

International climate agreements aim to reduce anthropogenic greenhouse gas (GHG) emissions over the coming decades. A substantial share of these emissions originates from localized point sources, such as power plants and coal mines. As emissions potentially become smaller, quantification methods must become more precise and robust in order to reliably detect these changes. Satellite observations are well suited for this task due to their global coverage, but most current missions rely on passive sensors that measure reflected sunlight. Their capabilities are therefore limited under clouds, over dark surfaces, and during night or polar winter.

Active remote sensing with Integrated Path Differential Absorption (IPDA) lidar overcomes these constraints. This dissertation employs the airborne IPDA lidar system CHARM–F to quantify CO_2 and CH_4 emissions from point sources using data from the 2018 CoMet campaign in Europe. Two case studies of increasing complexity demonstrate its capabilities.

Case Study I investigates the isolated CO_2 plume of the Jänschwalde coal-fired power plant. Using the cross-sectional flux method, I derive an average emission of $20.3 \pm 7.9\ \mathrm{Tg\,a^{-1}}$, which agrees within uncertainty with annually reported inventory data. The variability between overflights mainly results from turbulence-induced inhomogeneities in plume propagation and exceeds the formal measurement uncertainty. Individual overflights achieve flux estimates with uncertainties of only 8 – 10 %. Based on simulations, I show that these turbulence-driven limitations can be circumvented by conducting nighttime flights under stable conditions, where even a single instantaneous flux measurement reaches an accuracy of about 95 %.

Case Study II addresses multiple CH_4 emissions from coal mine ventilation shafts in the Upper Silesian Coal Basin. To disentangle overlapping plumes, I develop a novel inversion-driven clustering approach: by combining automated diagnostics with expert judgment, individual shafts aggregate into 13 emission clusters. Posterior emission estimates are obtained for each cluster, yielding a total basin-wide emission of $570 \pm 78\ \mathrm{kt\,a^{-1}}$, which is 16 % higher than officially reported inventory data. These results are consistent with independent observation-based studies, which highlights the robustness of the methodology despite transport and background uncertainties.

Together, these case studies show that airborne IPDA lidar provide reliable and independent emission estimates for both isolated and clustered point sources. The findings underline their value for validating inventories, reducing reporting uncertainties, and guiding the design of future airborne and spaceborne missions such as MERLIN, thereby strengthening the global framework for GHG monitoring.

List of Publications

First author

- **Determination of the emission rates of CO_2 point sources with airborne lidar** by: *Wolff, Sebastian*, Ehret, G., Kiemle, C., Amediek, A., Quatrevalet, M., Wirth, M., and Fix, A.. Atmospheric Measurement Techniques, 14(4):2717–2736, 2021. doi: 10.5194/amt-14-2717-2021.

  Chapters 2 and 3 were first published in Wolff et al. (2021). Figures and tables that were adapted or modified from the paper are explicitly indicated in their captions. Substantial parts of the text were taken literally or slightly revised from the published version to ensure consistency within the overall context of this thesis.

Co-author

- **Quantifying CH_4 emissions from hard coal mines using mobile sun-viewing Fourier transform spectrometry** by: Luther, A., Kleinschek, R., Scheidweiler, L., Defratyka, S., Stanisavljević, M., Forstmaier, A., Dandocsi, A., *Wolff, Sebastian*, Dubravica, D., Wildmann, N., Kostinek, J., Jöckel, P., Nickl, A.-L., Klausner, T., Hase, F., Frey, M., Chen, J., Dietrich, F., Nęcki, J., Swolkień, J., Fix, A., Roiger, A., and Butz, A.. Atmospheric Measurement Techniques, 12(10):5217–5230, 2019. doi: 10.5194/amt-12-5217-2019.

- **Evaluation of simulated CO_2 power plant plumes from six high-resolution atmospheric transport models** by: Brunner, D., Kuhlmann, G., Henne, S., Koene, E., Kern, B., *Wolff, Sebastian*, Voigt, C., Jöckel, P., Kiemle, C., Roiger, A., Fiehn, A., Krautwurst, S., Gerilowski, K., Bovensmann, H., Borchardt, J., Gałkowski, M., Gerbig, C., Marshall, J., Klonecki, A., Prunet, P., Hanfland, R., Pattantyús-Ábrahám, M., Wyszogrodzki, A., and Fix, A.. Atmospheric Chemistry and Physics, 23(4):2699–2728, 2023. doi: 10.5194/acp-23-2699-2023.

- **Identification and Quantification of CH_4 Emissions from Madrid Landfills using Airborne Imaging Spectrometry and Greenhouse Gas Lidar** by Krautwurst, S., Fruck, C., *Wolff, Sebastian*, Borchardt, J., Huhs, O., Gerilowski, K., Gałkowski, M., Kiemle, C., Quatrevalet, M., Wirth, M., Mallaun, C., Burrows, J. P., Gerbig, C., Fix, A., Bösch, H., and Bovensmann, H.. EGUsphere, 2024:1–52, 2024. doi: 10.5194/egusphere-2024-3182.

Contents

Zusammenfassung **vii**

Abstract **ix**

List of Publications **xi**

Acronyms **xv**

1 Introduction **1**
1.1 Motivation . . . 1
1.2 Satellite GHG Observations . . . 5
1.3 Research Objective . . . 11
1.4 Thesis Outline . . . 12

2 Methodology **13**
2.1 Measurement Techniques . . . 14
2.1.1 Lidar in Atmospheric Science . . . 14
2.1.2 The Airborne IPDA Lidar CHARM-F . . . 16
2.1.3 The CoMet 1.0 Campaign . . . 21
2.2 Numerical Modelling . . . 24
2.2.1 Atmospheric Transport Modelling . . . 24
2.2.2 Weather Research and Forecast Model . . . 25
2.2.3 WRF Setup . . . 27

3 Case Study I: Quantification of an Isolated CO_2 Point Source **33**
3.1 Cross-Sectional Flux Method . . . 34
3.1.1 Background Separation and Enhancement Integration . . . 37
3.1.2 Uncertainty Estimation . . . 39
3.1.3 CO_2 Flux Estimation . . . 41
3.2 Large Eddy Simulation . . . 44
3.2.1 WRF-LES Setup . . . 44
3.2.2 WRF-LES Simulation Results . . . 48
3.3 Summary & Conclusion . . . 52

4 Case Study II: Quantification of Multiple CH_4 Point Sources **55**
4.1 The Upper Silesian Coal Basin . . . 57
4.1.1 Previous Studies . . . 59
4.1.2 Airborne CHARM–F Observations . . . 62
4.2 Bayesian Inverse Modelling & Ensemble Approach . . . 65

4.2.1 CTDAS-WRF Setup 70
4.3 Initial Inversion & Source Clustering 76
4.3.1 Analysis of the Initial Inversion 76
4.3.2 Development of Inversion-Driven Source Clustering 85
4.4 Final Results & Discussion 95
4.4.1 Best-Estimate Inversion 95
4.4.2 Sensitivity Analysis 98
4.4.3 Total Emission Estimate 103
4.5 Summary & Conclusion 105

5 From Case Studies to Spaceborne Applications 107
5.1 Thesis Summary and Outcomes 107
5.2 Recommendations for Future Campaigns 109
5.3 Outlook 111

A Supplement 115
A.1 Calculation of Simulated DAOD 115
A.2 Auxiliary Equations 116
A.3 Supplementary Figures 117
A.4 Supplementary Tables 119

B Inverse Modelling for Regional CH_4 Emissions 121
B.1 Bayesian Formalism 122
B.2 Maximum a Posteriori Solution 124
B.3 Ensemble Kalman Filter 126
B.4 Prior Emissions for Non-Reporting Shafts 130

Bibliography 160

Acknowledgments 161

Acronyms

ACM	Active Coal Mines
ACMCZ	Active Coal Mines in Czechia
ACMX	Active Coal Mines no reported emissions
AFWA	Air Force Weather Agency
APD	Avalanche Photodiode
ARW	Advanced Research WRF
ATM	Atmospheric Transport Model
ACDL	Aerosol and Carbon Dioxide Detection Lidar
CAMS	Copernicus Atmosphere Monitoring Service
CHARM–F	CO_2 and CH_4 Remote Monitoring–Flugzeug
CNES	Centre National d'Études Spatiales
CO2M	Carbon Dioxide Monitoring Mission
CoMet	Carbon Dioxide and Methane Mission
CoMet ED	CoMet Emission Database
CRDS	Cavity Ring–Down Spectroscopy
CTDAS	Carbon Tracker Data Assimilation Shell
DAOD	Differential Absorption Optical Depth
DIAL	Differential Absorption Lidar
DLR	Deutsches Zentrum für Luft- und Raumfahrt
ECMWF	European Centre for Medium–Range Weather Forecasts
EDGAR	Emissions Database for Global Atmospheric Research
EnKF	ensemble Kalman filter
EnMAP	Environmental Mapping and Analysis Program

E-PRTR	European Pollutant Release and Transfer Register
FAA	Federal Aviation Administration
FDDA	Four–Dimensional Data Assimilation
flh	flight height
FUB	Freie Universität Berlin
GHG	greenhouse gas
GOSAT	Greenhouse Gases Observing Satellite
GST	Global Stocktake
HALO	High Altitude and Long Range Research Aircraft
ICM	Inactive/closing Coal Mines
IFS	Integrated Forecasting System
IPA	Institut für Physik der Atmosphäre
IPCC	Intergovernmental Panel on Climate Change
IPDA	Integrated Path Differential Absorption
ISS	International Space Station
JAS	Jena Air Sampler
JIG	Jena Instrument for Greenhouse gas measurements
LSM	Land–Surface Model
LEAG	Lausitz Energie Kraftwerke AG
LES	Large Eddy Simulation
lidar	Light Detection And Ranging
MAMAP	Methane Airborne MAPper
MAP	maximum a posteriori
MERLIN	Methane Remote Sensing Lidar Mission
MM5	Mesoscale Model 5
MRV	Measurement, Reporting, and Verification
MYNN	Mellor–Yamada Nakanishi Niino

NCAR	National Center for Atmospheric Research
NDC	Nationally Determined Contribution
NIR	Near Infrared
NOAA	National Oceanic and Atmospheric Administration
NWP	Numerical Weather Prediction
OCO	Orbiting Carbon Observatory
OPO	Optical Parametric Oscillator
PBL	Planetary Boundary Layer
PDF	probability density function
PIN	Positive Intrinsic Negative diode
PP	Power/Cogeneration Plants
PRISMA	Precursore Iperspettrale della Missione Applicativa
QCLS	Quantum Cascade Laser Spectrometer
RRTMG	Rapid Radiative Transfer Model for General Circulation Models
RQ	research question
RM	running mean
S5P	Sentinel–5 Precursor
sfc	surface
SNAP	Selected Nomenclature for Sources of Air Pollution
SNR	Signal–to–Noise Ratio
SWIR	Short–Wave Infrared
TCCON	Total Carbon Column Observing Network
TROPOMI	Tropospheric Monitoring Instrument
USCB	Upper Silesian Coal Basin
UNFCCC	United Nations Framework Convention of Climate Change
WMO	World Meteorological Organization
WRF	Weather Research and Forecast model

1 Introduction

1.1 Motivation

The Changing Climate

In 2024, the annual mean temperature on Earth surpassed 1.5 °C above pre-industrial levels for the first time on record (Tollefson 2025). The record-breaking heat of 2024 was not a mere statistical outlier, but a continuation of an ongoing warming trend. As shown in Fig. 1.1, even when 2024 is excluded, the 30-year trend still indicates that the 1.5 °C threshold will be reached by 2031 (Copernicus 2024).

Rising global temperatures lead to more energy in the Earth system, intensifying evaporation and increasing atmospheric water vapour. This enhances the potential for extreme weather, such as storms, heavy rainfall, and droughts, while also accelerating ice melt and contributing to sea level rise. Consistent with these physical mechanisms, the World Meteorological Organization (WMO) and the Intergovernmental Panel on Climate Change (IPCC) report that heatwaves, droughts, floods, and tropical storms have already increased in both frequency and intensity across many regions worldwide (Siegmund et al. 2020; IPCC 2021).

Recent events illustrate these trends vividly. After a prolonged drought from 2020 to 2023, heavy rainfall triggered severe flooding across much of East Africa from March to May 2024, resulting in hundreds of fatalities (Kimutai et al. 2024). In June 2024, devastating wildfires burned over 400 000 hectares in Brazil's Pantanal wetlands, destroying vast ecosystems and intensifying biodiversity loss (CAMS 2024; Barnes et al. 2024). That same month, over 1000 pilgrims died from extreme heat stress during the Hajj pilgrimage in Mecca, Saudi Arabia, where temperatures soared beyond 50 °C (Memish et al. 2024; Ripple et al. 2024). In September and October 2024, widespread flooding hit Spain and Central Europe, submerging towns and causing hundreds of fatalities and billions of dollars in economic losses (Munich Re 2025). During this time, hurricanes Helene and Milton brought extreme rainfall, high winds, and severe flooding to the southeastern United States, parts of Mexico, and the Antilles. This was fuelled by exceptionally high sea surface temperatures in the Gulf of Mexico (Barnes et al. 2024; Munich Re 2025). The incidence of severe tropical storms and intense rainfall has surged, a trend expected to continue without drastic climate change mitigation (Knutson et al. 2020, 2021; Parmesan et al. 2022).

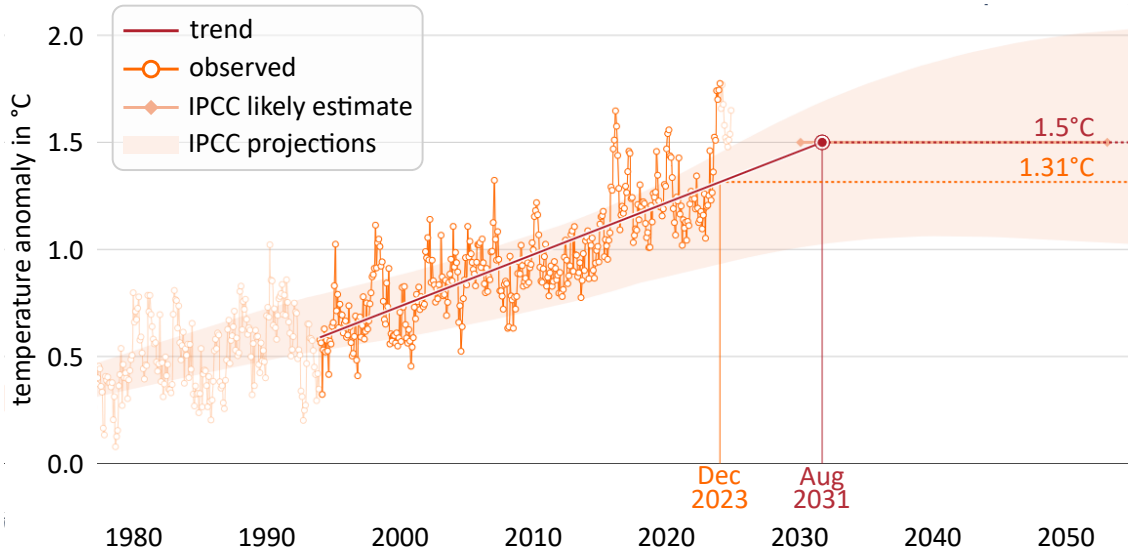

Figure 1.1: Global surface air temperature anomalies relative to the pre-industrial average (1850–1900), based on ERA5 reanalysis data (Copernicus 2024). The time series shown spans 1980 to 2025, with a linear trend (red line) fitted to the 30-year period ending in December 2023 (highlighted in dark orange). If this recent trend were to continue, global warming would reach 1.5 °C by August 2031. The shaded orange area represents the interquartile range of climate model projections from the IPCC Special Report on Global Warming of 1.5 °C, illustrating an uncertainty envelope under a moderate mitigation scenario. Plot downloaded from https://climate.copernicus.eu/ (accessed February 2025).

The socioeconomic consequences of these escalating climate extremes are profound. The *2024 State of the Climate Report* by Ripple et al. (2024) warns that rising temperatures are exacerbating food and water insecurity, displacing vulnerable populations, and straining economies. Heat stress threatens labour productivity, while droughts and shifting rainfall patterns reduce agricultural yields. The financial toll of extreme weather is mounting, with damages from storms, wildfires, and floods costing billions annually.

Emissions Accounting

Recognizing the severity of the climate crisis, the Paris Agreement explicitly acknowledges the necessity of limiting global warming to "well below" 2 °C relative to pre-industrial average air temperatures, with a preferable target of 1.5 °C (UNFCCC 2015). This commitment is based on the well-established fact that rising global temperatures are driven by increasing concentrations of atmospheric greenhouse gases (GHGs) caused by human activities (Cook et al. 2013; Lynas et al. 2021; IPCC 2021).

These gases influence the Earth's climate system by altering the radiative energy balance, a process known as radiative forcing. GHGs are trace constituents of the atmosphere that absorb and re-emit infrared radiation. Incoming solar radiation, primarily in the visible and near-infrared spectrum, mostly passes through the

atmosphere and warms the Earth's surface; the energy is re-emitted upward as radiation in the mid- to far-infrared spectrum. GHGs absorb part of this outgoing radiation and re-emit it in all directions, including back toward the surface, effectively trapping energy in the lower atmosphere. This greenhouse effect increases the downward infrared flux, reduces the loss of heat to space, and creates a radiative imbalance that leads to surface warming until a new thermal equilibrium is established. Observations from the National Oceanic and Atmospheric Administration (NOAA) Global Monitoring Laboratory show that concentrations of CO_2 and CH_4 have reached unprecedented levels in the modern observational record (Fig. 1.2).

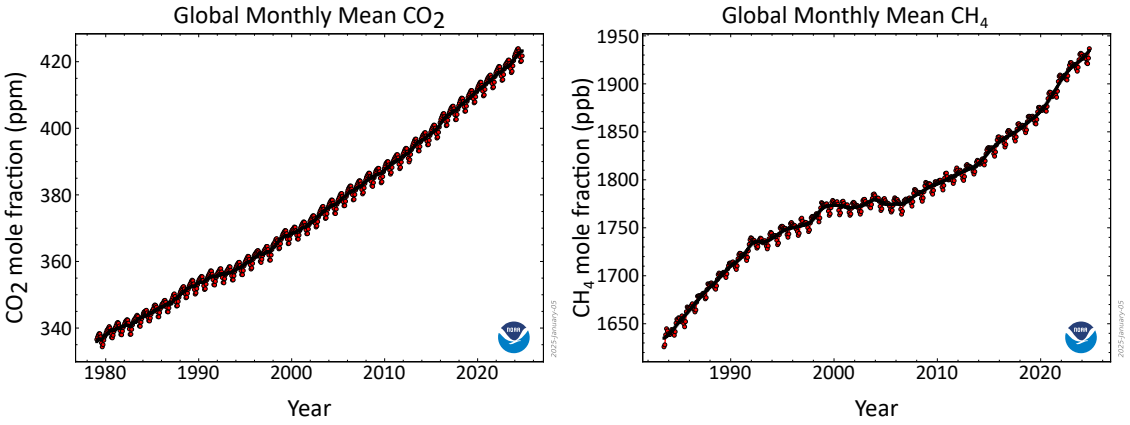

Figure 1.2: Global monthly mean mole fraction of CO_2 (left) and CH_4 (right) from NOAA's Global Monitoring Laboratory (Lan et al. 2025a,b, last updated: 05.01.2025). The red line with dots represents raw monthly mean values, while the black line depicts the long-term trend with the average seasonal cycle removed. Data are based on marine surface measurements from a globally distributed network of air sampling sites.

While the focus of this discussion lies on anthropogenic emissions, it is important to note that natural sources and sinks also contribute substantially to the atmospheric budgets of both CO_2 and CH_4. For CO_2, key natural fluxes include plant and soil respiration as well as ocean-atmosphere exchange, with uptake by terrestrial biomass and oceanic absorption acting as the main natural sinks (Friedlingstein et al. 2023). In the case of CH_4, natural emissions primarily originate from wetlands, followed by freshwater systems, geological seepage, and wildfires. Its removal from the atmosphere occurs mainly through oxidation in the troposphere, particularly via reaction with hydroxyl radicals (OH), ultimately producing CO_2 and H_2O (Saunois et al. 2025). Although these natural fluxes have generally remained near equilibrium under undisturbed conditions, recent trends — particularly the pronounced rise in atmospheric atmospheric CH_4 in the last two decades — may also reflect changes in natural emissions. In this context, wetland contributions represent a key area of ongoing research and scientific uncertainty.

Nonetheless, anthropogenic activities are widely recognised as the dominant drivers of the long-term increase in atmospheric GHG concentrations. Anthropogenic CO_2 emissions from sources such as fossil fuel combustion, industrial processes, and

land-use changes have increased atmospheric CO_2 mole fractions from a pre-industrial baseline of approximately 280 ppm to over 420 ppm as of 2025 (Friedlingstein et al. 2023; Lan et al. 2025a). Simultaneously, CH_4 mole fractions have more than doubled from approximately 735 ppb to over 1940 ppb, largely due to agricultural activities, fossil fuel extraction, waste management, and biomass burning (Saunois et al. 2025; Lan et al. 2025b).

To effectively curb further warming, each signatory state to the Paris Agreement has committed to so-called Nationally Determined Contributions (NDCs). These NDCs outline emission reduction measures based on each country's capabilities and economic development (UNFCCC 2015). A central mechanism for assessing the effectiveness of these measures is the Global Stocktake (GST), to be conducted every five years since 2023. As part of this process, countries compile national GHG emission inventories, which are submitted to the United Nations Framework Convention of Climate Change (UNFCCC) to evaluate progress toward individual NDCs and ensure collective progress in mitigating GHG emissions.

Two principal approaches exist for quantifying emissions: bottom-up and top-down methods. Bottom-up inventories estimate emissions based on local activity data and process-specific emission factors, scaling these estimates up to regional or national levels. This approach allows for clear attribution of emissions to specific sources and sectors, providing insights into where emissions originate. However, it relies heavily on assumed emission factors, which are often uncertain and require continuous verification. Moreover, bottom-up inventories can only account for expected emissions and fail to capture unintended or unknown emission sources, such as leakages, wetland emissions, or wild fires.

In contrast, top-down approaches estimate emissions based on observations of atmospheric GHG concentrations, combined with information on atmospheric transport and sinks. As outlined by Jacob et al. (2022), top-down methods comprise a wide variety of techniques, spanning from global to local spatial scales. One such technique is the cross-sectional flux method, which quantifies emission rates by multiplying the mean wind speed with the integrated concentration enhancement along a cross-sectional overflight of the exhaust plume, relative to a known background. This requires that the full plume is intercepted and clearly distinguishable from other sources, as uncertainties in background concentrations directly affect the accuracy of the flux estimate. This method has been widely applied in both airborne and satellite-based studies.

Another key method in this category is inverse modelling, which uses mathematical optimization techniques to infer surface fluxes from atmospheric measurements (Houweling et al. 2017). Unlike bottom-up methods, inverse modelling does not require prior knowledge of emission processes or sectoral classifications. This makes it particularly valuable for identifying unexpected or underestimated sources. However, this advantage comes with its own challenges: the accuracy of the inferred emissions depends critically on the quality of the atmospheric transport models used. Errors in wind fields or mixing processes can lead to incorrect emission estimates, and the spatial resolution of these methods is often too coarse to attribute emissions precisely

to specific sources. Furthermore, the accuracy of top-down estimates is fundamentally limited by observational constraints. Many regions remain poorly sampled, leading to gaps in spatial coverage and maintaining high levels of uncertainty. Sparse or infrequent measurements contribute to an underdetermined inversion problem, whereby the same data can be explained by multiple emission patterns. Furthermore, discrepancies between observations and model representations (e.g. due to differences in timing, scale, or physical assumptions) can introduce further biases.

Following the IPCC's Guidelines from 2006, national inventories are primarily compiled using bottom-up methodologies (IPCC 2006). Since then, however, top-down methods, i.e. global and regional inverse modelling systems, have advanced considerably. They now incorporate data from ground-based networks, aircraft, and satellites (Houweling et al. 2017). Despite recent advances, substantial differences between bottom-up and top-down estimates persist. According to the latest *Global Methane Budget* by Saunois et al. (2025), the discrepancy has narrowed compared to the 2020 assessment, but the global estimates still diverge significantly. For example, bottom-up estimates suggest global CH_4 emissions of $669\,\mathrm{Tg\,a^{-1}}$ [512–$849\,\mathrm{Tg\,a^{-1}}$], while top-down inversions yield a lower estimate of $575\,\mathrm{Tg\,a^{-1}}$ [553–$586\,\mathrm{Tg\,a^{-1}}$]. Similarly, land-use change emissions of CO_2 remain highly uncertain, contributing to a budget imbalance of approximately $1\,\mathrm{Pg\,a^{-1}}$ (Friedlingstein et al. 2023).

Recognizing the complementary value of top-down constraints, the IPCC's *Refinement to the 2006 Guidelines* from 2019 acknowledges that comparisons between bottom-up inventories and independent top-down estimates can help identify inconsistencies and improve inventory accuracy (IPCC 2019). In line with the UNFCCC reporting framework, developed countries are encouraged to complement bottom-up inventories with independent atmospheric measurements as part of a robust Measurement, Reporting, and Verification (MRV) system. This includes the use of top-down approaches to help reduce uncertainties and improve transparency in national GHG reporting.

1.2 Satellite GHG Observations

Satellite instruments provide global observations with consistent spatial and temporal resolution. They enable systematic monitoring even in regions with sparse in situ networks and reduce cross-platform calibration uncertainties. Recent studies have demonstrated the benefits of satellite-based top-down approaches for emissions verification. Specifically, Worden et al. (2023) and Byrne et al. (2023) examined how CH_4 and CO_2 measurements improve emission estimates. Both studies confirm that top-down constraints enhance the accuracy of GHG monitoring. However, they struggle to resolve localized sources due to their coarse spatial resolution.

Addressing this limitation, Jacob et al. (2022) emphasize that satellite observations with finer spatial resolution are necessary to pinpoint and quantify CH_4 emissions from sources such as oil and gas infrastructure, landfills, and agricultural activities. Moreover, Williams et al. (2025) highlight that a disproportionate fraction of CH_4 emissions originates from numerous small, diffuse sources, many of which remain undetected by current satellite instruments due to sensitivity and resolution

limits. Complementing this, Cusworth et al. (2022) demonstrate that strong point sources, such as super-emitters from oil and gas infrastructure, contribute disproportionately to regional CH_4 budgets — accounting for up to 40 % of total emissions in major U.S. oil and gas basins.

Similarly, Strandgren et al. (2020) demonstrate that spaceborne monitoring of localized CO_2 emissions requires higher spatial resolution for improved quantification, particularly for medium-sized power plants ($1 - 10$ Mt a^{-1}). Many of these sources contribute significantly to the overall CO_2 emissions, yet they remain below the detection threshold of current missions. In fact, power plants alone account for 38 % of global CO_2 emissions from fossil fuels (Crippa et al. 2024), with medium-sized plants accounting for around two-thirds of total power plant emissions. Yet they remain below the detection threshold of current missions (Strandgren et al. 2020).

Given that a substantial share of anthropogenic GHG emissions stems from localized point sources (e.g. coal-fired power plants, landfills, and fossil fuel extraction sites), accurate detection and quantification of these emitters is critical for effective emissions monitoring and climate policy enforcement.

Passive Remote-Sensing

Most existing satellite missions that provide insights into point source emissions of CO_2 and CH_4 rely on passive remote-sensing instruments, measuring solar radiation reflected from the Earth's surface. The Japanese Greenhouse Gases Observing Satellite (GOSAT) series, operational since 2009, is a pioneer in satellite-based GHG monitoring. It was the first dedicated satellite program to measure atmospheric CO_2 and CH_4 concentrations globally and has now delivered over 16 years of continuous observations. These long-term records represent the longest space-based time series of column-averaged greenhouse gas concentrations and serve as a critical reference for background levels and trend detection (Matsunaga and Tanimoto 2022; Tanimoto et al. 2025). Although its spatial resolution limits its ability to detect localized point sources, its value lies in enabling broad-scale flux estimates and in complementing higher-resolution satellites by providing coverage in regions with sparse observations (Hancock et al. 2025; Gadhavi et al. 2024).

Subsequently, the Orbiting Carbon Observatory (OCO) missions have expanded on these capabilities with improved spatial resolution and more flexible targeting. Currently, they provide the most advanced capabilities to quantify CO_2 emissions from localized sources. Launched in 2014, OCO-2 follows a sun-synchronous orbit and observes preselected locations, such as validation sites and a limited number of large emission sources (Nassar et al. 2021). OCO-3 has been mounted on the International Space Station (ISS) since 2019. It has greater observational flexibility than OCO-2 and can target emission sources more dynamically (Cusworth et al. 2023). However, its coverage is constrained by the orbit of the ISS, limiting observations to latitudes between approximately 52 °S and 52 °N (Moeini et al. 2025). Both missions have demonstrated the feasibility of quantifying CO_2 emissions from space. Even so, their sensitivity is limited to the largest point sources worldwide, like the coal-fired power plants Bełchatów (Poland) and Matimba (South Africa), which emit tens to hundreds

of kilotons of CO_2 per day (Nassar et al. 2021).

Detecting CO_2 plumes from anthropogenic sources is particularly challenging due to the high and variable atmospheric background. By contrast, CH_4 often exhibits sharper spatial gradients and stronger absorption features in spectral regions accessible to a broader range of remote-sensing instruments. Beyond that, CH_4 is increasingly integrated into satellite observation strategies due to its unique appeal as a mitigation target. Emission reductions are often technically straightforward and economically attractive, especially in the fossil fuel sector, where leak detection directly translates into resource savings (Nisbet et al. 2020; Kuhlmann et al. 2025). Furthermore, CH_4 has a relatively short atmospheric lifetime of less than 10 years (Prather and Zhu 2024), compared to CO_2's lifetime of hundreds to thousands of years (Archer et al. 2009). Thus, reducing CH_4 emissions rapidly yields tangible climate benefits by swiftly lowering radiative forcing and near-term warming. Accordingly, the combination of clearer detection capabilities and immediate climate benefits has driven an increasing number of satellite missions dedicated to CH_4 in recent years (Nisbet et al. 2020; Jacob et al. 2022).

The Tropospheric Monitoring Instrument (TROPOMI) plays a central role in the large-scale identification of CH_4 emitters. It was launched in October 2017 on board the Sentinel–5 Precursor (S5P) satellite as part of the European Copernicus programme. With its daily global coverage and high sensitivity to large CH_4 sources, TROPOMI provides a unique capability for systematic detection of major emitters. It has been successfully used to identify strong emissions from various sectors, including oil and gas infrastructure (Dubey et al. 2023), landfills (Tu et al. 2022a) and hard-coal mining (Tu et al. 2022b). However, due to its relatively coarse spatial resolution of approximately $5.5 \times 5.5\,\mathrm{km}$, TROPOMI cannot precisely detect smaller emissions ($< 25\,\mathrm{t/h}$), localize emission sources within a facility, or distinguish between multiple nearby sources (Lauvaux et al. 2022).

To refine emission estimates and pinpoint exact source locations, high-resolution satellite imagery is used complementary to TROPOMI detections. Several studies have shown that missions such as Sentinel-2, the Precursore Iperspettrale della Missione Applicativa (PRISMA) or the Environmental Mapping and Analysis Program (EnMAP) can detect large CH_4 plumes under favourable conditions, although they were not originally designed for CH_4 detection (Varon et al. 2021; Guanter et al. 2021; Ehret et al. 2022; Roger et al. 2024). These and other imaging spectrometers offer spatial resolutions in the range of 20–30 m, but have lower spectral resolution and/or operate in spectral bands that are not optimal for detecting CH_4. Furthermore, their spatial coverage is significantly lower than that of TROPOMI, with revisit times that are typically much longer, ranging from several days to weeks depending on the satellite and location. Moreover, some instruments must be actively pointed at a region of interest, either through pre-scheduled acquisitions or on-demand tasking. This limits their ability to systematically monitor emissions over time.

In addition to publicly available missions, several commercial and restricted-access satellites record high-resolution CH_4 observations. Commercial platforms such as GHGSat and WorldView-3 offer facility-scale monitoring (Varon et al. 2020; Jervis et al. 2021; Sánchez-García et al. 2022). However, their coverage is often

limited to targeted acquisitions rather than systematic global monitoring. Similarly, some government-operated missions, including Gaofen-5, Ziyuan-1, and Huanjing-2B, operate under restricted data policies, further limiting their use for independent verification and systematic global monitoring.

Despite these limitations, several comparative studies have evaluated their detection capabilities (Irakulis-Loitxate et al. 2021, 2022; Sherwin et al. 2023, 2024). These studies highlight that detection performance of all passive satellite instruments is often strongly influenced by surface reflectivity and cloud cover, regardless of their spectral or spatial resolution. In particular, low-albedo surfaces such as water bodies, forests, and snow-covered areas remain especially challenging for reliable retrievals (Ehret et al. 2022). As a result, many studies have focused on homogeneous surfaces with high albedo, such as deserts and snow-free regions, where the increased reflected radiation enhances backscattered signal and thus the detection sensitivity. Key study areas include Algeria, Turkmenistan, and China's Shanxi region, as well as fossil fuel production basins such as the Permian Basin in the U.S. (Guanter et al. 2021; Irakulis-Loitxate et al. 2021, 2022; Sánchez-García et al. 2022).

Aggravating these issues, cloud cover and aerosols pose major limitations, particularly in tropical regions. Here, persistent shallow cumulus clouds result in extremely low data yields, often below 1 %, even for dedicated GHG missions such as OCO-2 (Frankenberg et al. 2024). As a consequence, CH_4 emissions from key oil and gas basins frequently remain obscured from satellite view, especially during the wet season (Lauvaux et al. 2022). In regions where sporadic clear-sky conditions limit single-pass observations, many studies rely on long-term data collection from multiple overpasses over several years to improve the reliability of emission estimates (Tu et al. 2022b; Dubey et al. 2023). Offshore emissions present an additional challenge, as they can only be observed under sunglint conditions, where the solar incidence angle is equal to the instrument view angle (Roger et al. 2024).

These limitations cause persistent gaps, particularly in the detection of weaker point sources and in achieving frequent global coverage. The upcoming Copernicus Carbon Dioxide Monitoring Mission (CO2M), a constellation of three satellites in sun-synchronous orbit, is scheduled for launch in 2027[1]. It will enhance the quantification of anthropogenic CO_2 and CH_4 emissions by providing higher spatial resolution ($\sim 2\,\mathrm{km}$) and more frequent observations than current missions, achieving a revisit time of 2–3 days (Meijer et al. 2020; Sierk et al. 2021). The mission's primary instrument is an imaging spectrometer which will retrieve CO_2 and CH_4 concentrations using Near Infrared (NIR) and Short–Wave Infrared (SWIR) spectroscopy at a spectral resolution of 0.3 nm (Strandgren et al. 2020; Reuter et al. 2025). The addition of NO_2 retrievals will help distinguish fossil fuel-related CO_2 emissions from natural background variability by co-detecting NO_2 plumes, which are associated with combustion processes (Kuhlmann et al. 2021; Fuentes Andrade et al. 2024). To further improve retrieval accuracy, CO2M incorporates additional sensors. A multi-angle polarimeter will characterize aerosols, reducing their impact on CO_2 and CH_4 retrievals. A dedicated cloud imager will enhance cloud screening, mitigating biases caused by partial cloud cover (Spilling and Thales 2021; Reuter et al. 2025).

[1] See https://www.sron.nl/en/missions/in-development/co2m/ (last access 20.08.2025)

Despite these significant improvements, CO2M remains fundamentally constrained by inherent limitations of passive remote-sensing. Observations still depend on surface reflectivity, and region-specific retrieval biases may arise from low albedo, atmospheric scattering, or aerosol loading — factors that restrict detection capabilities and affect the accuracy of emission estimates across different geographic regions. For instance, reduced sunlight intensity and lower solar elevation angles at high latitudes limit measurement accuracy, while observations become entirely impossible during polar winter. Moreover, persistent convective cloud cover in tropical regions severely limits observations, leaving critical data gaps. These high-latitude and tropical regions are not only important for anthropogenic emissions but are also crucial for understanding climate-driven changes in natural emissions, particularly from boreal and tropical wetlands (Yu et al. 2023).

Active Remote-Sensing

Active remote-sensing in the optical spectral range is a effective measurement approach for overcoming these observational limitations. Unlike passive sensors, which rely purely on reflected sunlight, active systems emit their own signal and detect how it interacts with the atmosphere. In the context of atmospheric GHG monitoring, the key active remote-sensing technique is differential absorption lidar (Light Detection And Ranging).These instruments transmit short laser pulses at specific wavelengths and measure the returned signal after scattering by atmospheric constituents. By applying the time-of-flight principle at multiple wavelengths, they can infer trace gas concentrations providing range-resolved information (e.g. water vapour volume mixing ratio). One specialized technique is Integrated Path Differential Absorption (IPDA) lidar, which relies entirely on the echoes from so-called hard targets like the Earth surface or cloud tops. This helps to improve the measurement sensitivity by more than two orders of magnitude.

In spaceborne applications, IPDA lidar enables global measurements both day and night, and across all surface types, including water and low-reflectivity regions (Ehret et al. 2008). It can be operated under different climatic conditions, retrieve signals through cloud gaps, and is largely unaffected by aerosol interference (discussed in more detail in Sect. 2.1.2). Taken together, these factors significantly improve observational coverage and measurement reliability.

China's Aerosol and Carbon Dioxide Detection Lidar (ACDL), launched in 2022 onboard the DQ-1 satellite, marks the first spaceborne lidar dedicated to CO_2 detection (Shi et al. 2023). Han et al. (2024) demonstrated its capability to quantify emissions from a wide range of power plants worldwide. Reported emission estimates range from $6 \pm 1\,\mathrm{Tg\,a^{-1}}$ for Shenhua Guoneng Hami power station in China, $15 \pm 4\,\mathrm{Tg\,a^{-1}}$ for Jim Bridger in the U.S., up to $21 \pm 3\,\mathrm{Tg\,a^{-1}}$ for Majuba in South Africa. Compared to passive sensors, ACDL achieved significantly greater observational coverage, surpassing the combined data availability of OCO-2 and OCO-3. This advantage was particularly pronounced in high-aerosol environments, such as Northern China, where passive sensors suffered from strong signal attenuation, while ACDL maintained nearly complete observational coverage. These results demonstrate

the potential of spaceborne lidar to overcome limitations associated with cloud cover and aerosol interference, enabling more consistent and reliable CO_2 monitoring.

Similar improvements in observational coverage and data reliability can be expected for CH_4 in the near future. The upcoming Methane Remote Sensing Lidar Mission (MERLIN) is a joint French-German initiative by Centre National d'Études Spatiales (CNES) and Deutsches Zentrum für Luft- und Raumfahrt (DLR) and is scheduled for launch in 2030 (Ehret et al. 2017; Bousquet et al. 2018). It will be the first dedicated spaceborne CH_4 lidar, providing unprecedented measurement capabilities for global CH_4 monitoring. By leveraging IPDA technology, MERLIN is expected to address key data gaps, particularly in crucial regions for understanding climate-sensitive natural CH_4 sources, such as boreal and tropical wetlands, as mentioned above. While anticipated benefits of MERLIN have primarily been emphasised for high-latitude CH_4 observations, its global coverage, low systematic errors, and resilience to cloud interference make it equally valuable for monitoring anthropogenic emission hotspots, particularly in tropical and mid-latitude regions, as well as over water surfaces, where passive systems fall short.

While spaceborne IPDA lidar missions like ACDL and MERLIN significantly enhance global CO_2 and CH_4 monitoring, airborne measurements remain indispensable for both mission development and operational validation. Airborne lidar systems serve as crucial testbeds for refining retrieval algorithms, calibrating satellite instruments, and improving emission quantification methodologies. Notably, the CO_2 and CH_4 Remote Monitoring–Flugzeug (CHARM–F) lidar system has played a pivotal role in developing IPDA technology for space applications (Amediek et al. 2017). It is the only IPDA lidar system worldwide that is capable of simultaneously measuring both CO_2 and CH_4 and serves as an airborne demonstrator for MERLIN and other future spaceborne IPDA GHG lidar missions. CHARM–F has been instrumental in validating the lidar retrieval concept, optimizing measurement strategies, and assessing systematic errors (Fix et al. 2011; Amediek and Wirth 2017).

Beyond technological developments, airborne campaigns are critical to bridge the scale between ground-based in situ networks and satellite-based observations, enabling high-resolution validation of emission estimates and improving our understanding of atmospheric transport processes (Nisbet et al. 2020). Aircraft measurements also offer unique flexibility to investigate specific sources under targeted conditions, allowing rapid deployment in response to satellite detections or public reporting. A notable example is provided by Krautwurst et al. (2024), where airborne measurements conclusively verified CH_4 emissions from a landfill in Madrid that was not listed as an active emitter despite clear satellite indications. Such campaigns demonstrate the value of aircraft-based validation as an independent tool for source attribution and policy-relevant emission verification. While aircraft alone cannot provide long-term monitoring of transient sources, they remain essential for validating satellite observations, investigating anomalies, and capturing emissions under challenging conditions. As such, airborne platforms continue to play a vital role in the calibration, validation, and verification framework for spaceborne missions, helping to ensure the reliability and credibility of global GHG monitoring efforts (CEOS 2024).

1.3 Research Objective

Building on recent advances in airborne IPDA lidar technology, this dissertation aims to improve the quantification of CO_2 and CH_4 emissions from point sources. The focus lies on point sources with high emissions, which require precise quantification due to their significant impact on both regional and global GHG budgets. This work supports the broader aim of developing reliable, high-resolution methodologies for independent emissions monitoring, an essential component of verifying mitigation efforts under international climate agreements such as the Paris Agreement.

Airborne IPDA lidar systems, such as CHARM–F, provide highly precise column measurements and can resolve emissions from individual facilities. As a demonstrator for the future MERLIN satellite mission, CHARM–F also allows the development and validation of techniques that will later be used in spaceborne applications. This study builds on high-resolution lidar observations from the airborne CHARM–F system, collected during the 2018 Carbon Dioxide and Methane Mission (CoMet) in Europe (see Sect. 2.1.3). These data are combined with atmospheric transport modelling to investigate two distinct case studies:

- **Case study I:** A scenario involving an *isolated CO_2 point source* — the Jänschwalde coal-fired power plant. The analysis focuses on retrieving emission rates using the so-called cross-sectional flux method and assess their accuracy against reported inventory emissions. The absence of nearby sources allows a direct association between the observed plume and facility-level emissions.

- **Case study II:** A more complex setting with *multiple CH_4 sources* — specifically several coal mine ventilation shafts in the Upper Silesian Coal Basin (USCB), which form overlapping CH_4 exhaust plumes. Here, inverse modelling is applied to disentangle source contributions and evaluate the extent to which airborne observations can constrain emission attribution.

Atmospheric transport modelling is employed in both cases to better understand the dynamics of plume dispersion and to evaluate how different flight strategies and meteorological conditions affect emission quantification. This leads to the formulation of the following research questions (RQs):

- **RQ1:** How accurately can the **cross-sectional flux method quantify** CO_2 emissions from an **isolated point source**?

- **RQ2:** Can a combination of airborne IPDA lidar and **inverse modelling** be used to **quantify** and **spatially attribute** overlapping atmospheric signals from CH_4 emissions from **multiple sources**?

- **RQ3:** Under which atmospheric conditions and flight geometries do **uncertainties** in IPDA-based emission quantification become most pronounced, and how can **future flight planning** be adapted to **mitigate** these effects?

To answer these questions, this dissertation integrates observational data, numerical modelling, and methodological development to evaluate both the potential and

limitations of IPDA lidar for emissions monitoring. The two case studies span different levels of complexity and target different GHGs, offering a comprehensive assessment of current capabilities and guiding the design of future airborne and spaceborne campaigns.

1.4 Thesis Outline

To address the **RQs** outlined in Section 1.3, , this thesis progresses from methodological groundwork to two applied case studies. This stepwise approach is designed to gradually increase real-world complexity, beginning with an isolated, well-characterised point source to build methodological confidence, and advancing to a more complex region with overlapping plumes to test the robustness and limitations of the applied methods. In doing so, the thesis evaluates the potential and challenges of airborne IPDA lidar for quantifying GHG emissions from point sources under varying observational and atmospheric conditions.

Chapter 2 presents the methodological framework used throughout this work. It introduces the principles of lidar and IPDA measurements, describes the airborne CHARM–F system, and summarises the CoMet campaign, during which the key observational dataset was collected (Sect. 2.1). Additionally, the chapter explains the atmospheric transport models employed in the analysis, focusing on the setup and use of the Weather Research and Forecast model (WRF) (Sect. 2.2). This methodological foundation is essential for interpreting the case studies and is particularly relevant for understanding the conditions under which the **RQs** can be addressed.

Chapter 3 investigates an isolated CO_2 point source: the Jänschwalde power plant. The cross-sectional flux method is applied to quantify emissions based on airborne lidar observations and WRF simulations (Sect. 3.1). This case study is designed to answer **RQ1**, regarding the accuracy of emission quantification from isolated sources. Furthermore, by incorporating high-resolution Large Eddy Simulation (LES) (Sect. 3.2), it also addresses aspects of **RQ3**, examining the role of atmospheric turbulence and uncertainty under near-ideal conditions.

Chapter 4 examines CH_4 emissions in a more complex environment: the USCB, characterised by multiple closely spaced coal mine ventilation shafts. The study employs an inverse modelling framework (Carbon Tracker Data Assimilation Shell (CTDAS)-WRF) to disentangle overlapping emission plumes and quantify source-specific contributions. This chapter provides the basis for answering **RQ2**, while also contributing to **RQ3** by assessing the impacts of plume interference, spatial aggregation, and transport model limitations.

Chapter 5 summarises the findings from both case studies and concludes the thesis. It relates the results to the overarching **RQs**, highlights methodological strengths and limitations, and discusses implications for airborne and satellite-based point-source monitoring. In doing so, it provides definitive answers to **RQ1**–**RQ3**, reflects on the role of airborne IPDA lidar in the context of future satellite missions such as MERLIN, and outlines specific recommendations for future campaigns as well as key directions for further research.

2 Methodology

This chapter presents the methodological framework developed to address the research questions formulated in Sect. 1.3. It describes the measurement techniques and modelling tools required to quantify CO_2 and CH_4 emissions from anthropogenic point sources under the conditions relevant for this work. The focus lies on the capabilities and limitations of airborne IPDA lidar observations (Sect. 2.1) and on the atmospheric transport models used to interpret these measurements (Sect. 2.2). These components form the basis for evaluating the accuracy of the cross-sectional flux method for isolated sources (**RQ1**), for applying inverse modelling to complex multi-source environments (**RQ2**), and for assessing the influence of atmospheric variability and observational geometry on emission estimates (**RQ3**). While the methodological design is tailored to the two case studies examined in this thesis — the Jänschwalde coal-fired power plant and the USCB mining region — it could also be applied to other sources of a similar type.

Section 2.1 introduces the active remote-sensing methods used to measure atmospheric GHG concentrations downwind of emission sources. It begins with an overview of lidar technology in atmospheric science (Sect. 2.1.1), followed by the CHARM–F airborne IPDA lidar used in this work (Sect. 2.1.2). CHARM–F was deployed in several airborne campaigns as a demonstrator for the German–French MERLIN mission, including the CoMet campaign that provided the data for both case studies (Sect. 2.1.3).

Section 2.2 describes the numerical modelling used to interpret the lidar observations. It outlines the principles of atmospheric transport modelling (Sect. 2.2.1), provides a brief description of the Weather Research and Forecast model (WRF) model (Sect. 2.2.2), and presents the general WRF setup applied in both case studies (Sect. 2.2.3). The modelling is crucial for reducing the uncertainties in emission rate estimates, accounting for factors such as atmospheric turbulence, plume meandering, and the influence of other nearby sources.

The methodology described in this chapter forms the common foundation for both case studies. Different approaches are then applied to calculate the emission rates of the respective point sources, as detailed in Chapters 3 and 4. These chapters also describe the case-specific adaptations of the general WRF setup.

2.1 Measurement Techniques

2.1.1 Lidar in Atmospheric Science

Light Detection And Ranging (lidar) is a remote sensing system that consists of a laser and a receiver. Laser pulses are emitted from the instrument and propagate through the atmosphere. Along their path, they interact with atmospheric constituents and a fraction of this light is scattered back to the receiver. By analysing the backscattered signal, it is possible to infer the type of interaction between the laser pulse and atmospheric components. This is achieved by examining the signal's intensity attenuation, the elapsed time between emission and detection, and, potentially, its polarisation. In this way, lidar provides a distance-resolved profile of various atmospheric parameters.

The principle of light scattering, which underlies lidar technology, was first explored by Lord Rayleigh in the 19$^{\text{th}}$ century. In his work on the transmission of light through the atmosphere, Rayleigh proposed the theory that small particles, including air molecules, scatter light of short wavelengths more effectively than light of long wavelengths, whereby he famously explained the blue colour of the sky for the first time (Rayleigh 1899). However, applying this effect to active atmospheric measurements requires intense, coherent light sources that were not yet available.

Building on this concept, Edward H. Synge had the idea of using powerful light beams to probe atmospheric properties at high altitudes in the 1930s. He proposed a system that could measure atmospheric densities up to 30 km by directing a large array of searchlights into the night sky and collecting the backscattered light with parabolic mirrors (Synge 1930). This approach laid the groundwork for "light detection and ranging", although the necessary technology to fully realize it would only emerge decades later.

The breakthrough for lidar came with the invention of the laser developed by Theodore H. Maiman in 1960 (Maiman 1960). Using a synthetic ruby crystal as the lasing medium, Maiman's device produced coherent, monochromatic light through the process of stimulated emission. This first operational laser could emit highly focused pulses of light. In the following decades, a variety of applications were innovated and thus, lidar became an indispensable tool for atmospheric science.

Today's applications range from measuring wind speeds (e.g. Reitebuch et al. 2009), classifying aerosols (e.g. Groß et al. 2013), and acquiring temperature profiles (e.g. Kaifler and Kaifler 2021) to monitoring GHG concentrations (e.g. Ehret et al. 2012). These systems are operated ground-based (e.g. Wildmann et al. 2018) or from a variety of platforms including ships (e.g. Rubio et al. 2022), aircraft (e.g. Barton-Grimley et al. 2022) and satellites (e.g. Lux et al. 2020). In other words, lidar systems provide detailed observations of the atmosphere at both local and global scales.

Basic Lidar Principle

As indicated above, a lidar system consists of a laser transmitter, a receiver with a telescope, and a data acquisition unit. Short, intense pulses of laser light are transmitted and propagate through the atmosphere. Some of the pulses' photons are scattered back to the receiver, creating a backscatter signal.

To determine the distance to scattering events, lidar systems measure the elapsed time t (or "time-of-flight") between the transmission of a pulse and the detection of its backscattered signal. Since the speed of light c is constant, the range R to the scattering point can be calculated as:

$$R = \frac{c \cdot t}{2} \tag{2.1}$$

This relationship enables lidar to produce distance-resolved profiles, revealing how atmospheric properties vary with altitude or range. The data acquisition system counts the number of photons received in specific time intervals Δt, allowing calculation of range bins with a length $\Delta R = c \cdot \Delta t \,/\, 2$. It is important that the time interval Δt is larger than the effective pulse length t_{eff} to avoid overlap between consecutive range bins.

The extinction, which a laser pulse is subjected to while propagating through matter for a range of R, is described by the famous Lambert Beer's law in Eq. 2.2:

$$N(R) = N_0 \cdot e^{-\tau} \quad \text{with} \quad \tau \equiv \int_0^R \sigma \cdot n \ \mathrm{d}r \tag{2.2}$$

N being the number of photons and the subscript 0 indicating the initial number of photons in each laser pulse. The term $e^{-\tau}$ is the so-called transmittance of the medium. The particle density n and the absorption cross section σ are material-specific. As they depend on temperature and pressure, which change in the vertical course of the atmosphere, the optical depth τ must be calculated by a path integral.

The number of laser photons $N(R)$ received in a bin at range R collected by the telescope is described by the lidar equation (e.g.Gimmestad and Roberts 2023):

$$N(R) = \underbrace{N_0 \cdot \nu \cdot \Omega(R) \cdot \frac{A_{\text{tel}}}{R^2} \cdot \frac{c \cdot t_{\text{eff}}}{2}}_{\text{instrumental}} \cdot \underbrace{\beta(R) \cdot e^{-2 \cdot \int_0^R \sigma \cdot n \ \mathrm{d}r}}_{\text{atmospheric}} \tag{2.3}$$

ν is the efficiency of the entire optical module (transmitter and receiver), $\Omega(R)$ is the overlap function of the laser beam with the receiver field of view, A_{tel} is the telescope's aperture, $(c \cdot t_{\text{eff}} \,/\, 2)$ is the range bin length. $\beta(R)$ is the backscatter coefficient by atoms, molecules and particles. Since the atmosphere is traversed twice, the optical depth is multiplied by a factor of two within the exponential function.

Differential Absorption Lidar

The Differential Absorption Lidar (DIAL) technique, pioneered by Schotland in the 1960s (Schotland 1964, Schotland 1974), measures concentrations of trace gases by using two laser pulses. The pair of two sequentially emitted laser pulses, with differing but closely adjacent wavelengths, is emitted. The returning laser pulses are detected in the receiving optics after they have traversed virtually the same air column.

The wavelength of one pulse corresponds to the absorption line of the investigated trace gas. Its intensity is predominantly reduced by the extinction caused due to the trace gas in the atmosphere. This laser pulse is called the *online* pulse. The second one is called the *offline* pulse, because its wavelength is slightly shifted from the absorption line and therefore serves as a baseline reference as its intensity is less attenuated. By comparing the backscattered intensities of the two wavelengths at various distances, DIAL can derive a vertical profile of the gas concentration along the laser path.

Integrated Path Differential Absorption Lidar

The Integrated Path Differential Absorption (IPDA) lidar applies the DIAL principle in a simplified form, where the the backscatter signal reflects off a "hard" target, e.g. the Earth's surface, sea surfaces or cloud tops, (Ehret et al. 2008; Amediek et al. 2017; Mao et al. 2018; Barton-Grimley et al. 2022) instead of relying on atmospheric backscatter. These hard target reflections provide a higher Signal–to–Noise Ratio (SNR), which enhances column-averaged measurement precision and accuracy. This can be achieved without the higher laser power or more sensitive detectors that would be required to provide fine altitude resolution within the column. Thus, IPDA is particularly suited for nadir-viewing measurements from airborne or satellite platforms, where the laser beam illuminates the surface (or cloud tops) within a narrow footprint determined by the beam divergence and platform altitude (Menzies and Tratt 2003; Ehret et al. 2008; Abshire et al. 2010).

2.1.2 The Airborne IPDA Lidar CHARM-F

CHARM–F (CO_2 and CH_4 Remote Monitoring–Flugzeug) is an IPDA lidar, which was developed at DLR's Institute of Atmospheric Physics (IPA) at the department Lidar. Installed onboard the German research aircraft HALO (High Altitude and Long Range Research Aircraft), it serves as the airborne demonstrator for the MERLIN satellite mission and is the core instrument in its preparation and validation campaigns (see Figure 2.1).

In contrast to MERLIN, which measures only CH_4, CHARM–F simultaneously measures CO_2 and CH_4. For this purpose, two separate laser systems are installed for CO_2 and CH_4, which alternately emit laser pulses. Both systems share the laser electronics and cooling as well as the electronics for wavelength stabilisation and data acquisition. The measurement principle for both GHGs is the same. In each case, a diode-pumped Nd:YAG laser pumps an Optical Parametric Oscillator (OPO). Single-

Figure 2.1: Left: the German research aircraft HALO before take-off. Right: inside High Altitude and Long Range Research Aircraft (HALO)'s cabin, showing the full CHARM–F system. From left to right: lasers and receivers; laser cooling and controlling; PCs for laser operation, wavelength stabilisation and data acquisition. Both photos taken by A. Fix.

mode operation of both the pump and the OPO is achieved by injection seeding, resulting in a linewidth close to the transform limit (typically a few megahertz; Amediek et al. 2008; Fix et al. 2011; Amediek et al. 2017). The wavelength of the seed laser is stabilized with the help of a cell filled with CO_2 and CH_4, enabling absolute wavelength calibration (Amediek et al. 2008).

In total, four receiving optics are used: for each GHG one large telescope (200 mm ⌀) with a Positive Intrinsic Negative diode (PIN) and one small telescope (60 mm ⌀) with an Avalanche Photodiode (APD) (cf. Table A.1). This allows a direct comparison of the two detector types under real flight conditions. Due to the aircraft's high velocity, the ground spots of the two pulses are displaced only slightly, as shown in Fig. 2.2.

Spectrally, the on- and offline wavelengths are in such close proximity to each other that, apart from the absorption of the GHG of interest, the interaction with other atmospheric constituents and with the reflecting surface is expected to be nearly identical. Accordingly, any difference in the backscattered signals comes from the extinction of the respective GHG in the surveyed column. By the same reasoning, the atmospheric GHG concentration of the vertical column can be derived from the backscattered intensities of the laser pulse pair. In the following, such an online-offline pulse pair measurement is referred to as a "single-shot measurement".

Due to the spatial divergence of the laser, the volume surveyed by a laser pulse corresponds to a cone. The length of the cone is very large compared to the diameter of the reflection surface. In common literature, as well as in the following, the surveyed part of the atmosphere is hence referred to as a vertical air column, or simply column measurement. By additionally measuring the laser pulse pair's time-of-flight, the distance between the aircraft and the backscattered surface (i.e. the range R) is determined very precisely. The on- and offline wavelengths are tuned and stabilized to well-characterized absorption lines of the investigated GHG.

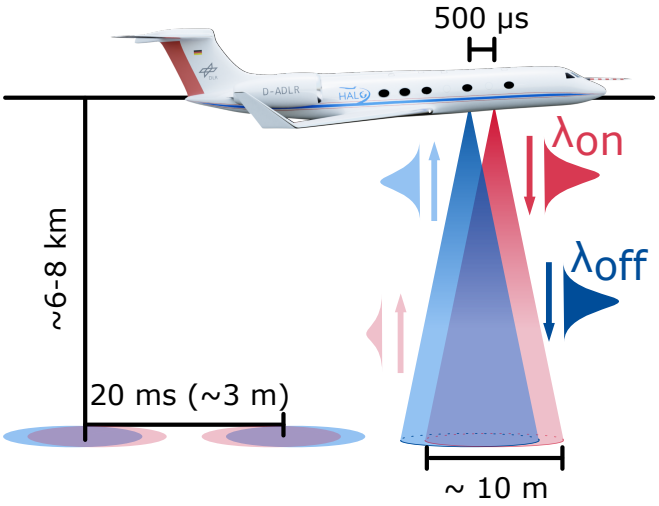

Figure 2.2: The measurement geometry of the CHARM–F instrument installed on the HALO aircraft. Two laser pulses are emitted towards the Earth with a short delay. The concentration in the surveyed cone volume can be derived from the ratio of the backscattered online and offline intensities. The volume measured is commonly referred to as a vertical air column. The order in which the on-off pairs are emitted alternates. In fact, successive measurements overlap, as the diameter of the footprint on the floor is greater than the distance between them. However, they are shown here with increased separation for clarity. Modified from Wolff et al. (2021).

For IPDA the lidar equation Eq. 2.3 can be expressed to model the optical power $P_{\mathrm{on/off}}$ entering the lidar's receiver (Grant 1982; Ehret et al. 2008):

$$P_{\mathrm{on/off}} = \frac{E_{\mathrm{on/off}}}{t_{\mathrm{eff}}} \cdot \nu \cdot \Omega \cdot \frac{A_{\mathrm{tel}}}{R^2} \cdot \varrho \cdot e^{-2\cdot(\tau_0+\tau_{\mathrm{on/off}})} \tag{2.4}$$

For each individual laser pulse, a beam splitter deflects a small portion of its energy onto a detector. In this way, the laser pulse energy E_{on} and E_{off} are determined separately as a reference within the lidar system. The reflectivity of the surface is designated as ϱ.

The optical depth due to extinction by air molecules, aerosols, and clouds is denoted τ_0, while $\tau_{\mathrm{on/off}}$ is the column optical depth from molecular extinction by CO_2, CH_4, and H_2O:

$$\tau_{\mathrm{on/off}} = \sum_{\xi} \tau_{\xi,\mathrm{on/off}} \quad \text{with} \quad \xi \in \{\mathrm{CO_2}, \mathrm{CH_4}, \mathrm{H_2O}\} \tag{2.5}$$

By inverting Eq. 2.4 and subtracting the two optical depths, the following relationship between the observed Differential Absorption Optical Depth (DAOD) δ_{obs} and the backscattered intensities is obtained:

$$\delta_{\mathrm{obs}} = \tau_{\mathrm{on}} - \tau_{\mathrm{off}} = \frac{1}{2} \cdot \ln\left(\frac{P_{\mathrm{off}}/E_{\mathrm{off}}}{P_{\mathrm{on}}/E_{\mathrm{on}}}\right) \tag{2.6}$$

With a single-shot measurement we determine a measure for the column-averaged concentration of either CO_2 or CH_4. The wavelengths of the respective on- and

offline laser pulses are carefully selected to minimize absorption by other atmospheric gases. Moreover, the offline wavelength in particular is selected in a way that as little absorption as possible takes place. Figure 2.3 shows the column optical depths of CH_4 (a) and CO_2 (b) for a standard atmosphere over a wavelength range at the selected absorption lines. Figure 2.3 shows the absorption line for CH_4 and CO_2.

At the on- and offline wavelengths used for the CH_4 measurement, absorption by H_2O and CO_2 is not strictly zero. Hence the raw observed DAOD is $\delta_{\text{obs,raw}} = \delta_{CH_4} + \delta_{CO_2} + \delta_{H_2O}$. The interfering terms are computed with auxiliary information: water vapour from ECMWF-IFS data (ECMWF 2018, cf. Sect. 2.2.2), while the small contributions of CO_2 at the CH_4 wavelengths (and vice versa) are estimated from standard profiles. These modelled contributions are denoted with a hat. The corrected DAODs are then:

$$\begin{aligned} \delta_{CH_4} &= \delta_{\text{obs,raw}} - \widehat{\delta}_{CO_2} - \widehat{\delta}_{H_2O} \\ \delta_{CO_2} &= \delta_{\text{obs,raw}} - \widehat{\delta}_{CH_4} - \widehat{\delta}_{H_2O} \end{aligned} \tag{2.7}$$

The offline wavelength for CH_4 is chosen so that the absorption by H_2O is equal to the online wavelength and the contribution of the differential absorption is minimized. This is particularly important because the water vapour concentration in the atmosphere can be very variable leading to a greater error potential than with CO_2 if not exactly known. For the CO_2 absorption line shown in Fig. 2.3b, things are much simpler, as the absorption of the other gases is negligible.

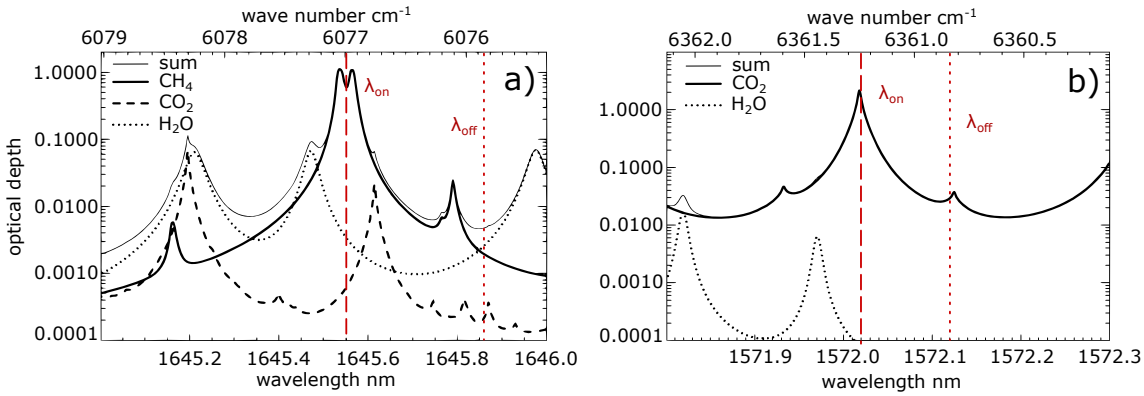

Figure 2.3: a) by Kiemle et al. (2011) and b) by Ehret et al. (2008) show the total vertical column optical depth for standard atmosphere. The thin line shows the sum over all GHGs, and the thick line shows the greenhouse gas of particular interest, i.e. CH_4 in a) and CO_2 in b). The dotted line shows H_2O. Additionally, the dashed line in a) shows the contribution of CO_2. The additional optical depth due to CH_4 is negligible in b). The dashed vertical red lines mark the wavelengths of the on- and offline laser pulses.

Based on the general definition of optical depth (Eq. 2.2), the DAOD of each individual absorbing atmospheric constituents ξ can also be represented by:

$$\delta_\xi = \int_{z_{\text{sfc}}}^{z_{\text{flh}}} n_\xi(z) \cdot \Delta\sigma_\xi\left(p(z), T(z)\right) \, \mathrm{d}z \quad \text{with} \quad \xi \in \{CO_2, CH_4, H_2O\} \tag{2.8}$$

The integration limits are the height of the reflection surface (sfc) and the flight height (flh). $\Delta\sigma_\xi(p,T) = \sigma_\xi(\lambda_{\text{on}},p,T) - \sigma_\xi(\lambda_{\text{off}},p,T)$ is the pressure and temperature dependent differential absorption cross section, which arises from the interaction between the specific molecule and the laser pulses at the chosen wavelengths λ_{on} and λ_{off}. At low altitudes, the density n_ξ is higher, then drops exponentially with atmospheric height. The contribution of the particle density thus weights the path integral in Eq. 2.8 to lower altitudes. Applying the hydrostatic equation (Eq. A.4) allows the reformulation of the vertical path integral in Eq. 2.8 to a pressure integral:

$$
\begin{aligned}
\delta &\overset{\text{A.4}}{=} \sum_\xi \int_{p_{\text{flh}}}^{p_{\text{sfc}}} n_\xi(p) \cdot \Delta\sigma_\xi\left(p, T(p)\right) \cdot \frac{1}{g(z(p)) \cdot \rho(p)} \,\mathrm{d}p \qquad (2.9)\\
&\overset{\text{A.5}}{=} \sum_\xi \int_{p_{\text{flh}}}^{p_{\text{sfc}}} n_\xi(p) \cdot \frac{\Delta\sigma_\xi\left(p, T(p)\right)}{g(z(p)) \cdot n_{\text{dry}}(p) \cdot \left(m_{\text{dry}} + m_{\text{H}_2\text{O}} \cdot r_{\text{H}_2\text{O}}(p)\right)} \,\mathrm{d}p\\
&= \sum_\xi \int_{p_{\text{flh}}}^{p_{\text{sfc}}} \underbrace{\frac{n_\xi(p)}{n_{\text{dry}}(p)}}_{\equiv r_\xi(p)} \cdot \frac{\Delta\sigma_\xi\left(p, T(p)\right)}{g(z(p)) \cdot \left(m_{\text{dry}} + m_{\text{H}_2\text{O}} \cdot r_{\text{H}_2\text{O}}(p)\right)} \,\mathrm{d}p\\
&= \sum_\xi \int_{p_{\text{flh}}}^{p_{\text{sfc}}} r_\xi(p) \cdot \underbrace{\frac{\Delta\sigma_\xi\left(p, T(p)\right)}{g(z(p)) \cdot \left(m_{\text{dry}} + m_{\text{H}_2\text{O}} \cdot r_{\text{H}_2\text{O}}(p)\right)}}_{=: w_\xi(p)} \,\mathrm{d}p
\end{aligned}
$$

Here, $r_\xi(p)$ is the mole fraction with respect to dry air at pressure p (given in µmol/mol or ppm), which is generally defined as the ratio of the number of GHG particles ξ to the number of other dry-air molecules. m_{dry} and $m_{\text{H}_2\text{O}}$ are the molar masses of dry-air and water vapour, respectively, $r_{\text{H}_2\text{O}}$ is the mole fraction of water vapour and g is the gravitational acceleration. The pressure and temperature dependence of the differential absorption cross section $\Delta\sigma_\xi$ are determined by spectroscopic laboratory measurements (Gordon et al. 2017). The corresponding pressure, temperature, and humidity profiles at the time and location of the airborne measurement can be obtained from a numerical weather simulation.

The second multiplicative term in the last line of Eq. 2.9 acts as a weighting function for the air masses in the vertical pressure integral, thereby defining the sensitivity of the IPDA measurement. Consequently, it is defined as the so-called weighting function w (Amediek et al. 2017):

$$
w(p) := \frac{\Delta\sigma\left(p, T(p)\right)}{g(z(p)) \cdot \left(m_{\text{dry}} + m_{\text{H}_2\text{O}} \cdot r_{\text{H}_2\text{O}}(p)\right)} \qquad (2.10)
$$

The weighted dry-air column-averaged mole fraction XCO_2 (or equivalently XCH_4) is widely used as a metric for GHG measurements in remote sensing. It is generally defined by a vertically weighted mean of the GHG's mole fraction r (Rodgers 2000; Dufour and Bréon 2003; O'Dell et al. 2012; Bousquet et al. 2018):

$$
X\text{CO}_2 = \frac{\int r \cdot w\left(p\right) \,\mathrm{d}p}{\int w\left(p\right) \,\mathrm{d}p} \qquad (2.11)
$$

However, it should be noted that the vertical weighting varies in the literature. In some studies, XCO_2 is weighted by total number of air molecules (e.g. Reuter et al. 2010), while in other studies the mole fractions are weighted by pressure (e.g. Connor et al. 2008). In passive remote sensing, where the sun is used as light source, the vertical weighting is often expressed in column averaging kernels, which are calculated with radiative transfer models and depend on solar zenith angle and the a priori atmospheric state (Wunch et al. 2010; Krings et al. 2011).

By comparing the measured DAOD δ (i.e. Eq. 2.6) with its definition derived by the Lambert Beer's Law (last line of Eq. 2.9) it is apparent that δ becomes equivalent to the enumerator in Eq. 2.11, by defining w as has been done in Eq. 2.10. Consequently, dividing the measured DAOD δ by the vertically integrated weighting function w fulfils the definition of the column-weighted average dry-air mole fraction XCO_2 in Eq. 2.11 (Amediek et al. 2017):

$$XCO_2 = \frac{\delta}{\int w\,(p)\ \mathrm{d}p} \tag{2.12}$$

The weighting function w in Eq. 2.10 is an inherent part of the IPDA measurement principle and determined by the chosen online and offline wavelengths. It defines the vertical sensitivity of the measurement. IPDA systems with different wavelengths will have different weighting functions and thus yield slightly different DAOD values, even for the same atmospheric state. Therefore, meaningful comparisons require that simulated GHG fields or in situ profiles are sampled with the wavelength-dependent weighting function of the instrument under consideration (see Eq. 2.11).

The overall purpose of this work, as described in the Introduction, is to quantify anthropogenic emissions that occur near the surface and propagate as plumes within the Planetary Boundary Layer (PBL). With the wavelengths chosen for CHARM–F (see Table A.1), the measurement sensitivity is maximized in the boundary layer and decreases with altitude (Kiemle et al. 2017). This corresponds to a high absorption cross-section at high pressure and a lower one at low pressure.

2.1.3 The CoMet 1.0 Campaign

The Carbon Dioxide and Methane Mission (CoMet) is a series of campaigns designed to prepare and validate the satellite mission MERLIN. CoMet's objective is to use state of the art measurement instrumentation to improve our current understanding of the global distribution of the two main human-influenced greenhouse gases CO_2 and CH_4, with special emphasis on their regional and local sources and sinks. One such instrument is MERLIN's airborne demonstrator CHARM–F (see Sect. 2.1.2). The first deployment of CHARM–F on the German research aircraft HALO was in 2015, when initial performance tests and the methodology for determining emission rates were carried out (Amediek et al. 2017).

In addition to the CHARM–F measurements, various auxiliary measurements are made, to measure e.g. pressure, temperature, wind, humidity directly on the aircraft (Giez et al. 2023). Moreover, the close cooperation with the Institute of Environmental Physics, (University of Bremen), and the Max Planck Institute for

Table 2.1: CoMet 1.0 airborne instrumentation

Instrument	Description	Aircraft
CHARM–F	IPDA lidar	HALO
JIG	cavity ring-down spectrometer	HALO
JAS	flask sampler	HALO
miniDOAS	differential optical absorption spectroscopy	HALO
BAHAMAS	HALO basic data acquisition system	HALO
dropsondes	meteorological sondes	HALO
FOKAL	frequency comb	HALO
MAMAP	NIR-SWIR spectrometer	FUB Cessna
QCLS	quantum cascade laser spectrometer	DLR Cessna
CRDS	cavity ring-down spectroscopy	DLR Cessna
METPOD	Cessna basic data acquisition system	DLR Cessna
sampler	flask sampler	DLR Cessna

Biogeochemistry (Jena) needs to be emphasized, as they participate in each CoMet campaign with the passive spectrometer MAMAP (Methane Airborne MAPper, Gerilowski et al. 2011) and the JIG/JAS instruments (Jena Instrument for Greenhouse gas measurements/Jena Air Sampler, Gałkowski et al. 2021b), respectively. MAMAP retrieves column-averaged dry-air mole fraction anomalies of CO_2 and CH_4 relative to a background, while JIG/JAS are in situ instruments measuring through inlets through inlets in HALO's fuselage.

For the preparation of the research flights, it is essential to have a flight plan customized for each target area and to the synoptic situation of each flight day. Therefore, all campaigns are supported by IPA's Earth System Modelling department. With their global and regional chemistry-climate model MECO(n) (Kerkweg and Jöckel 2012; Mertens et al. 2016), the regional distribution of the GHGs from the specific sources is forecast to allow for optimal flight planning. Furthermore, support from atmospheric transport models is essential for the analysis and interpretation of the measurement data (Nickl et al. 2020; Kostinek et al. 2021; Brunner et al. 2023; Hanfland et al. 2024). Beside these regular campaign collaborations and instrumentations, there are contributions that vary from campaign to campaign.

CoMet 1.0, the first edition of the campaign series, took place in May and June 2018 (Fix et al. 2020) with the objective of quantifying European anthropogenic GHG emission sources. The campaign's flagship was the German research aircraft HALO, which surveyed on the continental scale and was based in Oberpfaffenhofen, Germany. In coordination with HALO, two short-range Cessna aircraft operated from Katowice Pyrzowice airport, focusing on the greater Berlin area and the USCB. The first, a Cessna T207A operated by Freie Universität Berlin (FUB), carried the passive spectrometer MAMAP (Krings et al. 2011). The second, a Cessna 208 Grand Caravan operated by DLR, was equipped with a Cavity Ring–Down Spectroscopy (CRDS) analyser measuring CH_4, CO_2 and H_2O (Fiehn et al. 2020) as well as a modified Quantum Cascade Laser Spectrometer (QCLS) (Aerodyne) for additional trace gases

(Kostinek et al. 2021). A complete list of the airborne instrumentation during CoMet 1.0 is given in Table 2.1.

Furthermore, the USCB was of prime interest for the campaign, as it is one of Europe's major CH_4 emission hotspots, where the gas is predominantly released from coal mine ventilation shafts (see Sect. 4.1). Therefore, ground-based measurements were carried out there to complement the airborne activities. These included portable (Luther et al. 2019) and stationary (Luther et al. 2022) sun-viewing Fourier-transform infrared spectrometers (EM27/SUN, Doppler wind lidars (Leosphere Windcube 200S, Wildmann et al. 2020), and car-mounted integrated cavity output spectroscopy (MGGA - 918, Menoud et al. 2021). Lastly, another CRDS was installed aboard a small quadrocopter drone to sample CO_2 and CH_4 downwind of individual ventilation shafts and determine their emission rates (Andersen et al. 2023).

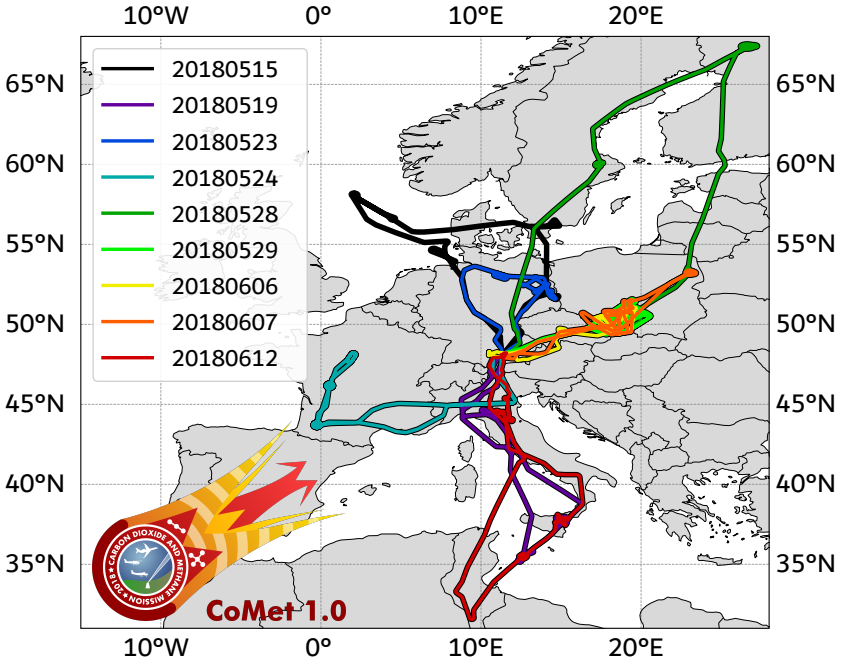

Figure 2.4: Map of all HALO flight tracks during the campaign in May and June 2018. The blue track to eastern Germany is analysed in Chapter 3, the orange track to southern Poland in Chapter 4. Modified from Fix et al. (2020).

The activities of this campaign provide a unique and comprehensive dataset. This thesis analyses two research flights with CHARM–F onboard HALO during CoMet 1.0 to address the research questions posed in Sect. 1.3. On 23 May 2018, HALO flew over the coal-fired power plant Jänschwalde near the German–Polish border (blue track in Fig. 2.4). This isolated CO_2 point source forms the basis of **Case Study I**, in which the cross-sectional flux method is applied to quantify emissions and address **RQ1**. On 7 June 2018, HALO overflew the USCB in southern Poland (orange track in Fig. 2.4). The numerous ventilation shafts in this region produce overlapping plumes that cannot be separated with the cross-sectional flux method. This forms the basis of **Case Study II**, in which inverse modelling is used to disentangle source contributions and address **RQ2**.

2.2 Numerical Modelling

To properly interpret the observed GHG concentrations, a detailed knowledge of their atmospheric transport is essential. Ideally, enhanced concentrations would appear downwind of the emission sites, with background concentrations found upwind. In practice, however, the observed signals are often more complex. Interference from nearby sources or long-range transport can make it difficult to identify a representative background concentration. In addition, local turbulence can cause meandering and inhomogeneities in plume propagation.

This study focuses on relatively short timescales of a few days and regional domains of several hundred by several hundred kilometres. In order to relate the observed signals to point source emissions under these conditions, it is necessary to model their atmospheric transport. Numerical Weather Prediction (NWP) models provide global fields of the atmospheric state by assimilating a large number of observations and numerically solving a set of physical equations. The European Centre for Medium–Range Weather Forecasts (ECMWF) operates one of the most advanced global NWP systems, whose output offers a realistic representation of the mesoscale circulation. In this work, external fields from the ECMWF are used to drive finer-scale regional simulations of transport processes (see Sect. 2.2.2).

Given this focus, the term Atmospheric Transport Model (ATM) is used in the following instead of NWP, in order to emphasize the specific application. Sect. 2.2.1 introduces the basic concepts of ATMs, followed by a description of the Weather Research and Forecast model (WRF), which is the regional model employed in this work. The general WRF setup is summarized in Sect. 2.2.3, while case-specific adaptations are described in Chapter 3 and Chapter 4.

2.2.1 Atmospheric Transport Modelling

Atmospheric Transport Models (ATM) describe the motion of the atmosphere by solving the *Navier–Stokes equations*, complemented by the continuity and energy equations. Together, these form a system of non-linear partial differential equations of second order, with temperature, wind, humidity, and pressure as the key prognostic variables. In atmospheric applications viscosity is usually neglected, which reduces the system to the *Euler equations*. These can be expressed in two perspectives. First, the *Lagrangian* framework, where the trajectory of an individual air parcel is followed through space and time. Second, the *Eulerian* framework, where the state variables are defined on a fixed spatial grid and their changes are computed from fluxes across grid cell boundaries.

Both the Eulerian and the Lagrangian perspective provide valid frameworks for describing atmospheric motion, yet they are suited for different applications. Lagrangian models are particularly useful when following the trajectories of individual air parcels, for example to analyse the influence of specific sources on a fixed measurement location (Lin et al. 2003; Levin et al. 2020; Zhao et al. 2023). This approach is less practical in the present context, since the airborne measurements considered here are mobile. Instead, the fixed-grid approach of Eulerian models is

applied. It provides a continuous representation of atmospheric processes and is commonly used to simulate the dispersion of trace gases from fixed emission sources and distributed measurement locations (Krol et al. 2005; Zhu et al. 2021; Brunner et al. 2023). For the purposes of this work, the Eulerian approach is therefore the natural choice, ant the simulations presented herein were performed with the Eulerian Weather Research and Forecast model (WRF).

2.2.2 Weather Research and Forecast Model

The WRF model has been developed in collaboration between the National Center for Atmospheric Research (NCAR), the NOAA, the Air Force Weather Agency (AFWA), the *Naval Research Laboratory*, the University of Oklahoma, and the Federal Aviation Administration (FAA). It is a community model that is widely used in atmospheric research and forecasting and offers a broad range of physical and numerical options (Powers et al. 2017). A full technical description of the Advanced Research WRF (ARW) configuration can be found in Skamarock et al. 2008, 2019.

In WRF-ARW the Euler equations are implemented in a compressible, nonhydrostatic manner and are cast in flux form using variables that have conservation properties. The prognostic variables are defined as perturbations from a hydrostatically balanced reference state (e.g. wind components, vertical velocity, potential temperature, geopotential, and surface pressure; see Skamarock et al. 2008, 2019). That is, the reference state is in hydrostatic balance and is solely dependent on height, while the temporal variability is embodied in the perturbations.

The hybrid sigma-pressure vertical coordinates η are based on dry hydrostatic pressure, formulated terrain-following and permitted to stretch vertically. The so-called eta values are expressed as values between 1 at the Earth's surface and 0 at the model's top at constant pressure. The η value is related to the hydrostatic component dry-air pressure at level k by the following equation (Skamarock et al. 2019):

$$\eta_k = \frac{p_k - p_{\text{top}}}{p_{\text{sfc}} - p_{\text{top}}} \tag{2.13}$$

The η-levels are defined manually by the user and are set such that the vertical resolution is finer near the surface and decreases with altitude. This vertical layering is constant over the horizontal domain. The exact distribution of the η-levels differs slightly between the two case studies and is shown in Sect. 3.2.1, Fig. 3.5 and Sect. 4.2.1, Fig. 4.6.

As mentioned in Sect. 2.1.3, the measurement flights analysed here were conducted only a few kilometres from the emission sources. To realistically represent the structure and propagation of the exhaust plumes, the simulations must therefore be run at high spatial resolution on the order of hundreds to thousands of metres. Since such simulations are computationally expensive, this high resolution is only applied in the target region (see Fig. 2.5).

For this purpose, the regional WRF simulations are based on global operational analysis fields from the ECMWF, which operates one of the most advanced Integrated Forecasting System (IFS) systems and assimilates the largest number of observations

worldwide (ECMWF 2018). Through this data assimilation process, meteorological observations from ground stations, satellites, radiosondes, and aircraft are continuously integrated into the model, resulting in an atmospheric state that is closer to reality. The ECMWF analysis fields provide temperature, geopotential, wind, specific humidity, vertical velocity, and surface pressure as initial and lateral boundary conditions for the regional simulations.

Driven by the ECMWF data, the spatial and temporal resolution is regionally increased by so-called "telescope nesting". In this process, smaller and more highly resolved child domains are embedded within coarser parent domains and inherit the meteorological conditions at their boundaries from the respective parent. Each child domain is fully contained within its parent domain and uses its time-dependent lateral boundary conditions. At each parent time step, the boundary conditions for the finer child grid are generated from the coarser parent grid by horizontal interpolation. The child domain then performs its calculations at higher temporal resolution until the next parent time step is reached.

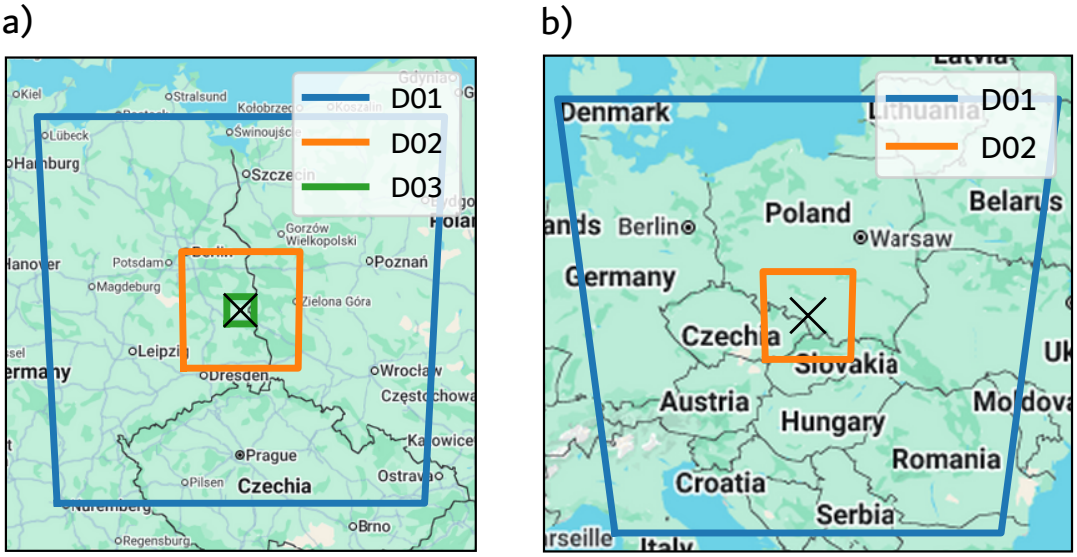

Figure 2.5: a) three domains over Jänschwalde. b) two domains over USCB.

In addition to the use of boundary conditions, the development of the two horizontal wind components, temperature, specific humidity and perturbation geopotential can be forced towards "trustworthy" driving meteorological fields, to avoid divergence within the domain. Such trustworthy fields could either be observations done within the domain, or external model data, here the ECMWF operational analysis data. This forcing is done using nudging, which in WRF has a built-in Four–Dimensional Data Assimilation (FDDA). In nudging the respective variables are pulled in the direction of the driving fields with a tendency term.

With these fundamental aspects of the WRF model introduced, the following subsection outlines the general setup used for the regional simulations. Detailed case-specific configurations are then described in Chapter 3 and Chapter 4.

2.2.3 WRF Setup

The coupling is implemented such that chemical tracers are transported consistently with the meteorology and, if activated, modified by emission processes and chemical sink reactions. This enables WRF-Chem to represent the transport, transformation, and removal of atmospheric species within a single framework.

However, the goal of the present study is to represent observed CO_2 and CH_4 plumes in the vicinity of their emission sources. These enhancements are confined to only a few kilometres downwind and to a residence timeframe of a few hours to a few days. In contrast, the atmospheric lifetime of CH_4 is on the order of ~ 10 years (Prather and Zhu 2024), whereas that of CO_2 extends to centuries (Archer et al. 2009). Consequently, for the purposes of this study, both gases can be treated as passive tracers without the need to account for chemical reactions or sinks.

Technically, two different tracer implementations are used. In **Case Study I** (Chapter 3), the standard WRF option for user-defined passive tracers is applied, as introduced by Blaylock et al. (2017). In **Case Study II** (Chapter 4), the passive tracer is implemented through WRF-Chem, as the coupling to CTDAS is built upon the WRF-Chem infrastructure (Reum et al. 2020). In both cases, the tracer is transported consistently with the meteorological fields, but no chemistry is activated.

The configuration presented here is based on a set of physics, dynamics, and boundary control options that have been demonstrated to perform well in previous studies and community applications of WRF (e.g. Blaylock et al. 2017). Rather than exploring the full range of namelist choices, a selection of established options was adopted following recommendations from experienced WRF users to ensure a robust setup for the present purpose. In this section, only the most relevant options are described and summarized in Table 2.2; further namelist parameters follow the defaults of the respective WRF version.

The vertical structure of the model comprises 57 levels, with a deliberately higher resolution near the surface in order to adequately resolve processes within the Planetary Boundary Layer (PBL). The model top is set at a constant pressure of $p_{\text{top}} = 200\,\text{hPa}$, while the vertical spacing increases with altitude. Depending on the location and the underlying orography, this configuration typically provides on the order of 15–25 layers within the lowest 1.5 km. This ensures that emissions from elevated sources, such as stacks or mine shafts, are released into model layers above the surface rather than into the surface layer. This is important because Brunner et al. 2019 demonstrated that emissions placed at the model surface lead to excessive drag in plume propagation.

The lateral boundary conditions for the outer domain (D01) differ from those of the nested domains. Along the domain edge, two buffer zones are defined. In D01, the outermost 5 rows and columns form the "specified zone" (namelist option $spec\_bdy\_width = 5$)[1], where values are determined by temporal interpolation of the ECMWF operational analysis data. Adjacent to this is the "relaxation zone",

[1] See Table 2.2 for a summary of namelist settings.

Table 2.2: Selected namelist settings for the two domains used in both case studies. The parameters are explained in the text.

Parameter	Domain 1	Domain 2
Boundary Control		
spec_bdy_width	5	5
relax_zone	4	4
FDDA (grid nudging)		
grid_fdda	1	0
guv	0.0003	0.0003
gt	0.0003	0.0003
gph	0.0003	0.0003
gq	4.5×10^{-5}	4.5×10^{-5}
Physics		
mp_physics	10	10
ra_lw_physics	4	4
ra_sw_physics	4	4
radt	30	15
sf_sfclay_physics	1	1
sf_surface_physics	2	2
bl_pbl_physics	5	5
cu_physics	5	0
cu_rad_feedback	true	false
cu_diag	1	0
Dynamics		
rk_ord	3	3
diff_opt	1	1
km_opt	4	4
diff_6th_opt	2	2
diff_6th_factor	0.3	0.3

consisting of 4 rows and columns ($relax\_zone = 4$)[1]. It is designed to achieve a smooth transition between the specified boundary conditions and the simulated values from WRF. This is accomplished by a combination of Newtonian and diffusive horizontal smoothing, as described in detail by Skamarock et al. (2008) following the scheme proposed by Davies and Turner (1977). Thus, the specified and relaxation zones in D01 serve as a transition between the lateral boundary conditions from the driving meteorology and the regional WRF simulation.

The introduction of D01 also marks the first refinement in spatial and temporal resolution compared to the driving ECMWF analysis data, which have a horizontal resolution of 0.125° and are provided every 6 h. For central Europe, this corresponds to approx. 9 km in the zonal direction and 14 km in the meridional direction. D01 is set with a horizontal resolution of 5 km and a temporal resolution of 30 s. Horizontally, the grid cells are quadratic and described in a Cartesian coordinate system, as the WRF simulation is run in a Lambert conformal conic projection (Deetz 1918).

A finer second domain (D02) increases the resolution to 1 km and 5 s. For **Case Study I** in Chapter 3, even a third domain is introduced (0.2 km, 1 s) to explicitly resolve local turbulence. This enables a realistic assessment of the effect of turbulent plume distortions on the reliability of the cross-sectional flux method. The nested domains use a two-way nesting approach, where the child domain inherits boundary conditions from its parent and, in turn, influences the parent domain by feeding back averaged values to coinciding grid cells.

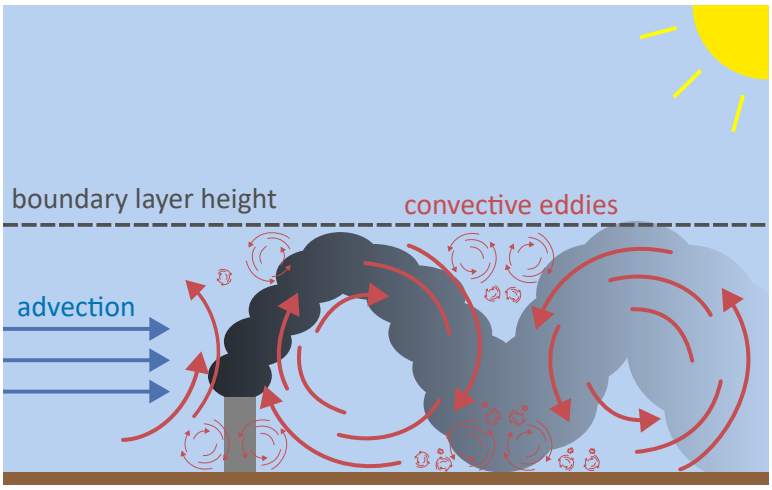

Figure 2.6: Schematic illustration of turbulent plume dispersion in the convective boundary layer. The blue arrows indicate the mean wind direction (advection), while the red curved arrows represent convective eddies of different sizes, generated by surface heating and buoyancy. These eddies cause the exhaust plume to oscillate vertically, meander, and become progressively diluted through turbulent mixing. The dashed line denotes the boundary layer height, which limits the vertical extent of the convective motions.

To prevent divergence within the domain, grid-nudging is employed, which is one of the options of the WRF built-in FDDA. In grid-nudging the model's prognostic variables (e.g. horizontal wind components, temperature, specific humidity, and perturbation geopotential) are pulled towards the driving meteorological fields from ECMWF analysis data with a tendency term, similar to how it is done in the relaxation zone for the boundary conditions. As shown by Ho et al. (2024), this technique produces results that align well with airborne in situ measurements, particularly in the Upper Silesian Coal Basin (USCB). Notably, grid-nudging is applied to every grid cell in D01 ($grid\_fdda = 1$)[1], while it is disabled in the inner domains ($grid\_fdda = 0$)[1]. There, the transport is intentionally determined by the finer-resolution processes specified by the chosen physical schemes.

One of the key processes is vertical motion in the PBL which is primarily driven by convective eddies. These are coherent rising and sinking air parcels that are generated by buoyancy, which is caused by surface heating and density differences (see Fig. 2.6). The kinetic energy of large convective eddies is transferred to progressively smaller eddies until it is eventually dissipated as molecular heat. This cascade of kinetic energy follows Kolmogorov's law (Qian 1994) and is the fundamental driver of

turbulence within the PBL. Because model resolution is finite, part of this turbulent spectrum cannot be explicitly resolved. The associated vertical transport must therefore be represented through parametrization. Different PBL schemes exist to provide such parametrizations, each with different assumptions and strengths, which can influence the representation of boundary layer processes. For this purpose, the simulations were performed using the Mellor–Yamada Nakanishi Niino (MYNN) Level 2.5 scheme ($bl\_pbl\_physics = 5$)[1], which is based on a second-order turbulence closure model (Nakanishi and Niino 2009). It accounts for buoyancy-pressure effects and stability on the turbulent length scale, with refinements such as a scale-aware mixing length and an eddy mass-flux option for non-local characteristics.

In WRF-ARW, the selection of a PBL scheme implies that the vertical mixing is handled exclusively by this scheme. However, the horizontal diffusion gradients are simply assessed along the coordinate levels η ($diff\_opt = 1$)[1]. Furthermore, for the calculation of the horizontal eddy viscosity, the Smagorinsky first-order closure approach is applied ($km\_opt = 4$)[1], where the horizontal diffusion is diagnosed just from horizontal deformation (Smagorinsky 1963).

An important aspect for vertical transport in the PBL schemes is the interaction with the surface layer, most importantly the sensible and latent heat fluxes to the boundary-layer scheme. This interaction is governed by a Land–Surface Model (LSM), which incorporates internal information on the land's state variables and land-surface properties. Furthermore, it exerts an influence on soil and surface processes, including the temperature and moisture profiles, the extent of snow cover, and interactions with vegetation. The LSM operates as one-dimensional column model at each land grid, and has no horizontal interaction on neighbouring grid cells.

Here, the Unified NOAH Land–Surface Model is selected (Tewari et al. 2004, $sf\_surface\_physics = 2$)[1], which comprises four layers. The layer thicknesses are 10, 30, 60 and 100 cm, from the top down to a total depth of 2 m. The LSM has the capacity to predict both soil temperature and moisture, as well as canopy moisture and snow cover. Further features of the Unified NOAH LSM include root zone, evapotranspiration, soil drainage, and runoff, taking into account vegetation categories, monthly vegetation fraction, and soil texture. The LSM utilizes friction velocities and exchange coefficients from the surface layer scheme, for which the Revised Mesoscale Model 5 (MM5) scheme is used (Jiménez et al. 2012, $sf\_sfclay\_physics = 1$)[1].

To realistically represent the energy budget of the atmosphere, radiative transfer processes must also be included, as they strongly influence atmospheric stability and thus boundary-layer dynamics. For this purpose, the Rapid Radiative Transfer Model for General Circulation Models (RRTMG) scheme is used for both shortwave and longwave radiation (Iacono et al. 2008, $ra\_sw\_physics = ra\_lw\_physics = 4$)[1]. The RRTMG employs prescribed lookup tables to accurately represent radiative processes due to H_2O, O_3, CO_2, and other trace gases, as well as accounting for cloud optical depth. In particular, CO_2 concentrations are prescribed as a simple linear function of calendar year to reflect its increasing atmospheric abundance.

Another notable interaction with the LSM is with the precipitation data from the Morrison two-moment scheme (Morrison et al. 2009, $mp\_physics = 10$)[1]. This

microphysics scheme's prognostic variables include cloud ice, rain, snow, and graupel/hail, and cloud droplets and water vapour. The prediction of two moments (number and mass mixing ratio) makes the calculation of particle size distributions more reliable. In turn, the particle size distributions are an integral part in the determination of microphysical process rates and the evolution of precipitation and clouds.

However, the effects of convective and shallow clouds on the sub-grid scale are represented by cumulus parametrization schemes. These schemes handle vertical fluxes due to potential unresolved updrafts and the associated latent heat release, as water vapour condenses in the cloud formation process. Here, the Grell 3D Ensemble Scheme is applied ($cu\_physics = 5$)[1]. It is a further development of the scheme introduced by Grell and Dévényi 2002), which is an ensemble cumulus scheme. Originally, it is an average of several cumulus schemes of the mass-flux type, which differ in the parameters for updrafts and downdrafts, the associated entrainment and detrainment as well as in the precipitation efficiency. Beyond that, the Grell 3D scheme allows subsidence effects to be spread to neighbouring grid columns, making the method more suitable to comparatively smaller grid sizes like the 5 km horizontal resolution domain in this setup (see Table 3.3). For the finer domains, where the grid spacing is sufficiently small to explicitly resolve convective cloud processes, no cumulus parametrization is applied.

3 Case Study I:

Quantification of an Isolated CO_2 Point Source

Case Study I focuses on the coal-fired power plant Jänschwalde, a single and isolated CO_2 point source. Power plants are among the largest individual emitters worldwide and represent a major share of national GHG budgets. Monitoring their emissions with high accuracy is therefore essential for reliable reporting, and also to provide independent checks that do not solely rely on operator-reported values. An isolated source like Jänschwalde offers a clear plume signature and thus an important intermediate step for method development and uncertainty characterization, before moving on to more complex multi-source environments as in **Case Study II**.

In this study the *cross-sectional flux method* is applied, since it is conceptually straightforward and has been widely used in both airborne and satellite-based studies. The method quantifies emissions by multiplying the mean wind speed with the integrated concentration enhancement along a cross-sectional overflight of the exhaust plume, relative to a known background. In principle, satellites can use this technique to constrain emissions from point sources, but this requires favourable wind conditions and typically only a single overpass is available.

Airborne IPDA lidar observations, by contrast, can provide repeated plume crossings. This allows a systematic assessment of the uncertainties associated with individual flux estimates and gives direct insight into the variability of results from successive overflights. This chapter therefore investigates two research questions:

- **RQ1:** How accurately can the **cross-sectional flux method quantify** CO_2 emissions from an **isolated point source**, such as the Jänschwalde power plant?
- **RQ3:** Under which atmospheric conditions and flight geometries do **uncertainties** in IPDA-based emission quantification become most pronounced, and how can **future flight planning** be adapted to **mitigate** these effects?

To address these questions, Sect. 3.1 presents the cross-sectional flux approach as adapted for airborne IPDA lidar. Sect. 3.1.1 outlines the necessary steps for background separation and enhancement integration. Sect. 3.1.2 describes the strategy used to quantify flux uncertainties, while Sect. 3.1.3 provides the emission results from four overflights conducted on 23 May 2018.

From the flux estimation, it becomes apparent that the variations between successive overflights exceed the estimated uncertainties. This discrepancy suggests that the variations are not merely due to measurement uncertainty but rather to real fluctuations in CO_2 concentrations, likely caused by inhomogeneities in plume propagation induced by local atmospheric turbulence. To explore this hypothesis, Sect. 3.2 reports on a WRF Large Eddy Simulation (LES). This section outlines the simulation setup (Sect. 3.2.1), examines the impact of turbulence on plume behaviour, and assesses how these dynamics contribute to the observed variability in the emission estimates (Sect. 3.2.2).

Finally, Sect. 3.3 brings together the measurement results and the modelling insights, and answers the overarching research questions of this case study.

3.1 Cross-Sectional Flux Method

The cross-sectional flux method determines the emission rate of a point source by calculating the downwind flux through an instantaneous cross-section of the exhaust plume. The method has been applied to air- and spaceborne nadir-viewing remote sensing (Menzies et al. 2014; Frankenberg et al. 2016; Varon et al. 2018; Reuter et al. 2019; Krautwurst et al. 2021; Jacob et al. 2022; Shi et al. 2023), portable ground-based sun-viewing remote sensing (Luther et al. 2019), and airborne in situ measurements (White et al. 1976; Cambaliza et al. 2014; Conley et al. 2016; Klausner et al. 2020; Fiehn et al. 2020). Amediek et al. 2017 describe how this principle can be realized with IPDA.

The IPDA-lidar CHARM–F directly measures the differential absorption between the online and offline laser pulses (see Sect. 2.1.2, Eq. 2.6). The resulting DAOD is proportional to the column mole fraction, expressed via the pressure integral of the weighting function in the denominator of Eq. 2.12. While the cross-sectional flux method is usually expressed in terms of column mole fractions, CHARM–F allows direct use of DAOD. This is a significant advantage as it means that the flux calculation relies solely on the measured observable rather than on weighting functions derived from numerical weather models. Consequently, one external dependency is eliminated and a potential source of systematic uncertainty avoided.

If the laser penetrates an exhaust plume, the DAOD signal is composed of a term representing the background and a term representing the absorption of the online signal by the enhanced CO_2 concentration (Amediek et al. 2017):

$$\begin{aligned}\delta &\overset{2.8}{=} \int_{z_{\mathrm{sfc}}}^{z_{\mathrm{flh}}} (n_{\mathrm{b}}(z) + \Delta n(z)) \cdot \Delta\sigma(z)\,\mathrm{d}z \\ &= \int n_{\mathrm{b}}(z) \cdot \Delta\sigma(z)\,\mathrm{d}z + \int \Delta n(z) \cdot \Delta\sigma(z)\,\mathrm{d}z \\ &= \delta_{\mathrm{b}} + \Delta\delta\end{aligned} \tag{3.1}$$

The background term δ_{b} is necessary because even in the absence of point source emissions, there is a background concentration n_{b} of CO_2 in the atmosphere that

varies spatially and temporally. The enhanced term $\Delta\delta$ results from the distribution of the CO_2 concentration in the exhaust plume.

$$\Delta\delta = \int_{z_{\mathrm{sfc}}}^{z_{\mathrm{flh}}} \Delta n(z) \cdot \Delta\sigma(z)\,\mathrm{d}z \;\approx\; \overline{\Delta\sigma} \int_{z_{\mathrm{sfc}}}^{z_{\mathrm{flh}}} \Delta n(z)\,\mathrm{d}z \tag{3.2}$$

During the time of the measurements, i.e. in the first minutes to hours after the emission took place (see Sect. 3.1.3), the plume is mostly constrained within the PBL (Gałkowski et al. 2021b). That means that contributions to the integral from beyond the top of the PBL tend towards zero. Within the PBL, the differential absorption cross section $\Delta\sigma$ exhibits only weak variability with height, since the selected laser wavelengths provide enhanced sensitivity in the lower troposphere where pressure and temperature conditions are relatively stable (Ehret et al. 2017). This allows the mean differential absorption cross section $\overline{\Delta\sigma}$ to be extracted from the integral. Amediek et al. 2017 investigated this approximation by representing the mean CO_2 enhancement with the "slender plume approximation", which assumes a Gaussian distribution of the concentration in the plume (Seinfeld and Pandis 1997; Stull 2017):

$$\Delta c\,(x,y,z) = \frac{q}{2\pi \cdot u \cdot \sigma_z(x) \cdot \sigma_y(x)} \cdot e^{-\frac{1}{2}\cdot\frac{y^2}{\sigma_y(x)^2}} \cdot \left(e^{-\frac{1}{2}\cdot\frac{(z-h)^2}{\sigma_z(x)^2}} + e^{-\frac{1}{2}\cdot\frac{(z+h)^2}{\sigma_z(x)^2}} \right) \tag{3.3}$$

q is the emission rate (in $\mathrm{kg\,s^{-1}}$) at emission height h. The mean wind speed u is defined along the propagation direction of the plume. $\sigma^2_{z/y}$ are the variances in the vertical and along flight track, respectively, and x_0 is the distance between the emission source and the cross-section of the flight ground track. Note that in this representation the emission source is arbitrarily set to $y = 0$. Moreover, the approximation assumes that the plume is reflected at the ground and remains confined to the atmosphere (i.e. that no soil uptake takes place). Mathematically, this condition is expressed by the two terms $(z_{\mathrm{flh}} - h)$ and $(z_{\mathrm{flh}} + h)$.

In the following derivation, the slender plume approximation is applied, in which the plume concentration is assumed to follow a Gaussian distribution. Inserting this representation into Eq. 3.2 yields:

$$\Delta\delta \approx \frac{e^{-\frac{1}{2}\cdot\left(\frac{y}{\sigma_y(x)}\right)^2}}{\sqrt{2\pi}\cdot\sigma_y(x)} \cdot \underbrace{\frac{q}{\sqrt{2\pi}\cdot u\cdot\sigma_z(x)} \cdot \frac{\overline{\Delta\sigma}}{M} \int_{z_{\mathrm{sfc}}}^{z_{\mathrm{flh}}} e^{-\frac{1}{2}\cdot\left(\frac{z-h}{\sigma_z(x)}\right)^2} + e^{-\frac{1}{2}\cdot\left(\frac{z+h}{\sigma_z(x)}\right)^2}\,\mathrm{d}z}_{=:A_\perp}\,, \tag{3.4}$$

with M denoting the molecular mass of the GHG of interest and $\overline{\Delta\sigma}$ the mean differential absorption cross section of the respective molecule, both typically determined from laboratory spectroscopy. Here, the absorption cross sections for CO_2 were taken from HITRAN2016 (Gordon et al. 2017). The mean wind is derived from the ECMWF analyses (ECMWF 2018) interpolated in space and time to the flight path at the altitude of the power plant's exhaust shaft. The parameter $A_\perp$ is defined by the integrated enhancement of the observed signal along the flight track (see blue

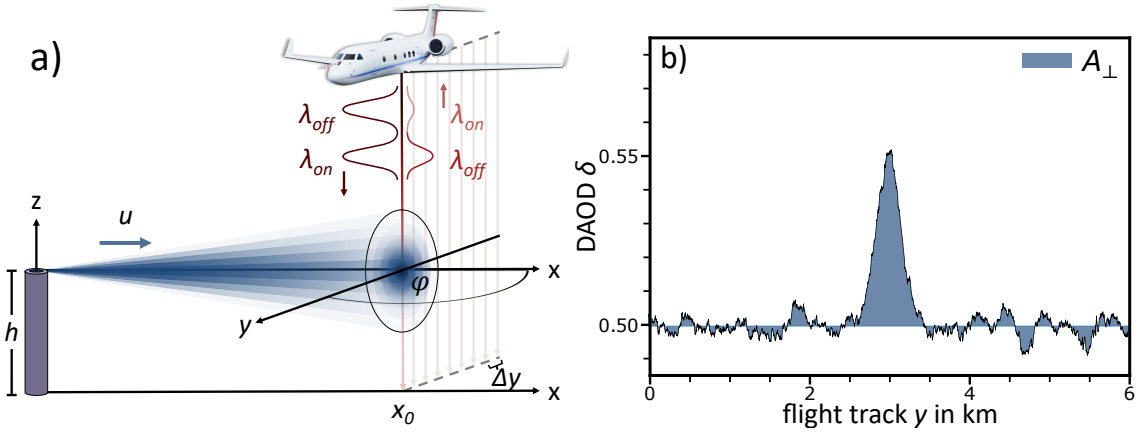

Figure 3.1: Cross-sectional survey of an exhaust plume using CHARM–F. a) Two laser pulses are emitted with a short delay: the online pulse at λ_{on} lies on the CO_2 absorption line, while the offline pulse at λ_{off} does not. Their backscattered intensities yield the DAOD via Eq. 2.6. An ideal exhaust plume has a Gaussian-shaped concentration distribution in both horizontal and vertical directions. b) A perpendicular crossing ($\varphi = 90°$) produces a Gaussian-shaped signal along the flight track. The integrated enhancement $A_\perp$ of the observed DAOD is shaded blue. Modified from Wolff et al. (2021).

shaded area in Fig. 3.1b). It can further be simplified by:

$$
\begin{aligned}
A_\perp \quad &:= \quad \frac{q}{\sqrt{2\pi}\cdot u\cdot \sigma_z(x)}\cdot\frac{\overline{\Delta\sigma}}{M}\int_{z_{\mathrm{sfc}}}^{z_{\mathrm{flh}}} e^{-\frac{1}{2}\cdot\left(\frac{z-h}{\sigma_z(x)}\right)^2}+e^{-\frac{1}{2}\cdot\left(\frac{z+h}{\sigma_z(x)}\right)^2}\,\mathrm{d}z \qquad (3.5)\\
&= \quad \frac{q}{2\cdot u}\cdot\frac{\overline{\Delta\sigma}}{M}\cdot\left[erf\left(\frac{z_{\mathrm{flh}}-h}{\sqrt{2}\cdot\sigma_z(x)}\right)+erf\left(\frac{z_{\mathrm{flh}}+h}{\sqrt{2}\cdot\sigma_z(x)}\right)\right]\\
&\overset{\substack{z_{\mathrm{flh}}\gg h\\ z_{\mathrm{flh}}\gg\sigma_z}}{=} \quad \frac{q}{u}\cdot\frac{\overline{\Delta\sigma}}{M}
\end{aligned}
$$

The flight altitude z_{flh} must be sufficiently higher than the emission height (h), and the vertical extent of the plume (σ_z), i.e. well above the PBL. For our IPDA measurements on HALO ($z_{\mathrm{flh}} \approx 6.5\,\mathrm{km}$), these conditions were fulfilled by design of the flight[1]. Rearranging Eq. 3.5 provides the cross-sectional flux formulation, in which the emission rate is determined by the integrated enhancement A observed by the lidar, together with additional parameters that must be obtained independently:

$$
q = A_\perp \cdot u \cdot \frac{M}{\overline{\Delta\sigma}} \qquad (3.6)
$$

[1]In practice, the flight altitude is chosen to balance several constraints. Ideally, the aircraft would fly directly above the PBL to capture all emissions confined within it. However, this is not possible because the detector could saturate at low altitudes. At the same time, flying much higher increases the risk of including long-range transport and, what is more, reduces the SNR. Flight regulations often impose upper limits, too. For the HALO aircraft, an altitude of about 6.5 km represents an optimal compromise and ensures that the assumptions of Eq. 3.5 are satisfied.

Crucially, Eq. 3.6 is not restricted to the Gaussian plume assumption. The slender plume representation was only used to obtain an analytical solution of the vertical integration. A deviation from Gaussian shape simply corresponds to a redistribution of mass, but the vertical integral remains mass-conserving. Therefore, even for plumes that cannot be described by a Gaussian distribution, Eq. 3.6 holds as long as the full cross-sectional enhancement is captured.

To account for deviations between the flight path and the true wind direction, Eq. 3.6 is extended by a geometric correction factor:

$$q = \sin\varphi \cdot A_{\perp} \cdot u \cdot \frac{M}{\overline{\Delta\sigma}} \tag{3.7}$$

Here, φ is the angle between the mean wind direction and the aircraft's flight track (see Fig. 3.1a). In practice, flights are planned such that $\varphi \approx 90°$, making $\sin\varphi \approx 1$. This choice not only maximizes the observed enhancement but also minimizes the impact of wind-direction errors, as will be shown in Sect. 3.1.2 with Eq. 3.10. The integrated enhancement $A_{\perp}$ is thus the only quantity directly measured by CHARM–F. Eq. 3.7 describes the instantaneous flux through the lidar cross-section at the time of overflight. In theory, this instantaneous flux equals the emission rate of the point source. In practice, however, Sect. 3.1.3 will show that fluxes vary significantly between successive crossings. A meaningful estimate of the emission rate can therefore only be obtained by averaging over multiple overflights. These fluctuations must not be confused with the uncertainty of the flux calculation, which is quantified separately in Sect. 3.1.2.

3.1.1 Background Separation and Enhancement Integration

For the calculation of the integrated enhancement A and its uncertainty it is crucial to separate the DAOD signal into two contributions: the part arising from the background concentration of CO_2 (hereafter denoted as δ_b), and the contribution from the exhaust plume of the point source ($\Delta\delta$) (see Eq. 3.1). A complicating factor is that the background term may not be constant. Small variations in local CO_2 concentrations can occur due to other anthropogenic sources (traffic, urban areas) or due to local biospheric uptake.

The separation procedure is shown in Fig. 3.2for a real-data example. The plume must first be detected as an enhancement that exceeds the noise in the data. To reduce noise, I apply a running mean (RM) to the observed DAOD (Fig. 3.2a). Increasing the window length reduces noise and makes plume enhancements more visible, but excessively wide windows can cause peak structures to become blurred. A window width of 0.2 km proved to be a useful compromise.

Starting from the middle of the plume enhancement I define the plume's limits as the intersections between the 0.2-km RM and another 4-km RM (Fig. 3.2b). A width of 0.2 km has been chosen, since it corresponds to the grid cell size of the simulation (see Sect. 3.2), thereby enabling better comparison between measured and simulated data. Hereby the values of the measured data can be compared with the simulated ones later. Experience suggests that by choosing a RM width of 4 km

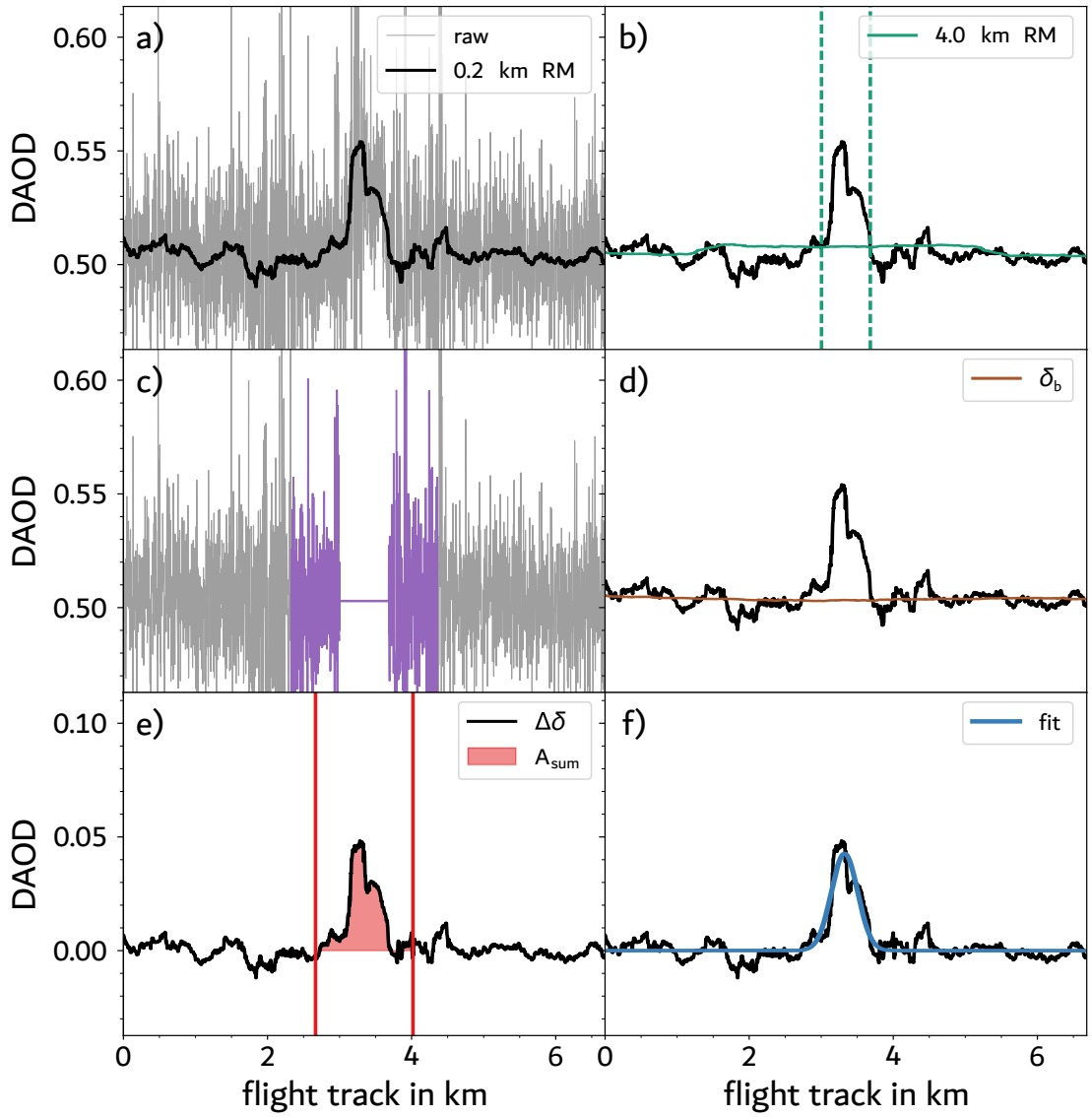

Figure 3.2: Plume crossing at a distance to the point source of 1.53 km. In (a) the grey curve shows the raw data, while the black curve shows a 0.2-km RM. In (b) the green curve is a 4-km RM. Green vertical dashed lines mark the intersections between the 0.2-km RM and 4-km RM, which are defined as the plume's limits. The purple line in (c) shows the region of the data used to construct a mean value of the data outside of the plume's limits. This mean value is used to bypass the plume enhancement and is also coloured purple. In (d) again a 4-km RM over the bypassed dataset is shown in brown. This brown data is used as background term δ_b. Finally, in (e) and (f) the enhanced term $\Delta\delta$, i.e. difference between 0.2-km RM and δ_b, is plotted in black. Note the different scale on the y-axis. In (e) the area underneath the curve is shaded red, as an example of the parameter A_{sum} determined with a Riemann sum. Alternatively, a Gaussian fit can be applied to $\Delta\delta$, providing the parameter A_{fit} as a fit-parameter, as shown as a blue line in (f). Adapted from Wolff et al. (2021).

the plume enhancement is so blurred that it blends into the background, as shown in Fig. 3.2b. The limits are then defined as the intersections between the 0.2-km RM and the 4-km RM.

Subsequently, the data within these limits is replaced by the arithmetic mean of the data outside these limits. For the calculation of this arithmetic mean I consider a window with a width equal to that of the plume, depicted as a purple line in Fig. 3.2c. Finally, I apply another 4-km RM to the raw dataset, with bypassed plume, resulting in the background term δ_{b}, shown in brown in Fig. 3.2d.

This procedure allows for variability in the background term on a few-hundred-metre scale. However, smaller-scale features cannot be attributed to the background and are therefore assigned to the enhancement term, $\Delta\delta$. In practice, this means that noise peaks are treated as part of the enhancement. This ensures that, if a peak value is due to a real enhancement rather than noise, the integrated area A would increase. However, this scenario is unlikely since there are no additional emission sources in the vicinity of the flight track, and onboard camera systems provide visual confirmation of the plume context. Consequently, residual noise peaks are incorporated into ΔA but do not bias the background estimate δ_{b}.

As explained in the previous section, the only parameter that results from a measurement by CHARM–F is the integrated enhancement A. For this purpose Amediek et al. 2017 described two distinct methods. The first method is a Riemann sum over all enhancement values $\Delta\delta_i$, multiplied with their respective spatial distance Δy_i between two successive data points:

$$A_{\mathrm{sum}} = \sum_i \Delta\delta_i \cdot \Delta y_i \tag{3.8}$$

The second method applies a nonlinear least-squares fit to the $\Delta\delta$ values of the plume, which is approximated by a Gaussian function (Eq. 3.9).

$$F(y) = \frac{A_{\mathrm{fit}}}{\kappa_2 \cdot \sqrt{2\pi}} \cdot e^{-\frac{1}{2}\cdot\left(\frac{y-\kappa_1}{\kappa_2}\right)^2} \tag{3.9}$$

This way, the integrated enhancement is obtained as the fit parameter A_{fit}. κ_1 is the peak's position along the flight track and κ_2 the turbulent dispersion parameter, which is a measure for the width of the plume. The fit method typically yields very low values for the uncertainty of the parameter A_{fit}. In contrast to the Gaussian fit, the Riemann sum is not depending on any model assumption for the calculation of the integrated enhancement along the flight track. Both methods were investigated in the course of this work and showed nearly identical results (Wolff 2018). Therefore, the results for A correspond to the mean value of the two methods, as presented in Table 3.1 in the following section.

3.1.2 Uncertainty Estimation

For CHARM–F, the two closely spaced sounding wavelengths are selected such that the differential extinction by unknown particles is minimized, while keeping the absorption by water vapour as low as possible. For water vapour this is achieved

because its differential absorption cross section is more than four orders of magnitude smaller than that of CO_2 (see Fig. 2.3b). Thus, the influence of additional water vapour in the plume released by the cooling or coal drying systems of the power plant is negligible (Kiemle et al. 2017). Moreover, the selected CO_2 absorption line is sufficiently temperature insensitive such that the influence of temperature variations within the plume can also be neglected (see also Kiemle et al. 2017).

Under these conditions, the flux error is primarily influenced by the uncertainty of the parameters A, $\Delta\sigma$, u, and φ. Assuming these parameters are uncorrelated, the relative accuracy of the flux calculation can be estimated using error propagation.

$$\frac{\delta q}{q} = \sqrt{\left(\frac{\delta A}{A}\right)^2 + \left(\frac{\delta(\Delta\sigma)}{\Delta\sigma}\right)^2 + \left(\frac{\delta u}{u}\right)^2 + \left(\frac{\delta\varphi}{\tan(\varphi)}\right)^2} \tag{3.10}$$

With $\delta A/A$, $\delta(\Delta\sigma)/\Delta\sigma$, $\delta u/u$, and $\delta\varphi/\tan(\varphi)$ denoting the relative uncertainties of these parameters. From Eq. 3.10 it is obvious that crossing the plume perpendicular to the wind direction would give the highest accuracy for any fluctuation of the wind direction $\delta\varphi$. On the other hand, atmospheric conditions at low wind speeds or situation with high atmospheric turbulence are generally less favourable because of the high relative uncertainty in the mean wind speed and wind direction. Varon et al. 2018 have identified $2\,\mathrm{m\,s^{-1}}$ as the reasonable minimum threshold of wind speed for the applicability of the cross-sectional flux method. This minimum value is also referred to by Sharan et al. (1996), arguing that above this threshold, advection dominates over diffusion.

To assess how noise in the observed DAOD $\Delta\delta$ propagates into the uncertainty of the integrated enhancement A_{sum}, I compute 15 Riemann sums with varying integration limits. The minimum integration range is defined as twice the plume limits determined in Sect. 3.1.1 (see Fig. 3.2e), ensuring that the entire plume is covered. To test the sensitivity to residual noise, the integration width is then expanded stepwise by 400 m, yielding a total of 15 different integration ranges.

To obtain the value of $\Delta\sigma$ required in Eq. 3.7 and to quantify its contribution to the error budget, the differential absorption cross section $\Delta\sigma$ is calculated using the Voigt-profile model with input from HITRAN2016 data base for the line parameters (Gordon et al. 2017). This calculation requires the knowledge of pressure and temperature profiles, which are extracted from the WRF simulation (see Sect. 3.2). For the lidar measurements, the online wavelength was tuned to the CO_2 absorption line centre at $\lambda_{\mathrm{on}} = 1572.02\,\mathrm{nm}$, while the offline wavelength was adjusted to $\lambda_{\mathrm{off}} = 1572.12\,\mathrm{nm}$ in the wing of this line (cf. Fig. 2.3b). Based on this wavelength selection and a flight altitude of 8 km, the background DAOD δ_{b} is approximately 0.5, while the plume causes a $\approx 10\,\%$ enhancement (≈ 0.05), as depicted in Fig. 3.2.

A potential source of error arises from the fact that the absorption cross section is not constant over the vertical extent of the plume. With increasing altitude, decreasing pressure leads to reduced collisional line broadening, which slightly modifies $\Delta\sigma(z)$. The question is therefore whether the vertical dispersion of the plume can introduce a systematic bias into the flux calculation. To assess this effect, representative mean values of $\Delta\sigma$ were calculated at two downwind distances, $x_1 =$

1.5 km and $x_2 = 4.7$ km (see Table 3.1), using the slender plume approximation (Amediek et al. 2017; Seinfeld and Pandis 1997). The corresponding mean differential absorption cross sections were obtained according to:

$$\Delta\sigma\left(x_{1,2}\right) = \frac{\int_{z_0}^{z_{\max}} \Delta\sigma(z) \cdot \left(e^{-\frac{(z-h)^2}{2\cdot\sigma_z(x_{1,2})^2}} + e^{-\frac{(z+h)^2}{2\cdot\sigma_z(x_{1,2})^2}} \right) \mathrm{d}z}{\int_{z_0}^{z_{\max}} \left(e^{-\frac{(z-h)^2}{2\cdot\sigma_z(x_{1,2})^2}} + e^{-\frac{(z+h)^2}{2\cdot\sigma_z(x_{1,2})^2}} \right) \mathrm{d}z} \tag{3.11}$$

Here, $z_0 = 0$ km and $z_{\max} = 4$ km define the integration boundaries, and $h = 120$ m is the release height of the emission shafts. The parameter σ_z describes the vertical dispersion and thus links the turbulence intensity to the vertical extent of the plume. For moderately turbulent conditions, plume widths of $\sigma_z = 170$ m and 600 m were estimated for the two distances, while weaker turbulence yields narrower plumes of $\sigma_z = 90$ m and 250 m. Since no further turbulence information was available, both scenarios were considered. The vertical dependence of $\Delta\sigma(z)$ itself was approximated by a 2$^{\text{nd}}$-order polynomial fit to representative Voigt-profile simulations up to 4000 m altitude (cf. Wolff et al. 2021):

$$\Delta\sigma(z) = 7.10652 \cdot 10^{-27}\mathrm{m}^2 + 8.60755 \cdot 10^{-31}\mathrm{m} \cdot z + 8.02673 \cdot 10^{-35} \cdot z^2 \tag{3.12}$$

The deviation of this polynomial from the exact Voigt-profile values is below 0.1 %, which is negligible for the present purpose. Applying Eq. 3.11 with this parameterisation yields $\overline{\Delta\sigma}$ =$7.27 \cdot 10^{-27} \pm 0.04 \cdot 10^{-27}$ m^2 for $x_1 = 1.5$ km and $7.47 \cdot 10^{-27} \pm 0.24 \cdot 10^{-27}$ m^2 for $x_2 = 4.7$ km. At 1.5 km downwind, the relative uncertainty in the mean differential absorption cross section is only 0.6 % and thus negligible. At 4.7 km, the larger vertical spread of the plume increases this value to 3.2 %, which represents a relevant contribution to the overall error budget in Eq. 3.10. Possible systematic errors, due to uncertainties of the line parameters, are less than 2 % (Gordon et al. 2017). Wavelength setting errors of the CHARM–F instrument are very small (~ 0.5 %, Amediek et al. 2017) and can be neglected compared to the other error sources.

As mentioned before, the wind data are taken from operational analysis data of the ECMWF-IFS (ECMWF 2018). This is done by first interpolating the 4-dimensional gridded model data onto the flight path at the altitude of the power plant's exhaust shaft. Secondly, a mean value of the wind speed and direction along the flight track, as well as an estimate of their relative errors, is calculated according to Ackermann 1983. These wind uncertainties are not negligible and directly propagate into the flux estimates. Their quantitative impact are evaluated together with the flux results in the following section.

3.1.3 CO_2 Flux Estimation

In the German federal state of Brandenburg the Lausitz Energie Kraftwerke AG (LEAG) operates the coal-fired power plant *Jänschwalde*, close to the German-Polish

border (cf. Fig. 3.3). The power plant's primary fuel is lignite, a type of brown coal, but it is also a certified for the co-incineration of processed waste. It has an installed capacity of 2000 MW, spread over four power plant units and, as mentioned in the Introduction, is one of the largest power plants in Europe, both in terms of annual electricity generation as well as annual CO_2 emissions.

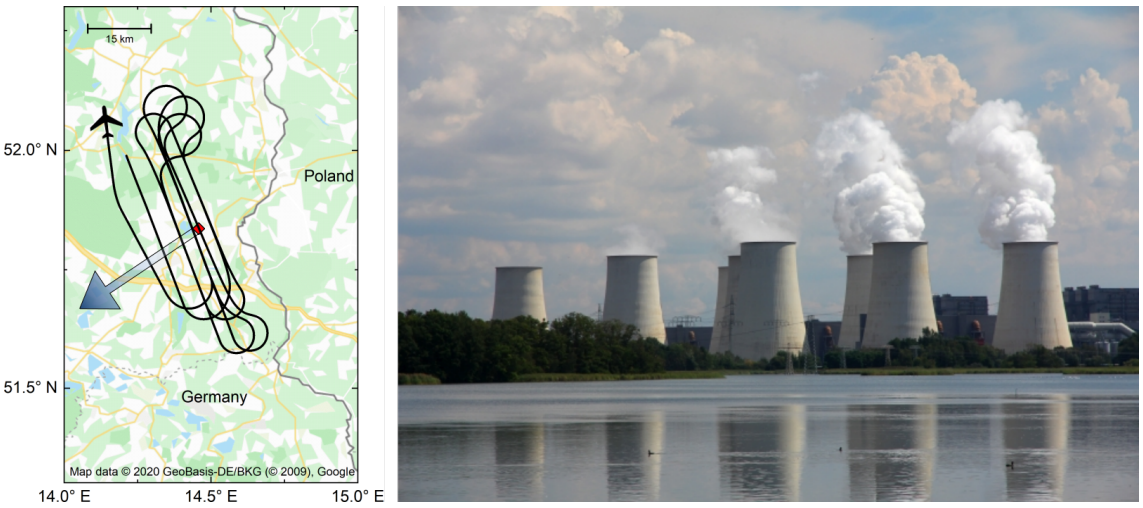

Figure 3.3: Left: The black line depicts the flight track of HALO between 10:24 and 11:36 CEST on 23 May 2018. The red square marks the position of the power plant. The arrow shows the mean wind direction during the observation period. The grey line marks the German-Polish border. Right: Picture of the coal-fired power plant Jänschwalde. The exhaust gases are released through the nine cooling towers. Adapted from Wolff et al. (2021).

In March 2024, two 500 MW units were taken off the grid as part of Germany's ongoing coal phase-out and energy transition policies. The Jänschwalde site is to be maintained and transformed beyond the coal phase-out on the basis of gas, hydrogen and storage technologies (LEAG 2024). Despite this, in 2018, when the measurements discussed here were recorded, the power plant was still operational with coal. The operators reported a total CO_2 emission of 23.1 Tg to the European Environment Agency (E-PRTR 2023). Unlike similarly sized power plants, its emissions are not released through high stacks but through six of its nine cooling towers. This design results from the modern flue gas treatment system, which cools the exhaust to temperatures too low for stack venting (Busch et al. 2002). Consequently, the effective release height is relatively low and the buoyancy rise is limited. The cooling towers are 120 m high and arranged in three parallel rows, with a distance of roughly 50 m between the rows and 250 m between adjacent towers within a row (cf. Fig. 3.3).

In this work the measurement flight of HALO on 23 May 2018 between 10:24 and 11:36 CEST (08:24–09:36 UTC) is investigated. Figure 3.3 shows the flight track of the aircraft. In total, the point source was flown over seven times downwind, two times upwind, and once directly over the cooling towers. In three of the downwind overflights, no enhancement in DAOD is detectable. For these transects, the distance

to the point source is greater than 4.6 km. At such distances, it can be assumed that the exhaust gases are too diluted with the surrounding air to generate a detectable signal. The remaining four downwind overflights, however, are well suited for the cross-sectional flux estimation.

Table 3.1 shows the measured integrated enhancements, the wind data, and the resulting fluxes for the four exploitable overflights, alongside the obtained mean values, under the assumption that during the measurement both the wind direction and the wind speed were reasonably constant. The flight segments were not exactly perpendicular to the mean wind direction. With a relative wind direction of $\varphi = 103°$ a correction factor of $\sin(103°) = 0.97$ is applied (see Eq. 3.7). The mean wind speed of $u = 5.06\,\mathrm{m\,s^{-1}}$ is well above the threshold of $2\,\mathrm{m\,s^{-1}}$, introduced in Sect. 3.1.2.

Table 3.1: Flight measurement results for the Jänschwalde power plant on 23 May 2018, following the nomenclature of Eq. 3.7. Shown are the instantaneous flux q, integrated enhancement $A_\perp$, and differential absorption cross section $\Delta\sigma$, together with flown path length and source distance. The mean wind speed is u =5.06 ± 0.36 $\mathrm{m\,s^{-1}}$ and the mean relative wind direction $\varphi = 103.34° \pm 6.40°$. Modified from Wolff et al. (2021).

Crossing			**Measurement**			
local time	path in km	distance in km	**mean q in kg/s**	**q in kg/s**	A in m	$\Delta\sigma$ in $10^{-27}\,\mathrm{m^2}$
10:50	200	1.46	**650 ± 240**	**760 ± 60**	15.36 ± 0.67	7.27 ± 0.04
10:57	268	4.77		**470 ± 40**	9.04 ± 0.42	7.47 ± 0.24
11:10	388	1.67		**950 ± 80**	19.29 ± 0.46	7.27 ± 0.04
11:27	536	1.78		**420 ± 40**	8.45 ± 1.11	7.27 ± 0.04

The individual flux uncertainties, calculated with Eq. 3.10, are relatively small and range between 8 % and 10 %. On average, 2/10 of this uncertainty arises from the integrated enhancement $\delta A/A$, 1/10 from the combined uncertainties of the mean differential absorption cross section of CO_2 $\delta(\Delta\sigma)/\Delta\sigma$ and the mean relative wind direction $\delta\varphi/\tan(\varphi)$, while the dominant contribution of 7/10 stems from the mean wind speed $\delta u/u$. This highlights the importance of accurate wind information. The reported value of $760\,\mathrm{kg\,s^{-1}}$ ($24.0\,\mathrm{Tg\,a^{-1}}$, E-PRTR 2023) lies within the error range of the mean value of 650 ± 240 $\mathrm{kg\,s^{-1}}$ (20.3 ± 7.9 $\mathrm{Tg\,a^{-1}}$).

Nevertheless, the variations between the individual crossings are much larger than the formal measurement errors (cf. Table 3.1). For example, the second and third crossings differ by approximately a factor of two. The pronounced discrepancy is also evident in Fig. A.1b) and c), where the plume enhancements exhibit distinctly different amplitudes. Such discrepancies cannot be explained by the quantified uncertainties and are therefore hypothesized to result mainly from turbulence-induced inhomogeneities in the plume. This hypothesis will be investigated in the following section.

3.2 Large Eddy Simulation

The pronounced variability between individual flux estimates suggests that turbulence plays a major role in shaping the observed plume. To test this hypothesis, high-resolution modelling is required. In a Large Eddy Simulation (LES), the dominant turbulent eddies are explicitly resolved, while only the smallest unresolved scales (subgrid-scale turbulence) are parametrized. This differs fundamentally from a conventional mesoscale WRF run at, for example, 5 km resolution, where all turbulent motions below the grid size are represented only through simplified parameterisations. LES therefore demands a much finer horizontal grid spacing, typically on the order of 10 – 500 m, but in return it provides a physically realistic representation of local eddies, updrafts, and downdrafts within the plume.

This capability is essential for the present study. I hypothesize that the variability between successive overflights is driven by turbulence-induced heterogeneity in the plume rather than by measurement errors. With LES, such localized structures — puffs of enhanced CO_2 or constrictions of lower concentration — can be simulated explicitly, whereas a coarser mesoscale model would smooth them out and reproduce only a mean Gaussian-like plume. Using LES thus allows me to demonstrate that turbulence-driven fluctuations account for the observed spread of instantaneous flux estimates and that the variability reflects plume dynamics rather than instrumental noise. In this context, the simulations are used to address **RQ3**: Under which atmospheric conditions and flight geometries do uncertainties in IPDA-based emission quantification become most pronounced, and how can future flight planning be adapted to mitigate these effects?

3.2.1 WRF-LES Setup

The following section describes the setup of the numerical simulations. For this purpose, WRF version 3.8.1 (Skamarock et al. 2008) is employed. WRF is a widely used and well-established platform for investigating plume transport processes (Zhao et al. 2019; Bhimireddy and Bhaganagar 2018; Yver et al. 2013). The specific model configuration employed in this study is summarized in Table 3.2.

Considering the typical source distances of the measurement crossings (Table 3.1) and the observed plume spread (Fig. A.1), a horizontal resolution in the sub-kilometre range is required. To achieve this, three nested domains were introduced, centred on the middle cooling tower (Fig. 3.4). The outermost domain (D01, 5 km) ensures consistency with the ECMWF boundary data, while the intermediate domain (D02, 1 km) provides a mesoscale description of the regional flow. The innermost domain (D03) is configured as a LES with 200 m horizontal resolution. Following Powers et al. (2017), this setup explicitly resolves the dominant turbulent eddies and thus captures the plume variability observed in the measurements. Several studies have demonstrated that WRF-LES is well suited for modelling plume trajectories together with turbulence and passive tracer dispersion (Moeng et al. 2007; Nunalee et al. 2014; Nottrott et al. 2014). The corresponding configurations are summarized in Table 3.3.

Table 3.2: WRF model configuration. Applicable WRF namelist option is given in italics.

	Setting	Reference
WRF version	WRF 3.8.1	Skamarock et al. 2008
Simulated time span	06:00 UTC 21 June - 06:00 UTC 24 June 2018	
Spin-up	6 h	
Number of vertical layers	56	
Model top	200 hPa	
Radiation	Rapid Radiative Transfer Model scheme $ra\_lw\_physics = ra\_sw\_physics = 4$	Iacono et al. 2008
Microphysics	Morrison two-moment scheme $mp\_physics = 10$	Morrison et al. 2009
Land surface model	Unified Noah land-surface model $sf\_surface\_physics = 2$	Tewari et al. 2004
Surface layer physics	Revised MM5 Scheme $sf\_sfclay\_physics = 1$	Jiménez et al. 2012

Table 3.3: Configuration of quadratic domains. For more information on the PBL physics scheme MYNN level 2.5 refer to Nakanishi and Niino 2009. For the LES PBL scheme refer to Moeng et al. (2007). Modified from Wolff et al. (2021).

Domain	D01	D02	D03
Horizontal resolution	5 km	1 km	0.2 km
Computational time step	30 s	5 s	1 s
Number of grid cells	100 x 100	150 x 150	175 x 175
Domain size	500 x 500 km^2	150 x 150 km^2	35 x 35 km^2
PBL physics scheme	MYNN level 2.5 $bl\_pbl\_physics = 5$	MYNN level 2.5 $bl\_pbl\_physics = 5$	LES PBL $bl\_pbl\_physics = 0$
Eddy coefficient option	2D deformation $km\_opt = 4$	2D deformation $km\_opt = 4$	3D TKE $km\_opt = 2$
Turbulence and mixing option	Simple diffusion $diff\_opt = 1$	Simple diffusion $diff\_opt = 1$	Full diffusion $diff\_opt = 2$

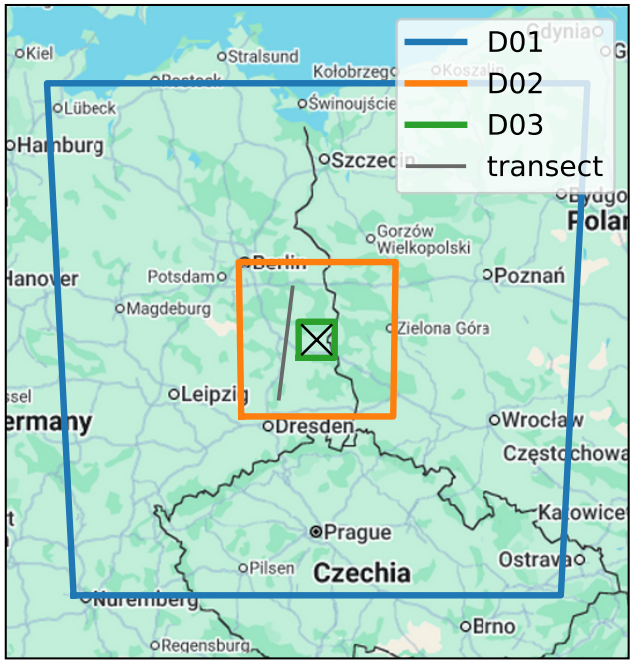

Figure 3.4: Location of three time-nested domains of the WRF simulation. They are centred on the power plant Jänschwalde (black cross). The domains have a side length of 500 (D01), 150 (D02), and 35 km (D03) and a horizontal resolution of 5 km (D01), 1 km (D02), and 0.2 km (D03). The virtual transect marked in D02 corresponds to the vertical cross-section shown in Fig. 3.5b–c. Modified from Wolff et al. (2021).

A virtual transect is depicted across D02 (Fig. 3.4) to serve as a reference for examining the vertical model structure. Along this transect, Fig. 3.5 shows the 57 terrain-following vertical η-levels, highlighting the fine resolution near the surface. The vertical discretisation was designed such that a full model layer lies below the effective release height of the power plant ($h = 120\,\mathrm{m}$). As discussed in the previous section, the exhaust gases are released through cooling towers after passing through a modern flue gas treatment system, which reduces their temperature to a level too low for stack venting. Consequently, the effective release height is comparatively low, the buoyancy rise is minimal and no additional plume-rise parametrization is required. This setup has been shown to produce realistic plume characteristics when compared with observations and other ATMs (see Brunner et al. 2023).

No atmospheric CO_2 background field is simulated, meaning only the exhaust plume of the power plant is present in the simulation. For this purpose, WRF allows the definition of a passive tracer variable $\mathrm{tr}(t, x, y, z)$, as introduced by Blaylock et al. (2017). This tracer follows the transport and dispersion of the emissions without chemical reactions. A detailed description of the calculation of simulated DAOD can be found in the Supplement, where Eq.(A.3) is used to derive the DAOD enhancement from the horizontal tracer distribution.

The WRF simulation provides a data output every 2 min. One virtual plume

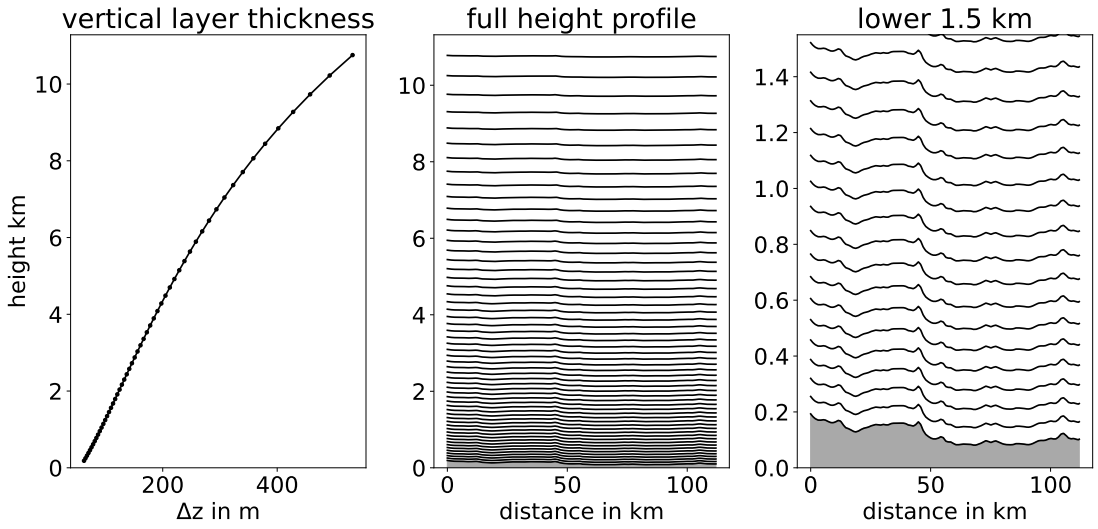

Figure 3.5: Vertical layers in WRF. The ground is displayed in grey, the vertical layer interfaces in black. a) displays the vertical layer thickness Δz. The vertical resolution is relatively fine at low altitudes and decreases at higher altitudes. b) shows all 57 vertical layer interfaces from the Earth's surface up to the model's top (200 hPa) along the virtual transect drawn into Fig. 3.4 flight track. c) shows a zoom into the lower 1.5 km above sea level. The lowest level is equivalent to the Earth's surface. Moreover, the terrain-following nature of the η-level can be seen.

crossing is evaluated for each output time step at a point source distance of 1.5 km, corresponding to the measurements presented in Table 3.1. For the determination of the integrated enhancement, it does in principle not matter at which distance to the point source the virtual flyover takes place, as neither background field nor noise is simulated. Nonetheless, I try to match the virtual survey as closely as possible to real conditions. Just as in the real measurement, the virtual crossings are arranged perpendicular to the propagation direction of the plume (cf. Sect. 3.1). However, in a turbulent atmosphere, it is not trivial to precisely identify this direction of propagation. In this work, I consider the centre of mass of the emitted tracers within a radius of twice the point source distance, i.e. 3 km. A connecting line between this centre of mass and the point source corresponds to the propagation direction.

For the calculation of the virtually retrieved emission rate, the mean wind speed and direction are needed (see Eq. 3.7). To obtain these from the simulation, the following procedure is performed. First, for each data output step the horizontal wind components at the mean height of the plume are retrieved by vertical integration, weighted with tracer mass content. Second, the resulting 2D wind field is linearly interpolated onto the virtual flight path, yielding a 1D field with the horizontal wind components along the flight track. Last, the wind components are integrated and weighted with the DAOD along the flight track, resulting in the mean wind used for calculation.

3.2.2 WRF-LES Simulation Results

The WRF-LES simulations reproduce plume dispersion with realistic characteristics (see Fig. 3.6). The simulated DAOD enhancements are of the same order of magnitude as the values observed with the CHARM–F instrument, indicating good consistency between model and measurements. Exemplary snapshots of the simulated plume at different times of day (approximately every two hours) are provided in the Supplement (see Fig. A.2). Additionally, an animated GIF of the simulated plume can be found under https://doi.org/10.5281/zenodo.4266513 (Wolff 2020). In the nocturnal absence of solar irradiation, the turbulence decreases, leading to narrow, homogeneous plume dispersion within a laminar flow. The exhaust plume follows Gaussian behaviour, as depicted in Fig. 3.6 at 23:30 CEST. By contrast, daytime conditions are characterized by boundary layer turbulence. Solar heating of the

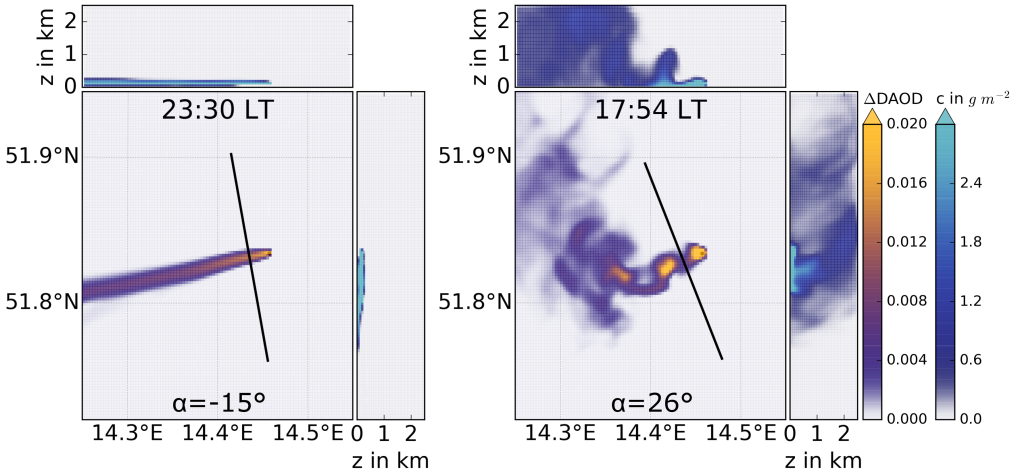

Figure 3.6: Exemplary snapshots of simulated exhaust plumes. The flight track of the virtual plume overflight is shown as a black line. At the top of the respective middle panels, the local time is given in Central European summer time (CEST, i.e. UTC+2), and at the bottom α denotes the local solar altitude. The first colour bar represents the DAOD enhancement and refers to the respective middle panel, which shows the horizontal dispersion of the plume. The second colour bar represents the mass per area and refers to the top and right panels, which show the vertical dispersion. In a corresponding measurement, DAOD enhancement values below 0.008 would not be distinguishable from noise and are therefore displayed in blue. Values higher than 0.01 exceed the noise and can be identified as plume enhancement in a real measurement. A value of 0.02 corresponds to an enhancement of 4 % with respect to a background of 0.5 (cf. Fig. 3.2). Adapted from Wolff et al. (2021).

surface generates convective air masses, which in turn cause a cascade of eddies. Along these eddies, counter-gradient flow emerges, i.e. flow opposite to the main wind direction. This results in local puffs of above-average column concentration enhancements within the exhaust plume. Meanwhile, eddy-generated local flow in the same direction as the ambient wind causes constrictions of lower concentrations in the plume (Stull 1988). These plume structures deviate from Gaussian behaviour,

as can be seen in Fig. 3.6 at 17:54 CEST.

A locally increased CO_2 column concentration results in a high value of the integrated enhancement A, in contrast to an overflight over a constriction. According to Eq. (3.7) this corresponds to a high value of the emission rate q. It should also be noted that such puffs have a smaller spatial extent than complementary constrictions. Therefore, a skewed distribution of the retrieved emission rates is to be expected, as confirmed by Fig. 3.7.

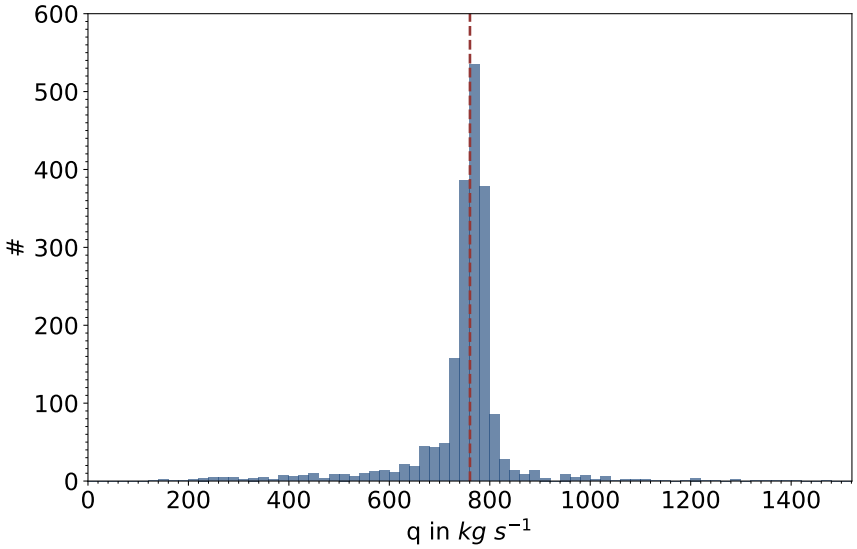

Figure 3.7: Histogram of virtually retrieved emission rates, showing a slight skew towards smaller values than the input emission rate (dashed red line). It includes all 1980 retrievals between 12:00 UTC on 21 May and 06:00 UTC on 24 May. Adapted from Wolff et al. (2021).

On 23 May 2018, four measurement flyovers of the Jänschwalde power plant took approximately 1 h, as presented in Sect. 3.1.3. The first 6 h of the simulation are discarded as spin-up (see Table 3.2). This leaves 66 h of simulation, which corresponds to a total of 1980 virtual plume flyovers. The results of the virtually "measured" emission fluxes, which are calculated using Eq. (3.7), are displayed as a histogram in Fig. 3.7 and as a time series in Fig. 3.8a).

Figure 3.8a) shows how the diurnal course of solar altitude α influences the retrieved emission rates q. The random occurrence of inhomogeneities in plume propagation, caused by local turbulence, leads to significant variations in successive crossing results. Turbulence lags behind solar altitude because the surface needs time to heat up. It is also apparent that the emission rate deviations vary from day to day, both in intensity and in dwell time. The implications for the measurement results can be reduced by averaging over a multitude of retrieved emission rates.

Next, I investigate how often the exhaust plume must be surveyed to determine an emission rate with satisfactory accuracy on average. Based on experience from the

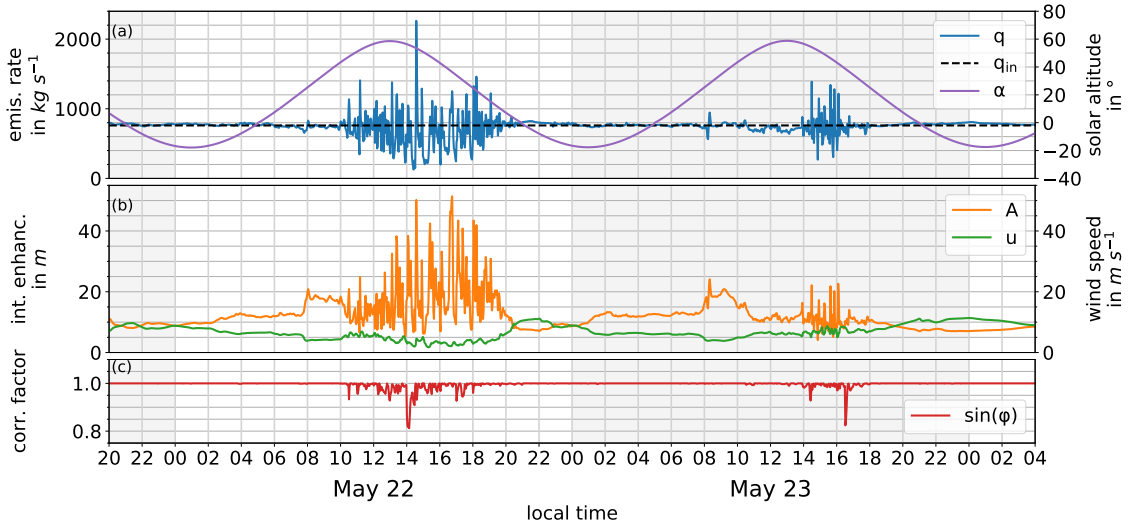

Figure 3.8: Virtual overflight results in the course of the day. In (a) it can be seen that rising solar altitude α entails turbulence. Especially midday turbulence causes deviations in the retrieved emission rate q from the input emission rate q_{in}. In (b) the integrated enhancement A shows equivalent behaviour, while the variations in wind speed u are comparatively small. It is during the midday turbulence that the virtual flight tracks are not exactly perpendicular to the instantaneous wind direction at the plume crossing, which becomes apparent in the correction factor $\sin(\varphi)$ in (c). In the night hours, as well as the morning, the retrieved emission rates agree well with the input emission rate q_{in}. The wind speed u surpasses the threshold value of $2\,\mathrm{m\,s^{-1}}$ at all times. Adapted from Wolff et al. (2021).

measurement flights presented in Sect. 3.1.3, as well as other point source surveys during the CoMet campaign not shown here, I prescribe a time delay of 6 min to 18 min between two successive crossings. With typical wind speeds of $5\,\mathrm{m\,s^{-1}}$ to $8\,\mathrm{m\,s^{-1}}$ and simulated spatial scales of puffs and constrictions of 1 km to 2 km, this delay exceeds the residence time of coherent plume structures and thus prevents repeated sampling of the same air masses.

The model setup provides one virtual crossing every 2 min, yielding a large number of possible permutations for merging successive transects (Table 3.4). For each permutation, I calculate a mean value and compare it with the prescribed emission rate q_{in}. To assess turbulence-induced inhomogeneity over the course of a

Table 3.4: Number of permutations of successive virtual crossings used for averaging. Adapted from Wolff et al. (2021).

Number of overflights	Number of possible permutations
1	60
4	5000
7	312500
10	9765625

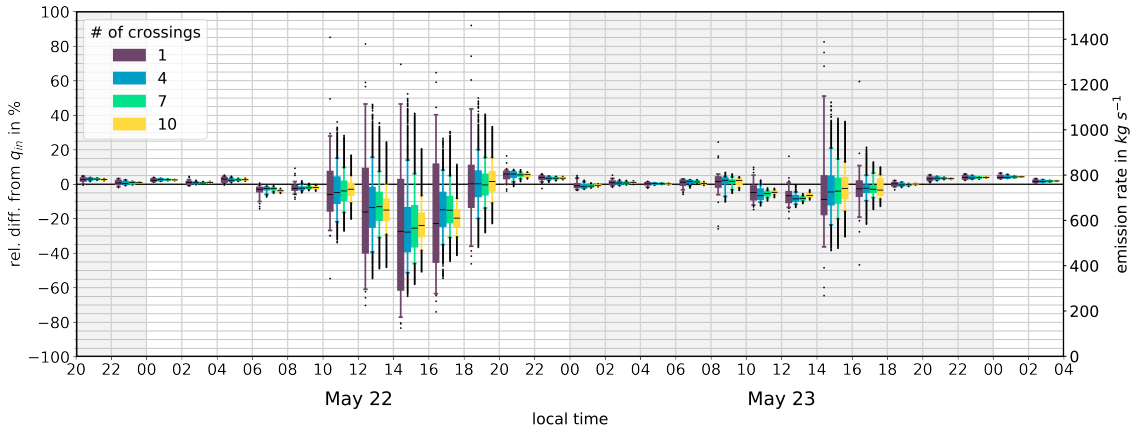

Figure 3.9: Box-whisker plots of the relative difference to the input emission rate q_{in} within 2 h-time frames. The right axis shows the associated retrieved emission rates. Different colours represent different number of virtual crossings merged for averaging. The inner boxes range from the first to the third quartile, thus containing 50 % of the values. The median is marked within as a black dash. The upper whisker is drawn up to the 95^{th} percentile, while the lower whisker is drawn to the 5^{th} percentile. Consequently, 90 % of the values are in between the two whiskers. All values outside the whiskers are outliers and plotted as dots. Adapted from Wolff et al. (2021).

day, I analyse 2 h-time frames, each containing 60 virtual overflights. The number of possible permutations rises quickly, from about 5000 for four merged crossings to over 300 000 for seven (Table 3.4). These high numbers stem from the identical set of 60 single-crossing emission rates, shown as purple box-whisker plots in Fig. 3.9.

Figure 3.9 presents the resulting distribution of this relative difference to the input emission rate as a box-whisker plot. The spread of the respective box-whisker plot is an indicator of turbulence. It is evident that with an increasing number of overflights merged for averaging, the spread of the relative differences decreases, while the measurement precision increases. A high emission rate measured by a single overflight scanning a puff is compensated for if the subsequent overflight measures a lower emission rate. With a higher number of overflights averaged, it is more likely to measure both high- and low-concentration air masses. Yet, although the precision can be improved by increasing the number of overflights, even ten overflights are inferior to the precision of one nighttime measurement. Additionally, not only the precision but also the accuracy is compromised during times of strong turbulence, i.e. in the afternoon. As mentioned above, the spatial extent of turbulence-induced puffs is smaller than the one of the complementary constrictions. This asymmetry resembles the well-known structure of turbulent motions in the convective boundary layer, where strong and narrow updrafts are surrounded by broader regions of subsidence (Stull 1988; Schmidt and Schumann 1989; Schumann 1989). Therefore, such puffs are likely to be less frequent and only partially scanned when measured at a low sampling frequency. Consequently, the retrieved emission rates will be biased low. This is an effect that occurs especially during strong turbulence. In Fig. 3.9 a strongly turbulent

day (22 May) is compared to a less turbulent day (23 May). Both precision and accuracy are superior on a less turbulent day.

In contrast, the night hours show little turbulence and high precision. Even with a single overflight, small differences to the true emission rate are to be expected. Here, a higher number of overflights will only cause minor improvements. At this point, it should be mentioned that the representation of nightly plume propagation must be critically reviewed. The plume height decreases so much that the propagation takes place only in the lowest four model layers. The fact that a bias of approx. $\pm 5\,\%$ remains at night is not surprising from this point of view. This study should therefore be understood as a qualitative assessment. The key finding is that avoiding situations of high turbulence brings an enormous improvement for both precision and accuracy. Even with a significantly higher number of measurement overflights, a comparable improvement cannot be attained.

3.3 Summary & Conclusion

Case Study I builds upon the work of Amediek et al. (2017), who demonstrated the feasibility of airborne IPDA lidar flux quantification at coal mine sources. Here, I extend these investigations to a large coal-fired power plant and systematically examine the reliability of the cross-sectional flux method using repeated overflights of the Jänschwalde power plant during the CoMet campaign in 2018. The aim is to address **RQ1** and **RQ3**.

The lidar measurements on 23 May 2018 yield mean emission rates of $20.3 \pm 7.9\,\mathrm{Tg\,a^{-1}}$, which is consistent with the operator's reported value of $24.0\,\mathrm{Tg\,a^{-1}}$ (E-PRTR 2023). The exhaust plume generated column enhancements in the DAOD with a SNR of about 10 %. The product of the enhanced column concentration, integrated along the flight track, and the mean wind speed provides the instantaneous flux through the lidar cross-section. The flux of an individual overflight can be determined with an uncertainty of 8 – 10 %, mainly driven by errors in the integrated enhancement, the differential absorption cross section, the relative wind direction, and the horizontal wind speed. On average, 2/10 of this error is due to the integrated enhancement of the DAOD signal, 1/10 arises from the differential absorption cross section and wind direction, while the dominant 7/10 is linked to the horizontal wind speed. This highlights the critical need for more accurate wind information.

Beyond the formal error budget, there are restrictions regarding the flight geometry. At source distances greater than 4.6 km, no plume enhancement becomes detectable and the cross-sectional flux method can no longer be applied. At closer distances of about 1.5 km, distinct plume enhancements are observed, and the uncertainty linked to the mean differential absorption cross section becomes negligible. The closer the overflight is to the source, the more compact and pronounced the plume signal. However, fewer data points lie within the plume cross-section. For CHARM–F, this can be compensated by the high repetition rate. Overall, flying close to the source, while avoiding too much dilution, provides the most favourable conditions.

To further investigate turbulence-induced variability, high-resolution transport modelling was performed with WRF in an LES setup. As only four overflights are available in the measurement, no statement on the absolute accuracy of the simulation can be made, which is also not the intention here. Qualitatively, however, the simulation provides valuable insights. At night, the plume remains weakly distorted and close to Gaussian because laminar flow dominates. Over the course of the day, turbulence increases, peaks in the afternoon, and distorts the plume into non-Gaussian shapes. According to the simulation, nighttime conditions are so stable that even a single instantaneous flux measurement can reach accuracies of up to $\sim 95\,\%$. By contrast, in strongly turbulent afternoons, even ten averaged overflights perform worse in both precision and accuracy than a single nighttime crossing.

At this stage, no strict limits on solar altitude or time of day can be derived, since the intensity of turbulence varies from day to day (see Figs. 3.8 & 3.9). In general, the strongest turbulence occurs in the afternoon. Consequently, flight planning should avoid midday conditions and, wherever possible, target nighttime or morning hours. In this respect, intrinsic independence from solar irradiation is a clear advantage of active remote sensing over passive approaches. The turbulence-induced variability diagnosed here is generic and should equally affect passive and in situ observations. Whether these systems can realize a net benefit from avoiding peak turbulence, however, depends on system-specific trade-offs, such as reduced radiance and larger retrieval errors for passive sensors at low solar altitude, or limited access to the boundary layer for in situ aircraft at night. The present study provides the first explicit quantification of turbulence effects for lidar and thus an actionable basis for flight planning. Assessing the net benefit for passive and in situ systems requires dedicated studies by those communities.

In answer to **RQ1**, isolated point-source emissions can be quantified with airborne IPDA lidar using the cross-sectional flux method with good reliability. The main source of uncertainty is wind speed, which should ideally be measured directly from the aircraft to improve accuracy. In regard to **RQ3**, the limiting factor is turbulence. Strong turbulence causes plume variability that dominates over measurement noise and formal errors. To mitigate this, future flight planning should prioritise nighttime or early-morning flights and avoid large downwind distances where the plume is diluted beyond detectability.

4 Case Study II:

Quantification of Multiple CH_4 Point Sources

While the previous chapter focused on **Case Study I** — a well-isolated CO_2 plume from a single, known point source — this chapter takes it a step further by exploring **Case Study II**: a fundamentally different setting involving multiple, spatially distributed CH_4 point sources. In many regions, CH_4 is not emitted from a single, dominant hotspot but from spatially distributed sources. Examples of such regions include oil and gas fields, and coal mining areas. The USCB is one such region, where CH_4 is released from numerous coal mine ventilation shafts. The spatial proximity of emitting shafts leads to overlapping plumes, which complicates source attribution and limits the applicability of traditional cross-sectional flux estimates. In contrast to the simple observational geometry of **Case Study I**, the spatial attribution of emissions in such complex environments is inherently ambiguous.

Future satellite missions such as MERLIN are designed to constrain continental- to global-scale CH_4 budgets using IPDA lidar, but are not designed to resolve individual plumes or sources routinely. This may only occur under favourable conditions, for example when wind direction causes a plume to be intersected nearly orthogonally by the satellite track. Particularly for sources like wetlands or agriculture, where emissions are both widely distributed and dynamically variable in space and time, inverse modelling becomes essential. Compared to those unknown and diffuse source settings, the USCB offers a more spatially well-characterized but still challenging environment, making it a valuable intermediate step for methodological development.

This chapter therefore serves a dual purpose: It investigates whether airborne IPDA lidar data can be used in combination with inverse modelling to constrain emissions in a multi-source region, and it acts as a methodological stepping stone for future satellite-based inversions. To my knowledge, this is the first demonstration of a regional inversion framework using IPDA lidar observations, providing an important proof-of-concept in the context of MERLIN preparation.

To address this challenge, an ensemble-based Bayesian inversion framework, i.e. the Carbon Tracker Data Assimilation Shell (CTDAS), is deployed, combining airborne lidar observations with atmospheric transport modelling. This approach provides a pathway to constrain regional emissions by leveraging prior knowledge of spatial source distributions and estimated source emissions, while incorporating meteorological dynamics through the atmospheric transport model WRF.

Thereby, **Case Study II** directly addresses two key research questions:

- **RQ2:** Can a combination of airborne IPDA lidar and inverse modelling be used to quantify and spatially attribute overlapping CH_4 emissions from multiple sources?
- **RQ3:** What are the major sources of uncertainty in IPDA-based emission quantification, and how can flight planning or methodological choices reduce them?

This chapter is structured as follows: Section 4.1 introduces the target region (USCB) and outlines its relevance as a major coal mining area with significant CH_4 emissions. Section 4.1.1 summarizes key findings from earlier studies in the region, highlighting existing uncertainties and gaps. Section 4.1.2 describes the airborne measurement campaign conducted on 7 June 2018, including the CHARM-F flight path and observed CH_4 enhancements.

A formal introduction to the Bayesian inversion methodology, including the derivation of the cost function and ensemble Kalman filter mechanics, is given in Appendix B. However, Sect. 4.2 briefly recapitulates the core components of the Bayesian approach, including the formulation of the posterior state vector and its covariance matrix. The latter plays a key role in the source attribution strategy developed later in this chapter. Furthermore, it outlines the inversion setup using CTDAS-WRF, including prior assumptions and model parameters (Sect. 4.2.1).

Section 4.3 presents an initial inversion run, in which each emitting WRF grid cell is optimized individually. This is a diagnostic step to assess the performance of the prior setup and define adjustments for a best-estimate inversion. One key adjustment is introduced in Sect. 4.3.1, which identifies systematic mismatches between model and observations and implements targeted data flagging to exclude affected measurement segments. A second key adjustment is based on a novel clustering approach, developed in this work and presented in Sect. 4.3.2. This method aggregates spatially correlated sources into joint state vector elements to reduce ambiguity in source attribution.

Based on the resulting clustered setup, the inversion is refined and re-run. Section 4.4 presents the outcome of this best-estimate inversion and evaluates its robustness through targeted sensitivity tests. Ultimately, it concludes with a comparison of total emissions with external inventories and previous studies.

Finally, Sect. 4.5 provides a concise summary and general conclusions, reflecting on how these findings inform future airborne and satellite-based inversion strategies.

4.1 The Upper Silesian Coal Basin

Figure 4.1a) displays a map of central European CH_4 emissions. The Upper Silesian Coal Basin (USCB) in southern Poland (approx. 50°N, 19°E) stands out as Europe's largest CH_4 emission hotspot, releasing 500 – 700 kt CH_4 annually (Swolkień et al. 2022; Gałkowski et al. 2021a). These emissions, primarily from coal mining activities, make the region a critical focus for climate and air quality studies.

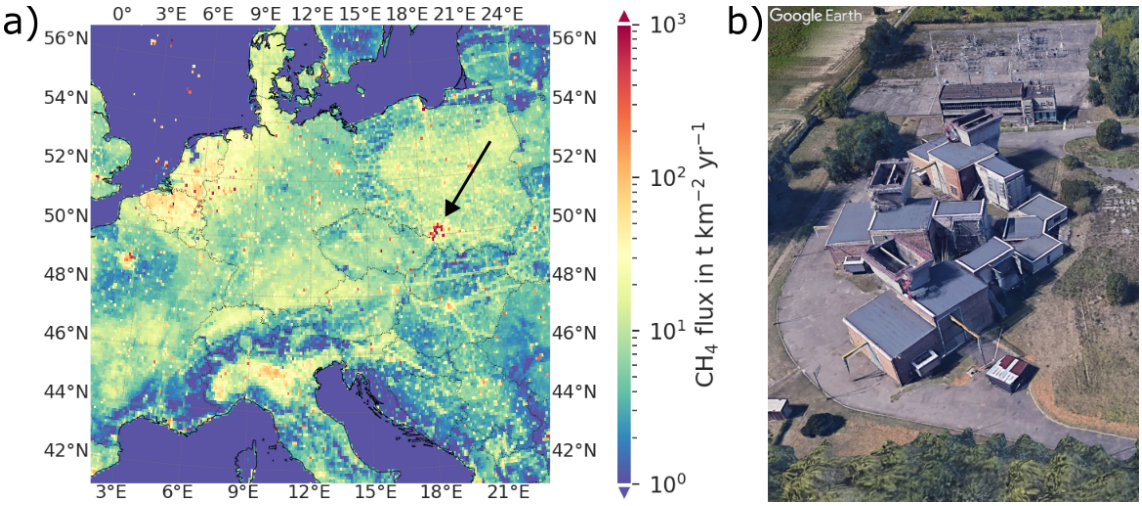

Figure 4.1: a) Anthropogenic CH_4 emission fluxes over central Europe on a 0.1°×0.1° grid for the year 2018 (Emissions Database for Global Atmospheric Research (EDGAR) v7.0, Crippa et al. 2021). Highest emissions are from southern Poland in the Upper Silesian Coal Basin, marked by the black arrow. Please note the logarithmic scale.
b) Ventilation shaft V of the Sośnica coal mine (50.2565°N, 18.7220°E), operated by Polska Grupa Górnicza S.A.. Annual CH_4 emissions in 2018 were approx. 2.6 t/h.
Google Earth (3D Buildings mode), accessed June 2025. Satellite imagery © 2025 Airbus, image date: 5/3/2024.

The USCB is a plateau elevated between 200 – 300 m above sea level and bordered to the south by the Western Carpathians (see Fig. 4.2). Westward, the basin extends across the Czech border into the Ostrava region in the Czech Republic. An important topographic feature is the Moravian Gate, a lowland corridor between the Sudetes and the Carpathian Mountains. Under north-easterly wind conditions, it can act as a channel for advecting CH_4 plumes.

The USCB is rich in high-quality bituminous coal, a sedimentary rock of biogenic origin mostly consisting of elemental carbon (Kotarba 2001). This coal was formed through the carbonization of organic material under high pressure and temperature, a process that generated various hydrocarbons. This includes significant quantities of CH_4, which remains trapped in coal seams and surrounding rock strata (Kreiner and Żyła 2006). During mining operations, the disturbance of coal seams releases this trapped CH_4 into underground galleries.

Methane-air mixtures become explosive when the CH_4 content ranges between 5 % and 15 %, depending on oxygen concentration and temperature (Kędzior and

Dreger 2019). The tragic explosion at the ČSM coal mine in the Ostrava-Karviná industrial region in December 2018, which killed 13 miners, is a sombre reminder of the real danger posed by uncontrolled CH_4 accumulation (see e.g. The New York Times 2018; BBC News 2018; Die Zeit 2018; Reuters 2018). This accident occurred only a few months after the airborne survey conducted as part of this study, during which ČSM was one of the sites investigated.

To mitigate the risk of explosions, Polish mining regulations stipulate that CH_4 concentrations in the exhaust ventilation air must not exceed 0.75 % (Journal of Laws 2017). To comply with this threshold and ensure operational safety in the mining galleries, all active shafts are equipped with continuous ventilation systems.

In addition to ventilation systems, Polish mines use CH_4 drainage systems to reduce gas concentrations in the rock mass before, during and after mining. These systems extract gas from coal seams via boreholes and transfer it to installations on the surface. However, the captured gas typically contains unstable methane-air mixtures, with CH_4 concentrations fluctuating between 40 % and 60 %, which makes it difficult to use economically. It cannot be fed into the high-methane distribution grid and must be combusted in dedicated facilities. Storage limitations further restrict its utilization. Consequently, only a portion of the drained gas is used for energy production, while the remainder is either released into the atmosphere as so-called "discharge" gas or flared, depending on operational conditions. However, there is no publicly available data specifying the proportion processed by either method (Kędzior and Dreger 2019; Swolkień et al. 2022). Furthermore, even after mining operations cease, CH_4 continues to be released from abandoned mines due to residual gas stored in coal seams and surrounding strata. CH_4 can diffuse through fractured rock into remaining shafts, through which it can slowly escape to the surface (Kędzior and Dreger 2019).

Overall, the USCB's persistently high emissions are closely linked to the region's geological and operational characteristics, which vary significantly across the basin. In the south, coal seams are mined at depths of up to 1200 m, and CH_4 content can exceed 18 m^3 per tonne of dry ash-free coal (Kędzior and Dreger 2019). In contrast, shallower seams in the northern region typically exhibit lower CH_4 content, often below 2.5 $m^3\,t^{-1}$. However, the number of Active Coal Mines (ACM) in the north remains comparatively high, so that substantial emissions continue to originate throughout the basin. Although total coal production in the USCB has steadily declined in recent decades, this has not led to a proportional decrease in CH_4 emissions (Kędzior and Dreger 2019; WUG 2019). One reason for this is the aforementioned ongoing shift towards deeper extraction. This trend offsets some of the expected emission reductions and illustrates that the USCB, as an industrial region, is in a state of continuous transition.

The historical prominence of coal mining in the USCB has not only driven CH_4 emissions but has also fundamentally shaped the region's settlement patterns and infrastructure. Over the course of more than a century, mining activity has contributed to the development of one of the most densely populated and urbanized areas in Poland. Cities such as Katowice, Rybnik, Bielsko-Biała, and Ostrava have grown around the mining infrastructure, creating a landscape where residential and

industrial zones are closely intertwined. A key feature of the mining infrastructure is the presence of numerous ventilation shafts (Fig. 4.1b). Almost a hundred of such shafts are scattered throughout the basin, often near or within urban peripheries. These shafts act as localized point sources of CH_4 emissions (Kostinek et al. 2021; Fiehn et al. 2020). Previous studies have also assessed other anthropogenic sources of CH_4 in the region, such as landfills, wastewater treatment plants, and livestock operations. Kostinek et al. (2021) and Luther et al. (2022) have stated that their overall contribution is small in relation to the uncertainty associated with coal mine emission estimates. In the context of this work, these non-mining emissions are considered part of the regional background, while the focus is on quantifying point-source emissions from coal mine ventilation infrastructure.

4.1.1 Previous Studies

Several studies have investigated the spatial structure and magnitude of CH_4 emissions in the USCB region, mostly based on measurements collected during the CoMet 1.0 campaign.

Andersen et al. (2023) focused on the emission quantification of individual shafts using drone-borne aircore samplers. They report shaft-specific emission rates between 0.8 and 14.4 $\mathrm{kt\,a^{-1}}$, confirming the large heterogeneity in source strength, but without aiming at a domain-wide synthesis.

Fiehn et al. (2020) used in-situ measured data from the DLR Cessna aircraft, which flew a closed loop around the USCB, performing multiple stacked transects downwind to capture the vertical distribution of CH_4 enhancements from coal mine ventilation shafts. The measured CH_4 data were inter- and extrapolated using the Kriging algorithm to construct a two-dimensional representation of the downwind enhancements. Based on these data, a simple mass balance approach was applied to estimate total CH_4 emissions from the basin. This method assumes conservation of mass within a virtual box surrounding the source region and uses the observed horizontal wind speed and direction to infer the flux through the downwind face of the box. Results from two research flights are reported, yielding total emission estimates of $435 \pm 136 \mathrm{kt\,a^{-1}}$ and $476 \pm 126 \mathrm{kt\,a^{-1}}$, respectively. While conceptually straightforward, the interpolation and extrapolation of in situ data introduce structural uncertainty, especially in heterogeneous flow conditions.

Kostinek et al. (2021) extended this approach by combining in situ data with WRF-FLEXPART dispersion simulations and an inverse modelling framework, arriving at consistent emission estimates (423 – 451 $\mathrm{kt\,a^{-1}}$). To assess the role of meteorological uncertainty, they conducted eight sensitivity simulations in which key transport parameters (i.e. wind speed, wind direction, planetary boundary layer height, and source location) were systematically varied within plausible ranges. The resulting spread in emission estimates demonstrated that each factor contributed comparably to the total uncertainty. However, since flux estimates are ultimately derived from the plume segments intersected by the aircraft, unobserved portions of the vertical or lateral plume extent can introduce systematic biases.

Moreover, both approaches are sensitive to the accuracy of the PBL height, which

directly influences the inferred plume volume. Since the closed-loop flight pattern is time-consuming, the aircraft cannot simultaneously sample individual shafts in detail, limiting the spatial resolution of the emission attribution.

A conceptually similar approach to Kostinek et al. (2021) was adpoted by Luther et al. (2022), who deployed a network of ground-based EM27/SUN spectrometers and Doppler wind lidar to constrain a Phillips-Tikhonov inversion, also driven by WRF-FLEXPART simulations. While the modelling framework closely resembles that of Kostinek et al. (2021), the observations are column-integrated rather than in situ, and constrained emissions from individual shaft clusters under favourable wind conditions. Their results suggest that reported values from the European Pollutant Release and Transfer Register (E-PRTR) substantially underestimate the true emissions, with estimated instantaneous emission rates ranging from $80\,\mathrm{kt\,a^{-1}}$ to $133\,\mathrm{kt\,a^{-1}}$ for the southeastern part of the USCB, and up to $790\,\mathrm{kt\,a^{-1}}$ for larger aggregated subsets.

Luther et al. (2019) conducted mobile column measurements with vehicle-mounted EM27/SUN spectrometers to quantify emissions from individual shafts using a mass balance approach. Although limited in spatial and temporal coverage, their results demonstrate the feasibility of mobile remote sensing for localized CH_4 flux estimates, with reported emissions ranging from 6 to $109\,\mathrm{kt\,a^{-1}}$ per source. The employed stop-and-go sampling strategy required stationary measurement periods of up to 2.5 minutes per stop, forcing a trade-off between spatial resolution and temporal consistency: shorter transect duration improves the chances of capturing a quasi-steady plume, but reduces the number of sampling points. Conversely, finer spatial sampling increases the risk of plume deformation due to changing winds or source variability during the measurement period. In addition, vehicle routes were constrained to public roads, which are not always aligned ideally with plume directions, thereby limiting geometric coverage and plume orthogonality.

Krautwurst et al. (2021) used the passive spectrometer Methane Airborne MAPper (MAMAP) on board a small aircraft to retrieve column-integrated CH_4 concentrations downwind of selected shaft clusters. Their regional quantification for five clusters yielded emissions of 9 – 79 $\mathrm{kt\,a^{-1}}$ each. The emission calculation was based on a cross-sectional flux method conceptually similar to that used in **Case Study I** of this thesis (cf. Sect. 3). A key element of their retrieval was the application of the CH_4–over–CO_2 proxy method, which assumes a spatially homogeneous background concentration of CO_2 for normalization. While this approach effectively reduces light path errors in the passive remote sensing retrieval, it introduces uncertainty in regions with heterogeneous CO_2 sources. Given the urbanized and industrial character of the USCB, the assumption of a constant CO_2 background is not strictly valid and could bias CH_4 flux estimates. Moreover, due to the spatial overlap of plumes from multiple sources, a separation of individual shafts was not attempted, and the spatial resolution of the flux attribution remained limited. Furthermore, as a passive spectrometer, MAMAP relies on reflected sunlight and can thus only operate around solar noon, when surface brightness and solar elevation are high. However, as demonstrated in Sect. 3.2.2, these are also the conditions under which local turbulence tends to be strongest, leading to enhanced variability in wind fields

and plume dispersion. Therefore, this observational constraint can amplify the uncertainty of flux estimates, due to increased atmospheric variability during midday hours.

Table 4.1: Overview of compared studies quantifying CH_4 emissions in the USCB.

Study	Platform/ instrument	Method	Spatial/ temporal scope	Emission estimates
Andersen et al. (2023)	Drone-borne air-core samplers	Mass balance	Individual shafts (June 2018)	0.8 – 14.4 $kt\,a^{-1}$ per shaft
Fiehn et al. (2020)	Airborne in situ	Mass balance	Entire basin, 2 flights (June 2018)	$435 \pm 136 kt\,a^{-1}$; $476 \pm 126 kt\,a^{-1}$
Kostinek et al. (2021)	Airborne in situ	Inverse modelling	Entire basin, 1 flight (June 2018)	423 – 451 $kt\,a^{-1}$
Luther et al. (2019)	Mobile interferometer (EM27/SUN)	Mass balance	Individual shafts (June 2018)	from 6 ± 1 $kt\,a^{-1}$ per shaft to 109 ± 33 $kt\,a^{-1}$ for a subregion
Luther et al. (2022)	Ground-based interferometer (EM27/SUN)	Inverse modelling	Shaft clusters (June 2018)	80 – 133 $kt\,a^{-1}$ (south-eastern basin); up to 790 $kt\,a^{-1}$ aggregated
Krautwurst et al. (2021)	Airborne spectrometer MAMAP	Cross-sect. flux + CH_4/CO_2 proxy	Shaft clusters (June 2018)	9 – 79 $kt\,a^{-1}$ per cluster
Tu et al. (2022b)	Spaceborne spectrometer (TROPOMI)	Wind-assigned anomaly inversion	Entire basin (3-year period, Nov. 2017–Dec. 2020)	437 – 496 $kt\,a^{-1}$
Gałkowski et al. (2021a)	Database compilation	Reported inventories	Entire basin and shafts (2018)	Annual shaft-level reports; basin total 450 $kt\,a^{-1}$

Tu et al. (2022b) used satellite observations from TROPOMI and IASI to constrain CH_4 emissions in the USCB. Their inversion based on a wind-assigned anomaly method estimated total emissions of 437 – 496 $kt\,a^{-1}$. The method relies on a simplified cone plume model driven by ERA5 reanalysis wind fields, enabling large-scale regional attribution without requiring detailed transport simulations. However, to achieve emission estimates with such low uncertainty, the study aggregates data over a three-year period (November 2017–December 2020), which includes but far exceeds the measurement period of the airborne CHARM–F observations presented here. The resulting fluxes represent a long-term mean rather than temporally resolved snapshots, and are not directly comparable to day-specific measurements.

Finally, Gałkowski et al. (2021a) have compiled the CoMet Emission Database (CoMet ED) as part of the CoMet campaign (Sect. 2.1.3), which was also utilized in some of the previously mentioned studies. The database v4.01 provides detailed information on the location and annual emission rates of individual CH_4 sources across the USCB and its surroundings. It integrates European-scale reporting data from the 2018 release of the European Pollutant Release and Transfer Register (E-PRTR 2021), as well as national Polish mining statistics from the Polish State Mining Authority Wyższy Urząd Górniczy (WUG 2019), and internal measurement

data voluntarily provided by a few of the operating mining companies via personal communication. The shaft's locations have been cross-validated with satellite imagery where available.

4.1.2 Airborne CHARM–F Observations

While these studies have significantly advanced our understanding of CH_4 emissions in the USCB, the airborne CHARM–F measurements used in this work provide a unique combination of spatial coverage, temporal coherence, and column sensitivity that sets them apart. The high-altitude overflight of the region by HALO on 7 June 2018 captured a dense sequence of plume transects within a time span of just two and a half hours. This results in an observational dataset that equals or surpasses the spatial coverage achieved in many earlier studies, but with the temporal consistency of a single meteorological situation. As shown in Fig. 4.2, this flight yields a rich structure of downwind XCH_4 enhancements across the basin, aligned with the prevailing wind and influenced by multiple point sources.

Figure 4.2 provides an overview of the HALO flight pattern across the USCB on 7 June 2018 between 10:30 and 13:30 CEST (08:30–11:30 UTC). Panel a) shows the spatial distribution of coal-related point sources from the CoMet database, colour-coded by emission category (see Table 4.2), along with the flight track colour-coded by local time (CEST), enabling reconstruction of the temporal sequence from the colour gradient. For ease of interpretation, the local-time colour coding from Fig. 4.2a) is also applied to the x-axis of Fig. 4.3, effectively linking the time series to the respective flight segments shown on the map. Panel b) presents the same track, now coloured by retrieved XCH_4 from CHARM–F, alongside point sources from the CoMet database shaded by their reported CH_4 emission rates. Small data gaps appear along the track due to aircraft turns and retrieval quality filtering.

Figure 4.2a) show that ACM form a dense cluster around the city of Rybnik, with additional scattered sites in the Katowice metropolitan area and north of the city of Bielsko-Biała. Active coal mines that do not report any emissions (ACMX) are located on the southern and southeastern outskirts of Katowice, with another dense cluster further north. Two Power/Cogeneration Plants (PP) are co-located with shafts, including the Żory facility adjacent to the Budryk mine and the Bieruń plant southeast of Katowice. Inactive/closing Coal Mines (ICM) are distributed more sparsely across the region. The Active Coal Mines in Czechia (ACMCZ) are situated across the Polish–Czech border within the Moravian Gate. They are included in the CoMet ED, but with no reported emission values. This implies that the operators did not submit CH_4 emissions for the year 2018 under the E-PRTR reporting requirements. For colour coding and category counts, see Table 4.2.

The flight track was strategically designed based on plume transport forecasts provided in-house by the MECO(n) chemistry-climate model (Nickl et al. 2020), tailored specifically for the CoMet 1.0 campaign. These forecasts predicted north-easterly winds and associated plume propagation patterns across the USCB. On this basis, the flight was planned to sample three key air mass regimes: upwind background air, near-field plumes from major point sources, and far-field enhancements integrating

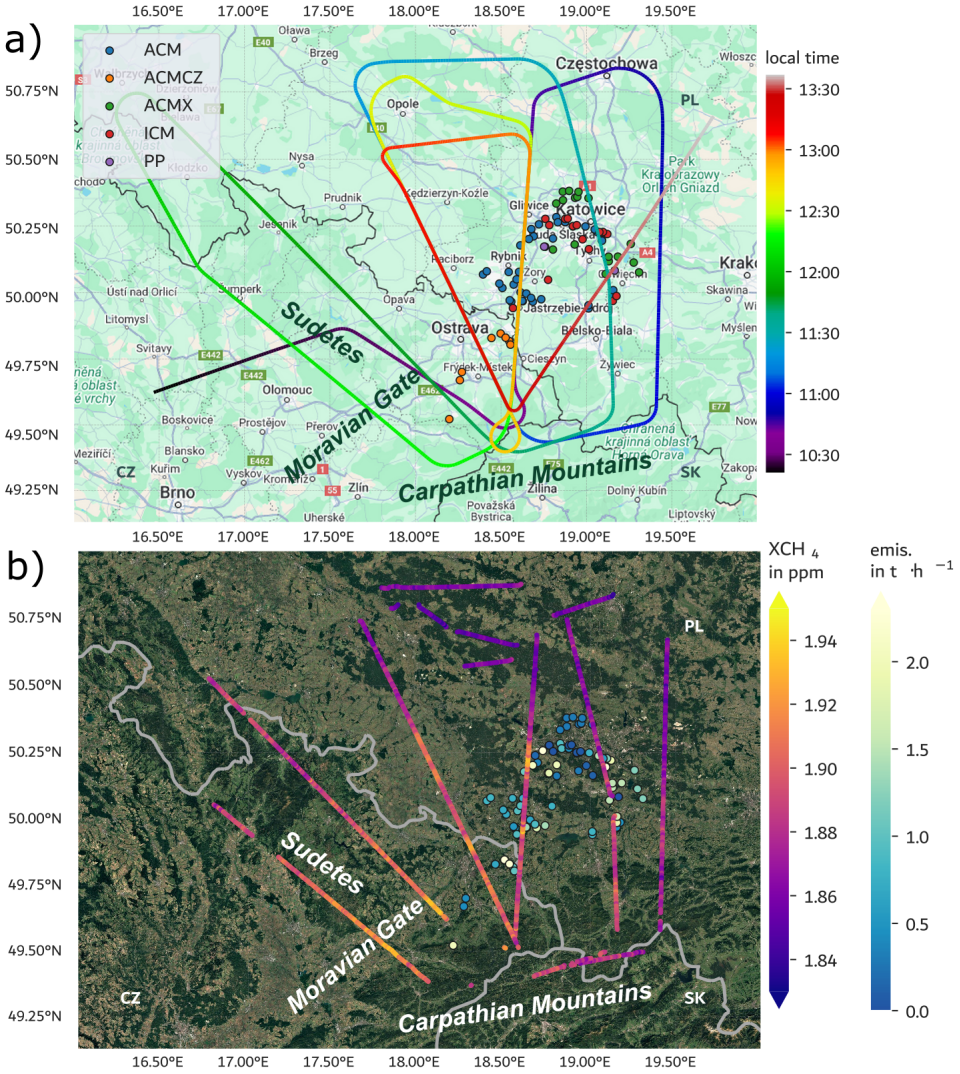

Figure 4.2: Overview of HALO flight operations over the USCB on 7 June 2018. The flight pattern was designed based on in-house plume transport forecasts from the MECO(n) model, which predicted north-easterly winds with a characteristic bend in wind direction toward the Moravian Gate.
a) Flight track colour-coded by local time (CEST), with individual point sources marked by category according to CoMet ED v4.01 (see Table 4.2).
b) Same flight track overlaid with CHARM–F XCH_4 observations (colour-coded in ppm) and source locations (colour-coded by emission rates in tonnes per hour), also based on CoMet ED v4.01. Plume enhancements are visible in the observations and match the forecasted plume propagation.

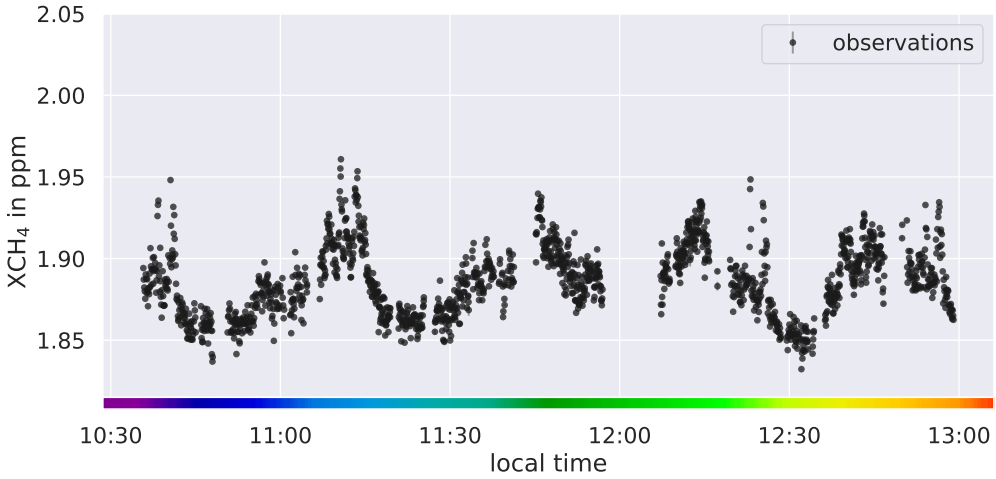

Figure 4.3: Time series of XCH_4 retrieved from CHARM–F during the HALO overflight of the USCB on 7 June 2018. The x-axis is colour-coded by local time (CEST), using the same scale as in Fig. 4.2a), thereby enabling direct linkage of the measured values to the corresponding flight segments on the map.

Table 4.2: Categories of coal-related CH_4 emission sources depicted in Fig. 4.2a).

Abbreviation	**Description**	**Colour**	**Count**
ACM	Active Coal Mines	blue	39
ICM	Inactive/closing Coal Mines	red	14
ACMX	Active Coal Mines no reported emissions	green	17
ACMCZ	Czech Active Coal Mines no reported emis.	orange	8
PP	Power/Cogeneration Plants	purple	2

basin-wide fluxes. While the spatial layout of the pattern reflected scientific priorities, the precise timing of each segment was governed by operational factors such as air traffic control and minimizing fuel consumption. The following description is thus ordered by the scientific logic of sampled air masses rather than by flight chronology.

Based on the flight pattern, a regional gradient can be identified. The lowest XCH_4 values are detected north of the shafts (i.e. north of 50.5°N), indicating that background airmasses were sampled there. Despite being upwind, the leg to the east of the shafts still shows an increase in the observed XCH_4 values from north to south. This is probably due to a mesoscale background gradient caused by the accumulation of residual CH_4 along the southern border of the basin. Here, the Sudetes and Carpathian mountain ranges could be impeding the regional outflow, leading to partial pooling. This general pattern is also present in the Copernicus Atmosphere Monitoring Service (CAMS) fields, which are used as the initial and boundary conditions in the WRF-Chem simulations presented in Sect. 4.3.1, and it re-emerges in the simulated background distributions (see Fig. 4.11).

In addition to the background gradient, enhanced XCH_4 levels associated with

individual sources are evident in the legs that cross the USCB or are downwind of the sources. In particular, the typical propagation along the Moravian Gate, as described above, can already be inferred from the few transects

Several of these downwind legs were repeated to ensure observational redundancy. Three such transects targeted a dense cluster of high-emitting shafts in the Rybnik/Żory area and immediately southwest of Katowice. These are shown in Fig. 4.2a) and the corresponding segments of the time series in Fig. 4.3, colour-coded as the purple legs (10:35–10:40), the light green to yellow legs (12:22–12:27) and the orange legs (12:50–12:55). All three followed a south-to-north orientation and were designed to detect near-field plume signals from the most prominent sources.

To capture the downwind plume at intermediate distances, two additional cross-basin transects were flown northeast of Ostrava, but still southwest of all Polish shafts. The blue legs (11:05–11:20) and yellow (12:32–12:47) legs intercepted the regional plume further downwind, providing integral constraints on aggregated emissions.

Complementing the intermediate transects, two extended legs over Czech territory (dark green and light green, 11:30–12:22) intercepted the exhaust plume from the entire basin, which was fully developed and well-mixed.

The red segment from 13:00–13:20 was conducted at a lower altitude for in situ sampling (not used in this work), during which CHARM–F measurements were suspended due to laser safety constraints at low altitude. Lastly, HALO exited the domain toward the northeast (red to white, 13:30 onwards).

To realise the full potential of this dataset, a Bayesian inverse modelling framework was applied that was tailored to the specific design of the research flight. Rather than relying on simplified analytical plume models or long-term averaging, this framework assimilates the high-resolution CHARM–F data into a transport simulation ensemble to infer spatially resolved fluxes for the observed day. The following section provides details of the underlying inversion setup, including its treatment of observational and model uncertainty.

4.2 Bayesian Inverse Modelling & Ensemble Approach

This study builds on established inverse modelling methods (Peters et al. 2005; van der Laan-Luijkx et al. 2017) and applies the Carbon Tracker Data Assimilation Shell (CTDAS) as the inversion tool. A detailed derivation of the implementation of the algorithms is provided in Appendix B. Appendix B.1 establishes the Bayesian cost function, Appendix B.2 derives the analytical maximum a posteriori (MAP) solution, and the ensemble formulation in Appendix B.3. In brief, CTDAS is a modular data assimilation system designed to estimate surface–atmosphere fluxes of GHGs using atmospheric observations. At its core, CTDAS employs an ensemble Kalman filter (EnKF) to optimize a set of scaling factors that adjust prior emission estimates $\mathbf{q}_\mathrm{p}$ such that simulated mole fractions match the observed CHARM–F measurements, while remaining consistent with their respective uncertainties.

These prior emissions $\mathbf{q}_\mathrm{p}$ are derived primarily from the reported shaft-level emission rates in the CoMet ED and are visualized in Fig. 4.2b). A detailed description of how the prior emission vector is constructed and prepared for use in CTDAS-WRF is provided in Sect. 4.2.1. To each emission value in the prior vector $\mathbf{q}_\mathrm{p}$, a corresponding multiplicative scaling factor is assigned. These scaling factors are initialized with a prior value of 1.0 and form the state vector $\mathbf{x}$. The state vector thus has the same dimension S as $\mathbf{q}_\mathrm{p}$, where S refers to the number of emission *sources* or *state vector elements* to be optimized. The initial inversion setup includes $S = 76$ such elements.

The observation vector $\mathbf{y}$ contains the XCH_4 values measured by CHARM–F. A detailed description of how these observations are processed and how associated uncertainties are assigned is provided in Sect. 4.2.1. In brief, the high-resolution CHARM–F retrievals are horizontally averaged onto the corresponding WRF grid cells. This binning process reduces the native measurement resolution to match the WRF-Chem grid and yields $M = 1576$ aggregated observations used in the inversion, where M denotes the number of *measurements* assimilated. While it would be possible to retain the native resolution of the CHARM–F observations, this would not yield additional information, since the model output is interpolated to the observation locations. Instead, binning reduces the length of the observation vector while preserving its information content, which improves computational efficiency during the sequential assimilation process (see Appendix B.3).

With the state vector $\mathbf{x}$ and the observation vector $\mathbf{y}$ defined, the inversion problem can be expressed in probabilistic terms. Specifically, the optimal solution for $\mathbf{x}$ is obtained by minimizing the Bayesian cost function (Peters et al. 2005):

$$J(\mathbf{x}) = \frac{1}{2}(\mathbf{y} - \mathbf{H}\mathbf{x})^\mathrm{T}\mathbf{R}^{-1}(\mathbf{y} - \mathbf{H}\mathbf{x}) + \frac{1}{2}(\mathbf{x} - \mathbf{x}_\mathrm{p})^\mathrm{T}\mathbf{P}_\mathrm{p}^{-1}(\mathbf{x} - \mathbf{x}_\mathrm{p})\,. \tag{4.1}$$

The observation operator $\mathbf{H}$ ($[M \times S]$) maps the state vector $\mathbf{x}$ to observations space, yielding the simulated observation vector $\mathbf{H}\mathbf{x}$. This includes scaling the prior emissions $\mathbf{q}_\mathrm{p}$ with the state vector $\mathbf{x}$, mapping them to the WRF grid, simulating the atmospheric transport of the emitted CH_4 via WRF-Chem, interpolation on the flight track, and performing weighted vertical integration (see Eq. 2.11 in Sect. 2.1.2). $\mathbf{R}$ and $\mathbf{P}_\mathrm{p}$ are the error covariance matrices in observation and state vector space, respectively. To provide clarity on the mathematical notation used throughout this chapter, Table 4.3 provides an overview of all the relevant quantities.

The cost function $J(\mathbf{x})$ balances the mismatch between model and observations with deviations from the prior, expressing the optimization problem in probabilistic terms. In data assimilation, these terms are referred to as the innovation and the increment, respectively. The innovation $(\mathbf{y} - \mathbf{H}\mathbf{x}_\mathrm{p})$ quantifies the mismatch between observations and their prior simulation, while the increment $(\mathbf{x} - \mathbf{x}_\mathrm{p})$ describes the adjustment applied to the prior state to reduce this mismatch. The remaining difference after optimization is the residual $(\mathbf{y} - \mathbf{H}\mathbf{x}_\mathrm{a})$. These relationships are illustrated in Fig. 4.4. In essence, the cost function weights the residual and the increment by their respective error covariance matrices ($\mathbf{R}$ and $\mathbf{P}_\mathrm{p}$), and finds the posterior state vector $\mathbf{x}_\mathrm{a}$ that balances the two.

This formulation follows standard Bayesian statistics, in which both the prior knowledge and the observations are assumed to follow Gaussian distributions. This

Table 4.3: Reference list of mathematical symbols used in this work, along with their names, units, and dimensions. Adapted from Peters et al. (2005).

Symbol	Name	Unit	Dimension
$\mathbf{q}$	emission rate vector	kg/s	$S = 76$
n	ensemble member index ($n \in \{1, 2, \ldots, N = 150\}$)	-	1
$\mathbf{x}_n$	state vector ensemble member n	-	S
$\overline{\mathbf{x}}$	state vector ensemble mean	-	S
$\mathbf{x'}_n$	state vector deviation ensemble member n	-	S
$\mathbf{P}$	state-error covariance matrix	-	$S \times S$
$\mathbf{y}$	observation vector	µmol/mol	$M = 1576$
$\mathbf{R}$	observation-error covariance matrix	$(\mu\text{mol/mol})^2$	$M \times M$
$\mathbf{D}$	state deviation matrix	-	$S \times N$
$\mathcal{H}$	observation operator	- $\rightarrow$ µmol/mol	$S \rightarrow M$
$\mathbf{H}$	linear observation operator (matrix form)	- $\rightarrow$ µmol/mol	$S \times M$
$\mathbf{Hx}$	simulated observation vector	µmol/mol	M
$\mathbf{K}$	Kalman gain matrix	µmol/mol $\rightarrow$ -	$M \times S$

assumption is an integral part of the Bayesian approach, not a specific decision made in this study. It enables the posterior probability distribution to be derived analytically, making the problem mathematically tractable. Therefore, minimizing $J(\mathbf{x})$ is therefore equivalent to finding the so-called MAP estimate under these Gaussian assumptions. A full derivation of the Bayesian formalism is provided in Appendix B.1. The posterior state vector $\mathbf{x}_\mathrm{a}$ and its covariance matrix $\mathbf{P}_\mathrm{a}$ are given by:

$$\begin{aligned} \mathbf{x}_\mathrm{a} &= \mathbf{x}_\mathrm{p} + \mathbf{K}(\mathbf{y} - \mathbf{H}\mathbf{x}_\mathrm{p}) \\ \mathbf{P}_\mathrm{a} &= \mathbf{P}_\mathrm{p} - \mathbf{K}\mathbf{H}\mathbf{P}_\mathrm{p}\,, \end{aligned} \tag{4.2}$$

with the Kalman gain matrix:

$$\mathbf{K} = \mathbf{P}_\mathrm{p}\mathbf{H}^\mathrm{T}\left(\mathbf{R} + \mathbf{H}\mathbf{P}_\mathrm{p}\mathbf{H}^\mathrm{T}\right)^{-1}\,. \tag{4.3}$$

The Kalman gain $\mathbf{K}$ determines how much weight is given to the innovation relative to the confidence in prior knowledge. It balances the uncertainty in the observations, represented by $\mathbf{R}$ and the prior uncertainty, represented by $\mathbf{P}_\mathrm{p}$, to compute the posterior update. As can be seen in Eq. 4.2, the increment is given by $\mathbf{K}(\mathbf{y} - \mathbf{H}\mathbf{x}_\mathrm{p})$.

In the three-hour observation window analysed in this study, emissions are assumed to be constant. This eliminates the need for sequential time-stepping, and $\mathbf{x}_\mathrm{a}$ is the "analysed" state obtained after a single assimilation step. In other studies, particularly those involving longer time periods or evolving emissions (e.g. over weeks to months), sequential or time-resolved inversions are required. In such cases, the same subscript "a" is sometimes used to indicate an "advanced" or time-propagated state (e.g. Thanwerdas et al. 2025).

While this formulation is conceptually valuable, its implementation requires explicit construction of the linearized observation operator $\mathbf{H}$ and manipulation of the

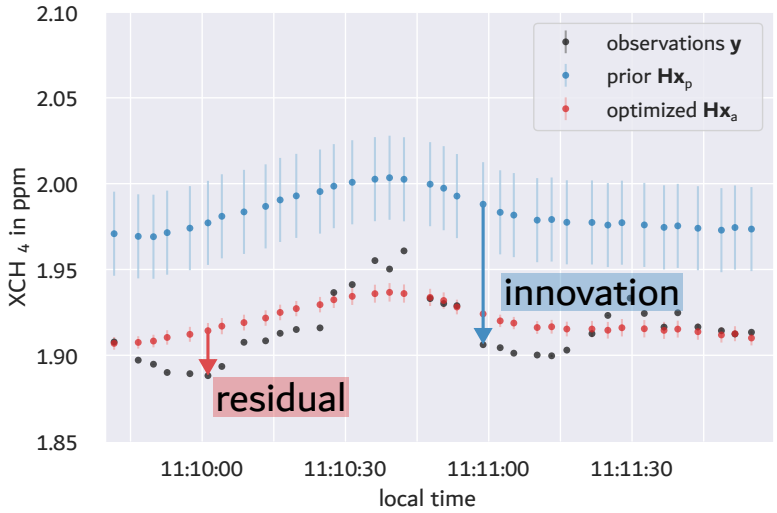

Figure 4.4: Illustration of the innovation and residual in a representative segment of the CHARM–F XCH_4 time series. The innovation ($\mathbf{y} - \mathbf{H}\mathbf{x}_\mathrm{p}$) is the mismatch between the observations (black) and their prior simulation (blue). The residual ($\mathbf{y} - \mathbf{H}\mathbf{x}_\mathrm{a}$) is the difference to the optimized simulation (red). Arrows mark example data points where both are negative. The increment ($\mathbf{x}_\mathrm{a} - \mathbf{x}_\mathrm{p}$) is not shown here, as it resides in state vector space. Since each state vector element affects multiple observations, the inversion fits the full time series, not pointwise mismatches. This explains why some observations (e.g. 11:10:30–11:10:45) fall between prior and posterior.

full covariance matrices $\mathbf{P}_\mathrm{p}$ and $\mathbf{R}$. The observation operator is a matrix of size $[M \times S]$, and the state covariance matrix scales as $[S \times S]$.

In this study, the dimensionality of the state vector ($S = 76$) and the observation vector ($M = 1576$) is moderate and would, in principle, permit an analytical inversion. Nonetheless, a formulation was chosen that not only addresses the current problem effectively, but also lays the foundation for more complex future applications. As outlined in Sect. 1.3, the goal is to develop a scalable and robust framework for assimilating IPDA lidar data. This includes the airborne CHARM–F observations used here, as well as future satellite missions such as MERLIN and studies involving spatially uncertain and distributed sources, for example wetland CH_4 emissions. These use cases will require flexible methods capable of handling large state vectors and non-linear transport processes. In global CH_4 inversions at 1° resolution, for instance, the number of state vector elements can easily reach $S \sim \mathcal{O}(10^5)$, making explicit matrix construction computationally prohibitive.

To address these computational challenges and enable scalability, the EnKF formulation used within CTDAS avoids explicitly constructing the full $[S \times S]$ covariance matrix $\mathbf{P}_\mathrm{p}$. Instead, the prior distribution is approximated using an ensemble of state vectors $\mathbf{x}_n$, where $n \in \{1, 2, \ldots, N\}$. Each member is defined as:

$$\mathbf{x}_n = \overline{\mathbf{x}} + \mathbf{x'}_n \,, \tag{4.4}$$

where $\mathbf{x'}_n$ is a random deviation drawn from a multivariate normal distribution. Each

member thus represents a possible realization of the prior distribution with mean $\bar{\mathbf{x}}$, resulting in a discrete but statistically representative ensemble. The ensemble size N determines the statistical resolution of the prior covariance structure and is typically chosen to balance robustness against computational cost. In this study, $N = 150$ is used, and the rationale for this choice is discussed in the next Sect. 4.2.1.

Each state vector element, corresponding to a specific emission source, is thus represented by N ensemble members. These realizations sample the space of plausible scaling factors that modify the prior emissions. To define the spread of this ensemble, CTDAS requires the user to specify a single global relative uncertainty. In this study, a value of 100 % was selected to allow for maximum flexibility (further discussed in Sect. 4.2.1), including the possibility that some reported sources may be inactive and should be scaled to zero if the innovation suggests it (see Sect. 4.1). While this implementation does not support individual uncertainty assignments per source, a uniform relative uncertainty is consistent with the expectation that emission magnitudes scale approximately with coal production. This makes extreme upward adjustments for small sources implausible and ensures that the uncertainty range remains physically meaningful.

A square-root representation of the covariance matrix $\mathbf{P}$ is given by arranging the deviations of the ensemble members into columns of the state deviation matrix $\mathbf{D}$:

$$\mathbf{P} = \mathbf{D}\mathbf{D}^{\mathrm{T}} \quad \text{with} \quad \mathbf{D} = \frac{1}{\sqrt{N-1}} \begin{bmatrix} \mathbf{x'}_1 & \mathbf{x'}_2 & \dots & \mathbf{x'}_N \end{bmatrix} \tag{4.5}$$

In the WRF-Chem model, each ensemble member is implemented as an independent tracer, yielding simulated observations $\mathbf{H}\mathbf{x}_n$ for each member. These are directly used to compute the matrix products $\mathbf{P}\mathbf{H}^{\mathrm{T}}$ and $\mathbf{H}\mathbf{P}\mathbf{H}^{\mathrm{T}}$, which contribute to the computation of the Kalman gain $\mathbf{K}$ in Eq. 4.3. The detailed derivation and computational implementation of these ensemble-based terms is provided in Appendix B.3.

Once the Kalman gain is available, the posterior ensemble is computed by updating both the ensemble mean and the individual deviations. The mean is updated according to Eq. 4.2, using the ensemble mean innovation $(\mathbf{y} - \mathbf{H}\bar{\mathbf{x}}_\mathbf{p})$. The deviations, in contrast, are updated in a way that reflects the reduced uncertainty and reproduce the updated covariance structure:

$$\mathbf{x'}_{\mathrm{a},n} = \mathbf{x'}_{\mathrm{p},n} - \mathbf{k'}\mathbf{H}\mathbf{x'}_{\mathrm{p},n} \quad \text{with} \quad \mathbf{k'} = \mathbf{K}\left(1 + \sqrt{\frac{\mathbf{R}}{\mathbf{H}\mathbf{P}_\mathrm{p}\mathbf{H}^{\mathrm{T}} + \mathbf{R}}}\right)^{-1} \tag{4.6}$$

Rather than computing the posterior covariance matrix via the analytical expression in Eq. 4.2, it is reconstructed from the updated deviations as $\mathbf{P}_\mathrm{a} = \mathbf{D}_\mathrm{a}\mathbf{D}_\mathrm{a}^{\mathrm{T}}$.

In summary, the ensemble-based Bayesian inversion framework provides a systematic approach to combine prior information with observations. The result is a posterior estimate $\mathbf{x}_\mathrm{a}$ that minimizes the combined mismatch. The updated emission estimates are obtained by scaling the prior emission rates $\mathbf{q}_\mathrm{p}$ with the optimized factors $\mathbf{x}_\mathrm{a}$: $\mathbf{q}_\mathrm{a} = \mathbf{q}_\mathrm{p}\mathbf{x}_\mathrm{a}$.

4.2.1 CTDAS-WRF Setup

The inversions in this work were performed using the CTDAS-WRF, which is available for download under https://git.wur.nl/ctdas/CTDAS/-/tree/ctdas-wrf. CTDAS is an open-access data assimilation framework originally coupled to the global model TM5 (van der Laan-Luijkx et al. 2017; Krol et al. 2005). Thanks to CTDAS's modular design, it is in principle possible to operate it with different ATMs. Reum et al. (2020) have adopted it in such a way that it is coupled to WRF-Chem (Grell et al. 2005) to enable high-resolution, regional-scale applications.

WRF-Chem is the online chemistry module coupled to WRF (Grell et al. 2005). In the context of atmospheric transport modelling of CH_4, the most relevant chemical processes are sink reactions (e.g. oxidation by OH). These processes are slow and result in an atmospheric lifetime of nearly ten years for CH_4. On the timescale of a few hours considered here (i.e. 08:30–11:30 UTC), chemical loss is therefore negligible. Consequently, CH_4 is implemented as a passive tracer. Accordingly, the capability of WRF-Chem to simulate explicit chemical reactions is not needed here, which reduces computational complexity and lowers the simulation's runtime.

The simulation was initialized at 12:00 UTC on 6 June 2018 and ran until 12:00 UTC on 7 June, covering exactly 24 hours. This setup captures the key phases of the diurnal cycle, including the contraction of the PBL at night and its subsequent re-growth during the day. Thus, the model has sufficient spin-up, allowing the PBL to develop realistically and the model to stabilize before the start of the observations.

The WRF-Chem configuration implements the general setup of Sect. 2.2.3; the domain configuration and notable namelist options are summarized in Table 4.4. Two square nested domains (d01 and d02) are centred over the USCB (see Fig. 4.5).

Table 4.4: Configuration of quadratic domains.

Domain	**D01**	**D02**
Horizontal resolution	5 km	1 km
Computational time step	30 s	5 s
Number of grid cells	280 x 280	280 x 280
Domain size	1400 x 1400 km^2	280 x 280 km^2
Planetary boundary layer physics	MYNN level 2.5 $bl\_pbl\_physics = 5$	MYNN level 2.5 $bl\_pbl\_physics = 5$
Eddy coefficient option	2D deformation $km\_opt = 4$	2D deformation $km\_opt = 4$
Turbulence and mixing option	Simple diffusion $diff\_opt = 1$	Simple diffusion $diff\_opt = 1$

Figure 4.5: Nested model domains used in the WRF-Chem simulation. Both domains are square and centred over the USCB. The outer domain (D01) spans 1400 km with a horizontal resolution of 5 km, while the inner domain (D02) covers 280 km at 1 km resolution. The virtual transect marked in D02 corresponds to the vertical cross-section shown in Fig. 4.6b-c.

Compared to the LES-based **Case Study I** in Chapter 3, where cross-sectional transects were performed only 1 – 5 km downwind of a single source to resolve local plume structure and turbulence in detail, **Case Study II** requires a substantially extended model setup. Both D01 and D02 are therefore larger than those used in the LES study to accommodate the area of interest and the regional-scale transport patterns (see Fig. 4.5). Here, flight observations cover distances ranging from a few to several hundred kilometres downwind of the sources. Moreover, the emission sources are scattered over an area of approx. 10 000 km^2, with measurements covering an area of up to 40 000 km^2 (cf. Fig. 4.2).

Given this spatial extent, a trade-off between computational cost and horizontal resolution is necessary. The inner domain D02 is setup with a horizontal resolution of 1×1 km^2, which has been shown to be sufficient to capture mesoscale features in complex terrain and provide realistic near-surface wind fields (Jiménez et al. 2013). Comparisons between simulated tracer plumes and airborne lidar observations confirm that this resolution adequately resolves the regional plume transport patterns of interest.

For the lateral boundary and initial CH_4 conditions, the CAMS inversion-optimized GHG analysis product (v20r1, CAMS 2022) was used. It provides global CH_4 fields constrained by surface and satellite observations, offering realistic large-scale distributions suitable for regional nesting. For meteorological initial and lateral boundary conditions operational analysis data of the ECMWF model (ECMWF 2018) is used, as already discussed in Sect. 2.2.2.

As described above in Sect. 4.1, the most accurate CH_4 emission estimates for individual coal mine shafts in the USCB are obtained from the CoMet ED v4.01 dataset. These emissions are spatially resolved at the shaft level, representing the highest available spatial fidelity and source-specific detail within the domain. To account for the remaining anthropogenic CH_4 sources, the annual emission data from the EDGAR v7.0 inventory (Crippa et al. 2021) is used for the year 2018. At the time the model setup was created, this represented the most recent dataset. EDGAR provides annual CH_4 emissions with a spatial resolution of $0.1° \times 0.1°$ grid (approx. 10 km), and emissions are reported by Selected Nomenclature for Sources of Air Pollution (SNAP) source sectors. This allows for the targeted replacement of the "fuel exploitation" sector, which combines emissions from coal, oil, and gas production, by the CoMet ED emissions.

To account for emission variations during the diurnal cycle time-dependent scaling factors were applied to the respective emission source categories, based on standard temporal profiles for SNAP sectors as reported by van der Gon et al. (2011). For the fuel exploitation sector, the scaling factor remains constant at 1.0 throughout the day, implying no diurnal variability in these emissions. This is consistent with the CoMet ED where available temporally resolved emissions are also constant during the overflight period.

For several non-reporting shafts, however, no emission data were available. As discussed in Sect. 4.1, even inactive or unreported shafts may continue to emit CH_4, and observations during the flight indicate downwind enhancements in regions dominated by such sources (c.f. 11:08 in Fig. 4.9a and 11:32 in Fig. 4.11c).

To enable their inclusion in the inversion, approximate prior emissions were estimated using rough coal production figures and a regional average emission factor of 11.83 kg per tonne extracted coal, as reported by Fiehn et al. (2020). These were partly based on outdated or indirect sources, and do not reflect accurate flux estimates. Nevertheless, they provide plausible order-of-magnitude inputs for the inversion to operate. A detailed overview of the derivation is provided in Appendix B.4.

Typical ventilation shafts in the USCB emit at a height of approx. 25 m (cf. Fig. 4.1b). Hyperspectral imaging of ventilation shaft plumes, acquired in 2022, shows that considerable plume rise and vertical expansion can occur within the first 50 m to 100 m downwind (Knapp et al. 2023). This rise is caused by mechanically forced ventilation from underground galleries (see Sect. 4.1) and shaped by ambient wind conditions. Knapp et al. also note that buoyant rise dominates only within the first few meters, after which plume transport is governed by advection. Their data capture only the near-field plume structure, which is significantly smaller than the resolution of a single WRF-Chem grid cell. Nevertheless, they clearly indicate that emissions should not be released at surface level in the model. Emitting at surface level would subject tracers to unrealistic drag effects and distort initial plume dispersion.

Actual plume evolution depends strongly on meteorological conditions and may exceed or remain below the rise heights observed in the hyperspectral images. To accommodate this variability, the vertical model resolution near the surface was

increased compared to **Case Study I** (see Fig. 4.6c). This adjustment allows for a simple but targeted sensitivity analysis to be conducted. Inversion experiments were carried out using three different vertical model levels as injection heights: $k = 1$ (approx. 20 – 45 m), $k = 2$ (approx. 45 – 72 m), and $k = 3$ (approx. 72 – 104 m). These levels are plausible when compared to the observed plume rise by Knapp et al. (2023) and enable investigation of how variations in vertical mixing influence the inversion results.

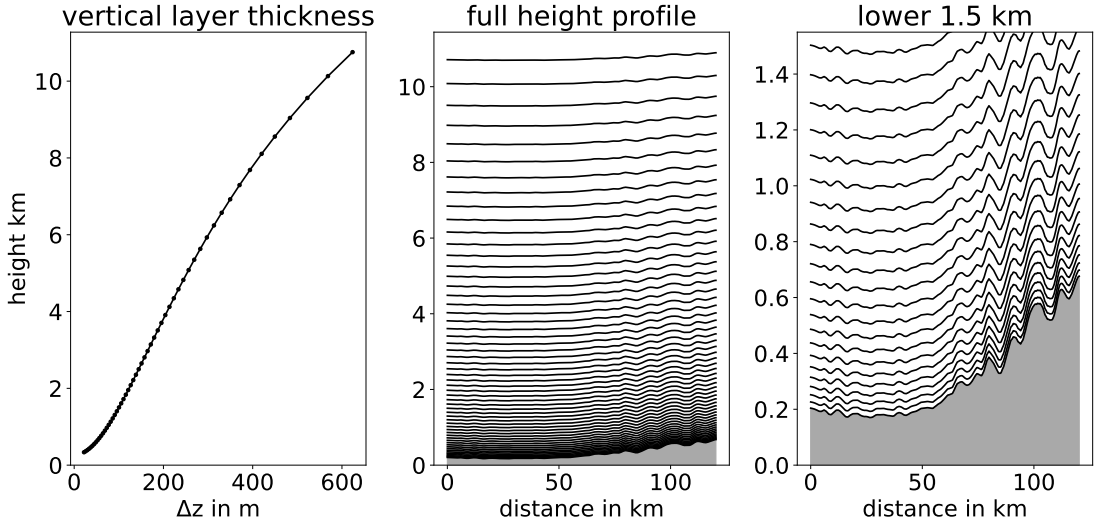

Figure 4.6: Vertical layers in WRF. The ground is displayed in grey, the vertical layer interfaces in black. a) displays the vertical layer thickness Δz. The vertical resolution is relatively fine at low altitudes and gets coarser at higher altitudes. b) shows all 57 vertical layer interfaces from the Earth's surface up to the model's top (200 hPa) along the virtual transect depicted in Fig. 4.5. c) shows a zoom into the lower 1.5 km above sea level. The lowest level is equivalent to the Earth's surface. Moreover, the terrain-following nature of the η-level can be seen.

The CoMet ED initially provides 80 individual point sources. However, when multiple shafts are co-located within the same 1×1 km^2 WRF-Chem grid cell, their emissions cannot be distinguished by the model and are therefore aggregated into a single point source. Accordingly, the state vector comprises 76 elements: 74 for the aggregated or individual point sources; one additional element accounts for the regional background emissions from all grid cells not associated with any shaft location, effectively scaling the EDGAR emissions in the domain; and one element serves as an additive offset to correct for a potential systematic bias between the CHARM–F measurements and the CH_4 background simulated by WRF-Chem, which is effectively shaped by the CAMS-derived initial and boundary conditions. This offset is not a scaling factor but a uniform shift applied to all modelled column values, enabling the inversion to reconcile potential mismatches in the background CH_4 concentration field.

An ensemble size of $N = 150$ is selected in this study, consistent with previous

findings by Peters et al. (2007), who demonstrated that this ensemble size is sufficient to capture the key features of the prior covariance structure and ensure robust inversion performance in regional setups (see also Appendix B.3). Each of the 150 ensemble members is represented as an independent passive tracer in the WRF-Chem simulation. This allows direct access to ensemble-specific simulated observations without requiring explicit construction of the linearized observation operator. In CTDAS, the prior state vector deviations are constructed from a single global relative uncertainty, which was set to 100 % in this study. This choice reflects the considerable uncertainty in shaft-level emissions. For most sources, only annual total emissions reported by mine operators are available. These values are temporally downscaled to obtain hourly rates, assuming constant emission throughout the year. However, actual emissions on the day of measurement can deviate substantially from the annual average, depending on mining activity, ventilation strategy, and operational schedules. As the CoMet ED does not provide uncertainty estimates, the generous prior uncertainty allows the inversion to flexibly adjust source strengths, including assigning near-zero scaling factors to individual shafts if supported by the observations.

In addition to prior uncertainty, the model–data mismatch error $\boldsymbol{\varepsilon}$ plays a critical role in the inversion framework. It represents the total uncertainty associated with each of the $M = 1576$ elements of the observation vector and embodies the corresponding entries of the diagonal observational error covariance matrix $\mathbf{R}$, as introduced in the Bayesian framework described in Sect. 4.2. $\boldsymbol{\varepsilon}$ is defined as:

$$\boldsymbol{\varepsilon} = \sqrt{\boldsymbol{\sigma}_y^2 + \boldsymbol{\sigma}_{\mathcal{H}}^2} \tag{4.7}$$

The term $\boldsymbol{\sigma}_y$ is derived from the retrieval error of the individual CHARM–F measurements after binning onto the WRF-Chem grid. Assuming independent errors, this binning process reduces the effective observational uncertainty per grid cell approx. with $\sim 1/\sqrt{m}$, where m is the number of measurements contributing to that cell (Ehret et al. 2017). As a result, $\boldsymbol{\sigma}_y$ becomes comparatively small. In atmospheric inverse modelling, overly small observational uncertainties can lead to an over-constraint of the inversion, disproportionately amplifying the influence of individual observations. Therefore, a user-defined representation uncertainty $\boldsymbol{\sigma}_{\mathcal{H}}$ is introduced to account for discrepancies arising from model transport limitations, spatial mismatch between observations and grid cells, and, beyond that, an imperfect representation of plume structure. This term $\boldsymbol{\sigma}_{\mathcal{H}}$ dominates the total model–data mismatch.

Selecting a meaningful value for $\boldsymbol{\sigma}_{\mathcal{H}}$ is inherently challenging and ideally requires dedicated sensitivity studies that examine model–observation mismatch under different transport regimes and measurement instruments. Since such an extensive analysis is beyond the scope of this work, a conservative but well-justified value of 25 ppb was chosen. Sheng et al. (2018) estimate a model transport error standard deviation of 12 ppb from residuals between GEOS-Chem simulations and Total Carbon Column Observing Network (TCCON) XCH_4 column observations; but their residual spread extends well beyond 20 ppb. Gałkowski et al. (2020) applied a transport error initialized with 30 ppb when comparing WRF-based simulations with in situ CH_4

data from the FDLR Cessna over the USCB during the same CoMet 1.0 campaign. However, it should be noted that in situ observations are generally more variable than total column data.

A more sophisticated, simulation-dependent formulation was proposed by Steiner et al. (2024b), who scale $\boldsymbol{\sigma}_{\mathcal{H}}$ with the simulated CH_4 enhancement, and further developed in Steiner et al. (2024a) into a flow-dependent scheme using the ensemble spread as a proxy for model mismatch. CTDAS-WRF does not support dynamic error specification without source code changes. The fixed 25 ppb used here is therefore both conservative and consistent with the generous prior uncertainty (set to 100 %).This ensures that the inversion remains robust, limits the observational weight to avoid overfitting, and still responds clearly to the atmospheric observations, as confirmed by agreement between posterior and observed XCH_4 in test runs.

With the setup described above, the CTDAS-WRF framework is now fully configured to simulate atmospheric CH_4 transport and to perform the inversion experiments. In Fig 4.7 the right map illustrates an example of the resulting simulated CH_4 plume for a representative snapshot (13:35-13:40), overlaid with the complete HALO flight track. This visualization provides an initial impression of the spatial alignment between the observed enhancements and the prior modelled distribution of XCH_4.

4.3 Initial Inversion & Source Clustering

To address **RQ2**, two inversion runs are conducted: an initial run (presented in this section) and a best-estimate run (see Sect. 4.4.1). The initial run serves two purposes: it enables a performance assessment of the prior simulation by comparing simulated XCH_4 values against both the observations and the optimized posterior state, and it provides a first set of spatially disaggregated emission estimates along with key diagnostics on the system's ability to resolve individual sources. Each WRF grid cell containing one or more ventilation shafts is represented by a separate element in the state vector, preserving maximal spatial detail. However, the ability to disentangle emissions from individual sources depends strongly on their spatial distribution, prevailing wind conditions, and the alignment of the flight path in relation to the plumes. In cases where sources cannot be reliably differentiated — indicated by strong posterior anti-correlation of their associated state vector elements — emissions are aggregated into a joint vector element. This so called spatial clustering is a key achievement of this work and introduced in Sect. 4.3.2. The resulting aggregated state vector is then used in the second, best-estimate inversion run (Sect. 4.4.1). This two-step approach enhances the ability to attribute observed enhancements more precisely to individual or clustered ventilation shafts. It ensures that this spatial disaggregation remains consistent with both the observational constraints and the simulated transport.

4.3.1 Analysis of the Initial Inversion

With the inversion system configured and the observational data assimilated, the first step is a direct comparison of simulated and observed XCH_4 values, undertaken in this section. This reveals the extent to which the prior simulation reproduces key plume features and whether systematic biases exist.

Additionally, this comparison allows the identification of measurement segments where significant model-data mismatches clearly indicate transport errors. The atmospheric inverse model assumes unbiased transport and cannot correct for systematic errors. Including such segments would bias emission estimates, as transport-related discrepancies would be misattributed to source strengths. The following section describes how these segments are detected and under which conditions they occur. As part of the quality control, the affected observations are flagged and excluded from the best-estimate inversion (Sect. 4.4.1).

Figure 4.7 shows the full time series of observed XCH_4 values from CHARM–F (black), together with the simulated values from the prior (blue), and optimized state (red). All values are plotted as dots with associated uncertainty bars. The error bars of the observations show the model-data mismatch $\boldsymbol{\varepsilon}$, which is comprised of the representation uncertainty and the observational uncertainty (cf. Eq. B.2). The constant representation uncertainty $\boldsymbol{\sigma}_{\mathcal{H}}$ of 25 ppb is relatively large, while the observational uncertainty $\boldsymbol{\sigma}_y$ is inherently small for IPDA-based column retrievals and is further reduced by spatial binning to the WRF grid (cf. Sect. 4.2.1). After

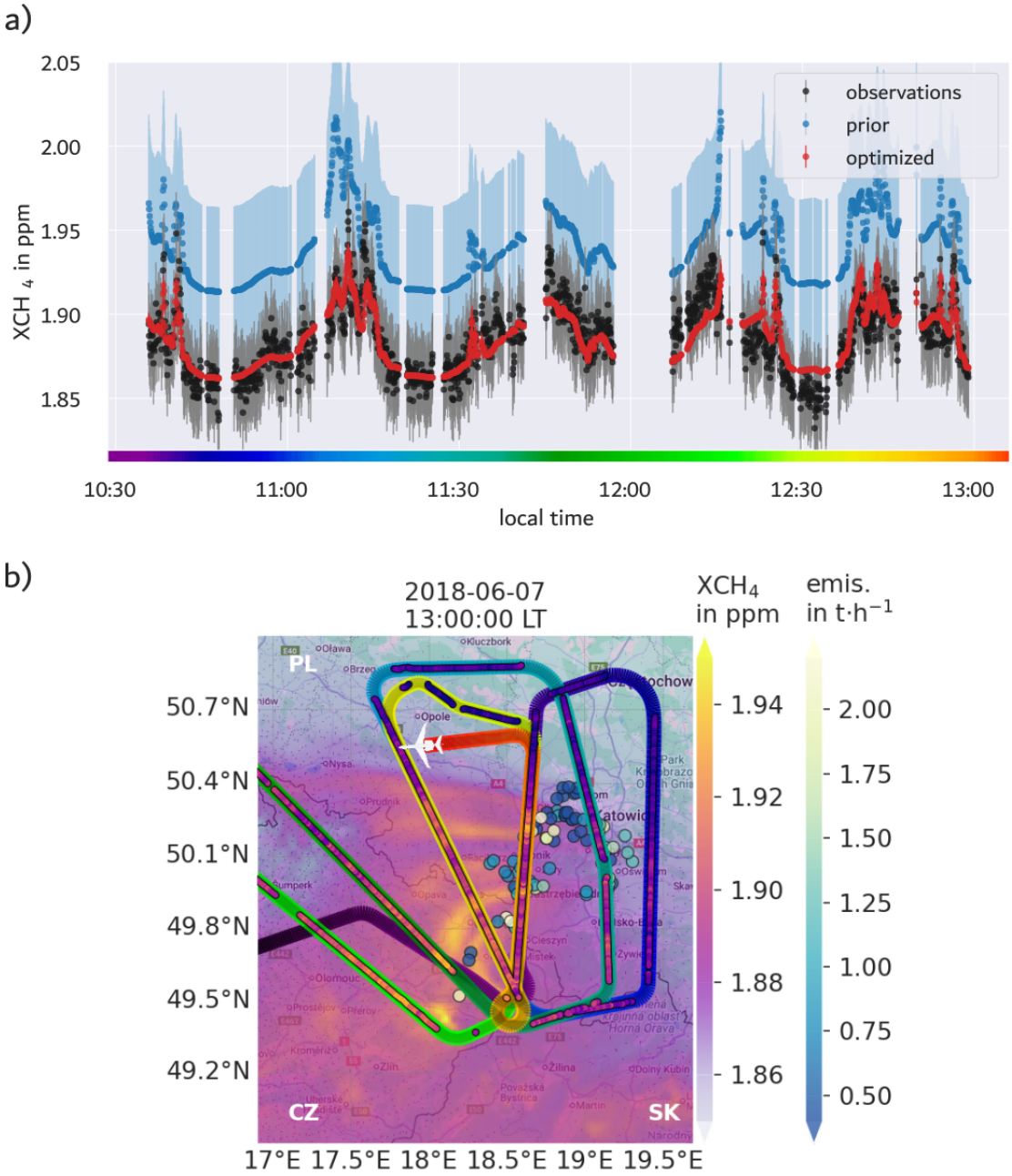

Figure 4.7: a) Time series of retrieved XCH_4 from CHARM–F (black), prior simulation (blue), and optimized simulation from the initial inversion run (red). Error bars of the observations show the model-data-mismatch error $\boldsymbol{\varepsilon}$, which comprises the observational error as well as a constant representation uncertainty. The error bars of the prior and optimized simulation show the ensemble spread.
b) The trajectory line of the HALO flight track is colour-coded by local time to facilitate spatial–temporal association with the time series on the left. Dots along the track indicate airborne CHARM–F observations coloured by the retrieved XCH_4. The background field displays a snapshot of prior simulated XCH_4 values from 7 June 2018 (13:00 CEST). To enable consistent visual comparison with the observed CHARM–F measurements using a shared colour scale, the retrieved optimized bias terms is uniformly subtracted.

binning, the mean uncertainty for the full observation vector drops to $\overline{\boldsymbol{\sigma}_y} = 0.2\,\text{ppb}$. Thus, $\boldsymbol{\sigma}_y$ contributes little to the total model-data mismatch $\boldsymbol{\varepsilon}$, given the much larger representation uncertainty $\boldsymbol{\sigma}_{\mathcal{H}}$.

The uncertainty of the optimized simulation, here expressed as the standard deviation of the posterior ensemble, is notably smaller than that of the prior. This demonstrates that the inversion can effectively overcome the generous prior uncertainty and produce posterior estimates with substantially improved confidence. The reduced spread of the optimized ensemble reflects the information content provided by the CHARM–F observations in combination with the atmospheric transport model.

The inversion yields an additive offset of 51 ppb[1]. This value is subtracted from the simulated columns to adjust the overall baseline of the prior simulation (cf. Sect. 4.2.1). As a result, the optimized and the observed baseline aligns well.

A closer look at the time series in Fig. 4.7a) shows that this agreement holds across large parts of the domain, both in the background and within the plumes, particularly in segments close to the ventilation shafts. Some localized discrepancies remain: in the southwestern part of the domain (green segment, 11:45-12:20), the optimized values stay below the observations, whereas in the northeastern background (lightgreen-yellow, 12:25-12:35), they are slightly too high. Overall, however, the inversion captures the main structures of the observed signal well enough to support meaningful source attribution. The following section highlights to what extent plume-related enhancements are reproduced and where the system shows limitations.

Successful Plume Simulation in the Near Field

Figure 4.8 shows three south-north transects flown in the lee of major ventilation shafts at close range. Simulated and observed enhancements agree well. In all segments the first plume is associated with shafts north of Jastrzębie-Zdrój. The subsequent double peak originates from shafts west of Katowice.

While the overall structure aligns well, the observed plumes tend to be narrower than their simulated counterparts. This is reflected in the fact that observed peak values often exceed the simulated ones, while falling below the simulation along the flanks. As established in Sect. 3.1, the physically relevant quantity linking observed enhancements to emission rates is the integrated enhancement over the plume cross-section. Hence, such shape differences (e.g. narrower peaks) do not necessarily imply a flux mismatch, as long as the total enhancement remains consistent.

Nevertheless, the sharper structure in the observations suggests that in the model the turbulent mixing may be stronger than in reality. Comparisons between observed and simulated plume enhancements provide a useful indicator of how well turbulent mixing is represented in the model. In principle, the choice of the numerical diffusion parameter $diff\_6th\_factor$ (cf. Table 2.2), which controls the strength of a sixth-order smoothing term (larger values yield smoother, smaller values yield sharper structures), could be optimized against such observations. This lies outside the scope of the present study, as each test would require rerunning the WRF simulation.

[1]Please note that for visual consistency, in all upcoming plots a uniform offset of 51 ppb is subtracted from the prior simulation in both the time series and the plume maps.

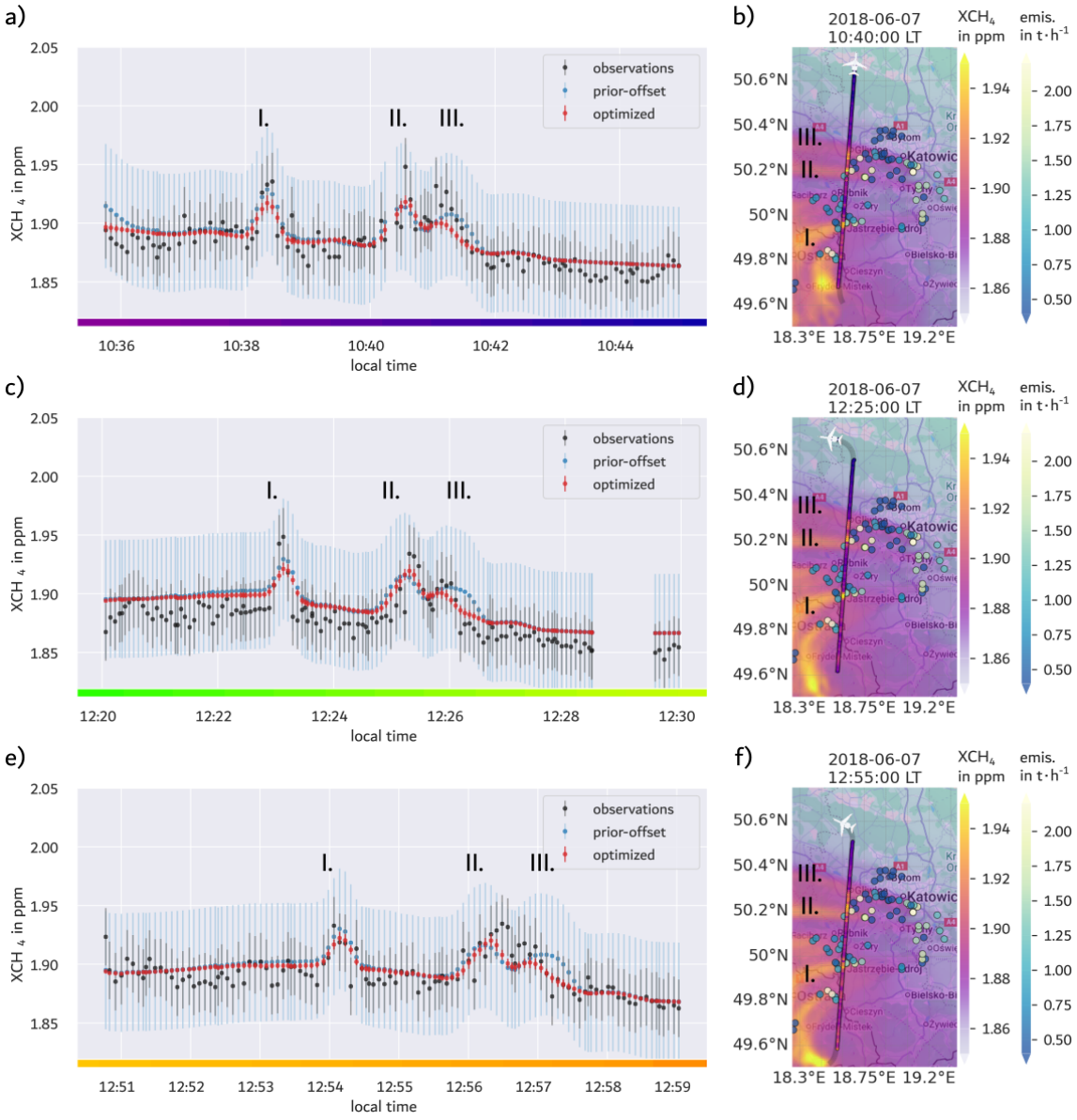

Figure 4.8: Left panels: Time series of observed and simulated XCH_4 for three south-north transects flown in close proximity to major ventilation shafts. Right panels: Corresponding flight segments shown on maps of prior-simulated XCH_4. All three transects exhibit similar good agreement between model and observations. The plumes on the maps are numbered to make them easier to find in the time series.

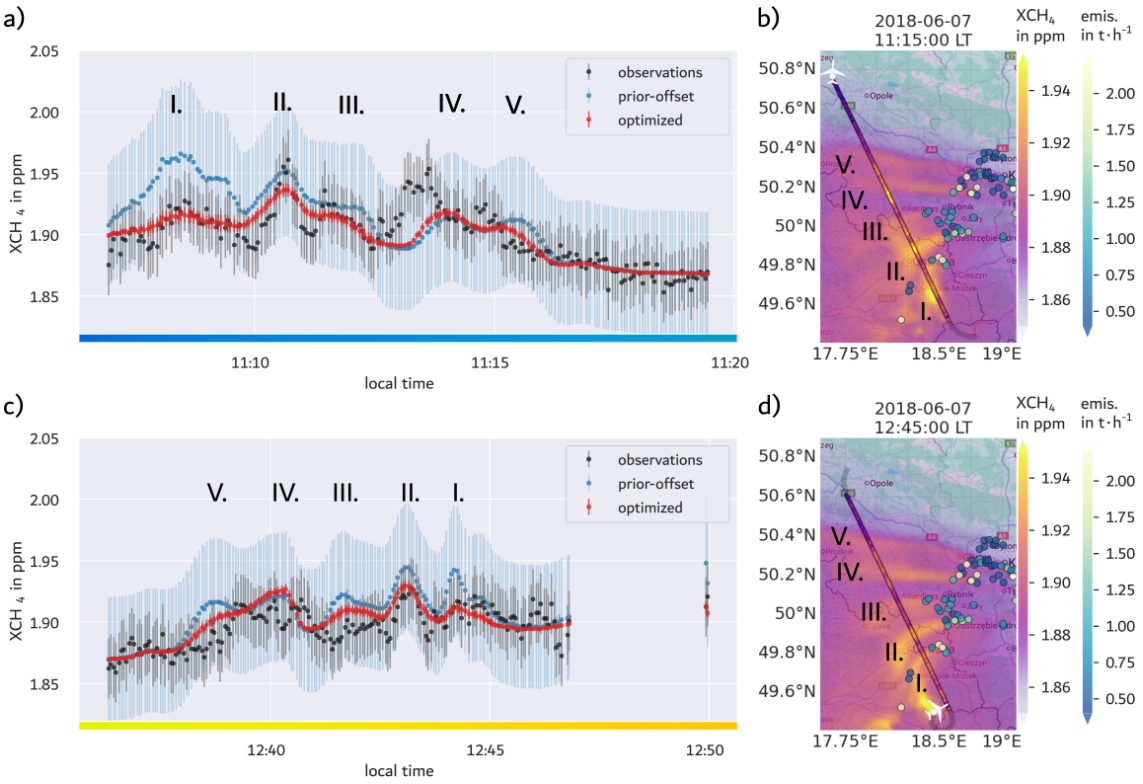

Figure 4.9: Two extended transects across the domain, flown first south-north (a–b) and then north-south (c–d). A spatial mismatch between observed and simulated enhancements is evident in the region of the northerly double plume. In both time series (a, c), observed XCH_4 peaks appear further south than the simulated plume. This displacement is also visible in the spatial maps, especially in (b), where between 50.1°N and 50.2°N the observed enhancements clearly deviate from the modelled plume, indicating a localized wind direction error. Plumes on the maps are numbered to help finding them in the time series.

Effects of Wind Direction Error on Emission Estimates

A mismatch during the first transect (Fig. 4.8a) shows a simulated enhancement around 10:36 that is absent in the observations. It stems from Czech sources east of Ostrava and can be followed across the plume panels (Fig. 4.8b, d, f) along the wind direction, suggesting that in reality it was displaced relative to the flight path and therefore not captured. Such a mismatch would cause the inversion to downscale Czech sources; to avoid this, the data points before 10:36:35 are flagged and excluded from the best-estimate inversion (cf. Sect. 4.4.1).

Figure 4.9 shows two extended transects, first south-north (top, a–b) and then north-south (bottom, c–d). The time series in (a) and (c) are therefore mirrored. In the first segment (a), the flight crosses the same CH_4 accumulation downwind of Czech sources east of Ostrava as in Fig. 4.8b. The feature appears in both observations and simulation, though with weaker and more diffuse enhancements in the observations, likely due to greater distance from the sources and stronger turbulent dispersion.

Shortly after 11:10, a narrow observed plume appears, which is also present in the simulation. However, the modelled version is again somewhat broader and blends into the following peak, consistent with the previously discussed tendency towards overly diffuse plumes (cf. Fig 4.8). What stands out in this case is that the observations show a clearer separation between two emission subregions. One originating from shafts directly north of the Czech border (approx. 49.9°N–50.0°N), and another from shafts near Rybnik (approx. 50.0°N–50.1°N). In the simulation, these sources merge more strongly into a continuous double plume.

At around 11:12–11:13 a pronounced local minimum follows, visible in both observed and simulated values. This marks a plume boundary around latitude 50.15°N, separating emissions from shafts north and south of Rybnik. This separation coincides with a diverging wind field over the region. The northern plumes are advected predominantly westward with a slight north-westerly tendency, while the southern plumes are transported more towards the southwest.

By comparing the time series with the maps a misalignment between observed and simulated enhancements becomes apparent, indicating a wind direction error. In the region of the northerly double-peak plume, the observations indicate enhanced CH_4 concentrations further south than the simulated plume (before approx. 11:14). Conclusively, the inversion increases emissions from shafts located around 50.15°N–50.22°N to match the earlier observed signal, while simultaneously decreasing emissions from shafts further north (50.25°N–50.30°N), where the simulation places the plume too late (after 11:15). This results in an overestimation of the more southern sources and an underestimation of the northern ones. Since this localized wind error is evident, the affected data segment is flagged and excluded from the best estimate inversion (see Sect. 4.4.1). Otherwise, this segment would degrade the quality of the posterior emissions estimates.

During the return transect (Fig. 4.9c), the same features are observed in reverse order. An additional background segment in the far north samples plume-free air, highlighting that both prior and optimized simulations slightly overestimate the background XCH_4 in the north.

Loss of Plume Signal in the Far Field

Figure 4.10 shows two additional transects further downwind over Czech territory. In both transects, measured XCH_4 values in the northwest are lower than in the south, consistent with overall downwind dilution of CH_4 enhancements, possibly superimposed by a misrepresentation of the background gradient.

Unlike in previous cases, the observed values lie almost entirely above the simulated ones. The observations also display substantial variability, indicative of turbulent plume remnants, whereas the simulations show no discernible structures. The spatial maps (Fig. 4.10b and d) suggest that the simulated plumes did not propagate far enough downwind. This supports earlier indications of excessive turbulent mixing in the model, which prevents plume signals from reaching the far-field transects.

Consequently, this data is not sensitive to any state vector elements related to shaft emissions. No adjustment of emission rates can improve the fit. The only

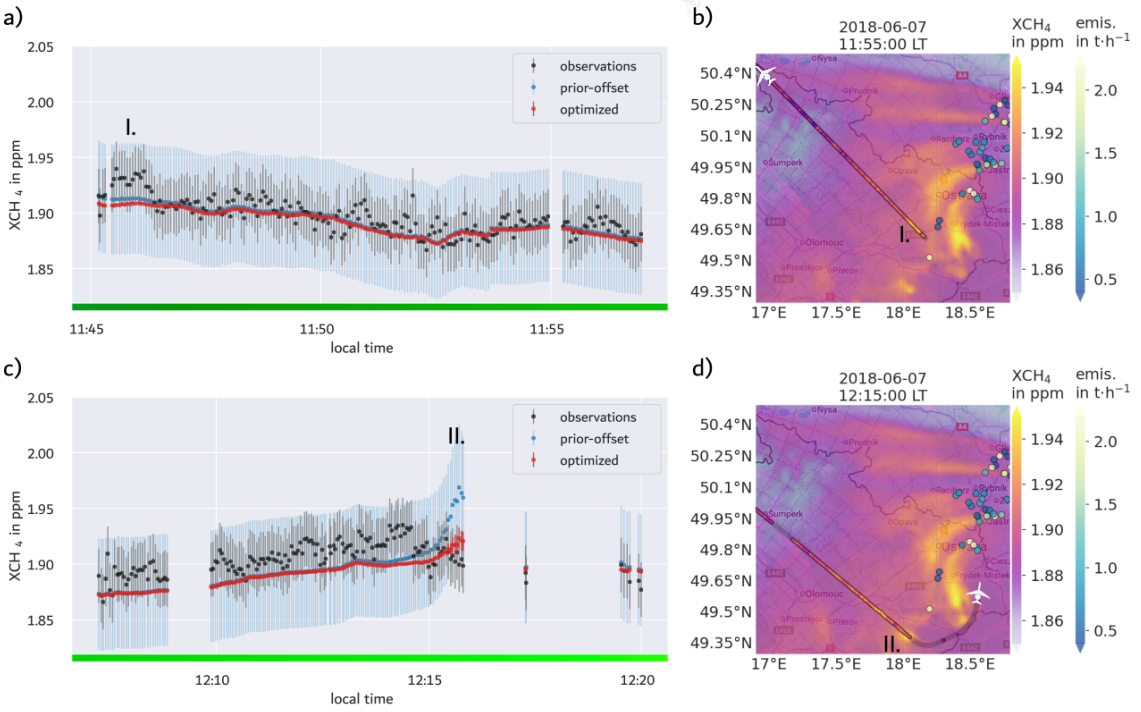

Figure 4.10: (a, c) time series of observed and simulated XCH_4 along two extended transects. (b, d) corresponding spatial maps. The time series are mirrored in direction. In (a) around 11:45–11:46 an observed enhancement (I.), presumably from shafts north of Jastrzębie-Zdrój, appears overly diluted in the model. Both (a) and (c) show turbulent variability in the observations that is absent in the simulation. Moreover, the time series in (c) shows observations that are, in comparison to the simulation, elevated over the entire transect. After 12:15, the prior simulation shows an accumulation at (II.), which is not given in the observations.

parameter affected is the background offset. Because the inversion interprets these far-field measurements as plume-free, the systematic positive residuals pull the optimized background upwards. A high-biased background influences the entire time series and leads to a systematic underestimation of all emission-related state vector elements. For this reason, the entire segment in Fig. 4.10 is flagged and excluded from the best estimate inversion (see Sect. 4.4.1).

A notable sharp enhancement appears in the prior simulation shortly after 12:15 (Fig. 4.10c), corresponding to an accumulation downwind of the southernmost isolated Czech shaft (Fig. 4.10d). No such feature is visible in the CHARM–F data. As in comparable cases discussed above, this highlights the difficulty of simulating such localized structures in WRF-Chem.

Background Gradients and Orographic Effects

Figure 4.11 (a–b) and (c–d) show two transects with a consistent north-south gradient in XCH_4, reflecting a prevailing large-scale background pattern. In both transects weak enhancements are visible in the southeastern parts of the tracks. These may arise

partly from counter-gradient flow, which allows the main downwind plume to spread southeastward even under northeasterly winds. Moreover, the Western Carpathians, including the Tatra Mountains, form a natural barrier along the southern domain border, where flow diversion and reduced ventilation may promote accumulation of CH_4.

The zoomed-in segment (e–f) reveals a localized enhancement within a narrow mountain basin near the city of Żywiec (11:36–11:38, approx. 49.60°N–49.75°N). This feature cannot be linked to any known emission source. As shown in Fig. 4.11f), the data points are located in a basin-like orographic pocket surrounded by the Silesian Beskids to the west and the Little Beskids to the east. The only open connection is a narrow valley corridor leading north toward Bielsko-Biała along the S1 expressway. It is plausible that this terrain configuration enables a localized accumulation of CH_4 from earlier emissions under different wind conditions, which is not adequately resolved at the model's 1 km resolution.

As the enhancement cannot be linked to any local emission source or state vector element, it is likely caused by accumulated CH_4 trapped in the valley. Since this feature is not represented in the model, its inclusion would bias the optimized background upward. Data points from 11:36 to 11:38 are therefore flagged and excluded from the best estimate inversion (see Sect. 4.4.1).

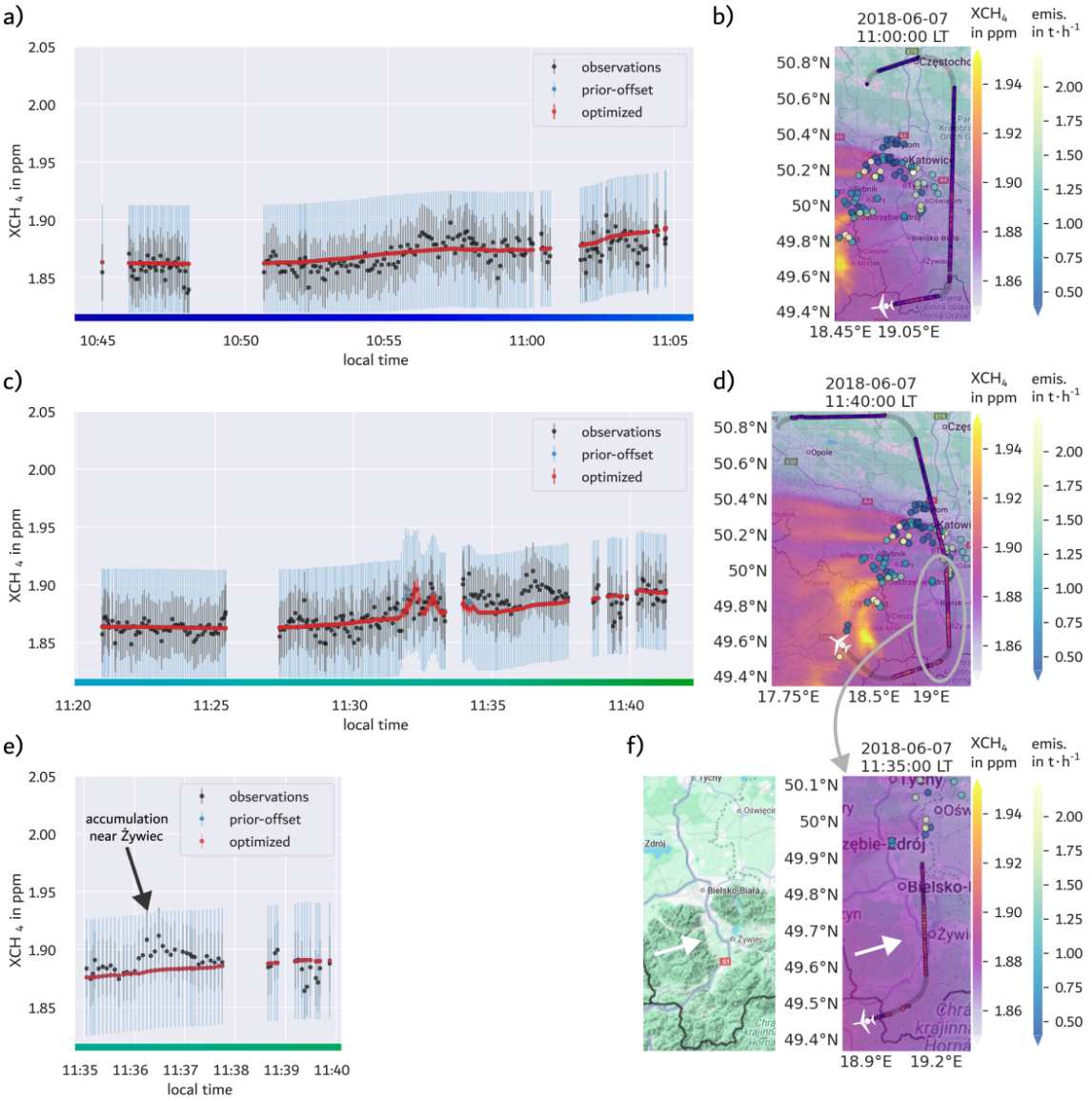

Figure 4.11: (a–b) show a background transect flown from north to south, east of the main source region. (c–d) display a second transect in the same direction (approx. half an hour later), with similar XCH_4 values in both the north and south. (e) zooms in on the central part of the time series in (c), while (f) presents two topographic views of the same area: Google Maps terrain screenshot without track overlay on the left and a Google street-map style on the right.

4.3.2 Development of Inversion-Driven Source Clustering

While the initial inversion yields posterior emission estimates at individual shaft level, this level of spatial resolution is not always supported by the observational constraints. In some cases, the observed CH_4 enhancements result from overlapping plumes emitted by multiple nearby shafts, making it difficult or even impossible to attribute observed enhancements to individual sources.

In such cases, the inversion may yield implausible results, such as negative posterior emission rates. In the following, two examples demonstrate how transport model errors and plume accumulation effects can lead to such artefacts. To address these limitations, this study introduces a novel clustering approach, developed here for the first time, in which strongly "entangled sources" are aggregated into joint state vector elements. Here, source entanglement refers to situations where exhaust plumes produce a common signal in the observations, such that the state vector elements of the respective sources cannot be optimized independently and their scaling factors become anti-correlated. The method includes a mathematical criterion for identifying source entanglement, a threshold definition, and a procedure for assigning sources to clusters. Instead of optimizing each source individually, the inversion yields a collective scaling factor applied to the entire cluster. This stabilizes the inversion in regions with overlapping plumes, where individual sources cannot be reliably resolved, and represents a key methodological contribution of this work.

Example 1: Spurious Downscaling due to Excessive Plume Broadening

Figure 4.12 displays a zoomed-in section of the transect from Fig. 4.8c–d. The aircraft crosses a CH_4 enhancement between 12:22:45 and 12:23:30, which in the simulation results from a superposition of emissions from several shafts. The integrated area under the full enhancement reflects the sum of contributions from all involved sources, in particular **Zofiowka IV** and **V** (co-located in the same WRF grid cell), the three **Pniowek** shafts, **Borynia VI**, and even long-range contributions from **Brzeszcze** and **Andrzej** further east. It is not possible to identify localized features within the observed enhancement that can be unambiguously assigned to one of these individual shafts alone.

However, given that **Borynia VI** is located in such proximity to the flight path, it is plausible that its emissions primarily affects the peak's flank at 12:23:15, where the observed XCH_4 values fall below the simulated ones. As discussed above, this localized undershoot can be explained by the general tendency of the model to simulate plumes that are too broad due to excessive turbulent mixing. In this case, the resulting negative mismatch coincides with the plume of the source **Borynia VI**, although the corresponding simulated data points still reflect the superposition with emissions from the other aforementioned sources.

Of all the sources contributing to the enhancement in this segment, **Borynia VI** is a relatively small source. Therefore, scaling its emission rate has only a small impact on the optimized plume shape. In the flank region, where the mismatch occurs, **Borynia VI** contribution is largely overshadowed by the broader signal originating from the **Pniowek** and **Brzeszcze** shafts. These larger sources, however,

are also constrained by data points on other parts of the enhancement, such as the central peak, which limits the extent to which their emissions are downscaled.

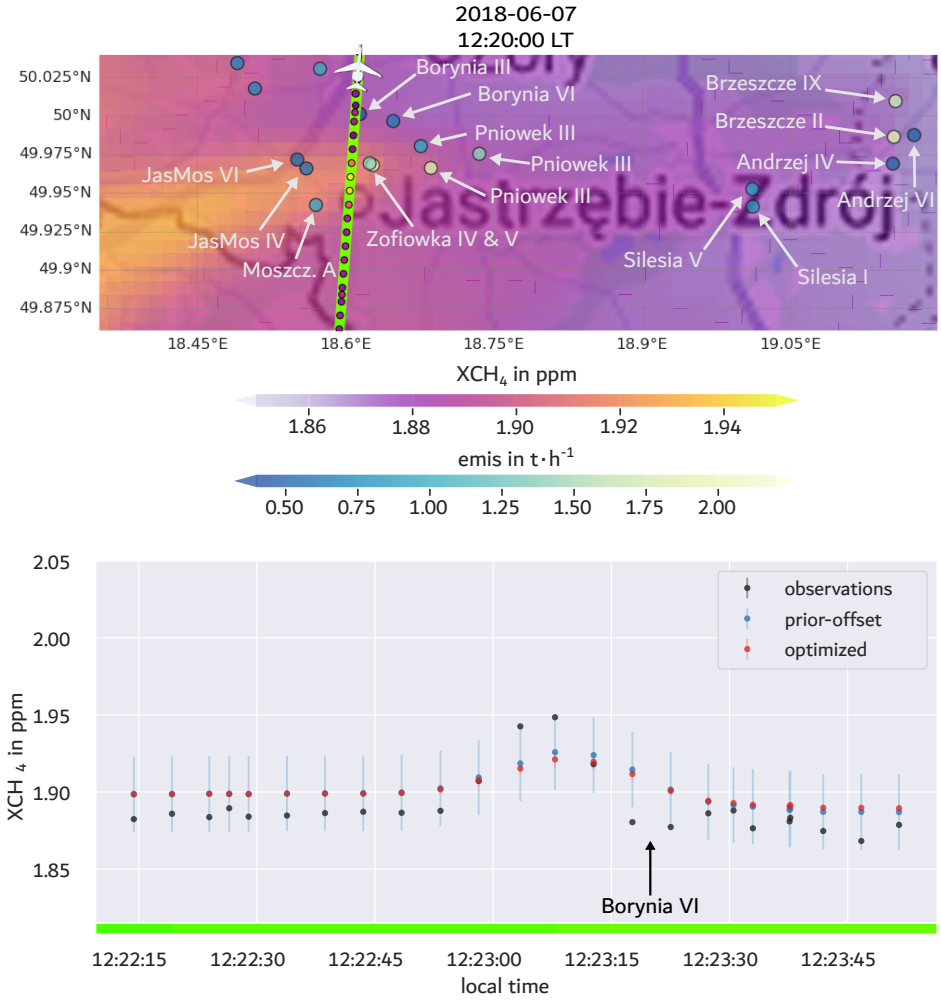

Figure 4.12: Zoom-in on the central segment of the transect shown in Fig. 4.8c–d, highlighting a CH_4 enhancement observed downwind of the **Zofiowka-Pniowek-Borynia** cluster. The simulated enhancement results from overlapping plumes of multiple sources, including long-range contributions from **Brzeszcze** and **Andrzej**. The arrow marks a set of negatively biased data points in the flank of the enhancement, which coincides with the simulated plume of **Borynia VI**.

As a result, the negative mismatch in the flank can most easily be reduced by downscaling **Borynia VI**, while the stronger sources remain comparatively fixed. Therefore, the inversion assigns **Borynia VI** a negative posterior emission rate (cf. Tab. 4.5), which lowers the penalty associated with the negative residual data points that are affected by its emissions and thereby decreases the overall cost function (Eq. 4.1).

This outcome reflects a particular combination of measurement geometry, transport, mixing errors, and spatial source arrangement, in which such a solution becomes mathematically favourable, even though it is not physically meaningful.

Table 4.5: Prior emission estimates and initial optimized values for shafts contributing to the observed accumulation enhancement in Fig. 4.12. **Zofiowka IV** and **V** are co-located in the same WRF grid cell. Emission rates are in $\mathrm{kt\,h^{-1}}$.

Shaft	Prior	Optimized
Borynia VI	0.63	−0.45
Zofiowka IV & **V**	3.49	3.61
Pniowek III	1.77	0.82
Pniowek IV	0.91	0.65
Pniowek V	1.40	0.80
Brzeszcze II	1.88	0.28
Brzeszcze IX	1.69	1.08
Andrzej IV	0.48	0.53
Andrzej VI	0.48	0.42

Example 2: Entanglement in Accumulated Plumes

Another illustrative example involves the Czech shafts between the cities of Ostrava and Karviná. As shown in Fig. 4.13 before 11:09, the aircraft crosses a diffuse yet extended enhancement in the simulated XCH_4 field. The prior simulation shows, that this signal originates from a morning accumulation of CH_4 emitted under initially stagnant wind conditions. As the wind picks up, this accumulated CH_4 is advected as a compact, coherent plume representing a superposition of emissions from multiple sources.

Such accumulations are notoriously difficult to simulate, both in terms of timing and morphology. In reality, the aircraft may have passed through the outskirts of the advected accumulation, whereas the simulation samples a more central and concentrated section. This discrepancy could explain why the simulated enhancement appears more pronounced than in the measurements. Alternatively, it is also conceivable that the simulation accurately represents the plume structure and sampling location, and that the actual emission rates were indeed lower than assumed in the prior. These two scenarios cannot be distinguished based on the available data. However, the inversion framework assumed that atmospheric transport is correctly represented and can only compensate for mismatches by scaling emissions. Consequently, the discrepancy is interpreted as an overestimation of emissions, resulting in a reduction in the emission rates of all contributing sources. This is reflected in the optimized values listed in Table 4.6, where almost all shafts' emission rates are reduced, including two with unphysical negative values: **ČSM B** and **ČSA A**.

Between 11:09 and 11:10, the aircraft reaches the downstream edge of the accumulation. In map view, this section shows the gradual transition from the broader accumulation to an emerging emission plume being emitted from **ČSA A**, **Lazy A**, and maybe even **Darkov A**. While this developing plume is partially superimposed on the remnant accumulation, it is already discernible in the spatial structure.

After 11:10, a similar behaviour occurs as previously discussed for **Borynia VI**. The flight track surveys another plume originating from northerly Polish shafts. In the

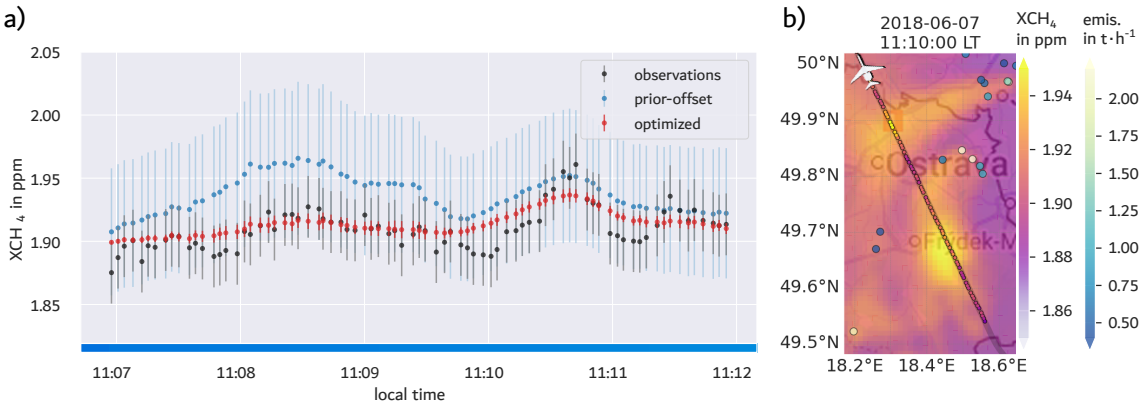

Figure 4.13: Zoom-in on the central segment of the transect shown in Fig. 4.9a–b, highlighting a CH_4 accumulation observed downwind of the Czech shafts near Ostrava. The enhancement is attributed to an accumulation of emitted CH_4 that formed under stagnant morning conditions and was later advected as a coherent plume. The simulated enhancement reproduces this feature but overestimates its magnitude and spatial extent, which likely reflects uncertainties in timing and localization within the transport model. Since it is not possible to determine whether the discrepancy arises from transport model error or from overestimated emissions, the inversion system reduces all contributing emission rates accordingly (cf. Tab. 4.6).

observations, this plume is clearly separated from the earlier enhancement, whereas in the simulation both plumes appear overly broadened, likely due to excessive turbulent mixing in the transport scheme. Thus, a residual negative mismatch arises that is falsely attributed to **ČSA A** and **Lazy A**.

Consequently, the inversion downscales their emissions not only to account for the undershooting flank at 11:10, but also in response to the broader accumulation feature sampled before. Within this accumulation their emissions are fully intermixed so that the observational constraint by the data prior to 11:09 becomes highly entangled, preventing a meaningful separation of their respective source contributions.

Table 4.6: Prior emission estimates and initial optimized values for Czech shafts contributing to the observed accumulation enhancement in Fig. 4.13.
Results are based on the initial inversion run and should not be interpreted as final best estimates. Emission rates are in $\mathrm{kt\,h^{-1}}$.

Shaft	Prior	Optimized
ČSM B	1.01	0.33
ČSM B	1.01	−0.53
Darkov A	2.23	2.24
ČSA A	3.19	−0.86
Lazy A	0.69	0.18

Altogether, the inversion result reflects a complex blend of contributing effects: a misrepresentation of the initial accumulation, excessive mixing, and partial overlaps with subsequent plumes. These effects lead to a reduction of all contributing emissions, with **ČSM B** and **ČSA A** even reaching unphysical negative values. As previously discussed, these mathematically favourable reallocations of emission rates may reduce the cost function, but they do not reflect physically meaningful distinctions, especially when the observations themselves no longer support a disentanglement of individual contributions.

Clustering Sources by Anti-Correlation

The above described ambiguity is further manifested by a chain of anti-correlations among the involved shafts shown in Table 4.7. These anti-correlations are a mathematical response to their geographical proximity and the overlapping influence of the plumes. This means that the corresponding state vector elements jointly affect the same subset of the simulated observation vector. Each observation within this subset causes an ensemble update in all contributing sources. This shared influence leads to coordinated changes across the affected ensemble deviations (cf. Eq. 4.6). As the posterior covariance matrix is reconstructed from these updated deviations, any coupling introduced by shared observational influence is encoded as statistical dependence, specifically in the form of negative correlation. To identify such cases, a correlation threshold can in principle be applied to the posterior correlation matrix to determine which state vector elements should be grouped into a joint cluster.

	Paskov A	ČSM B	ČSM A	Lazy A	Darkov A	ČSA A	Moszcz. A	Silesia I	Silesia V
Paskov A	1.0	-0.14	0.07	-0.02	-0.02	-0.01	0.01	0.02	0.01
ČSM B	-0.14	1.0	-0.46	-0.04	-0.01	0.03	0.1	-0.02	-0.07
ČSM A	0.07	-0.46	1.0	-0.04	-0.55	0.28	-0.06	-0.08	0.13
Lazy A	-0.02	-0.04	-0.04	1.0	0.14	-0.4	0.15	0.01	-0.08
Darkov A	-0.02	-0.01	-0.55	0.14	1.0	-0.68	0.08	0.12	-0.09
ČSA A	-0.01	0.03	0.28	-0.4	-0.68	1.0	-0.1	-0.08	0.05
Moszcz. A	0.01	0.1	-0.06	0.15	0.08	-0.1	1.0	-0.03	-0.16
Silesia I	0.02	-0.02	-0.08	0.01	0.12	-0.08	-0.03	1.0	-0.23
Silesia V	0.01	-0.07	0.13	-0.08	-0.09	0.05	-0.16	-0.23	1.0

Table 4.7: Extract from the initial posterior correlation matrix, showing a cluster of negative correlation values (shades of purple) among Czech shafts (**ČSM B**–**ČSA A**). Positive correlations are shown in shades of green. The observed pattern results from overlapping plume influence and the spatial proximity of the sources.

In the case of the Czech sources, these pairwise anti-correlations form a continuous chain: **ČSM A** and **ČSM B**, which are located next to each other (see Fig. 4.13), exhibit a strong negative correlation of -0.46 in their posterior estimates (Table 4.7).

ČSM A is likewise anti-correlated with **Darkov A**, which in turn anti-correlates with **ČSA A**, and so on, continuing through **Lazy A**. Together, these shafts form an anti-correlating cluster in the posterior covariance structure. This reflects the limited separability of the individual shafts and justifies aggregating them into a single cluster for the best-estimate inversion run to infer their combined emission rates.

While these Czech shafts form a clearly defined anti-correlating cluster, the situation is less straightforward for other source pairs. For instance, **Silesia I** and **Silesia V** exhibit a posterior anti-correlation of -0.23, which is noticeably weaker than the values observed among the Czech cluster. Even weaker is the anti-correlation between **Paskov A** and **ČSM B**, which is only -0.14. Given these values, the question arises: which anti-correlations are meaningful for clustering, and which merely reflect statistical noise?

To address this, it is important to recall the concept of spurious correlations. As discussed in Appendix B.3, each state vector element and its ensemble perturbations are generated independently. However, due to the finite size of the ensemble, the correlation values in the prior are not exactly zero. This introduces what is known as spurious correlations, which include both positive and negative values that arise by chance and are statistically insignificant by definition.

On the one hand, when two state vector elements are constrained by the same observations, the ensemble is adjusted such that the elements become anti-correlated in the posterior. On the other hand, if the elements are truly independent, their prior correlation is not significantly altered by the inversion.

This distinction becomes evident when comparing, for example, **Makoszowy A** and **Moszczenica A** (not shown in Table 4.7). These two sources exhibit a spurious prior anti-correlation of -0.27. In the posterior, their correlation changes only marginally to -0.26. Given their large spatial separation of roughly 40 km and their North–South alignment perpendicular to the wind direction (cf. Fig. 4.14a), it is safe to say that their exhaust plumes do not overlap and consequently they do not have any shared observational constraint. The inversion correctly recognizes their independence and leaves the spurious prior relationship essentially untouched. However, based on the posterior anti-correlation value alone, this pair would have been incorrectly marked for aggregation into a joint cluster. Instead, the difference between the posterior correlation matrix and the prior correlation matrix offers a more robust indicator. In the following this difference will be denoted by "correlation-shift matrix" (see Table 4.8). Such shifts in the correlation values highlight shaft pairs, where the inversion has caused mutual adjustments. This distinguishes them from random fluctuations.

In Table 4.8 the aforementioned Czech shafts form a pronounced cluster of negative correlation-shifts, indicated by their red shading. The two Silesian sources discussed earlier also show a transition from near-zero prior values to moderate posterior anti-correlations, supporting their classification as a weaker but still meaningful cluster.

	Paskov A	ČSM B	ČSM A	Lazy A	Darkov A	ČSA A	Moszcz. A	Silesia I	Silesia V
Paskov A	0.0	-0.04	-0.0	0.01	0.0	0.03	0.01	-0.0	0.03
ČSM B	-0.04	0.0	-0.48	-0.06	-0.15	0.15	-0.02	0.02	0.04
ČSM A	-0.0	-0.48	0.0	-0.04	-0.45	0.21	-0.04	0.0	0.06
Lazy A	0.01	-0.06	-0.04	0.0	0.19	-0.39	-0.0	-0.04	-0.04
Darkov A	0.0	-0.15	-0.45	0.19	0.0	-0.68	0.08	0.12	0.02
ČSA A	0.03	0.15	0.21	-0.39	-0.68	0.0	0.01	-0.06	0.01
Moszcz. A	0.01	-0.02	-0.04	-0.0	0.08	0.01	0.0	-0.02	-0.05
Silesia I	-0.0	0.02	0.0	-0.04	0.12	-0.06	-0.02	0.0	-0.21
Silesia V	0.03	0.04	0.06	-0.04	0.02	0.01	-0.05	-0.21	0.0

Table 4.8: Correlation shift matrix between selected shafts, showing the difference between posterior and prior correlation values. Red shades indicate shifts toward stronger anti-correlation, while blue shades mark shifts toward positive correlation. A threshold of -0.16 is used to identify statistically meaningful shifts. Based on this criterion, two distinct clusters are formed: a Czech cluster spanning from **ČSM B** to **ČSA A**, and a smaller cluster aggregating Silesia I and Silesia V.

In an ensemble system, the random anti-correlation values define the natural spread of the prior and can be used as a baseline to evaluate whether an observed shift is statistically significant. As will be detailed below in Sect. “Clustering Outcome & Threshold Selection”, the cutoff threshold was set to the 95th percentile of the prior anti-correlation distribution. In this case, the 95th percentile corresponds to a value of -0.16, which serves as an estimate of the maximum spurious correlation shift expected by chance. Any posterior shift exceeding this value is treated as a statistically meaningful adjustment introduced by the inversion. The threshold was determined through iteratively and was guided by physical interpretability. The goal was to identify a level at which entangled sources, such as the Czech shafts or the Silesian pair, are reliably grouped into clusters, while sources with distinguishable contributions remain disaggregated. To illustrate this, the resulting clustering is shown in Fig. 4.14.

Clustering Outcome & Threshold Selection

The polygons in Fig. 4.14 show the aggregated source clusters from the automated correlation-shift approach; the colours will be explained later. As expected, the resulting clusters generally align with the prevailing wind direction. This is especially evident for the elongated light green cluster, which connects the shafts **Borynia VI** and **Brzeszcze IX** over an along wind distance of >36 km. As discussed in Sect. 4.3.1 and shown in Fig. 4.12, the negative mismatch in the plume flank near **Borynia VI** is also affected by contributions from **Brzeszcze IX**. This shows that anti-correlating influence in the inversion can extend well beyond immediate proximity.

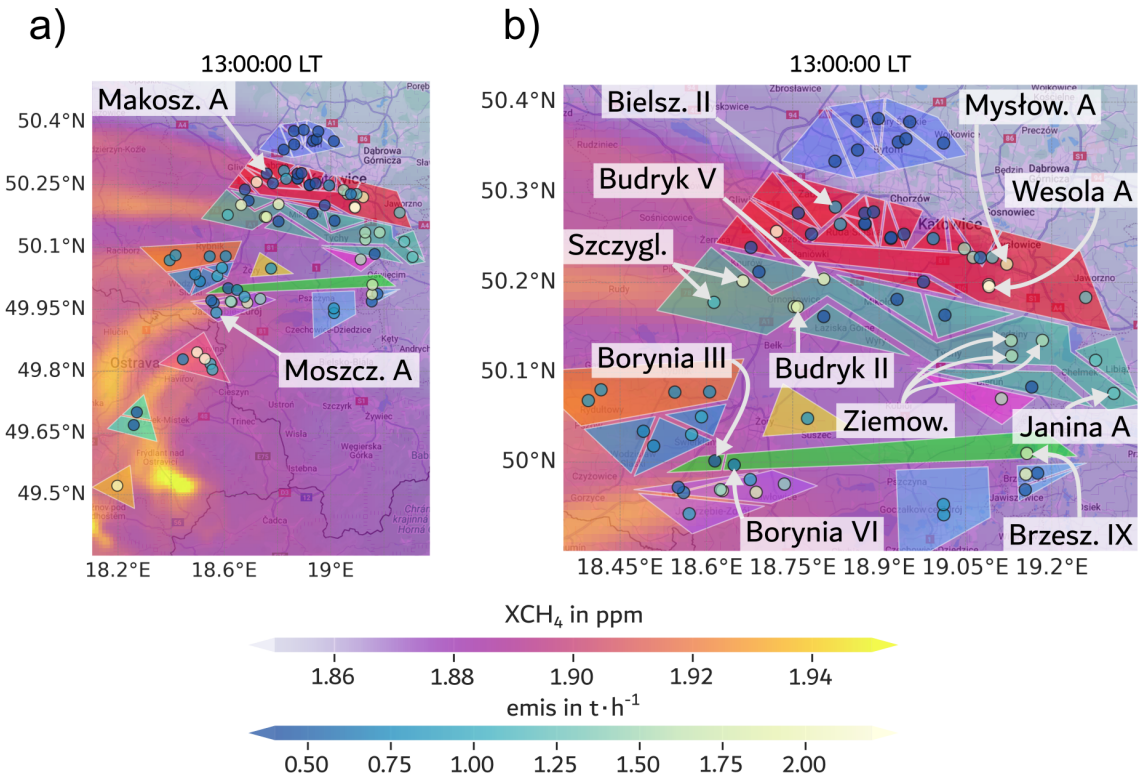

Figure 4.14: Automated source clusters derived from the correlation shift between prior and posterior, using a threshold of −0.16. Each polygon encloses a group of shafts connected through a chain of anti-correlations that exceed this threshold. This clustering is only applicable to the given flight pattern and wind direction. Panel (b) shows a zoom-in of the central to northern subregion.

The case of **Borynia VI** also illustrates an important limitation of this method. While **Borynia VI** and **Borynia III** lie along the same wind path, the latter is not included in the same cluster, as visible in the zoomed Fig. 4.14b. This apparent omission can be explained by the design of CTDAS: the prior uncertainty is defined as 100% of the prior emission rate. This means that the absolute uncertainty of low-emission sources is proportionally smaller, and their adjustment leads to a relatively larger penalty in the cost function. The method primarily captures higher-emission sources, which are more prone to posterior adjustments. In contrast, lower-emission shafts tend to remain close to their prior and do not develop strong anti-correlations.

A more striking example of this effect can be seen in the dark green polygon extending from **Janina A** in the east through the three **Ziemowit** shafts, across **Budryk V** and **II**, and further west to the two **Szczyglowice** shafts. Despite following a coherent along-wind direction, the cluster exhibits a zigzag pattern (see Fig. 4.14b), with several intermediate shafts being systematically excluded. Notably, these omissions involve smaller sources such as **Murcki A**, **Barbara A**, and **Boleslaw II**, which clearly lie within the same transport corridor, but which do not develop strong enough correlation shifts to meet the clustering threshold.

A similar pattern can be observed in the northern red polygons, and even more clearly in the dark blue polygons near the city of Bytom (around 50.35°N, 18.9°E), where despite their geographic alignment, only a few shafts are linked. A broader visual inspection confirms that sources with posterior emissions below approx. $0.75\,\mathrm{t\,h^{-1}}$ (blue to dark blue markers) rarely participate in clusters.

Recognizing this relationship is essential to understand the effect that a modification of the correlation-shift threshold would have. For instance, applying a slightly more relaxed cutoff using the 94th percentile (i.e. -0.158) of the prior anti-correlation distribution would lead to exactly two additional cluster links, both of which have substantial implications:

The first additional cluster link would be between **Budryk V** and **Wesola A**. As was previously observed for the Czech shafts (see Table 4.7), such pairwise links can quickly propagate into a continuous chain of anti-correlations. In this case, the coupling would trigger a cascade, merging **Budryk V** and **Wesola A** into a broader sequence of adjacent shafts spanning large parts of the green and red clusters (see Fig. 4.14b). However, this aggregation would negate the clearly distinguishable double-plume structure evident in both the simulation and the measurements (see Sect. 4.3.1 and Fig. 4.9). Consequently, the distinct peaks associated with the two subregions could no longer be scaled independently, which would undermine the physical interpretability of the posterior estimates. The purpose of clustering in the first place was to combine indistinguishable shafts based on their observational constraints. Since this is not the case here, clustering **Budryk V** and **Wesola A** would be too restrictive. The observational data clearly provide sufficient leverage to constrain them separately. Although some residual anti-correlation persists, it does not reach a level of ambiguity that would necessitate their aggregation. More generally, this example illustrates that the degree of ambiguity introduced by shared observational constraints spans a continuous spectrum. Accordingly, the resulting correlation shifts do not indicate binary separability, but rather a gradual transition. Therefore, choosing an appropriate threshold ultimately becomes a matter of balancing separation and robustness.

The second additional cluster connection would link **Bielszowice II** (50.28°N, 18.82°E) with **Mysłowice A** (50.22°N, 19.12°E). These sources are located along a common wind path, several kilometres apart, with multiple low-emission shafts situated between them. As discussed earlier, these smaller sources remain unclustered because their small prior uncertainty suppresses posterior updates, leaving their ensemble deviations largely unchanged and thus decoupled from the surrounding state vector elements. However, this does not mean that these small sources are unaffected by shared observations. Rather, the inversion primarily compensates for the resulting residuals through the more flexible, higher-emission sources (i.e. **Mysłowice A** and **Bielszowice II**). This reflects a mathematical preference for adjusting sources where penalty in the cost function is smaller, instead of an actual physical attribution of the observed signal. Consequently, the cumulative influence of the smaller shafts is not properly acknowledged in the posterior, despite their potential contribution to the observed enhancements.

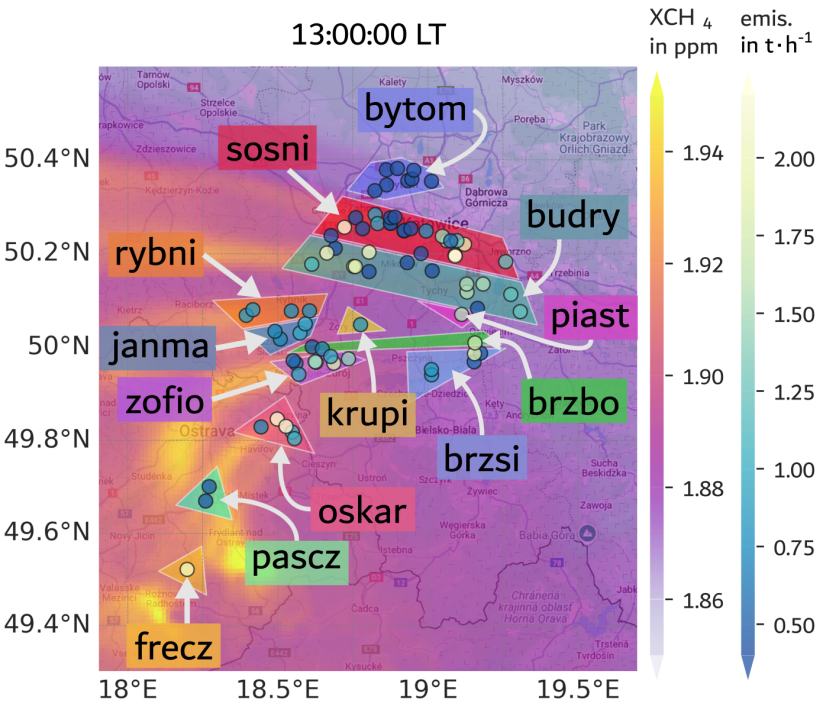

Figure 4.15: This method is based on the automated clustering shown in Fig. 4.14, but additionally comprises low-emission sources that were manually assigned to nearby clusters based on wind direction and observational geometry. The resulting cluster assignments are used in the best-estimate inversion and all sensitivity analyses.

Together, these two examples illustrate a central insight: the absence of a cluster does not guarantee physical separability, and the potential formation of a cluster does not necessarily require aggregation. Instead, both outcomes reflect the mathematical structure imposed by the inversion and must be interpreted in light of the physical context and observational constraints. Selecting the 95th percentile as a threshold resulted from iterative trial and error process. It began with a very strict criterion, requiring correlation shifts to exceed all values found in the prior anti-correlation distribution. This led to minimal clustering. The threshold was gradually relaxed until lowering it to the 94th percentile was found to be too restrictive, as demonstrated above. The 95th percentile of the prior anti-correlation distribution (i.e. -0.16) was therefore found to provide a reasonable trade-off. It avoids overly extensive clustering, while still capturing the dominant anti-correlating structure among the major sources.

This threshold, however, is not a generic solution. It worked well under the specific conditions of this case study, including the prevailing wind direction, source distribution, flight trajectory, and model transport characteristics. Notably, the threshold value itself is, in principle, independent of meteorological conditions; different wind fields would alter the correlation structure and thus which sources appear indistinguishable, but the same numerical threshold should remain valid as a criterion for clustering. However, its broader applicability remains untested.

Establishing a generally valid threshold for automated clustering based on posterior correlation shifts would require evaluating a large number of measurement days under different meteorological and observational conditions, which is beyond the scope of this work.

Nonetheless, the correlation-shift method itself is a very useful diagnostic tool for identifying significant anti-correlating structures in the posterior correlation matrix. It indicates which source groupings are mathematically supported by the inversion and highlights where observational constraints are strongly entangled. However, this approach inherently overlooks many smaller sources whose posterior estimates remain close to their prior because they are less responsive to updates.

To better capture the cumulative influence of minor emission sources — and to acknowledge that these sources cannot be treated as fully independent — they were manually aggregated into larger clusters for the best-estimate inversion run. This clustering approach builds upon the automated posterior correlation analysis, but additionally incorporates smaller shafts based on spatial proximity and plume alignment. The resulting configuration reduces the number of state vector elements to be optimized to 15, consisting of: 13 aggregated source clusters, 1 background flux term, and 1 offset parameter. The source clusters are displayed on the map in Fig. 4.15, with the colour indicating the aggregated state vector element to which each polygon is assigned. In the Appendix' Table A.2 provides a complete list of which individual emission sources are aggregated in which cluster, including an explanation of the clusters' naming.

4.4 Final Results & Discussion

This section presents the results of the best-estimate inversion run based on the clustered source configuration introduced in Sect. 4.3.2. The optimized emission estimates are evaluated with respect to their posterior uncertainty and the influence of observational coverage and transport conditions. In addition, several targeted sensitivity runs are analysed to assess the robustness of the inversion results under varying assumptions. Finally, a consolidated total emission estimate for the USCB region is derived and compared to values reported in previous studies and emission inventories.

4.4.1 Best-Estimate Inversion

The resulting prior and posterior emission distributions from the best-estimate inversion are shown for each cluster in Fig. 4.16. The respective violin plots are based on the $N = 150$ ensemble members (see Sect. 4.2.1). The prior uncertainty was set to 100 % (as discussed in Sect. 4.2.1), but small deviations in the 1-σ width reflect sampling variability due to the finite ensemble size. Table 4.9 lists the ensemble means, standard deviations, and uncertainty reductions for each source cluster.

As described in Sect. 4.2, the emission rate ensemble is obtained by multiplying the state vector ensemble with the prior emission vector, i.e. $\mathbf{q} = \mathbf{q}_\mathrm{p}\mathbf{x}$. This relation only applies to the emission-related elements of $\mathbf{x}$, i.e. the 13 aggregated source

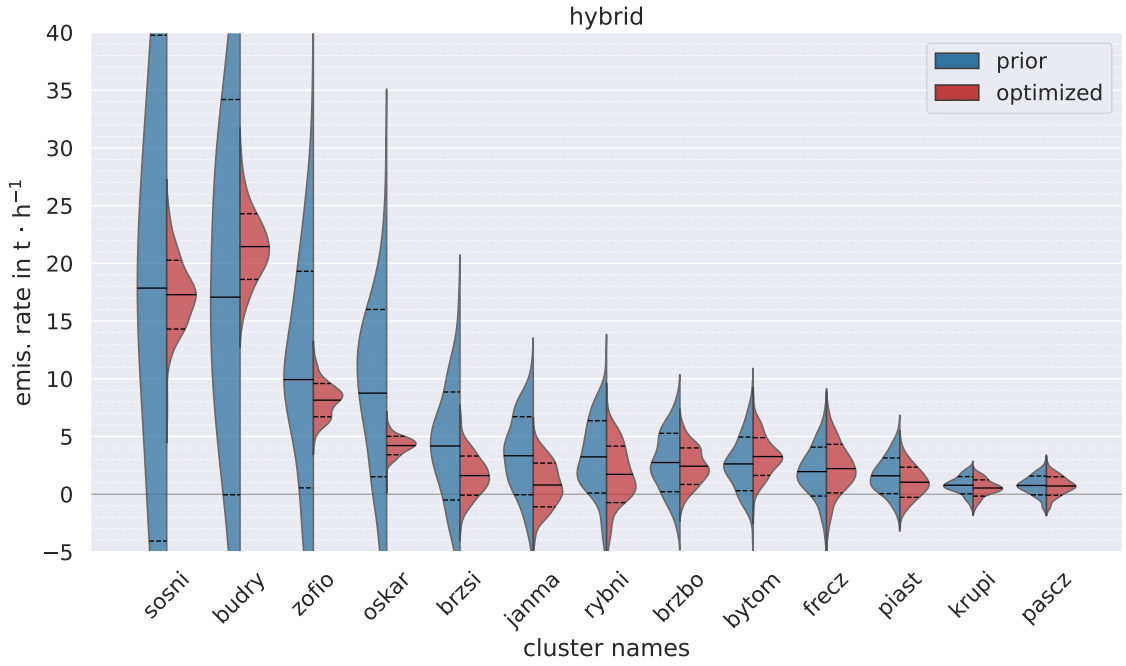

Figure 4.16: Prior (blue) and optimized (red) emission distributions for each source cluster from the best-estimate inversion run. Each violin plot visualizes the probability density function (PDF) spanned by the $N = 150$ ensemble members evaluated for each state vector element. Solid horizontal lines mark the ensemble mean, while dashed lines indicate the ensemble standard deviation. The range of the y-axis was deliberately chosen so that the prior violin diagrams would be truncated for clusters with high emissions, allowing the posterior distributions to be seen more clearly.

clusters and the background fluxes. It does not include the offset parameter. In the best-estimate inversion run, this offset converges to −57 ppb, which is slightly lower than the −51 ppb value found for the initial inversion (Sect. 4.3.1). This difference is primarily due to the exclusion of the biased far-field legs (discussed in Sect. 4.3.1), which would otherwise have pulled the background baseline to higher values.

All clusters exhibit a posterior adjustment, confirming the behaviour noted previously in Sect. 4.3.2. Clusters with smaller total emissions are less prone to updates by the inversion. This is a direct consequence of their proportionally smaller absolute uncertainties, which reduce their flexibility during optimization. Consequently, uncertainty reduction tends to be greater for high-emission clusters, whereas smaller clusters remain closer to their prior. The same applies to the background fluxes. While not negligible in total, their signal is spatially diffuse and comparatively weak in the observations. As a result, they remain effectively unchanged, with a scaling factor of 1.0 and no meaningful uncertainty reduction.

From all clusters the smallest uncertainty reductions are observed for **frecz** and **pascz**, at only 0.7 % and 2.2 %, respectively. This is not surprising, given that both far-field legs were flagged and excluded from the inversion, such that no observational data were left downwind of these shafts to constrain their emissions. Accordingly,

Table 4.9: Prior and posterior emission estimates for each cluster from the best-estimate inversion run (equivalent to the PDFs in Fig. 4.16). Prior and optimized values denote the ensemble mean. Note: The uncertainty values reported here correspond to the standard deviation of the posterior ensemble distribution ($N = 150$). They do not represent the final consolidated uncertainty. For a comprehensive uncertainty assessment that includes contributions from sensitivity tests, refer to Table 4.10. Emission rates in $\mathrm{t\,h^{-1}}$.

Cluster	Prior emis. rate	Scaling factor	Optimized emis. rate	Uncertainty reduction
sosni	19.6 ± 21.9	0.89	17.5 ± 3.0	86.4 %
budry	16.8 ± 17.1	1.27	21.3 ± 2.8	83.4 %
zofio	9.6 ± 9.4	0.84	8.1 ± 1.4	84.7 %
oskar	8.1 ± 7.2	0.51	4.1 ± 0.8	89.0 %
brzsi	4.5 ± 4.7	0.40	1.8 ± 1.7	63.8 %
janma	3.3 ± 3.4	0.24	0.8 ± 1.9	44.0 %
rybni	3.2 ± 3.1	0.53	1.7 ± 2.4	21.9 %
bytom	2.3 ± 2.3	1.30	3.0 ± 1.6	29.6 %
frecz	2.0 ± 2.1	1.15	2.3 ± 2.1	0.7 %
brzbo	2.5 ± 2.5	0.88	2.2 ± 1.6	37.6 %
piast	1.5 ± 1.5	0.67	1.0 ± 1.3	15.4 %
krupi	0.8 ± 0.7	0.75	0.6 ± 0.7	5.9 %
pascz	0.8 ± 0.8	1.00	0.8 ± 0.8	2.2 %

the inversion system is unable to meaningfully update the corresponding state vector elements, which therefore remain effectively tied to their prior values. However, a closer inspection of Table 4.9 reveals that the uncertainty reductions, despite being small, are not exactly zero. This suggests that spurious updates can occur within the ensemble system, even when there are no direct observational constraints. These should be therefore interpreted as statistical noise and not as meaningful posterior adjustments.

The greatest reduction in uncertainty is observed for the cluster **oskar** (Czech shafts between the cities Ostrava and Karviná), reaching 89.0 %. This is hardly surprising, as this region was densely sampled and the observed enhancement was intersected multiple times across different segments of the CH_4 accumulation, rather than merely being overflown perpendicular to its extent, as discussed in Sect. 4.3.1 and 4.3.2 (see e.g. Fig. 4.13). This accumulation had formed earlier under stagnant wind conditions and was subsequently advected as a coherent structure once the wind picked up. The flight path happened to align with the elongated axis of this advected enhancement, enabling a dense series of data points to be obtained within the plume core. Each observation sensitive to a given source contributes an update to the associated state vector element, which typically leads to a narrowing of the posterior ensemble distribution (Eq. 4.6). The greater the number of data points available to constrain a particular source, the greater the resulting uncertainty reduction — modulated, of course, by the observational error covariance.

However, in the specific case of the **oskar** cluster, the high posterior certainty

should be interpreted with caution. In this case, the dense observational coverage was not the result of a deliberate sampling strategy, but rather due to stagnant wind conditions before the flight, resulting in the coherent advection of accumulated CH_4 (as discussed before in Sect. 4.3.2). Such accumulation events are notoriously difficult to simulate for ATMs, particularly with regard to timing and spatial localization.

The simulation suggests that the flight track intersected the centre of the advected plume, where CH_4 concentrations are highest. However, there is no way to confirm whether this was the case in reality. If the actual accumulation was laterally displaced, the aircraft may have crossed its edge instead, resulting in a weaker signal observed. In that case, the inversion would incorrectly scale emissions to lower values. Alternatively, the simulated plume position may be accurate, and the observed signal may genuinely reflect lower emissions. While this situation would lead to an underestimation, the reverse effect is also possible in principle, namely that the simulation misses the plume centre while the aircraft crosses it in reality, in which case the inversion may overestimate emissions. Because such ambiguity cannot be resolved with the available information, the apparent posterior certainty must be interpreted with caution. The strong reduction in ensemble spread reflects internal consistency within the inversion system, but it does not account for potential systematic transport errors and should not be mistaken for accuracy.

Although the posterior covariance matrix provides a formal estimate of the uncertainty in the optimized emissions, it does not fully capture the robustness of the results. A key limitation is that the posterior uncertainty depends directly on the user-defined prior uncertainty. In this study, as no reliable source-specific uncertainty estimates were available, a relative standard deviation of 100 % was uniformly assigned to all sources. While this is a conservative assumption, it is still a subjective assumption that has considerable influence on the posterior spread.

In addition to prior uncertainty, the model-data mismatch term also influences the posterior uncertainty. While this term formally accounts for instrument precision, its dominant contribution comes from a large representation error. This inflation compensates for discrepancies in the geometry of high-resolution measurements and the coarser model grid. As described in Sect. 4.2.1, it also accounts for what can realistically be expected from the transport model in representing spatial plume features. However, this term primarily addresses random errors. Systematic transport errors, which may cause biased emission estimates, are not captured in the inversion and not reflected in the Bayesian uncertainty reduction. A more precise quantification of model-data mismatch would require a systematic performance assessment across a wide range of meteorological scenarios, which is beyond the scope of this study.

4.4.2 Sensitivity Analysis

Assessing the robustness of inversion results is of central importance, since posterior uncertainties derived from the Bayesian framework alone do not fully capture potential model errors. In principle, a comprehensive error assessment could involve multiple ensemble simulations with varied initial states or even comparisons across different

transport models. Such approaches, however, are computationally very demanding.

To provide a pragmatic first estimate, this study conducts a small number of targeted sensitivity runs. As introduced in Sect. 4.2.1, one set of tests evaluates the influence of initial vertical emission placement. To this end, the best-estimate inversion was repeated with emissions injected into higher vertical layers. In addition to the best-estimate's default configuration (injection into level $k = 1$[2], i.e. 20 – 45 m), two additional runs were performed with emissions placed into levels $k = 2$ (45 – 72 m) and $k = 3$ (72 – 104 m), respectively. These levels represent plausible variations in initial vertical mixing within the planetary boundary layer.

As discussed above, the optimized simulation applies an additive offset of 0.057 ppm to the prior simulation. While this correction aligns the overall baseline with the measurement average, systematic spatial discrepancies remain. Figure 4.17a shows the time series of observed and optimized XCH_4, with shaded regions indicating flight segments that sampled background concentrations. Based on the residual structure, three distinct types of background conditions can be identified: segments with consistently positive residuals (orange), negative residuals (purple), and segments with neutral or balanced residuals (gray/white).

Small shifts in the background baseline can directly influence the apparent amplitude of all plumes' enhancements. If the baseline is higher, the enhancement decreases and the inferred emission rate is smaller; if the baseline is lower, the opposite occurs. To assess this effect, I conducted three sensitivity runs, each retaining only one residual regime as background constraint while excluding the others. Because each plume measurement also carries implicit background information, the background residuals are not reduced to zero in any of these runs. Nevertheless, the comparison provides a reasonable estimate of how regional background biases can influence the inversion outcome. It also shows how the inversion outcome would respond if certain segments of background data were missing.

For each group of sensitivity runs, the deviation of the estimated total emission $\mathbf{q}_\mathrm{a}$ from the best-estimate $\mathbf{q}_\mathrm{a}^\mathrm{best}$ was evaluated. These deviations were weighted by their respective posterior standard deviation $\boldsymbol{\sigma}_\mathrm{a}$ of each run. The resulting metric represents the mean squared deviation normalized by the ensemble uncertainty:

$$\boldsymbol{\delta}_j^2 = \frac{\sum_s \left(\frac{\mathbf{q}_\mathrm{a}^s - \mathbf{q}_\mathrm{a}^\mathrm{best}}{\boldsymbol{\sigma}_\mathrm{a}^s}\right)^2}{\sum_s \frac{1}{\boldsymbol{\sigma}_\mathrm{a}^s}^2} \quad \text{with} \quad s \in \mathcal{S}_j, \tag{4.8}$$

where $\mathcal{S}_j$ denotes the set of inversion runs within sensitivity experiment group j. In this study, two such groups were defined: one probing the impact of vertical emission placement ($\mathcal{S}_k$), and one assessing sensitivity to background residual regimes ($\mathcal{S}_b$). Each contribution $\boldsymbol{\delta}_j^2$ is calculated independently and added in quadrature to the inversion's Bayesian posterior standard deviation $\boldsymbol{\sigma}_\mathrm{a}$ to derive a consolidated uncertainty estimate.

$$\boldsymbol{\sigma}_\mathrm{best} = \sqrt{\boldsymbol{\sigma}_\mathrm{a}^2 + \boldsymbol{\delta}_k^2 + \boldsymbol{\delta}_b^2} \tag{4.9}$$

[2]Note that the vertical level indexing in WRF starts from $k = 0$ as the surface layer.

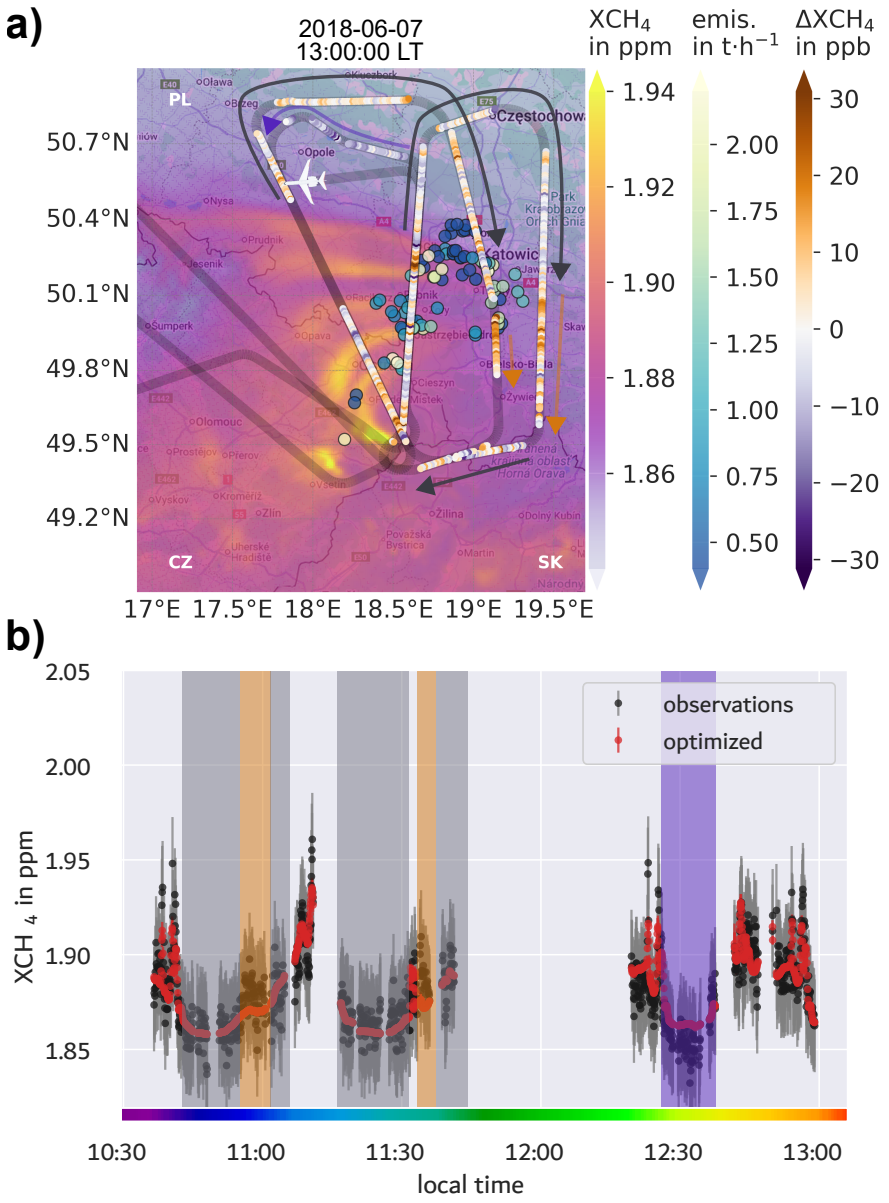

Figure 4.17: Panel (a) shows the flight track overlaid on the prior plume output (13:00–13:05) from the best-estimate inversion run. The coloured points along the flight path represent the residuals between observations and optimized model output ($\Delta XCH_4 = \mathbf{y} - \mathbf{Hx}_a$). Orange segments indicate positive residuals (observations exceed the model), while purple segments denote negative residuals (model exceeds observations). Panel (b) displays the full time series of observed (black) and optimized (red) XCH_4 mole fractions, with shaded regions highlighting background segments categorized by residual regime. Each background regime is also marked by a corresponding coloured arrow in panel (a). In the background sensitivity runs, only one residual regime (orange, purple, or gray) was retained at a time, while the others were excluded from the background constraint. The remaining (unshaded) portions of the time series correspond to plume-influenced segments and were preserved in all runs.

Outcome of Sensitivity Runs

Figure 4.18 displays the total USCB emissions retrieved from each individual sensitivity run, together with their respective posterior uncertainties. The best estimate is shown in red, together with its consolidated uncertainty (Eq. 4.9). All vertical injection scenarios ($k = 1$, $k = 2$, $k = 3$) yield nearly identical emission estimates and posterior spreads. In contrast, the background sensitivity runs (neutral/positive/negative residual regimes) introduce larger variability, particularly in total emission magnitude. This is consistent with the quantitative breakdown of uncertainty contributions, given in the bottom row of Table 4.10. Of the total consolidated uncertainty of $8.9\,\mathrm{t\,h^{-1}}$, a share of 55.8 % originates from the posterior covariance matrix of the best-estimate inversion ($\boldsymbol{\sigma}_\mathrm{a}$). The background sensitivity ($\boldsymbol{\delta}_b$) accounts for 44.0 %, whereas the effect of vertical injection height is negligible at only 0.2 % ($\boldsymbol{\delta}_k$).

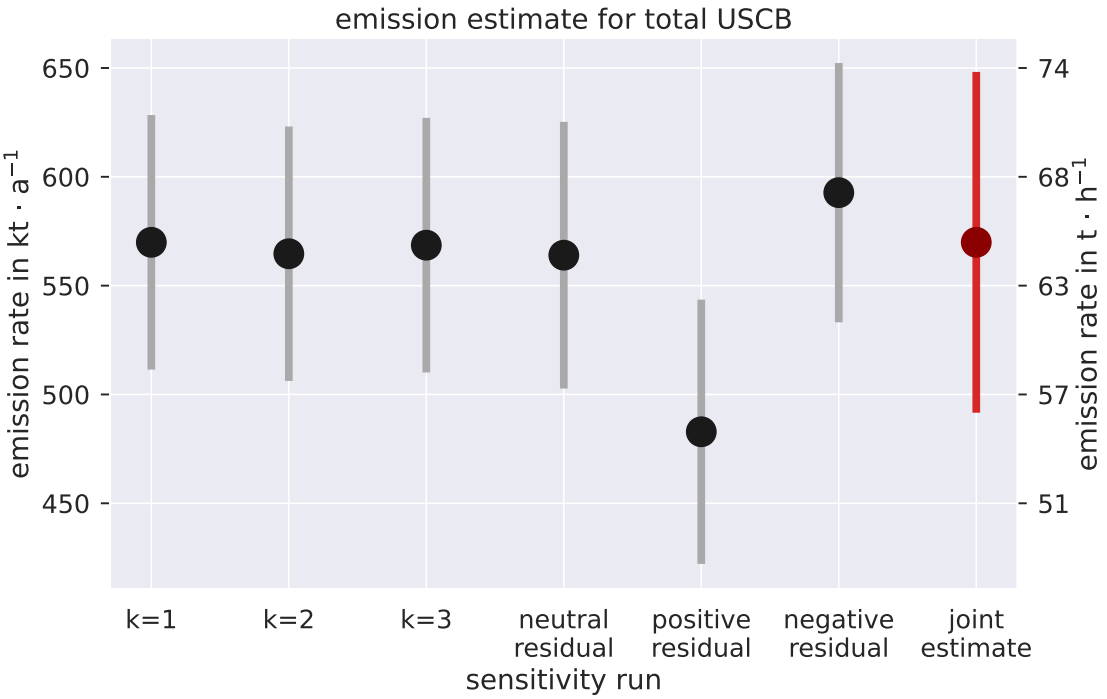

Figure 4.18: Total USCB emissions retrieved from each individual sensitivity run. The associated error bars indicate the Bayesian posterior covariance derived from the ensemble. The final bar in red shows the consolidated best estimate of $65.1 \pm 8.9\,\mathrm{t\,h^{-1}}$, which retains the same emission value as the $k = 1$ run but with an inflated uncertainty that accounts for all tested sensitivities (see Eq. 4.8 and Eq. 4.9).

Table 4.10 shows that the relative uncertainty contribution of each sensitivity analysis varies considerably between the individual clusters. For all clusters except **oskar**, the uncertainty contribution from variation in vertical injection height remains below 1 %. This low sensitivity is related to the nature of most observed plumes, which exhibit more stable plume propagation and are less susceptible to small changes in initial conditions. In contrast, the simulation of the CH_4 accumulation attributed

Table 4.10: Prior and consolidated posterior emission estimates for each cluster from the best-estimate inversion run. The prior values are identical to those in Table 4.9 and represent the ensemble mean and standard deviation of the $N = 150$ members. The optimized values shown here correspond to the best-estimate, but with their uncertainty inflated by the variations from all sensitivity runs (Eq. 4.9). The last three columns indicate the relative contributions of each uncertainty component to the total variance $\boldsymbol{\sigma}^2_{\text{best}}$. The share of the inversion's Bayesian posterior variance is denoted by $\boldsymbol{\sigma}^2_{\text{a}}/\boldsymbol{\sigma}^2_{\text{best}}$, the contribution from sensitivity to vertical emission placement by $\boldsymbol{\delta}^2_k/\boldsymbol{\sigma}^2_{\text{best}}$, and the impact of variations in background residual regimes by $\boldsymbol{\delta}^2_b/\boldsymbol{\sigma}^2_{\text{best}}$. Emission rates in $\mathrm{t\,h^{-1}}$.

Cluster	Prior emis. rate	Optimized emis. rate	Uncert. reduct.	$\boldsymbol{\sigma}^2_{\text{a}}/\boldsymbol{\sigma}^2_{\text{best}}$	$\boldsymbol{\delta}^2_k/\boldsymbol{\sigma}^2_{\text{best}}$	$\boldsymbol{\delta}^2_b/\boldsymbol{\sigma}^2_{\text{best}}$
sosni	19.6 ± 21.9	17.5 ± 3.5	84.0 %	72.9 %	0.1 %	27.0 %
budry	16.8 ± 17.1	21.3 ± 3.2	81.3 %	76.6 %	0.1 %	23.3 %
zofio	9.6 ± 9.4	8.1 ± 2.2	76.6 %	41.6 %	0.0 %	58.4 %
oskar	8.1 ± 7.2	4.1 ± 1.0	86.1 %	67.8 %	18.2 %	14.0 %
brzsi	4.5 ± 4.7	1.8 ± 2.0	57.4 %	69.3 %	0.4 %	30.3 %
janma	3.3 ± 3.4	0.8 ± 1.9	44.1 %	94.6 %	0.0 %	5.4 %
rybni	3.2 ± 3.1	1.7 ± 2.5	19.4 %	99.5 %	0.0 %	0.5 %
bytom	2.3 ± 2.3	3.0 ± 1.7	26.1 %	89.7 %	0.0 %	10.3 %
frecz	2.0 ± 2.1	2.3 ± 2.1	0.0 %	99.7 %	0.0 %	0.3 %
brzbo	2.5 ± 2.5	2.2 ± 1.6	36.0 %	94.0 %	0.1 %	5.9 %
piast	1.5 ± 1.5	1.0 ± 1.3	13.3 %	95.1 %	0.0 %	4.9 %
krupi	0.8 ± 0.7	0.6 ± 0.7	0.0 %	97.8 %	0.0 %	2.2 %
pascz	0.8 ± 0.8	0.8 ± 0.8	0.0 %	93.7 %	0.7 %	5.6 %
Total	$\mathbf{75.0 \pm 31.3}$	$\mathbf{65.1 \pm 8.9}$	**71.4 %**	**55.8 %**	**0.2 %**	**44.0 %**

to **oskar** is highly sensitive to initial transport parameters, which explains the comparatively higher variation with different vertical injection heights.

The limited impact of vertical injection height reflects the fact that the tested perturbations, which were based on vertical extent and plume rise observed in hyperspectral images (Knapp et al. 2023), introduced only minor variations in the simulated plume propagation. Within this observationally plausible range, the inversion results were largely insensitive to vertical emission placement.

However, this finding should not be interpreted as evidence that transport errors are negligible overall. Other model parameters, such as planetary boundary layer schemes, turbulence and surface layer options, may introduce more substantial differences in simulated transport.

While the sensitivity to vertical emission height is almost negligible, the influence of background variability is more pronounced. The clearest example of this is the cluster **zofio**, where background-related uncertainty even exceeds the Bayesian posterior uncertainty (see Table 4.10). This result is not a surprising results, given that **zofio** is directly downwind of the positive-residual background regime (cf. Fig. 4.15 and Fig. 4.17). Including or excluding of background data in this region directly affects

the optimized value for this cluster. Moreover, **zofio** is the third-largest emitter in the domain, which gives the inversion more freedom to adjust its emission strength. Nearby clusters, such as **brzsi** and **brzbo**, exhibit smaller adjustments and are less sensitive to background variations. This limited responsiveness reflects a broader tendency: clusters with lower prior emissions generally undergo less posterior change and therefore show reduced responsiveness in the sensitivity analysis.

This tendency is particularly evident among the weakest emitters. In clusters with low prior emissions, the inversion remains close to the initial estimates, regardless of background or transport variations. Consequently, the final uncertainty is dominated by the Bayesian posterior spread. For all clusters with a prior standard deviation below $3.4\,\mathrm{t\,h^{-1}}$, the Bayesian posterior uncertainty contributes at least 89 % of the total uncertainty.

4.4.3 Total Emission Estimate

The bottom row of Table 4.10 provides the consolidated emission estimate for the entire USCB, amounting to $65.1 \pm 8.9\ \mathrm{t\,h^{-1}}$. This equates to $570 \pm 78\ \mathrm{kt\,a^{-1}}$ when extrapolated to one year. Figure 4.19 shows a comparison of this value to those from other studies. Several findings emerge from this comparison.

Notably, the difference between the CoMet ED and the prior estimate is substantial: $23.6\,\mathrm{t\,h^{-1}}$ ($207\,\mathrm{kt\,a^{-1}}$). This offset reflects emissions from non-reporting shafts. These include all Czech shafts aggregated in the clusters **oskar**, **frecz**, and **pascz**, as well as additional non-reporting Polish shafts, including the entire cluster **bytom** as well as eastern parts of the **budry** cluster.

The prior assumptions for **oskar** were certainly generous, as presented in Appendix B.4 and confirmed by the downscaled posterior value of $4.1 \pm 1.0\ \mathrm{t\,h^{-1}}$ (reduction of 51 % compared to the prior). Nevertheless, the cluster emits significant amounts of CH_4 that were not captured by the reporting. No clear conclusions can be drawn for **frecz** and **pascz**, as the a posteriori uncertainty remains unchanged at 100 % due to a lack of downwind observations. Zero emissions are therefore still possible, but not confirmed. The situation is different for the northernmost Polish cluster, **bytom**. It only contains non-reporting shafts, but has a posterior estimate of $3.0 \pm 1.7\ \mathrm{t\,h^{-1}}$.

The two red bars in Fig. 4.19 represent the total posterior emissions retrieved from the initial and best-estimate inversion runs, respectively. The difference between these two inversions amounts to $14.3\,\mathrm{t\,h^{-1}}$, underscoring the cumulative impact of the methodological adjustments introduced after the initial run. These include the exclusion of segments with known transport mismatches (Sect. 4.3.1), particularly the far-field legs where the model failed to reproduce the observed plume signals (Sect. 4.3.1), and the implementation of source clustering based on inversion-driven correlation shifts (Sect. 4.3.2), which was developed in this thesis. Both adjustments addressed structural weaknesses of the initial setup, which had resulted in a biased posterior offset and unphysical negative scaling factors. Their removal leads to a higher and more robust total emission estimate in the best-estimate run.

Overall, the best-estimate result exceeds the values reported by E-PRTR and

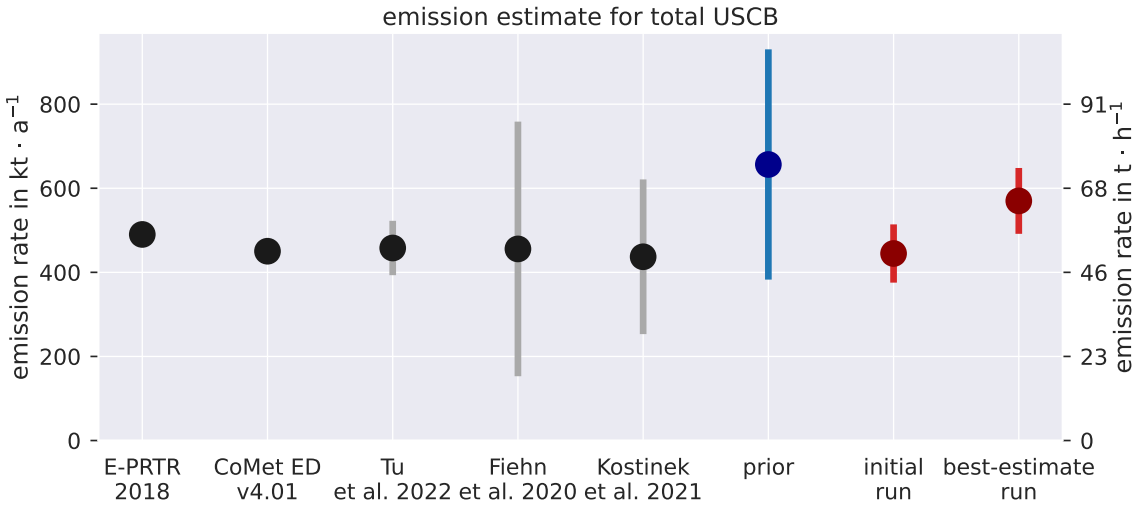

Figure 4.19: Comparison of total USCB CH_4 emissions from this study with inventory data and previous studies. Black dots indicate reported or previously published estimates. Values without error bars (e.g. E-PRTR, CoMet ED) do not include published uncertainty estimates. The blue bar denotes the prior estimate used in the inversion. Red bars show the total posterior emission estimates retrieved from the initial (Sect. 4.3.1) and best-estimate inversion runs (Sect. 4.4.1), respectively. Emission rates are expressed both in $\mathrm{kt\,a^{-1}}$ (left axis) and $\mathrm{t\,h^{-1}}$ (right axis).

CoMet ED by approximately 16 % and 27 %, respectively. Another factor contributing to this discrepancy is the temporal mismatch. Inventories report annual averages, whereas the inversion is based on observations from a single day. The extent to which daily emissions deviate from long-term averages remains uncertain. The same limitation applies to the estimate by Tu et al. (2022b), who derive 458 ± 65 $\mathrm{kt\,a^{-1}}$ using three years of satellite data from TROPOMI. Their comparatively narrow uncertainty range reflects the long averaging period.

A more direct comparison is possible with the results of Fiehn et al. (2020) and Kostinek et al. (2021), who analysed airborne in situ measurements taken on the same day, 7 June 2018. Their flight track did not cover the clusters **frecz** and **pascz**. Excluding these two clusters — which in any case remain close to their prior values — leads to a slightly lower posterior estimate of 62.0 ± 7.1 $\mathrm{t\,h^{-1}}$. This result is within the range of uncertainty with both Fiehn et al. (2020), who report 52.0 ± 34.6 $\mathrm{t\,h^{-1}}$, and Kostinek et al. (2021), who obtain 49.9 ± 21.0 $\mathrm{t\,h^{-1}}$. The uncertainty reported by Fiehn et al. (2020) combines measurement and interpolation errors with systematic contributions from sensitivity tests of transport and background conditions, whereas Kostinek et al. (2021) derive their error bars from a combination of the statistical fit uncertainty and systematic variations obtained from an ensemble of sensitivity runs.

Taken together, the agreement with previous studies and the plausible deviations from inventory data lend confidence to the robustness of the inversion results presented here. While certain limitations remain, particularly with regard to unconstrained

clusters and potential transport errors, the methodology yields emission estimates that are demonstrably consistent with observation-based estimates. These findings form a reliable basis for the broader conclusions drawn in the following section.

4.5 Summary & Conclusion

Case Study II addresses research questions **RQ2** and **RQ3**. To answer these, the Upper Silesian Coal Basin (USCB) in southern Poland was selected as the study region (see Sect. 4.1). The region is Europe's most significant hotspot for CH_4 emissions from coal mining and contains a large number of point sources, some of which are located in close proximity to each other. On 7 June 2018, during the CoMet campaign, multiple flight legs were conducted over the area using the airborne IPDA lidar system CHARM–F, resulting in comprehensive spatial coverage of CH_4 column enhancements. This work presents the first successful integration of IPDA lidar observations into a Bayesian inversion with the CTDAS-WRF framework, applied at regional scale with individual optimization of each point source (Sect. 4.2).

In an initial inversion run (Sect. 4.3), I evaluated the overall model performance and the spatial consistency between simulated and observed XCH_4 enhancements. The simulation reproduced the main features of the observed plumes near the sources but revealed clear discrepancies at larger downwind distances. Two flight legs showed a systematic wind direction error that displaced the simulated plume in the same region, while other legs were affected by excessive dilution of the transported CH_4. To avoid unphysical posterior results, I excluded these affected data sections for the best-estimate inversion (Sect. 4.4).

After data selection, I used posterior covariance diagnostics to determine which emission sources could be distinguished by the available observations. To enhance robustness in areas with plume overlap, observationally entangled sources were aggregated, combining automated diagnostics with expert judgement on plume alignment and wind direction. The automated approach alone tends to overlook low-emission shafts that remain close to their prior because their small absolute uncertainties prevent significant inversion updates. I therefore reviewed the unclustered minor sources and manually merged them with neighbouring clusters whose plumes were aligned and physically connected. This combination of statistical diagnostics and expert knowledge ensured that weak but non-negligible emitters were properly accounted for and that the spatial attribution remained consistent with observed plume structures. This hybrid clustering approach formed the basis for the best-estimate configuration and resulted in 13 aggregated source clusters. The geographical distribution of the clusters is shown in Fig. 4.15, and the corresponding posterior emission distributions in Fig. 4.16 (see Sect. 4.4.1).

Two targeted sensitivity experiments, each consisting of three runs, complemented the CTDAS posterior covariance (Sect. 4.4.2). The first varied the assumed emission height in WRF to represent perturbations in the initial vertical mixing. The second altered the selection of background segments in the CHARM–F data to test the effect of varying observational availability. Thus, the consolidated uncertainty includes not only contributions from the inversion itself, but also perturbations in the simulated

transport and observational constraint.

The consolidated posterior emission rates obtained from these sensitivity analyses are listed in Table 4.10. From these results, the domain-wide total can be derived by summing all cluster emissions. The entire coal mining region of the USCB amounts to $65.1 \pm 8.9\ \mathrm{t\,h^{-1}}$, which is equivalent to $570 \pm 78\ \mathrm{kt\,a^{-1}}$ (Sect. 4.4.3). This value exceeds the officially reported emissions in the E-PRTR inventory by 16 %. Given that the inversion is based on only three hours of airborne observations while the inventory represents an annual mean, this deviation is relatively small. It may reflect a combination of temporal variance from the annual mean and inventory uncertainty. At the same time, this result falls well within the uncertainty ranges of independent studies based on satellite and in-situ data, further supporting the credibility of the approach (cf. Fig. 4.19).

In conclusion, **RQ2** can be answered in the affirmative. The combined use of airborne IPDA lidar and the CTDAS-WRF inversion framework successfully quantified and spatially attributed overlapping CH_4 signals from multiple nearby sources. The inversion-driven hybrid clustering provided the maximum achievable spatial separability under the given observational and meteorological constraints, by aggregating 74 individual shafts into 13 source clusters.

With regard to **RQ3**, the analysis showed that transport-related errors increase with downwind distance and can ultimately limit the accuracy of inverse estimates. While this study identified clear discrepancies beyond approximately 40 km, no universal limit can be defined. The maximum tolerable downwind distance varies from case to case and depends on a wide range of factors such as meteorological conditions, orography, emission rates, and background variability. The results further revealed that a higher density of in-plume data points leads to substantial uncertainty reduction through increased observational constraint of the inversion. Consequently, flight designs aligned with the expected plume axis or using zigzag patterns are preferable for inverse modelling, while purely cross-sectional overflights tend to provide fewer effective constraints.

5 From Case Studies to Spaceborne Applications

5.1 Thesis Summary and Outcomes

This thesis set out to assess how active remote sensing can quantify greenhouse gas emissions from point sources and how the design of measurements and the configuration of the inversion framework influence the resulting uncertainties. The work addressed three research questions:

- **RQ1:** How accurately can the cross-sectional flux method quantify CO_2 emissions from an isolated point source?
- **RQ2:** Can a combination of airborne IPDA lidar and inverse modelling be used to quantify and spatially attribute overlapping CH_4 signals from multiple sources?
- **RQ3:** Under which atmospheric conditions and flight geometries do uncertainties in IPDA-based emission quantification become most pronounced, and how can flight planning mitigate these effects?

In **Case Study I**, I successfully applied the cross-sectional flux method to IPDA lidar data to determine CO_2 emissions from an isolated point source: the Jänschwalde coal-fired power plant. The estimated emission rate is consistent with the officially reported annual emissions, with an average of 20.3 ± 7.9 Mt a^{-1} over four instantaneous flux measurements. Limitations arise from atmospheric turbulence, which distorts the exhaust plume and causes strong variability in the instantaneous flux. These fluctuations dominate the overall uncertainty and exceed the combined measurement errors from instrument precision, spectroscopy, and wind data. In other words, while the measurement error of a single flux estimate is comparatively small, turbulent variability drives the main discrepancy between instantaneous fluxes and the true emission rate. These findings answer **RQ1** in the affirmative and inform **RQ3**: the main limitation is turbulence, which favours night or early-morning flights and moderate downwind distances that preserve detectability.

In **Case Study II**, I achieved the first successful integration of airborne IPDA lidar observations into a Bayesian inversion at regional scale. The study region was

the Upper Silesian Coal Basin (USCB) with many closely spaced CH_4 sources. After conducting an initial run and selecting data to avoid sections with clear transport errors, I developed an inversion-driven hybrid clustering approach to achieve robust spatial attribution under plume overlap. This approach combined a correlation-shift diagnostic with a threshold based on the 95th percentile of the prior anti-correlation and an expert review that merged low-emission shafts aligned with larger plumes. This retained observationally supported separability while ensuring that weak but non-negligible emitters are properly accounted for. The final configuration aggregated 74 point sources into 13 emission clusters.

I complemented the posterior covariance by performing two targeted sensitivity experiments that perturbed the emission heights in the Atmospheric Transport Model and varied the background segments in the observation data. Together with the best-estimate inversion these analyses yielded consolidated posterior emissions and uncertainties for each cluster and for the domain total. The total USCB emission amounts to $65.1 \pm 8.9\ \mathrm{t\,h^{-1}}$, that is $570 \pm 78\ \mathrm{kt\,a^{-1}}$, which is 16 % above the E-PRTR inventory and consistent with independent studies. These results answer **RQ2**: airborne IPDA lidar combined with inverse modelling can quantify and spatially attribute overlapping CH_4 signals from multiple nearby sources, with the hybrid clustering delivering the maximum achievable separability under the given conditions.

Regarding **RQ3**, I found that transport errors increase with downwind distance and limit inverse estimates once modelled and observed plumes begin to diverge. In this study, significant discrepancies appeared at distances beyond approximately 40 km, but no universal threshold can be defined since meteorology, orography, emission strength, and background variability differ from case to case. The analysis also showed that a higher density of in-plume observations strengthens the observational constraint and reduces posterior uncertainty, which motivates flight legs aligned with the plume or zigzag patterns for inverse modelling, whereas purely cross-sectional transects provide fewer effective constraints.

Main contributions of this thesis are:

- I explicitly quantified the impact of turbulence on flux estimates and translated these findings into practical guidance for flight planning.

- I achieved the first integration of airborne IPDA lidar into a Bayesian inversion at regional scale and successfully applied it to a complex multi-source basin.

- I developed an inversion-driven hybrid clustering that combines a correlation-shift diagnostic and expert judgement to maximize spatial attribution, including low-emission sources that would otherwise be overlooked.

- I established a consolidated uncertainty estimation that combines posterior covariance with targeted sensitivity analysis in transport representation and background data availability, reported at cluster and domain scales.

5.2 Recommendations for Future Campaigns

The insights gained from the two case studies also offer practical guidance for future field campaigns targeted at quantifying GHG emissions. While the present work focuses on IPDA lidar, most of the findings are equally relevant for other measurement techniques. Some recommendations, however are more readily applicable to active remote sensing, where lidar provides a particular advantage. By identifying common sources of uncertainty, this work provides specific recommendations on how to avoid or minimize common pitfalls. Well-informed flight design can thereby improve the accuracy of flux estimates and increase the reliability of subsequent source attribution.

Accurate background estimation proved essential for both the cross-sectional flux method and inverse modelling. In **Case Study II**, persistent residuals after the inversion illustrated how sensitive the results are to background selection. A targeted sensitivity analysis (Sect. 4.4.2) confirmed that different background choices alone can alter the total USCB emission by up to 9 % (cf. Fig. 4.18). Therefore, to account not only for spatial but also for potential temporal changes in background concentrations, background regions should be surveyed both at the beginning and at the end of each flight pattern. This allows for the detection of temporal drifts and improves the reliability of offset constraints in the inversion.

When applying the cross-sectional flux method, redundancy in background sampling is helpful, though not as critical. Typically, a single upwind leg is sufficient to assess whether additional sources contribute to the inflow. Even under spatially inhomogeneous or temporally variable background conditions (as encountered in **Case Study II**), a robust emission estimate can be achieved by determining the background locally along the same flight leg. This is done by identifying the plume within the transect, removing it, and reconstructing the background across the plume by linear interpolation between the pre- and post-plume segments (see Sect. 3.1.1). This method requires the segments before and after the plume to be sufficiently long. In the present **Case Study I**, a length of approximately three to five times the plume width on each side proved sufficient. This corresponded to a minimum flight distance of 12 km. Since it is not always possible to predict the plume width when planning a flight, it is advised to select the transect length a little too long rather than too short.

For the cross-sectional flux method, the dominant source of uncertainty was the turbulence-induced variability of flux estimates between individual overflights. To minimize this effect without requiring a large number of repeated transects, measurements should ideally be carried out under low-turbulence conditions, preferably at night when plume propagation tends to be more stable.

This recommendation highlights a particular advantage of active remote sensing. Passive techniques require solar illumination and therefore cannot be applied at night. Airborne in situ instruments, in turn, may face difficulties in accessing the very shallow nocturnal boundary layer without flying uncomfortably close to the ground. By contrast, IPDA lidar can operate independently of sunlight and thus fully exploit the enhanced stability of nighttime conditions. A dedicated simulation has

shown that, under such favourable circumstances, a single lidar overflight can already outperform the precision obtained from ten averaged midday transects (Sect. 3.2.2).

Improving inverse modelling requires different strategies. One of the most effective measures is to increase the number of data points within the plume. This can be achieved by designing flight patterns along the plume rather than perpendicular to it. However, this requires precise wind forecasts. If the actual wind direction differs from the forecast, a leg that is nominally aligned with the wind may miss the plume entirely. Zigzag patterns offer a more robust alternative in this regard, as they increase the likelihood of intersecting the plume even under forecast errors.

Conversely, cross-sectional flights are limited by definition to the minimum number of in-plume measurements. This is disadvantageous for inverse modelling. On the other hand, plume-aligned flight legs do not permit the determination of integrated enhancements, rendering the cross-sectional flux method inapplicable. In terms of the cross-sectional flux method, zigzag patterns would increase the number of in-plume observations and, in principle, improve the estimation of integrated enhancements. However, this benefit is negated by another error component. Specifically, the relative uncertainty includes a term that depends on the angle φ between the flight direction and the wind direction, which enters the uncertainty term proportional to $\frac{\delta\varphi}{\tan(\varphi)}$. As φ approaches 0°, the error term diverges and dominates the total uncertainty, whereas near 90° it becomes negligible. For this reason, the flight in **Case Study I** was deliberately designed to be close to perpendicular to the wind, ensuring that the angular contribution remained minimal.

The two methods thus have incompatible ideal flight patterns, and compromising between their respective requirements tends not to be beneficial. Therefore, before planning the exact pattern, a clear decision should be made as to whether the flight is primarily intended for cross-sectional flux evaluation or inverse modelling. If both objectives are to be addressed, dedicated flight sections should be designed for each approach. Otherwise, there is a considerable risk that neither objective will be adequately fulfilled. This strategy may increase the total flight time but ensures methodological clarity and robustness.

Nonetheless, **Case Study II** demonstrated that inverse modelling is effective, even with a primarily cross-sectional flight design. The dominant source of error was not the flight geometry, but a systematic transport error in the model. Significant deviations between the model and the observations were found in flight legs located more than 40 km downwind of the source or farther. These were mainly due to excessive mixing and inaccurate wind directions in the simulation. Near the sources, however, the model performed adequately. In hindsight, it would have been more effective to fly additional legs within a range of 1 – 10 km rather than taking transects at distances greater than 40 km. However, the ideal downwind distance depends strongly on the respective meteorological situation. Further sensitivity studies under a variety of different meteorological conditions — ideally at different times of the year and day — would need to be carried out before a universally valid recommendation for the ideal downwind distance for inverse modelling can be made.

When it comes to the ideal time of day for measurements, **Case Study I** provides an important insight. As mentioned above, the plume structure is highly inhomogeneous under turbulent conditions at midday. In theory, such inhomogeneities would not pose a problem for inverse modelling if the simulation reproduced them accurately. In practice, however, this is rarely the case because turbulence and boundary-layer schemes cannot resolve the exact position and timing of individual puffs. Therefore, it is advantageous for inverse modelling to avoid highly turbulent conditions, which improves the representativeness of simulated transport.

With regard to inverse modelling, however, caution should be exercised before implementing nighttime flights as an turbulence-avoidance strategy. As explained in **Case Study I**, the nighttime boundary layer shrinks to just a few model levels. This could lead to poorer simulation of boundary layer processes such as vertical mixing. Whether the advantage of reduced turbulence outweighs the potential degradation of model quality is still to be proven. A possible compromise could be flights in the early morning, when atmospheric stability and vertical model resolution in the boundary layer are both acceptable.

In conclusion, future flight campaigns should define from the very start whether the primary analysis will be based on cross-sectional flux estimates or inverse modelling. This decision has important implications for flight geometry and observational coverage. Attempting to satisfy both methods with a single flight plan will degrade the effectiveness of both. Instead, future campaigns should either separate their measurement objectives or allocate sufficient flight time to execute multiple dedicated patterns per target.

5.3 Outlook

The findings of this thesis demonstrate that active remote sensing data can be robustly integrated into inversion frameworks — a methodological step that paves the way for exploiting upcoming satellite missions at global scale. Unlike episodic measurement campaign data, as used in this thesis, future spaceborne missions such as MERLIN will provide continuous and global coverage. This shifts the scientific focus from sporadic emission quantification to systematic emission monitoring, budgeting, and trend analysis on regional and global scales.

As MERLIN operates on a sun-synchronous orbit at a fixed inclination angle, it is not possible to adjust the transects to local wind directions. Therefore, the cross-sectional flux method can only be applied in cases where the wind direction is perpendicular to the orbit. Under ordinary observation conditions, MERLIN data will thus primarily be evaluated using inverse modelling. At the same time, MERLIN will fill critical observational gaps by providing data at high latitudes and during nighttime — precisely the regions and times where passive instruments are blind, but where important sources such as boreal wetlands and thawing permafrost contribute substantially to the global CH_4 budget.

A major technical challenge in evaluating satellite data lies in the large number of potential emission sources. In principle, each model grid cell could be treated as a separate state vector element. However, this would introduce a greater number of degrees of freedom, which could result in artefacts such as negative emission rates (cf. **Case Study II**) and is computationally expensive. A key strategy to mitigate this problem is to reduce dimensionality by clustering anti-correlated emission sources and optimizing them jointly. When such clustering is guided by the inversion itself — i.e. by meteorological transport and observation geometry — it retains the maximum possible information content in emission attribution. In contrast, conventional approaches based on administrative boundaries (e.g. states or districts) fail to achieve this level of detail.

The achievable spatial resolution of such inversions is ultimately limited by the observational constraint, which is defined by the along-track sampling within the atmospheric plume. These measurements integrate the signal over an area that typically exceeds the size of the emitting sources. For MERLIN, which offers an effective horizontal resolution of about 50 km, it would therefore not be meaningful to define state vector elements on a finer grid. This sets a practical lower limit for the spatial discretization of future inversions using MERLIN data.

Applying the approach developed in **Case Study II** — i.e. performing an initial inversion at maximum feasible resolution of 50×50 km^2 and subsequently deriving an optimized clustering — would still be impractical for routine large-scale applications. Repeated pre-inversions would remain computationally demanding and thus the associated computational effort would still contradict the goal of reducing computational costs.

Future work should therefore aim to evaluate clustering strategies under realistic conditions. Synthetic MERLIN datasets could be generated for representative synoptic weather situations, focusing on regions where a meaningful observational constraint can be expected at 50 km resolution and are of particular interest to the global CH_4 budget. In the anthropogenic sector, these regions include coal mining areas such as the USCB (roughly 100×100 km^2) or Shanxi in China, as well as oil and gas regions such as the Permian Basin or the Bakken Formation. For natural emissions, relevant target regions would include wetlands such as the Hudson Bay Lowlands, the Pantanal or the Congo Basin. Targeted inversion-based analyses of these synthetic case studies could investigate the effect of different clustering strategies on emission estimates and their uncertainties.

Another idea is to introduce an emission-weighted threshold for detecting correlation shifts. This builds on the observation from **Case Study II** that smaller sources were more insensitive to inversion updates than large emitters, making them less likely to be automatically flagged for clustering. In such a weighted approach, the correlation shift required for a source to be considered entangled would scale with its emission strength. This could improve the detection of relevant groupings, however it could be very sensitive to spurious correlations. Further studies are needed to assess the practicability of this method.

As an alternative to the correlation-shift approach, future studies could also explore significance testing using a Student's t-test. This method assesses whether

the posterior scaling factors of two emission sources differ significantly from each other in a statistical sense. If not, the two sources could be considered observationally indistinguishable and thus eligible for clustering. In contrast to heuristic thresholds, this test would explicitly account for ensemble spread and sample size.

The USCB remains an ideal testing ground for developing and validating new clustering and inversion methods. The region has high emission rates, a complex source distribution and topographical features, as well as reliable and verifiable inventory data. This combination enables realistic yet controllable test scenarios to be created.

In addition to numerical sensitivity analyses, the USCB is also suitable as a target region for future validation flights with aircraft-based systems such as CHARM–F. With suitable wind directions, especially when the wind is approximately perpendicular to the MERLIN orbit, emissions could also be detected and quantified simultaneously. The region thus offers the opportunity for direct comparative studies between satellite and aircraft measurements.

The next step in methodological development could be to repeat the analysis carried out in **Case Study II** under different prior assumptions. This would enable investigation into how the results change when coarse prior information, such as the EDGAR inventory, is used instead of the specific CoMet ED. As the exact location of the sources would be unknown in this case, the inversion would have to consider significantly more model grid cells as scalable elements, increasing the degrees of freedom and the uncertainties. Comparing the resulting emission distributions in terms of their spatial attribution and total magnitudes could provide valuable insights into the robustness and transferability of the developed methods.

On top of the CoMet 1.0 flights in Europe that have already been analysed, the CoMet 2.0 Arctic campaign in Canada in 2022 provides a comprehensive set of data that can be used in future analyses (comet2arctic.de, last access: 05.08.2025). The mission focused on natural and anthropogenic sources in Arctic-boreal regions and provided valuable measurement data on extensive CH_4 sources in permafrost areas and North American wetlands. The region around Lake Winnipeg and the Hudson Bay Lowlands was flown over several times, revealing measurable, albeit very weak, gradients in the CH_4 signal accumulating along the wind direction. Detecting these signals is at the limit of what current instruments can achieve, making inverse modelling in such regions particularly challenging.

At the same time, anthropogenic emission sources were also surveyed as part of CoMet 2.0, including the Athabasca Oil Sands, petrochemical plants near Fort McMurray, power plants west of Edmonton, and oil and gas production facilities in the Lloydminster area. These Canadian oil and gas facilities are extremely numerous, with dense local groupings spread across a wide area, so that their aggregate signal resembles a mix between point and area sources. On several occasions, industrial exhaust plumes overlapped with CH_4 emissions from forest fires, which both complicated source attribution and added a relevant contribution to the global CH_4 budget.

With CoMet 3.0 Tropics, another mission is planned for 2026, focusing on tropical regions of Brazil. The campaign targets the extensive wetlands of the Pantanal and the southern Amazon basin, where CH_4 emissions are generally weak and spatially diffuse. Unlike point sources, these signals accumulate gradually over large distances and are often hard to detect as distinct enhancements. The region is marked by frequent cloud cover and highly dynamic meteorological conditions, which complicate airborne measurements. Natural wetland emissions are also superimposed by anthropogenic sources from agriculture, fossil fuel use, and biomass burning, making source attribution particularly challenging. Nevertheless, the mission offers a valuable opportunity to refine retrieval techniques under these conditions and contribute to the validation of current satellite missions.

Taken together, the European, Canadian, and Brazilian datasets trace a logical progression in complexity — from isolated point sources under favourable conditions, to widespread oil and gas facilities mixed with wildfires and wetlands, to tropical regions with diffuse natural emissions and frequent cloud cover. Each step builds on the previous one and helps prepare methodologies for increasingly challenging environments.

In this sequence, the launch of MERLIN, currently scheduled for 2030, marks the decisive step from regional campaigns to systematic, global monitoring. For the first time, active remote sensing data will be publicly available worldwide and continuously. Building on the concepts and tools developed in this work, the scientific community will then be in a position to fully exploit this new data stream and take a major step towards closing the global CH_4 budget.

A Supplement

A.1 Calculation of Simulated DAOD

At the initialization position of the power plant, the value of the tracer variable tr is increased by the value 1 at each time step. In this study, it is defined only in the inner domain D3.

$$\mathrm{tr}(t + \Delta t, x, y, z) = \mathrm{tr}(t, x, y, z) + 1 \tag{A.1}$$

Here, Δt corresponds to the computational time step of the third domain D3 (i.e. 1 s, see Table 3.3). At the same time the tracer is distributed in the domain D3 by advection and turbulent dispersion. The corresponding mass concentration $c(t, x, y, z)$ at any grid point x, y, z at time t is obtained as follows:

$$c(t, x, y, z) = \mathrm{tr}(t, x, y, z) \cdot \frac{q_{\mathrm{in}} \cdot \Delta t}{\Delta x \cdot \Delta y \cdot \Delta z(t, x, y, z)} \tag{A.2}$$

For the input emission rate q_{in} a constant value of $760\,\mathrm{kg\,s^{-1}}$ ($24.0\,\mathrm{Tg\,a^{-1}}$) is initialized, which corresponds to the total annual emissions for the year 2017 reported to the European Environment Agency by the operators (E-PRTR 2023). The horizontal size of a grid point Δx and Δy are temporally and spatially constant (0.2 km). The vertical layer size $\Delta z(t, x, y, z)$ corresponds to the spatial distance between two model levels. In the simulation this distance is computed in pressure coordinates and depends on all four dimensions. Since the pressure varies only slightly between successive time steps, the temporal dependence of Δz is small. At locations with flat topography the dependence of Δz on the horizontal coordinates x and y is also small, and at locations with large topographic changes (e.g. steep slopes) the dependence is more significant. The product $x \cdot y \cdot \Delta z(t, x, y, z)$ corresponds to the volume of the respective grid box. Within this volume the value of the tracer variable and thus the concentration is constant.

In order to compare the simulated data with an IPDA lidar measurement, the concentration array must be summed up vertically and multiplied by the quotient of the mean differential absorption cross section and the molecular mass.

$$\delta_{\mathrm{wrf}}(t, x, y) = \frac{\overline{\Delta\sigma}}{M} \cdot \sum_{j=1}^{j_{\mathrm{top}}} c(t, x, y, z_j) \cdot \Delta z_j(t, x, y, z_j) \tag{A.3}$$

The index j marks the respective vertical layer. Consequently, $j \in \{1, 56\}$ applies, and z_j is defined as corresponding to the lower edge of the respective layer.

A.2 Auxiliary Equations

$$\frac{\mathrm{d}p}{\mathrm{d}z} = -g \cdot \rho \tag{A.4}$$

$$\begin{aligned}
\rho &= \frac{M_{\text{tot}}}{V} \\
&= \frac{M_{\text{dry}} + M_{\text{H}_2\text{O}}}{V} \\
&= \frac{N_{\text{dry}} \cdot m_{\text{dry}} + N_{\text{H}_2\text{O}} \cdot m_{\text{H}_2\text{O}}}{V} \\
&= \frac{N_{\text{dry}}}{V} \cdot \left(m_{\text{dry}} + m_{\text{H}_2\text{O}} \cdot r_{\text{H}_2\text{O}}\right) \\
&= n_{\text{dry}} \cdot \left(m_{\text{dry}} + m_{\text{H}_2\text{O}} \cdot r_{\text{H}_2\text{O}}\right)
\end{aligned} \tag{A.5}$$

$$\begin{aligned}
Q &= \frac{M_{\text{H}_2\text{O}}}{M_{\text{dry}} + M_{\text{H}_2\text{O}}} \\
Q &= \frac{N_{\text{H}_2\text{O}} \cdot m_{\text{H}_2\text{O}} \cdot \frac{1}{Na}}{(N_{\text{dry}} \cdot m_{\text{dry}} + N_{\text{H}_2\text{O}} \cdot m_{\text{H}_2\text{O}}) \cdot \frac{1}{Na}} \\
Q &= \frac{N_{\text{dry}} \cdot r_{\text{H}_2\text{O}} \cdot m_{\text{H}_2\text{O}}}{N_{\text{dry}} \cdot (m_{\text{dry}} + r_{\text{H}_2\text{O}} \cdot m_{\text{H}_2\text{O}})} \\
(m_{\text{dry}} + r_{\text{H}_2\text{O}} \cdot m_{\text{H}_2\text{O}}) \cdot Q &= r_{\text{H}_2\text{O}} \cdot m_{\text{H}_2\text{O}} \\
m_{\text{dry}} \cdot Q &= r_{\text{H}_2\text{O}} \cdot m_{\text{H}_2\text{O}} \cdot (1 - Q) \\
\frac{m_{\text{dry}}}{m_{\text{H}_2\text{O}}} \cdot \frac{Q}{1 - Q} &= r_{\text{H}_2\text{O}}
\end{aligned} \tag{A.6}$$

$$X_{\text{CH}_4} = X_{\text{CH}_4,\text{hum}} \cdot \left(1 + \frac{Q}{1 - Q} \cdot \frac{m_{\text{dry}}}{m_{\text{H}_2\text{O}}}\right) \tag{A.7}$$

A.3 Supplementary Figures

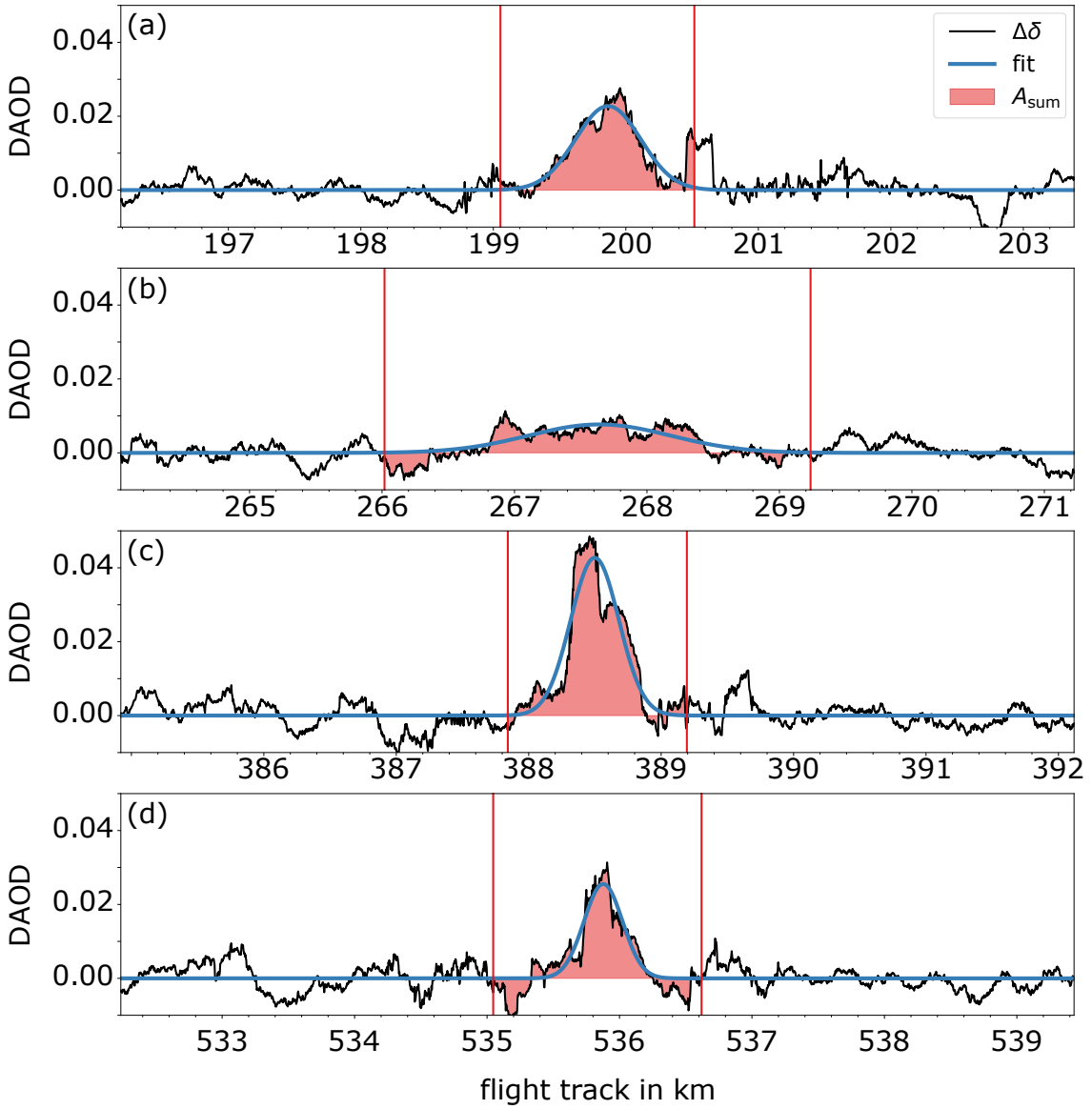

Figure A.1: Figures of individual HALO crossings on 23 May 2018, sorted equivalently to Table 3.1. The black line shows a 0.2 km (64 data points) running mean of the observed DAOD enhancement (cf. Sect. 3.1.1 and Fig. 3.2). Vertical red lines mark the smallest data extract used for the Riemann sum. The blue line represents a Gaussian fit. Adapted from Wolff et al. (2021).

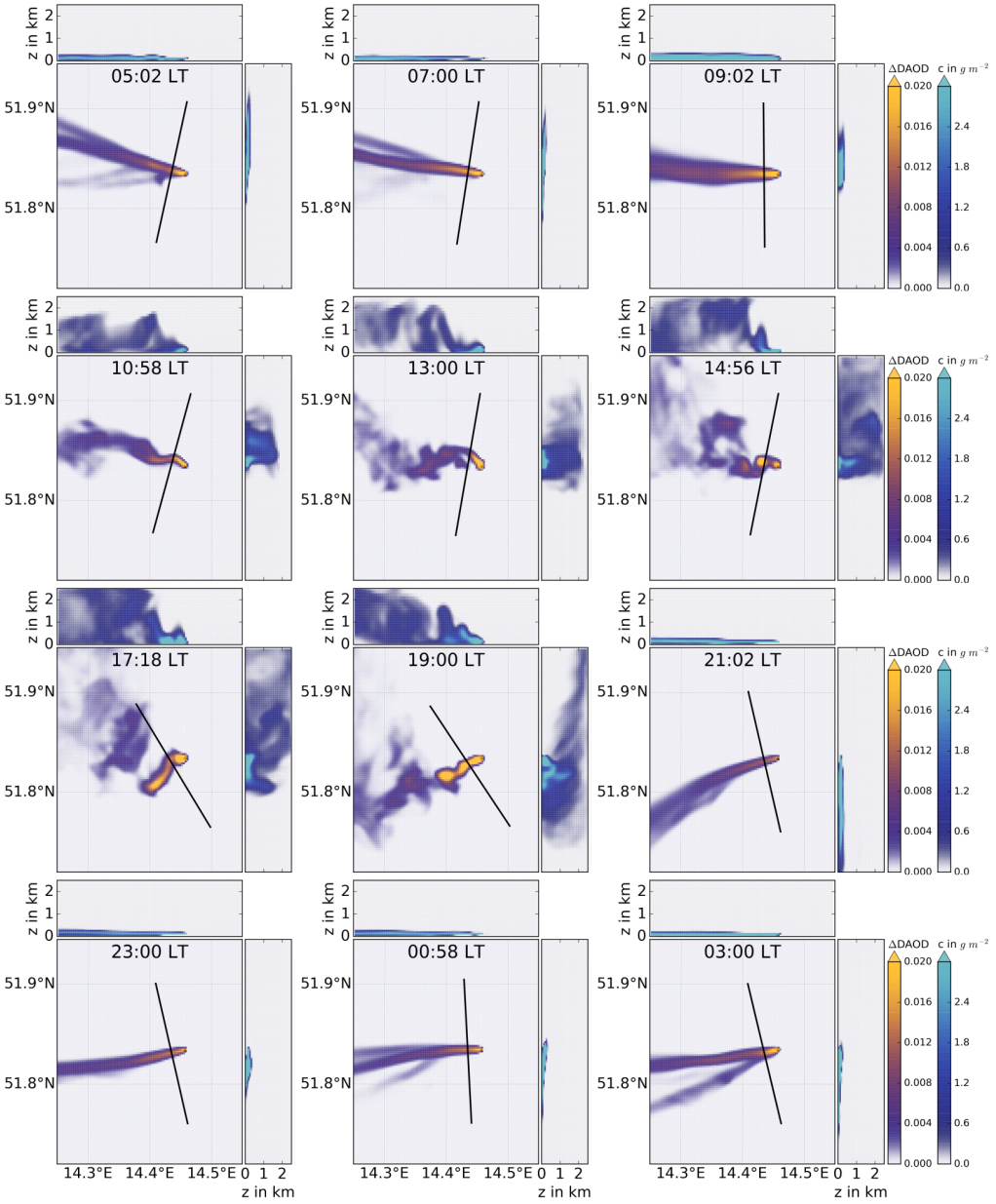

Figure A.2: Simulated plumes and virtual flight tracks. At the respective tops, local time is given in CEST, and at the bottom α denotes the local solar altitude. Every 2 min a virtual flyover is performed yielding 60 measurements within a time frame of 2 h. One representative snapshot within the 2 h time frame is shown. Some exhaust plumes are disjointed, due to vertical wind shearing. The discrete vertical layering in the model leads to distinctive horizontal advection directions. The colour maps follow the guidelines for a perception-based colour map presented by Stauffer et al. 2015. Adapted from Wolff et al. (2021).

A.4 Supplementary Tables

Table A.1: CHARM–F's Main System Parameters. Table by Amediek et al. (2017).

Laser type:	Nd:YAG-pumped OPOs, pulsed, two wavelengths (on, off) per trace gas
Laser wavelengths CO_2:	online: 1.572 02 µm offline: 1.572 12 µm
Laser wavelengths CH_4:	online: 1.645 55 µm offline: 1.645 86 µm
double pulse specifications:	50 Hz repetition rate 500 µs separation 20 ns pulse width 50 MHz spectral width 2 MHz rms OPO single-shot stability
Pulse energies:	CH_4: 10 mJ CO_2: 10 mJ (upgradeable)
Detector types:	APDs (60 mm telescopes) PINs (200 mm telescopes)
Transmitter divergence:	adjustable, max. 3 mrad
Laser ground spot diameter:	max. 50 m, typically 25 – 40 m
Typical aircraft velocity:	$\approx 200\,\mathrm{m\,s^{-1}}$

Cluster	Included Sites			
brzbo:	*Shafts include Brzeszcze IX and Borynias*			
	Brzeszcze IX	Borynia VI	Borynia III	
brzsi:	*Strongest emitters are Brzeszcze II and Silesias*			
	Brzeszcze II	Silesia I	Silesia V	Andrzej IV
	Andrzej VI			
budry:	*Strongest emitters are Budryk V and II*			
	Szczyglowice IV	Szczyglowice VI	Knurow A	Budryk V
	Budryk II →	← Zory	Boleslaw II	Barbara A
	Murcki A	Bierun	Ziemowit A	Ziemowit B
	Ziemowit C	Janina A	Janina B	
bytom:	*Located close to the city of Bytom*			
	Pstrowski A	Bobrek A	PowstSla A	PowstSla B
	Centrum A →	← Piekary C	Piekary B	Piekary A
frecz:	*Single shaft*			
	Frenstat A			
janma:	*Shafts include Jankowice and Marcel*			
	Jankowice III	Jankowice IV	Marcel II	Marcel IV
krupi:	*Single shaft*			
	Krupinski III			
oskar:	*Located between the cities of Ostrava and Karvina*			
	CSA A	CSM A	CSM B	Darkov A
	Lazy A			
pascz:	*Located close to the city of Paskov, Czech Republic*			
	Paskov A	Paskov B		
piast:	*Single shaft*			
	Piast IV			
rybni:	*Located close to the city of Rybnik*			
	Rydultowy A	Rydultowy B	Chwalowice V	Chwalowice VII
sosni:	*Strongest emitter is Sosnica V*			
	Knurow B	Sosnica V	Makoszowy B	Makoszowy A
	Bielszowice II	Bielszowice IV	Pokoj A	Pokoj B
	Halemba A →	← Halemba B	Halemba C →	← Slask III
	Slask IV	Murcki B	Wujek A	Staszic V
	Staszic IV	Wieczorek B	Wieczorek A	Wesola A →
	← Wesola B	Myslowice A	Jaworzno A	
zofio:	*Strongest emitter is Zofiowka V*			
	Pniowek V	Pniowek III	Pniowek IV	Zofiowka V →
	← Zofiowka IV	Moszczenica A	JasMos IV	JasMos VI

Table A.2: The table shows which shafts are aggregated in each cluster, along with a brief italicized explanation of the naming rationale for each cluster. Arrows indicate cases where neighbouring sources were located within the same WRF grid cell. The cell colours correspond to emission types (cf. Table 4.2 and Fig. 4.2). Blue are active mines, red are inactive mines, green are non-reporting mines, orange are Czech mines that also do not report, and purple are power/cogeneration plants.

B Inverse Modelling for Regional CH_4 Emissions

This chapter provides a concise summary of the theoretical background of inverse modelling, based mainly on Peters et al. (2005) and the *Lectures on Inverse Modelling* by Jacob (2007), where the reader can find a more detailed explanation. The presentation follows their notation and concepts and is included here to give the reader a self-contained overview of the Bayesian formalism applied in this thesis.

In this chapter, inverse modelling is introduced as a method to estimate regional CH_4 emissions based on observational data. This is achieved by combining prior estimates of emission rates with atmospheric concentration measurements. Inverse modelling leverages numerical models to connect prior estimates, such as bottom-up models or expert assessments, with atmospheric observations. These models represent atmospheric processes, such as transport, chemical reactions, and radiative transfer, allowing for a comprehensive simulation of how emissions relate to observed concentrations.

It is assumed that combining the two pieces of information will yield a result closer to the truth. In many inverse modelling applications, observational data often lack the density or spatial coverage needed to fully constrain all emission sources. Even if the flight patterns of the measurement field campaign are designed to notably enhance observational coverage, prior knowledge remains necessary to addressing potential gaps and ensuring a robust solution.

This approach is mathematically grounded in Bayes' Theorem, which is the framework for updating prior knowledge with new observational data. Bayes' Theorem allows to determine the conditional probability of a state vector $\mathbf{x}$ given the observation vector $\mathbf{y}$. In the mathematical formalism, the state vector $\mathbf{x}$ represents scaling factors that are applied to the prior CH_4 emission rates $\mathbf{q}_\mathrm{p}$, while the observation vector $\mathbf{y}$ contains the XCH_4 measurements of CHARM–F.

Table B.1: Reference list of mathematical symbols used in this work, along with their names, units, and dimensions. Adapted from Peters et al. (2005).

Symbol	Name	Unit	Dimension
$\mathbf{q}_\mathrm{p}$	prior emission rates	kg/s	S
$\mathbf{x}_n$	state vector	-	S
$\overline{\mathbf{x}}$	mean state vector	-	S
n	ensemble member index	-	1
$\mathbf{x'}_n$	state vector deviation	-	S
$\mathbf{P}_\mathrm{p}$	prior state covariance matrix	-	$S \times S$
$\mathbf{P}_\mathrm{a}$	posterior (analysed) state covariance matrix	-	$S \times S$
$\mathbf{D}$	state deviation matrix	-	$S \times N$
$\mathcal{H}$	observation operator	- $\rightarrow$ µmol/mol	$S \rightarrow M$
$\mathbf{H}$	linear observation operator (matrix form)	- $\rightarrow$ µmol/mol	$S \times M$
$\mathbf{y}$	observation vector	µmol/mol	M
$\mathcal{H}(\mathbf{x})$	simulated observation vector	µmol/mol	M
$\mathbf{R}$	observation-error covariance matrix	$(\mu\mathrm{mol/mol})^2$	$M \times M$
$\mathbf{K}$	Kalman gain matrix	µmol/mol $\rightarrow$ -	$M \times S$
$\mathbf{k'}$	Kalman deviation gain matrix	µmol/mol $\rightarrow$ -	$M \times S$
$\mathrm{CH_4}(n,t,x,y,z)$	simulated CH_4 field	µmol/mol	$N\times$ WRF grid

B.1 Bayesian Formalism

The foundation in inverse modelling is the relation between the observation vector $\mathbf{y}$ [dimension M] and the state vector $\mathbf{x}$ [S] through the observation operator $\mathcal{H}$ [$S \rightarrow M$], with a model-data-mismatch error $\boldsymbol{\varepsilon}$ [M]:

$$\mathbf{y} = \mathcal{H}(\mathbf{x}) + \boldsymbol{\varepsilon} \quad \text{with} \quad \boldsymbol{\varepsilon} \sim \mathcal{N}(0, \mathbf{R}) \tag{B.1}$$

The so-called observation operator $\mathcal{H}$ relates $\mathbf{x}$ to $\mathbf{y}$ by incorporating atmospheric transport modelled by WRF-Chem, as well as the interpolation and vertical integration that map the gridded $\mathrm{CH_4}(n,t,x,y,z)$ field to simulated $\mathrm{XCH_4}$ values. Internally, $\mathcal{H}$ applies the scaling factors $\mathbf{x}$ to the prior emission rates $\mathbf{q}_\mathrm{p}$, maps the emission rates to the WRF grid, and simulates their atmospheric transport. Finally, interpolation and vertical integration are performed to convert the three-dimensional $\mathrm{CH_4}(n,t,x,y,z)$ fields into simulated column-averaged mole fractions $\mathrm{XCH_4}(n,t) \equiv \mathbf{y}_n$.

The so-called model-data mismatch error $\boldsymbol{\varepsilon}$ represents the uncertainty introduced by discrepancies between modelled and observed data. This error arises from various sources, including the limitations of the atmospheric transport model, inaccuracies in the observation operator ($\boldsymbol{\sigma}_\mathcal{H}$), and errors in the observations themselves ($\boldsymbol{\sigma}_y$). It quantifies the expected discrepancy between observations and simulation, accounting for uncertainties in both the observations and the modelling process.

$$\boldsymbol{\varepsilon} = \sqrt{\boldsymbol{\sigma}_y^2 + \boldsymbol{\sigma}_\mathcal{H}^2} \tag{B.2}$$

The model-data mismatch error $\boldsymbol{\varepsilon}$ is assumed to follow a Gaussian (normal) distribution with a mean of zero and a covariance matrix $\mathbf{R}$ ($\boldsymbol{\varepsilon} \sim \mathcal{N}(0, \mathbf{R})$). It is further

assumed that the observational errors are uncorrelated, i.e. that $\mathbf{R}$ is a diagonal matrix. These assumptions facilitate the numerical solution.

The likelihood function $P(\mathbf{y}|\mathbf{x})$ quantifies how likely the observations $\mathbf{y}$ are for a given state vector $\mathbf{x}$, considering the uncertainties arising from the model and observations, which are mathematically embodied in the covariance matrix $\mathbf{R}$:

$$P(\mathbf{y}|\mathbf{x}) = \frac{1}{\sqrt{(2\pi)^M |\mathbf{R}|}} \cdot \exp\left(-\frac{1}{2}(\mathbf{y} - \mathcal{H}(\mathbf{x}))^{\mathrm{T}} \mathbf{R}^{-1} (\mathbf{y} - \mathcal{H}(\mathbf{x}))\right) \tag{B.3}$$

In addition to the model-data mismatch error, uncertainties in the prior emission estimates $\boldsymbol{\eta}$ are also taken into account. Again, they are assumed to be normally distributed with a mean of zero and a covariance matrix $\mathbf{P}_{\mathrm{p}}$:

$$\mathbf{x} = \mathbf{x}_{\mathrm{p}} + \boldsymbol{\eta} \quad \text{with} \quad \boldsymbol{\eta} \sim \mathcal{N}(0, \mathbf{P}_{\mathrm{p}}) \tag{B.4}$$

$P(\mathbf{x})$ is the prior PDF for the state vector $\mathbf{x}$ described by a Gaussian distribution:

$$P(\mathbf{x}) = \frac{1}{\sqrt{(2\pi)^S |\mathbf{P}_{\mathrm{p}}|}} \cdot \exp\left(-\frac{1}{2}(\mathbf{x} - \mathbf{x}_{\mathrm{p}})^{\mathrm{T}} \mathbf{P}_{\mathrm{p}}^{-1} (\mathbf{x} - \mathbf{x}_{\mathrm{p}})\right) \tag{B.5}$$

The prior distribution $P(\mathbf{x})$ reflects our initial knowledge of the state vector $\mathbf{x}$, while the likelihood function $P(\mathbf{y}|\mathbf{x})$ quantifies the probability of observing $\mathbf{y}$ given the state vector $\mathbf{x}$. To derive Bayes' Theorem, the joint probability density function $P(\mathbf{x}, \mathbf{y})$ needs to be considered. It quantifies the probability of both the state vector $\mathbf{x}$ and the observations $\mathbf{y}$ being in specific ranges $[\mathbf{x}, \mathbf{x} + \mathrm{d}\mathbf{x}, \mathbf{y}, \mathbf{y} + \mathrm{d}\mathbf{y}]$. This joint probability can be expressed in two equivalent forms:

$$P(\mathbf{x}, \mathbf{y})\mathrm{d}\mathbf{x}\mathrm{d}\mathbf{y} = P(\mathbf{x})\mathrm{d}\mathbf{x} P(\mathbf{y}|\mathbf{x})\mathrm{d}\mathbf{y}$$

or

$$P(\mathbf{x}, \mathbf{y})\mathrm{d}\mathbf{x}\mathrm{d}\mathbf{y} = P(\mathbf{y})\mathrm{d}\mathbf{y} P(\mathbf{x}|\mathbf{y})\mathrm{d}\mathbf{x}$$

Equating these two expressions yields:

$$P(\mathbf{x}|\mathbf{y}) = \frac{P(\mathbf{y}|\mathbf{x})P(\mathbf{x})}{P(\mathbf{y})} \tag{B.6}$$

The term $P(\mathbf{x}|\mathbf{y})$ is the posterior PDF, representing the updated knowledge of the CH_4 emission rates, given by the product $\mathbf{q}_{\mathrm{p}}\mathbf{x}$, after considering the XCH_4 observations $\mathbf{y}$. To find its MAP solution the equation $\nabla_{\mathbf{x}} P(\mathbf{x}|\mathbf{y}) = 0$ needs to be solved, where $\nabla_{\mathbf{x}}$ represents the gradient operator with respect to the state vector $\mathbf{x}$. The denominator $P(\mathbf{y})$ ensures proper normalization and as it is independent of $\mathbf{x}$ it can be ignored. Inserting equations (B.3) and (B.5) leads to:

$$P(\mathbf{x}|\mathbf{y}) \propto \exp\left(-\frac{1}{2}\left[(\mathbf{y} - \mathcal{H}(\mathbf{x}))^{\mathrm{T}} \mathbf{R}^{-1} (\mathbf{y} - \mathcal{H}(\mathbf{x})) + (\mathbf{x} - \mathbf{x}_{\mathrm{p}})^{\mathrm{T}} \mathbf{P}_{\mathrm{p}}^{-1} (\mathbf{x} - \mathbf{x}_{\mathrm{p}})\right]\right) \tag{B.7}$$

Because the exponential function is strictly monotonously increasing, finding the MAP solution is equivalent to minimizing the negative of the argument of the exponential function and thus defining the Bayesian cost function $J(\mathbf{x})$:

$$J(\mathbf{x}) = \frac{1}{2}(\mathbf{y} - \mathcal{H}(\mathbf{x}))^{\mathrm{T}}\mathbf{R}^{-1}(\mathbf{y} - \mathcal{H}(\mathbf{x})) + \frac{1}{2}(\mathbf{x} - \mathbf{x}_{\mathrm{p}})^{\mathrm{T}}\mathbf{P}_{\mathrm{p}}^{-1}(\mathbf{x} - \mathbf{x}_{\mathrm{p}}) \tag{B.8}$$

This cost function $J(\mathbf{x})$ balances the model-data misfit $(\mathbf{y} - \mathcal{H}(\mathbf{x}))^{\mathrm{T}}\mathbf{R}^{-1}(\mathbf{y} - \mathcal{H}(\mathbf{x}))$ and the deviation from the prior $(\mathbf{x} - \mathbf{x}_{\mathrm{p}})^{\mathrm{T}}\mathbf{P}_{\mathrm{p}}^{-1}(\mathbf{x} - \mathbf{x}_{\mathrm{p}})$.

B.2 Maximum a Posteriori Solution

The derivation of the maximum a posteriori (MAP) estimate builds on the Bayesian framework introduced in the previous section. This section slightly adapts the approach by substituting the observation operator $\mathcal{H}$ with its linearized matrix form, $\mathbf{H}$. The role of this linearization, its implications for theoretical formulations, and its circumvention in ensemble-based approaches are discussed later in Sect. B.3. However, for now we proceed with the linearized form $\mathbf{H}$, simplifying the mathematical formulation, which is particularly valuable for deriving analytical and numerical results. The Bayesian cost function $J(\mathbf{x})$, incorporating the linearized operator $\mathbf{H}$, is expressed as:

$$J(\mathbf{x}) = \frac{1}{2}(\mathbf{y} - \mathbf{H}\mathbf{x})^{\mathrm{T}}\mathbf{R}^{-1}(\mathbf{y} - \mathbf{H}\mathbf{x}) + \frac{1}{2}(\mathbf{x} - \mathbf{x}_{\mathrm{p}})^{\mathrm{T}}\mathbf{P}_{\mathrm{p}}^{-1}(\mathbf{x} - \mathbf{x}_{\mathrm{p}}) \tag{B.9}$$

Setting the derivative of $J(\mathbf{x})$ with respect to $\mathbf{x}$ to zero provides the condition to solve for the MAP solution $\mathbf{x}_{\mathrm{a}}$, here referred to as the *analysed* state vector or *a posterior*. In this work, the subscript "a" denotes the result after assimilating all observations in a single analysis step. In the literature, particularly in time-stepping or sequential assimilation frameworks, the same subscript is often used to indicate an "advanced" state, reflecting propagation in time. Since this study does not include such a forecast step, the interpretation as "analysed" is more appropriate.

$$\left.\frac{\partial J}{\partial \mathbf{x}}\right|_{\mathbf{x}=\mathbf{x}_{\mathrm{a}}} = (\mathbf{x}_{\mathrm{a}} - \mathbf{x}_{\mathrm{p}})^{\mathrm{T}}\mathbf{P}_{\mathrm{p}}^{-1} - (\mathbf{y} - \mathbf{H}\mathbf{x}_{\mathrm{a}})^{\mathrm{T}}\mathbf{R}^{-1}\mathbf{H} \stackrel{!}{=} 0 \tag{B.10}$$

By rearranging terms and applying standard matrix operations, the equation is solved for the posterior state vector $\mathbf{x}_{\mathrm{a}}$:

$$\begin{aligned}
(\mathbf{x}_{\mathrm{a}} - \mathbf{x}_{\mathrm{p}})^{\mathrm{T}}\mathbf{P}_{\mathrm{p}}^{-1} &= (\mathbf{y} - \mathbf{H}\mathbf{x}_{\mathrm{a}})^{\mathrm{T}}\mathbf{R}^{-1}\mathbf{H} \qquad (\mathrm{B.11})\\
\mathbf{x}_{\mathrm{a}} - \mathbf{x}_{\mathrm{p}} &= \mathbf{P}_{\mathrm{p}}\mathbf{H}^{\mathrm{T}}\mathbf{R}^{-1}(\mathbf{y} - \mathbf{H}\mathbf{x}_{\mathrm{a}})\\
\mathbf{x}_{\mathrm{a}} - \mathbf{x}_{\mathrm{p}} &= \mathbf{P}_{\mathrm{p}}\mathbf{H}^{\mathrm{T}}\mathbf{R}^{-1}\left((\mathbf{y} - \mathbf{H}\mathbf{x}_{\mathrm{p}}) - \mathbf{H}(\mathbf{x}_{\mathrm{a}} - \mathbf{x}_{\mathrm{p}})\right)\\
\mathbf{x}_{\mathrm{a}} - \mathbf{x}_{\mathrm{p}} + \mathbf{P}_{\mathrm{p}}\mathbf{H}^{\mathrm{T}}\mathbf{R}^{-1}\mathbf{H}(\mathbf{x}_{\mathrm{a}} - \mathbf{x}_{\mathrm{p}}) &= \mathbf{P}_{\mathrm{p}}\mathbf{H}^{\mathrm{T}}\mathbf{R}^{-1}(\mathbf{y} - \mathbf{H}\mathbf{x}_{\mathrm{p}})\\
\left(\mathbb{I} + \mathbf{P}_{\mathrm{p}}\mathbf{H}^{\mathrm{T}}\mathbf{R}^{-1}\mathbf{H}\right)(\mathbf{x}_{\mathrm{a}} - \mathbf{x}_{\mathrm{p}}) &= \mathbf{P}_{\mathrm{p}}\mathbf{H}^{\mathrm{T}}\mathbf{R}^{-1}(\mathbf{y} - \mathbf{H}\mathbf{x}_{\mathrm{p}})\\
\mathbf{x}_{\mathrm{a}} &= \mathbf{x}_{\mathrm{p}} + \underbrace{\left(\mathbb{I} + \mathbf{P}_{\mathrm{p}}\mathbf{H}^{\mathrm{T}}\mathbf{R}^{-1}\mathbf{H}\right)^{-1}\mathbf{P}_{\mathrm{p}}\mathbf{H}^{\mathrm{T}}\mathbf{R}^{-1}}_{\equiv\mathbf{K}}(\mathbf{y} - \mathbf{H}\mathbf{x}_{\mathrm{p}})
\end{aligned}$$

The bracketed expression is equivalent to the widely used definition of the Kalman gain matrix, $\mathbf{K}$, as e.g. defined in Peters et al. (2005):

$$\begin{aligned}\mathbf{K} &= \left(\mathbb{I} + \mathbf{P}_\mathrm{p}\mathbf{H}^\mathrm{T}\mathbf{R}^{-1}\mathbf{H}\right)^{-1}\mathbf{P}_\mathrm{p}\mathbf{H}^\mathrm{T}\mathbf{R}^{-1} \\ &= \mathbf{P}_\mathrm{p}\mathbf{H}^\mathrm{T}\left(\mathbb{I} + \mathbf{R}^{-1}\mathbf{H}\mathbf{P}_\mathrm{p}\mathbf{H}^\mathrm{T}\right)^{-1}\mathbf{R}^{-1} \\ \mathbf{K} &= \mathbf{P}_\mathrm{p}\mathbf{H}^\mathrm{T}\left(\mathbf{R} + \mathbf{H}\mathbf{P}_\mathrm{p}\mathbf{H}^\mathrm{T}\right)^{-1}\end{aligned} \quad \begin{matrix}\big)\ \textit{push-through identity} \\ \big)\ \textit{inverse of a product rule}\end{matrix} \tag{B.12}$$

From the first to the second row, $(\mathbb{I} + \mathbf{AB})^{-1}\mathbf{A} = \mathbf{A}(\mathbb{I} + \mathbf{BA})^{-1}$ is applied (*push-through identity*, Boyd and Vandenberghe 2018), which allows $\mathbf{P}_\mathrm{p}\mathbf{H}^\mathrm{T}$ to be moved to the front of the expression. From the second to the third row, the *inverse of a product rule* $\mathbf{B}^{-1}\mathbf{A}^{-1} = (\mathbf{AB})^{-1}$ is used. This permits the simplification of the inverse of the matrix product by rearranging $\mathbf{R}^{-1}$ and the remaining terms.

Hence, the posterior of the state vector can be expressed in terms of the Kalman gain matrix, $\mathbf{K}$ (Eq. B.12), which governs the relative influence of the prior and the observations:

$$\mathbf{x}_\mathrm{a} = \mathbf{x}_\mathrm{p} + \underbrace{\mathbf{P}_\mathrm{p}\mathbf{H}^\mathrm{T}\left(\mathbf{R} + \mathbf{H}\mathbf{P}_\mathrm{p}\mathbf{H}^\mathrm{T}\right)^{-1}}_{\mathbf{K}}(\mathbf{y} - \mathbf{H}\mathbf{x}_\mathrm{p}) \tag{B.13}$$

The Kalman gain matrix $\mathbf{K}$ optimally weights the increment to the prior state vector by the observations based on the observational uncertainty and the prior covariance.

The posterior covariance matrix $\mathbf{P}_\mathrm{a}$ defines the width of the posterior PDF within the Bayesian framework. It is associated with the exponent of the posterior PDF, represented by the quadratic term $(\mathbf{x} - \mathbf{x}_\mathrm{a})^\mathrm{T}\mathbf{P}_\mathrm{a}^{-1}(\mathbf{x} - \mathbf{x}_\mathrm{a})$. Correspondingly, $\mathbf{P}_\mathrm{a}$ quantifies the multidimensional "curvature" around the advanced state vector $\mathbf{x}_\mathrm{a}$. According to this notion, we equate the second derivative $\partial^2/\partial\mathbf{x}^2$ of the Bayesian cost function $J(\mathbf{x})$ (Eq. B.9), to the second derivative of $\frac{1}{2}(\mathbf{x} - \mathbf{x}_\mathrm{a})^\mathrm{T}\mathbf{P}_\mathrm{a}^{-1}(\mathbf{x} - \mathbf{x}_\mathrm{a})$:

$$\begin{aligned}\mathbf{P}_\mathrm{a}^{-1} &= \mathbf{H}^\mathrm{T}\mathbf{R}^{-1}\mathbf{H} + \mathbf{P}_\mathrm{p}^{-1} \\ \mathbf{P}_\mathrm{a} &= \left(\mathbf{H}^\mathrm{T}\mathbf{R}^{-1}\mathbf{H} + \mathbf{P}_\mathrm{p}^{-1}\right)^{-1} \\ \mathbf{P}_\mathrm{a} &= \mathbf{P}_\mathrm{p} - \underbrace{\mathbf{P}_\mathrm{p}\mathbf{H}^\mathrm{T}\left(\mathbf{R} + \mathbf{H}\mathbf{P}_\mathrm{p}\mathbf{H}^\mathrm{T}\right)^{-1}}_{\mathbf{K}}\mathbf{H}\mathbf{P}_\mathrm{p}\end{aligned} \quad \big)\ \textit{Woodbury identity} \tag{B.14}$$

In the last line $(\mathbf{A} + \mathbf{UCV})^{-1} = \mathbf{A}^{-1} - \mathbf{A}^{-1}\mathbf{U}\left(\mathbf{C}^{-1} + \mathbf{V}\mathbf{A}^{-1}\mathbf{U}\right)^{-1}\mathbf{V}\mathbf{A}^{-1}$ was used, which is the *Woodbury identity* (Henderson and Searle 1981). All together the equations for updating the state vector and covariance matrix are given by:

$$\begin{aligned}\mathbf{x}_\mathrm{a} &= \mathbf{x}_\mathrm{p} + \mathbf{K}(\mathbf{y} - \mathbf{H}\mathbf{x}_\mathrm{p}) \\ \mathbf{P}_\mathrm{a} &= \mathbf{P}_\mathrm{p} - \mathbf{K}\mathbf{H}\mathbf{P}_\mathrm{p}\end{aligned} \tag{B.15}$$

In summary, the Bayesian inverse modelling framework provides a systematic way to combine prior knowledge with observational data, yielding an posterior state vector $\mathbf{x}_\mathrm{a}$ that minimizes the combined mismatch with both prior and observations. The Kalman gain matrix, $\mathbf{K}$, balances the influence of the prior and observations based on their respective uncertainties. The a posteriori emission rates are then obtained by applying the optimized scaling factors $\mathbf{x}_\mathrm{a}$ to the prior emission rates, i.e. $\mathbf{q}_\mathrm{a} = \mathbf{q}_\mathrm{p}\mathbf{x}_\mathrm{a}$.

B.3 Ensemble Kalman Filter

The analytical framework of Bayesian inverse modelling becomes computationally demanding when applied to large-scale problems with extensive state vectors, such as global inversions of CH_4 emissions. In these scenarios, the state vector $\mathbf{x}$, defined across a global grid, can consist of a huge number of elements (e.g. $S \sim \mathcal{O}(10^5)$ for a horizontal resolution of $\sim 1°$). Computational costs are particularly dominated by two factors: the evaluation of the observation operator $\mathbf{H}$, which scales with the size of the state vector and the number of observations ($[M \times S]$ matrix), and the manipulation of covariance matrices $\mathbf{P}$, which scale as $[S \times S]$ matrices. As S grows large, both terms contribute significantly to the computational burden.

To address these challenges, ensemble data assimilation systems, such as the Carbon Tracker Data Assimilation Shell (CTDAS) (van der Laan-Luijkx et al. 2017; Peters et al. 2005), represent the state vector and its covariance matrix in a reduced-dimensional ensemble space. This is achieved by sampling the state vector PDF (with mean $\overline{\mathbf{x}}$ and covariance $\mathbf{P}$) with an ensemble of state vectors $\mathbf{x}_n$, where $n \in \{1, 2, \ldots, N\}$. Each ensemble member represents a possible realization of the state, composed of a mean state and deviations from the mean. By using $N \ll S$, the computational burden is significantly reduced while still capturing the essential statistical properties of the system. In this approach, the covariance matrix $\mathbf{P}$ is no longer computed explicitly as a full $[S \times S]$ matrix. Instead, the ensemble members are used to approximate $\mathbf{P}$, dramatically reducing the dimensionality of the problem.

While the dimensionality of the state vector in this study would in principle allow for an analytical inversion, the use of an ensemble-based approach was a deliberate and strategic choice. The decision to implement the ensemble Kalman filter (EnKF) within CTDAS was motivated not primarily by computational necessity, but by the broader goal of establishing and testing a scalable inversion framework suitable for more complex future applications. In particular, upcoming studies of diffuse and spatially uncertain sources — such as wetland CH_4 emissions — will require ensemble-based methods capable of handling high-dimensional state vectors and non-linear processes. Applying the method here, in a relatively controlled and interpretable setting, enabled methodological development and validation under realistic but manageable conditions.

Furthermore, ensemble-based formulations such as CTDAS offer increased flexibility for incorporating spatial correlations and uncertainty estimates, and are well suited for integration with transport models such as WRF. While this study focuses on a short observational window and a moderate number of sources, the adopted framework provides a foundation for future work where computational scalability and methodological robustness will be of greater relevance.

Construction of the Ensemble

The ensemble is constructed to reflect the prior knowledge of the state vector. Each ensemble member is a realization of a Gaussian distribution. Specifically, the mean of each state vector element $\overline{\mathbf{x}}$, is set to a scaling factor of 1 (i.e. prior emission

estimates are used), while the uncertainties and correlations in the prior determine the deviations $\mathbf{x'}_n$ of the n-th member. These deviations follow a multivariate normal distribution. The state vector of the n-th ensemble member is expressed as:

$$\mathbf{x}_n = \overline{\mathbf{x}} + \mathbf{x'}_n \tag{B.16}$$

In the WRF-Chem forward simulation, each ensemble member is represented as a separate tracer, allowing the simulated observations $\mathbf{Hx}_n$ for each ensemble member to be directly accessed from the simulation's output files.

The deviations of the ensemble members are organized into the columns of the state deviation matrix $\mathbf{D}$, providing a square-root representation of the covariance matrix $\mathbf{P}$:

$$\mathbf{P} = \mathbf{D}\mathbf{D}^{\mathrm{T}} \quad \text{with} \quad \mathbf{D} = \frac{1}{\sqrt{N-1}} \begin{bmatrix} \mathbf{x'}_1 & \mathbf{x'}_2 & \dots & \mathbf{x'}_N \end{bmatrix} \tag{B.17}$$

The Kalman gain matrix $\mathbf{K}$, used to compute the updates, is approximated in the ensemble framework using:

$$\mathbf{HPH}^{\mathrm{T}} \approx \frac{1}{N-1} \begin{bmatrix} \mathbf{Hx'}_1 & \mathbf{Hx'}_2 & \dots & \mathbf{Hx'}_N \end{bmatrix} \begin{bmatrix} \mathbf{Hx'}_1 & \mathbf{Hx'}_2 & \dots & \mathbf{Hx'}_N \end{bmatrix}^{\mathrm{T}} \tag{B.18}$$

$$\mathbf{PH}^{\mathrm{T}} \approx \frac{1}{N-1} \begin{bmatrix} \mathbf{x'}_1 & \mathbf{x'}_2 & \dots & \mathbf{x'}_N \end{bmatrix} \begin{bmatrix} \mathbf{Hx'}_1 & \mathbf{Hx'}_2 & \dots & \mathbf{Hx'}_N \end{bmatrix}^{\mathrm{T}} \tag{B.19}$$

Each entry $\mathbf{Hx'}_n$ denotes one column of ensemble modelled CH_4 deviations in observation space.

CTDAS processes the observations iteratively one after the other. For diagonal model-data mismatch matrices $\mathbf{R}$ and without localization (see below), the sequential assimilation is mathematically equivalent to assimilating all observations at once, and simplifies the computation: Equation B.18 thus simply describes a *dot product* of two vectors and $\mathbf{HPH}^{\mathrm{T}}$ becomes a $[1 \times 1]$ scalar value, while $\mathbf{PH}^{\mathrm{T}}$ is a $[S \times 1]$ vector. Through Equations (B.18) and (B.19), the Kalman gain matrix $\mathbf{K}$ linearly maps observed quantities to state vector elements as an average over all the ensemble members. The Kalman gain matrix $\mathbf{K}$ updates the ensemble mean as in Eq. B.13. The ensemble deviations are updated independently as (Whitaker and Hamill 2002):

$$\mathbf{x'}_{\mathrm{a},n} = \mathbf{x'}_{\mathrm{p},n} - \mathbf{k'Hx'}_{\mathrm{p},n} \quad \text{with} \quad \mathbf{k'} = \mathbf{K}\left(1 + \sqrt{\frac{\mathbf{R}}{\mathbf{HP}_{\mathrm{p}}\mathbf{H}^{\mathrm{T}} + \mathbf{R}}}\right)^{-1} \tag{B.20}$$

The updated mean state and ensemble deviations resulting from assimilating one observation serve as the prior for the next. This process is repeated iteratively until all observations are assimilated. To account for the state vector updates from previously assimilated observations, the simulated mean and deviations of all remaining observations must be updated accordingly. One approach to achieve this would be to rerun WRF-Chem for each observation, however, this would be very computationally intensive. Instead, they are updated using the previously calculated Kalman gain matrix $\mathbf{K}$, which is equivalent to Equations B.15 and B.20 but in observation space:

$$\begin{aligned} \mathcal{H}(\overline{\mathbf{x}}_{\mathrm{a}})_m &= \mathcal{H}(\overline{\mathbf{x}}_{\mathrm{p}})_m + \mathbf{H}_m\mathbf{K}\left(\mathbf{y} - \mathbf{H}\overline{\mathbf{x}}_{\mathrm{p}}\right) \\ \mathcal{H}(\mathbf{x'}_{\mathrm{a}})_m &= \mathcal{H}(\mathbf{x'}_{\mathrm{p}})_m - \mathbf{H}_m\mathbf{k'}\mathcal{H}(\mathbf{x'}_{\mathrm{p}}) \end{aligned} \tag{B.21}$$

Here, $\mathbf{H}_m$ represents the matrix form of the observation operator for observation m, and $\mathbf{k'}$ is derived in the same way as in the update of the deviation of the state vector (Eq. B.20). Calculating the term $\mathbf{H}_m\mathbf{K}$ leads to $\mathbf{H}_m\mathbf{P}_\mathrm{p}\mathbf{H}^\mathrm{T}$ in the numerator of the Kalman gain matrix (Eq. B.12). This results in a scalar value derived from Eq. B.18, where the first term on the right-hand side corresponds to the simulated deviations of the CH_4 concentrations, which still need to be assimilated, while the second term corresponds to the values associated with the observation currently being assimilated. If the transport model is perfectly linear, and in the absence of localization (see below), the update by Eq. B.21 is exact. Otherwise, it is an approximation.

In the ensemble-based implementation of the Kalman filter, the explicit construction of the linearized observation operator $\mathbf{H}$ is unnecessary. Instead, by running the atmospheric transport model N times — once for each ensemble member n — the observation vectors $\mathcal{H}(\mathbf{x}_n)$ are directly obtained. These ensemble outputs are then used to compute the terms required for the Kalman gain matrix $\mathbf{K}$, such as $\mathbf{HPH}^\mathrm{T}$ and $\mathbf{PH}^\mathrm{T}$. While the linearized operator $\mathbf{H}$ was introduced earlier for mathematical clarity, its explicit computation is avoided in practice. This distinction is discussed further in the subsection below.

The EnKF approach offers several advantages. First, by eliminating the need to compute or store $\mathbf{H}$ and large covariance matrices, the computation and storage demands are reduced significantly. Second, it avoids the need to explicitly linearize $\mathcal{H}$, enabling non-linear processes to be incorporated via direct forward simulation. Nevertheless, the ensemble-based approach still relies on the assumption that non-linearities remain moderate within the ensemble spread. Consequently, the equations derived earlier, though presented in their mathematical form for clarity, are seamlessly implemented within CTDAS-WRF by leveraging ensemble members and direct forward simulation. By operating directly on ensemble-based quantities, this method ensures efficient computation while preserving the statistical properties necessary for state vector optimization. The sequential implementation further simplifies the process, as each observation is assimilated iteratively, updating both the state vector and the covariance structure without explicit matrix-inversion of $\mathbf{R} + \mathbf{HP}_\mathrm{p}\mathbf{H}^\mathrm{T}$.

Comment on the Linearization of the Observation Operator

In classical formulations of Bayesian inverse modelling, the observation operator $\mathcal{H}$ is often linearized to facilitate analytical derivations. This yields the Jacobian matrix $\mathbf{H}$, which describes the sensitivity of observations to perturbations in the state vector and enables matrix operations such as transposition and inversion.

In this study, however, no explicit linearization is performed. Instead, the ensemble-based implementation directly uses the full (potentially non-linear) observation operator $\mathcal{H}$ by perturbing the state vector and propagating these perturbations through the forward transport model (WRF-Chem). As a result, ensemble-based methods eliminate the need to construct the matrix $\mathbf{H}$ explicitly, while still enabling the effective computation of terms such as $\mathbf{HPH}^\mathrm{T}$ or $\mathbf{PH}^\mathrm{T}$.

However, while ensemble methods do not require a linearized operator, they rely on the assumption that $\mathcal{H}$ behaves approximately linearly within the range

spanned by the ensemble. Strong non-linearities in $\mathcal{H}$ can lead to biased estimates or filter divergence if this assumption is violated. In this study, the transport model is treated as sufficiently linear over the ensemble spread, consistent with standard EnKF assumptions.

Localization

Each state vector element s and its ensemble perturbations $x'_{s,n}$ are generated independently. However, due to the finite size of the ensemble, the correlation values are not exactly zero, introducing what are known as spurious correlations between state vector elements. The observation operator $\mathcal{H}$ projects the state vector perturbations $\mathbf{x'}$ into the observation space. Applying $\mathcal{H}$ results in simulated perturbations in the observations, $\mathcal{H}(\mathbf{x'})$. A single observation may be influenced by multiple state vector elements (e.g. an observation located within the overlapping plume of several ventilation shafts), naturally creating meaningful correlations between the simulated observation and these state vector elements. However, spurious intra-state vector correlations can propagate from the state vector space into the observation space, even when no true physical relationship exists. In ensemble-based Kalman filter methods, such spurious correlations degrade the analysis quality by linking unrelated state vector elements and observations, introducing noise rather than meaningful information.

Localization addresses this issue by applying a factor between 0 and 1 to the Kalman gain matrix $\mathbf{K}$, thereby trying to eliminate erroneous state vector updates that are caused by spurious correlations. When the localization coefficient is 0, the state vector element sticks to its prior estimate for that specific observation. Conversely, when the localization coefficient is 1, the Kalman gain fully incorporates the covariance information, ensuring that observations contribute appropriately to the state vector update.

Traditional localization in EnKF methods often relies on spatial proximity to determine the influence of observations on state vector updates. This approach assumes that observations closer to a state vector element (emission source) are more relevant and assigns them localization coefficients closer to 1, effectively reducing the impact of spurious correlations over long distances (Peters et al. 2005, 2007).

Localization has been shown to significantly improve the robustness and accuracy of ensemble methods. For example, Peters et al. (2007) demonstrated that applying localization enables ensemble sizes as small as 150 members to perform effectively in their case, whereas >400 ensemble members were required without localization. This conclusion was supported by their analysis of CO_2 surface flux inversions. By focusing on significant correlations, localization reduces the need for larger ensembles, thereby improving computational efficiency.

That being said, in this work, however, the localization is not determined based on spatial distance, but rather on assessing whether the correlation between a simulated observation and a state vector element is statistically significant. In the so-called CT2007 implementation, the localization is assigned the binary value of 0 or 1, based on a Student's t-test. The critical t-value corresponds to a two-tailed test with a

95 % confidence interval. For an ensemble size of 150 members, as used in this study, the critical t-value is 1.976.

B.4 Prior Emissions for Non-Reporting Shafts

While most coal mine ventilation shafts in the USCB are associated with reported emission rates in the CoMet ED, a subset of sources lack such data entirely. These include Active Coal Mines no reported emissions (ACMX) as well as Active Coal Mines in Czechia (ACMCZ), where no reporting obligation exists under the E-PRTR. As discussed in Sect. 4.1, even abandoned shafts can continue to emit CH_4, and Sect. 4.3.1 demonstrates that plumes originating from several of these non-reporting shafts are clearly detectable in the CHARM–F observations — e.g at 11:08 CEST downwind of the Czech cluster (see Fig.4.9a), or at 11:32 CEST near the Ziemowit complex (see Fig.4.11c).

To avoid the methodological issue that zero prior emissions would inhibit any posterior updates, approximate prior values were assigned to these sources, based on rough production estimates and a emission factor of 11.83 kg CH_4 emission per tonne of coal produced. This factor is reported by Fiehn et al. (2020) as an average for the USCB region. The affected shafts, along with their assigned prior emission rates, assumed coal production volumes, and sources used for their derivation, are summarized in Table B.2.

For Czech shafts, shaft-specific prior emission rates reported by Fiehn et al. (2020) were adopted where available. For Frenstat A, the same value as for CSM was assumed, while Lazy A was assigned a lower estimate due to the absence of reported data.

For a group of non-reporting shafts north of Katowice either historical production figures or conservative lower-limit assumptions were used. For example, the PowstSla mine reported a monthly coal production of 11 kt in 2016, cited by Wikipedia (last access: 13 July 2025), which references the operator's website (accessed 2 February 2016). This corresponds to a prior of 0.28 t h^{-1} per shaft and was also applied to similar cases lacking data (cf. Tab. B.2).

For the Janina and Ziemowit mining complexes, production-based estimates were derived from publicly accessible sources. Janina and Jaworzno are operated by the same company, Tauron Wydobycie S.A. For these sites, values were taken from Wikipedia (last access: 13 July 2025), which cites Grudziński 2005. For Ziemowit and the adjacent Piast IV shaft, the source was the archived operator webpage via the Wayback Machine (last access: 13 July 2025). These sources suggest production capacities consistent with emission rates of 1.22 t h^{-1} (Janina A, B and Jaworzno A) and 1.52 t h^{-1} (Ziemowit A–C and Piast IV).

It is important to emphasize that these assigned prior emissions are not based on rigorous measurement or reporting data, and should not be interpreted as accurate flux estimates. Their purpose is solely to enable participation in the inversion framework, which requires non-zero prior values. As discussed in Sect. 4.2.1, a global relative uncertainty of 100 % was assigned to all prior emissions. This allows the inversion to downscale these rough estimates to near-zero levels in the absence

of observational support. Conversely, if plumes are detected, the inversion can adjust the corresponding fluxes accordingly. Nevertheless, the posterior estimates for these non-reporting shafts remain sensitive to the assumed prior, especially when observational constraints are weak. They should therefore be interpreted with caution and considered indicative rather than definitive.

Table B.2: Prior emission assumptions for non-reporting coal mine shafts. The estimated prior is based on rough production volumes and a regional emission factor of 11.83 $\mathrm{kg\,t^{-1}}$ (cf. Fiehn et al. 2020). Shafts without reported coal extraction are assigned proxy values (see text).

Shaft	**Type**	**Coal extraction in** $\mathrm{Mt\,a^{-1}}$	**Prior emission in** $\mathrm{t\,h^{-1}}$	**Method**	**Reference**
CSA A	ACMCZ	2.36	3.18	emis. factor	Fiehn et al. (2020)
CSM A	ACMCZ	0.75	1.01	emis. factor	Fiehn et al. (2020)
CSM B	ACMCZ	0.75	1.01	emis. factor	Fiehn et al. (2020)
Darkov A	ACMCZ	1.65	2.23	emis. factor	Fiehn et al. (2020)
Paskov A	ACMCZ	0.315	0.42	emis. factor	Fiehn et al. (2020)
Paskov B	ACMCZ	0.315	0.42	emis. factor	Fiehn et al. (2020)
Frenstat A	ACMCZ	–	2.02	proxy	–
Lazy A	ACMCZ	–	0.68	proxy	–
PowstSla A	ACMX	0.011	0.28	emis. factor	EKO-PLUS (2016)
PowstSla B	ACMX	0.011	0.28	emis. factor	EKO-PLUS (2016)
Barbara A	ACMX	–	0.28	proxy	–
Bobrek A	ACMX	–	0.28	proxy	–
Boleslaw II	ACMX	–	0.28	proxy	–
Centrum A	ACMX	–	0.28	proxy	–
Pstrowski A	ACMX	–	0.28	proxy	–
Piekary A	ACMX	–	0.28	proxy	–
Piekary B	ACMX	–	0.28	proxy	–
Piekary C	ACMX	–	0.28	proxy	–
Janina A	ACMX	0.933	1.22	emis. factor	Grudziński (2005)
Janina B	ACMX	0.933	1.22	emis. factor	Grudziński (2005)
Jaworzno A	ACMX	0.933	1.22	emis. factor	Grudziński (2005)
Piast IV	ACMX	1.125	1.52	emis. factor	KW S.A. (Wayback, 2010)
Ziemowit A	ACMX	1.125	1.52	emis. factor	KW S.A. (Wayback, 2010)
Ziemowit B	ACMX	1.125	1.52	emis. factor	KW S.A. (Wayback, 2010)
Ziemowit C	ACMX	1.125	1.52	emis. factor	KW S.A. (Wayback, 2010)

Bibliography

Abshire, J. B., Riris, H., Allan, G. R., Weaver, C. J., Mao, J., Sun, X., Hasselbrack, W. E., Kawa, S. R., and Biraud, S. Pulsed airborne lidar measurements of atmospheric CO2 column absorption. Tellus B: Chemical and Physical Meteorology, 62(5):770–783, 2010. doi: 10.1111/j.1600-0889.2010.00502.x. URL https://doi.org/10.1111/j.1600-0889.2010.00502.x.

Ackermann, G. R. Means and Standard Deviations of Horizontal Wind Components, 22. Journal of Applied Meteorology and Climatology, page 959–961, 1983. doi: 10.1175/1520-0450(1983)022<0959:MASDOH>2.0.CO;2. URL https://journals.ametsoc.org/view/journals/apme/22/5/1520-0450_1983_022_0959_masdoh_2_0_co_2.xml.

Amediek, A., Fix, A., Wirth, M., and Ehret, G. Development of an OPO system at 1.57 µm for integrated path DIAL measurement of atmospheric carbon dioxide. Applied Physics B, 92(2):295–302, 2008. doi: 10.1007/s00340-008-3075-6. URL https://doi.org/10.1007/s00340-008-3075-6.

Amediek, A., Ehret, G., Fix, A., Wirth, M., Büdenbender, C., Quatrevalet, M., Kiemle, C., and Gerbig, C. CHARM-F - a new airborne integrated-path differential-absorption lidar for carbon dioxide and methane observations: measurement performance and quantification of strong point source emissions. Appl. Opt., 56 (18):5182–5197, 2017. doi: 10.1364/AO.56.005182. URL https://opg.optica.org/ao/abstract.cfm?URI=ao-56-18-5182.

Amediek, A. and Wirth, M. Pointing Verification Method for Spaceborne Lidars. Remote Sensing, 9(1), 2017. ISSN 2072-4292. doi: 10.3390/rs9010056. URL https://www.mdpi.com/2072-4292/9/1/56.

Andersen, T., Zhao, Z., de Vries, M., Nęcki, J., Swolkień, J., Menoud, M., Röckmann, T., Roiger, A., Fix, A., Peters, W., and Chen, H. Local-to-regional methane emissions from the Upper Silesian Coal Basin (USCB) quantified using UAV-based atmospheric measurements. Atmospheric Chemistry and Physics, 23(9):5191–5216, 2023. doi: 10.5194/acp-23-5191-2023. URL https://acp.copernicus.org/articles/23/5191/2023/.

Archer, D., Eby, M., Brovkin, V., Ridgwell, A., Cao, L., Mikolajewicz, U., Caldeira, K., Matsumoto, K., Munhoven, G., Montenegro, A., and Tokos, K. Atmospheric Lifetime of Fossil Fuel Carbon Dioxide. Annual Review of Earth and Planetary Sciences, 37(Volume 37, 2009):117–134, 2009. ISSN 1545-4495. doi: https://doi.org/10.1146/annurev.earth.031208.100206. URL https://www.annualreviews.org/content/journals/10.1146/annurev.earth.031208.100206.

Barnes, C., Santos, F. L. M., Libonati, R., Keeping, T., Rodrigues, R., Alves, L. M., Sivanu, S., Vahlberg, M., Alcayna, T., Otto, F., Zachariah, M., Singh, R., Mugge, M., Biehl, J., Petryna, A., Dias, M., Reis, E., and Uzquiano, S. Hot, dry and windy conditions that drove devastating Pantanal wildfires 40% more intense due to climate change. Imperial College London, Faculty of Natural Sciences, Aug 2024. URL http://hdl.handle.net/10044/1/113726. Report, last accessed: 2025-02-25.

Barton-Grimley, R. A., Nehrir, A. R., Kooi, S. A., Collins, J. E., Harper, D. B., Notari, A., Lee, J., DiGangi, J. P., Choi, Y., and Davis, K. J. Evaluation of the High Altitude Lidar Observatory (HALO) methane retrievals during the summer 2019 ACT-America campaign. Atmospheric Measurement Techniques, 15(15):4623–4650, 2022. doi: 10.5194/amt-15-4623-2022. URL https://amt.copernicus.org/articles/15/4623/2022/.

BBC News. Czech coal mine methane gas explosion kills 13. BBC News, December 2018. URL https://www.bbc.com/news/world-europe-46644793. Last accessed: 15 July 2025.

Bhimireddy, S. R. and Bhaganagar, K. Short-term passive tracer plume dispersion in convective boundary layer using a high-resolution WRF-ARW model. Atmospheric Pollution Research, 9(5):901–911, 2018. ISSN 1309-1042. doi: https://doi.org/10.1016/j.apr.2018.02.010. URL https://www.sciencedirect.com/science/article/pii/S1309104217305597.

Blaylock, B. K., Horel, J. D., and Crosman, E. T. Impact of Lake Breezes on Summer Ozone Concentrations in the Salt Lake Valley. Journal of Applied Meteorology and Climatology, 56(2):353 – 370, 2017. doi: 10.1175/JAMC-D-16-0216.1. URL https://journals.ametsoc.org/view/journals/apme/56/2/jamc-d-16-0216.1.xml.

Bousquet, P., Pierangelo, C., Bacour, C., Marshall, J., Peylin, P., Ayar, P. V., Ehret, G., Bréon, F.-M., Chevallier, F., Crevoisier, C., Gibert, F., Rairoux, P., Kiemle, C., Armante, R., Bès, C., Cassé, V., Chinaud, J., Chomette, O., Delahaye, T., Edouart, D., Estève, F., Fix, A., Friker, A., Klonecki, A., Wirth, M., Alpers, M., and Millet, B. Error Budget of the MEthane Remote LIdar missioN and Its Impact on the Uncertainties of the Global Methane Budget. Journal of Geophysical Research: Atmospheres, 123(20):11,766–11,785, 2018. doi: 10.1029/2018JD028907. URL https://agupubs.onlinelibrary.wiley.com/doi/abs/10.1029/2018JD028907.

Boyd, S. and Vandenberghe, L. Introduction to Applied Linear Algebra: Vectors, Matrices, and Least Squares. Cambridge University Press, 2018. URL https://web.stanford.edu/~boyd/vmls/.

Brunner, D., Kuhlmann, G., Marshall, J., Clément, V., Fuhrer, O., Broquet, G., Löscher, A., and Meijer, Y. Accounting for the vertical distribution of emissions

in atmospheric CO_2 simulations. Atmospheric Chemistry and Physics, 19(7):4541–4559, 2019. doi: 10.5194/acp-19-4541-2019. URL https://acp.copernicus.org/articles/19/4541/2019/.

Brunner, D., Kuhlmann, G., Henne, S., Koene, E., Kern, B., Wolff, S., Voigt, C., Jöckel, P., Kiemle, C., Roiger, A., Fiehn, A., Krautwurst, S., Gerilowski, K., Bovensmann, H., Borchardt, J., Gałkowski, M., Gerbig, C., Marshall, J., Klonecki, A., Prunet, P., Hanfland, R., Pattantyús-Ábrahám, M., Wyszogrodzki, A., and Fix, A. Evaluation of simulated CO_2 power plant plumes from six high-resolution atmospheric transport models. Atmospheric Chemistry and Physics, 23(4):2699–2728, 2023. doi: 10.5194/acp-23-2699-2023. URL https://acp.copernicus.org/articles/23/2699/2023/.

Busch, D., Harte, R., Krätzig, W. B., and Montag, U. New natural draft cooling tower of 200 m of height. Engineering Structures, 24(12):1509–1521, 2002. ISSN 0141-0296. doi: https://doi.org/10.1016/S0141-0296(02)00082-2. URL https://www.sciencedirect.com/science/article/pii/S0141029602000822.

Byrne, B., Baker, D. F., Basu, S., Bertolacci, M., Bowman, K. W., Carroll, D., Chatterjee, A., Chevallier, F., Ciais, P., Cressie, N., Crisp, D., Crowell, S., Deng, F., Deng, Z., Deutscher, N. M., Dubey, M. K., Feng, S., García, O. E., Griffith, D. W. T., Herkommer, B., Hu, L., Jacobson, A. R., Janardanan, R., Jeong, S., Johnson, M. S., Jones, D. B. A., Kivi, R., Liu, J., Liu, Z., Maksyutov, S., Miller, J. B., Miller, S. M., Morino, I., Notholt, J., Oda, T., O'Dell, C. W., Oh, Y.-S., Ohyama, H., Patra, P. K., Peiro, H., Petri, C., Philip, S., Pollard, D. F., Poulter, B., Remaud, M., Schuh, A., Sha, M. K., Shiomi, K., Strong, K., Sweeney, C., Té, Y., Tian, H., Velazco, V. A., Vrekoussis, M., Warneke, T., Worden, J. R., Wunch, D., Yao, Y., Yun, J., Zammit-Mangion, A., and Zeng, N. National CO_2 budgets (2015–2020) inferred from atmospheric CO_2 observations in support of the global stocktake. Earth System Science Data, 15(2):963–1004, 2023. doi: 10.5194/essd-15-963-2023. URL https://essd.copernicus.org/articles/15/963/2023/.

Cambaliza, M. O. L., Shepson, P. B., Caulton, D. R., Stirm, B., Samarov, D., Gurney, K. R., Turnbull, J., Davis, K. J., Possolo, A., Karion, A., Sweeney, C., Moser, B., Hendricks, A., Lauvaux, T., Mays, K., Whetstone, J., Huang, J., Razlivanov, I., Miles, N. L., and Richardson, S. J. Assessment of uncertainties of an aircraft-based mass balance approach for quantifying urban greenhouse gas emissions. Atmospheric Chemistry and Physics, 14(17):9029–9050, 2014. doi: 10.5194/acp-14-9029-2014. URL https://acp.copernicus.org/articles/14/9029/2014/.

CAMS. CAMS global inversion-optimised greenhouse gas fluxes and concentrations. Copernicus Atmosphere Monitoring Service (CAMS) Atmosphere Data Store (ADS), 2022. URL https://ads.atmosphere.copernicus.eu/cdsapp#!/dataset/cams-global-greenhouse-gas-inversion?tab=form. AUTHORS Arjo Segers (TNO), Sander Houweling (VU), DOI 10.24381/ed2851d2, last accessed: 2022-05-12, v20r1.

CAMS, C. Copernicus: Pantanal and Amazon wildfires saw their worst wildfires in almost two decades. European Centre for Medium-Range Weather Forecasts (ECMWF), Sep 2024. URL https://atmosphere.copernicus.eu/copernicus-pantanal-and-amazon-wildfires-saw-their-worst-wildfires-almost-two-decades. news release, last accessed: 2025-02-25.

CEOS, G. A. Kuze, A. von-Bargen, A. Dehn, A. Taube, A. Kavvada, B. Lefer, B. Poulter, B. Greenaway, C. Deniel, C. Bognar, D. Crisp, F. Chevallier, G. Gostinicchi, G. Balsamo, H. Pohjola, H. Suto, J.-C. Lambert, J. Privette, J. Schulz, J. Worden, J. Marshall, K. Pryor, K. Bowman, L. Zhang, M. Dowell, N. Donoho, N. Bradshaw, P. Green, O. Tarasova, P. Palmer, R. Nassar, R. Engelen, R. Lang, S. Burns, S. Combley, S. Kondragunta, S. Elliott, S. Pinnock, S. Briggs, S. Ramage, W. Su, Y. Meijer: CEOS-CGMS Greenhouse Gas Roadmap. Joint CEOS-CGMS Working Group on Climate, Issue 2, Version 1.0, October 2024. URL https://ceos.org/document_management/Publications/Publications-and-Key-Documents/Atmosphere/CEOS_CGMS_GHG_Roadmap_Issue_2_V1.0_FINAL.pdf.

Conley, S., Franco, G., Faloona, I., Blake, D. R., Peischl, J., and Ryerson, T. B. Methane emissions from the 2015 Aliso Canyon blowout in Los Angeles, CA. Science, 351(6279):1317–1320, 2016. doi: 10.1126/science.aaf2348. URL https://www.science.org/doi/abs/10.1126/science.aaf2348.

Connor, B. J., Bösch, H., Toon, G., Sen, B., Miller, C., and Crisp, D. Orbiting Carbon Observatory: Inverse method and prospective error analysis. Journal of Geophysical Research: Atmospheres, 113(D5), 2008. doi: https://doi.org/10.1029/2006JD008336. URL https://agupubs.onlinelibrary.wiley.com/doi/abs/10.1029/2006JD008336.

Cook, J., Nuccitelli, D., Green, S., Richardson, M., Winkler, B., Painting, R., Way, R., Jacobs, P., and Skuce, A. Quantifying the consensus on anthropogenic global warming in the scientific literature. Environmental Research Letters, 8(2):024024, may 2013. doi: 10.1088/1748-9326/8/2/024024. URL https://dx.doi.org/10.1088/1748-9326/8/2/024024.

Copernicus, C. C. S. Climate Indicator: Temperature, April 2024. URL https://climate.copernicus.eu/climate-indicators/temperature. Last updated on 22 April 2024. Implemented by ECMWF as part of the Copernicus Programme. Last accessed: 2025-02-19.

Crippa, M., Guizzardi, D., Solazzo, E., Muntean, M., Schaaf, E., Monforti-Ferrario, F., Banja, M., Olivier, J., Grassi, G., Rossi, S., and Vignati, E. GHG emissions of all world countries - 2021 Report. Publications Office of the European Union, EUR 31182 EN, 2021. doi: https://doi.org/10.2760/173513. URL https://edgar.jrc.ec.europa.eu/dataset_ghg70. JRC126363.

Crippa, M., Guizzardi, D., Pagani, F., Schiavina, M., Melchiorri, M., Pisoni, E., Graziosi, F., Muntean, M., Maes, J., Dijkstra, L., Van Damme, M., Clarisse, L., and Coheur, P. Insights into the spatial distribution of global, national,

and subnational greenhouse gas emissions in the Emissions Database for Global Atmospheric Research (EDGAR v8.0). Earth System Science Data, 16(6):2811–2830, 2024. doi: https://doi.org/10.5194/essd-16-2811-2024. URL https://essd.copernicus.org/articles/16/2811/2024/.

Cusworth, D. H., Thorpe, A. K., Miller, C. E., Ayasse, A. K., Jiorle, R., Duren, R. M., Nassar, R., Mastrogiacomo, J.-P., and Nelson, R. R. Two years of satellite-based carbon dioxide emission quantification at the world's largest coal-fired power plants. Atmospheric Chemistry and Physics, 23(22):14577–14591, 2023. doi: 10.5194/acp-23-14577-2023. URL https://acp.copernicus.org/articles/23/14577/2023/.

Cusworth, D. H., Thorpe, A. K., Ayasse, A. K., Stepp, D., Heckler, J., Asner, G. P., Miller, C. E., Yadav, V., Chapman, J. W., Eastwood, M. L., Green, R. O., Hmiel, B., Lyon, D. R., and Duren, R. M. Strong methane point sources contribute a disproportionate fraction of total emissions across multiple basins in the United States. Proceedings of the National Academy of Sciences, 119(38):e2202338119, 2022. doi: 10.1073/pnas.2202338119. URL https://www.pnas.org/doi/abs/10.1073/pnas.2202338119.

Davies, H. C. and Turner, R. E. Updating prediction models by dynamical relaxation: an examination of the technique. Quarterly Journal of the Royal Meteorological Society, 103(436):225–245, 1977. doi: https://doi.org/10.1002/qj.49710343602. URL https://rmets.onlinelibrary.wiley.com/doi/abs/10.1002/qj.49710343602.

Deetz, C. H. The Lambert conformal conic projection. US Department of Commerce, US Coast and Geodetic Survey, Special Publication, (47):1–61, 1918. URL https://geodesy.noaa.gov/library/pdfs/Special_Publication_No_47.pdf. National Oceanic and Atmospheric Administration, Special Publication No. 47.

Die Zeit. 13 Tote nach Explosion in Bergwerk in Tschechien. DIE ZEIT, December 2018. URL https://www.zeit.de/news/2018-12/21/13-tote-nach-explosion-in-bergwerk-in-tschechien-181221-99-310805. Last accessed: 15 July 2025.

Dubey, L., Cooper, J., and Hawkes, A. Minimum detection limits of the TROPOMI satellite sensor across North America and their implications for measuring oil and gas methane emissions. Science of The Total Environment, 872:162222, 2023. ISSN 0048-9697. doi: https://doi.org/10.1016/j.scitotenv.2023.162222. URL https://www.sciencedirect.com/science/article/pii/S0048969723008380.

Dufour, E. and Bréon, F.-M. Spaceborne estimate of atmospheric CO_2 column by use of the differential absorption method: error analysis. Appl. Opt., 42(18):3595–3609, Jun 2003. doi: 10.1364/AO.42.003595. URL https://opg.optica.org/ao/abstract.cfm?URI=ao-42-18-3595.

E-PRTR. Industrial Reporting under the Industrial Emissions Directive 2010/75/EU and European Pollutant Release and Transfer Register Regulation (EC) No 166/2006. European Environment Agency, 2021. URL https://www.eea.europa.eu/ds_resolveuid/9d55e39efe954e998a1dca7689207482. version 4, March 2021, last access: 14.06.2021.

E-PRTR. The European Pollutant Release and Transfer Register (EPRTR). European Environment Agency, Dez. 2023. URL https://doi.org/10.2909/63a14e09-d1f5-490d-80cf-6921e4e69551. reported under IED Art.72, version 10.0.

ECMWF. IFS Documentation CY45R1 - Part III : Dynamics and numerical procedures. IFS Documentation CY45R1, 3, 2018. doi: 10.21957/ddbrpvy90. URL https://www.ecmwf.int/node/18713. last access: 2020-07-27.

Ehret, G., Kiemle, C., Wirth, M., Amediek, A., Fix, A., and Houweling, S. Spaceborne remote sensing of CO_2, CH_4, and N_2O by integrated path differential absorption lidar: a sensitivity analysis. Applied Physics B, 90(3):593–608, Mar 2008. ISSN 1432-0649. doi: 10.1007/s00340-007-2892-3. URL https://doi.org/10.1007/s00340-007-2892-3.

Ehret, G., Amediek, A., and Quatrevalet, M. Towards a Greenhouse Gas Lidar in Space, pages 799–813. Springer Berlin Heidelberg, Berlin, Heidelberg, 2012. ISBN 978-3-642-30183-4. doi: 10.1007/978-3-642-30183-4_48. URL https://doi.org/10.1007/978-3-642-30183-4_48. editor: Ulrich Schumann.

Ehret, G., Bousquet, P., Pierangelo, C., Alpers, M., Millet, B., Abshire, J. B., Bovensmann, H., Burrows, J. P., Chevallier, F., Ciais, P., Crevoisier, C., Fix, A., Flamant, P., Frankenberg, C., Gibert, F., Heim, B., Heimann, M., Houweling, S., Hubberten, H. W., Jöckel, P., Law, K., Löw, A., Marshall, J., Agusti-Panareda, A., Payan, S., Prigent, C., Rairoux, P., Sachs, T., Scholze, M., and Wirth, M. MERLIN: A French-German Space Lidar Mission Dedicated to Atmospheric Methane. Remote Sensing, 9(10), 2017. ISSN 2072-4292. doi: 10.3390/rs9101052. URL https://www.mdpi.com/2072-4292/9/10/1052.

Ehret, T., De Truchis, A., Mazzolini, M., Morel, J.-M., d'Aspremont, A., Lauvaux, T., Duren, R., Cusworth, D., and Facciolo, G. Global Tracking and Quantification of Oil and Gas Methane Emissions from Recurrent Sentinel-2 Imagery. Environmental Science & Technology, 56(14):10517–10529, 2022. doi: 10.1021/acs.est.1c08575. URL https://doi.org/10.1021/acs.est.1c08575. PMID: 35797726.

Fiehn, A., Kostinek, J., Eckl, M., Klausner, T., Gałkowski, M., Chen, J., Gerbig, C., Röckmann, T., Maazallahi, H., Schmidt, M., Korbeń, P., Nęcki, J., Jagoda, P., Wildmann, N., Mallaun, C., Bun, R., Nickl, A.-L., Jöckel, P., Fix, A., and Roiger, A. Estimating CH_4, CO_2 and CO emissions from coal mining and industrial activities in the Upper Silesian Coal Basin using an aircraft-based mass balance approach. Atmospheric Chemistry and Physics, 20(21):12675–12695, 2020. doi: 10.5194/acp-20-12675-2020. URL https://acp.copernicus.org/articles/20/12675/2020/.

Fix, A., Büdenbender, C., Wirth, M., Quatrevalet, M., Amediek, A., Kiemle, C., and Ehret, G. Optical parametric oscillators and amplifiers for airborne and spaceborne active remote sensing of CO_2 and CH_4. In Singh, U. N. and Pappalardo, G., editors, Lidar Technologies, Techniques, and Measurements for Atmospheric Remote Sensing VII, volume 8182, page 818206. International Society for Optics and Photonics, SPIE, 2011. doi: 10.1117/12.898412. URL https://doi.org/10.1117/12.898412.

Fix, A., Amediek, A., Büdenbender, C., Ehret, G., Kiemle, C., Quatrevalet, M., Wirth, M., Wolff, S., Bovensmann, H., Butz, A., Gałkowski, M., Gerbig, C., Jöckel, P., Marshall, J., Nęcki, J., Pfeilsticker, K., Roiger, A., Swolkień, J., Zöger, M., and the CoMet team. CH_4 and CO_2 IPDA Lidar Measurements During the Comet 2018 Airborne Field Campaign. EPJ Web Conf., ILRC 29, 2020. doi: 10.1051/epjconf/202023703005. URL https://doi.org/10.1051/epjconf/202023703005. Volume 237, Article Number 03005.

Frankenberg, C., Thorpe, A. K., Thompson, D. R., Hulley, G., Kort, E. A., Vance, N., Borchardt, J., Krings, T., Gerilowski, K., Sweeney, C., Conley, S., Bue, B. D., Aubrey, A. D., Hook, S., and Green, R. O. Airborne methane remote measurements reveal heavy-tail flux distribution in Four Corners region. Proceedings of the National Academy of Sciences, 113(35):9734–9739, 2016. doi: 10.1073/pnas.1605617113. URL https://www.pnas.org/doi/abs/10.1073/pnas.1605617113.

Frankenberg, C., Bar-On, Y. M., Yin, Y., Wennberg, P. O., Jacob, D. J., and Michalak, A. M. Data Drought in the Humid Tropics: How to Overcome the Cloud Barrier in Greenhouse Gas Remote Sensing. Geophysical Research Letters, 51(8):e2024GL108791, 2024. doi: https://doi.org/10.1029/2024GL108791. URL https://agupubs.onlinelibrary.wiley.com/doi/abs/10.1029/2024GL108791. e2024GL108791 2024GL108791.

Friedlingstein, P., O'Sullivan, M., Jones, M. W., Andrew, R. M., Bakker, D. C. E., Hauck, J., Landschützer, P., Le Quéré, C., Luijkx, I. T., Peters, G. P., Peters, W., Pongratz, J., Schwingshackl, C., Sitch, S., Canadell, J. G., Ciais, P., Jackson, R. B., Alin, S. R., Anthoni, P., Barbero, L., Bates, N. R., Becker, M., Bellouin, N., Decharme, B., Bopp, L., Brasika, I. B. M., Cadule, P., Chamberlain, M. A., Chandra, N., Chau, T.-T.-T., Chevallier, F., Chini, L. P., Cronin, M., Dou, X., Enyo, K., Evans, W., Falk, S., Feely, R. A., Feng, L., Ford, D. J., Gasser, T., Ghattas, J., Gkritzalis, T., Grassi, G., Gregor, L., Gruber, N., Gürses, O., Harris, I., Hefner, M., Heinke, J., Houghton, R. A., Hurtt, G. C., Iida, Y., Ilyina, T., Jacobson, A. R., Jain, A., Jarníková, T., Jersild, A., Jiang, F., Jin, Z., Joos, F., Kato, E., Keeling, R. F., Kennedy, D., Klein Goldewijk, K., Knauer, J., Korsbakken, J. I., Körtzinger, A., Lan, X., Lefèvre, N., Li, H., Liu, J., Liu, Z., Ma, L., Marland, G., Mayot, N., McGuire, P. C., McKinley, G. A., Meyer, G., Morgan, E. J., Munro, D. R., Nakaoka, S.-I., Niwa, Y., O'Brien, K. M., Olsen, A., Omar, A. M., Ono, T., Paulsen, M., Pierrot, D., Pocock, K., Poulter, B., Powis, C. M., Rehder, G., Resplandy, L., Robertson, E., Rödenbeck, C., Rosan, T. M., Schwinger, J., Séférian, R., Smallman, T. L., Smith, S. M., Sospedra-Alfonso, R.,

Sun, Q., Sutton, A. J., Sweeney, C., Takao, S., Tans, P. P., Tian, H., Tilbrook, B., Tsujino, H., Tubiello, F., van der Werf, G. R., van Ooijen, E., Wanninkhof, R., Watanabe, M., Wimart-Rousseau, C., Yang, D., Yang, X., Yuan, W., Yue, X., Zaehle, S., Zeng, J., and Zheng, B. Global Carbon Budget 2023. Earth System Science Data, 15(12):5301–5369, 2023. doi: 10.5194/essd-15-5301-2023. URL https://essd.copernicus.org/articles/15/5301/2023/.

Fuentes Andrade, B., Buchwitz, M., Reuter, M., Bovensmann, H., Richter, A., Boesch, H., and Burrows, J. P. A method for estimating localized CO_2 emissions from co-located satellite XCO_2 and NO_2 images. Atmospheric Measurement Techniques, 17(3):1145–1173, 2024. doi: 10.5194/amt-17-1145-2024. URL https://amt.copernicus.org/articles/17/1145/2024/.

Gadhavi, H. S., Arora, A., Jain, C., Sha, M. K., Hase, F., Frey, M., Ramachandran, S., and Jayaraman, A. Validation and assessment of satellite-based columnar CO_2 and CH_4 mixing-ratios from GOSAT and OCO-2 satellites over India. Atmospheric Measurement Techniques Discussions, 2024:1–23, 2024. doi: 10.5194/amt-2024-167. URL https://amt.copernicus.org/preprints/amt-2024-167/.

Gałkowski, M., Marshall, J., Koch, F.-T., Chen, J., Fiehn, A., Roiger, A., Eckl, M., Kostinek, J., Swolkień, J., and Gerbig, C. Estimating emissions of methane and carbon dioxide sources using analytical Bayesian inversion system based on WRF-GHG tagged tracer simulations. In EGU General Assembly 2020, Online, 4–8 May 2020, May 2020. EGU, Copernicus Meetings. doi: https://doi.org/10.5194/egusphere-egu2020-16082. URL https://presentations.copernicus.org/EGU2020/EGU2020-16082_presentation.pdf. EGU2020-16082.

Gałkowski, M., Fiehn, A., Swolkień, J., Stanisavljevic, M., Korbeń, P., Menoud, M., Nęcki, J., Roiger, A., Röckmann, T., Gerbig, C., and Fix, A. Emissions of CH4 and CO2 over the Upper Silesian Coal Basin (Poland) and its vicinity, 2021a. URL https://meta.icos-cp.eu/objects/4YLOpOtT0keMUckH1MrhxZZW. doi: 10.18160/3K6Z-4H73. Version: ED_v4.01. License: ICOS CCBY4 Data Licence.

Gałkowski, M., Jordan, A., Rothe, M., Marshall, J., Koch, F.-T., Chen, J., Agusti-Panareda, A., Fix, A., and Gerbig, C. In situ observations of greenhouse gases over Europe during the CoMet 1.0 campaign aboard the HALO aircraft. Atmospheric Measurement Techniques, 14(2):1525–1544, 2021b. doi: 10.5194/amt-14-1525-2021. URL https://amt.copernicus.org/articles/14/1525/2021/.

Gerilowski, K., Tretner, A., Krings, T., Buchwitz, M., Bertagnolio, P. P., Belemezov, F., Erzinger, J., Burrows, J. P., and Bovensmann, H. MAMAP – a new spectrometer system for column-averaged methane and carbon dioxide observations from aircraft: instrument description and performance analysis. Atmospheric Measurement Techniques, 4(2):215–243, 2011. doi: 10.5194/amt-4-215-2011. URL https://amt.copernicus.org/articles/4/215/2011/.

Giez, A., Zöger, M., Mallaun, C., Nenakhov, V., Schimpf, M., Grad, C., Numberger, A., and Raynor, K. Determination of the Measurement Errors for the HALO Basic Data System BAHAMAS by Means of Error Propagation. Technical report, DLR-Forschungsbericht, Januar 2023. URL https://doi.org/10.57676/5rdc-q708. DLR-FB-2022-27.

Gimmestad, G. G. and Roberts, D. W. Lidar Engineering: Introduction to Basic Principles. Cambridge University Press, 2023. ISBN 9781139014106. doi: 10.1017/9781139014106. URL https://www.cambridge.org/core/books/lidar-engineering/B794EC0EF93BA883031498865FF91F78.

Gordon, I., Rothman, L., Hill, C., Kochanov, R., Tan, Y., Bernath, P., Birk, M., Boudon, V., Campargue, A., Chance, K., Drouin, B., Flaud, J.-M., Gamache, R., Hodges, J., Jacquemart, D., Perevalov, V., Perrin, A., Shine, K., Smith, M.-A., Tennyson, J., Toon, G., Tran, H., Tyuterev, V., Barbe, A., Császár, A., Devi, V., Furtenbacher, T., Harrison, J., Hartmann, J.-M., Jolly, A., Johnson, T., Karman, T., Kleiner, I., Kyuberis, A., Loos, J., Lyulin, O., Massie, S., Mikhailenko, S., Moazzen-Ahmadi, N., Müller, H., Naumenko, O., Nikitin, A., Polyansky, O., Rey, M., Rotger, M., Sharpe, S., Sung, K., Starikova, E., Tashkun, S., Auwera, J. V., Wagner, G., Wilzewski, J., Wcisło, P., Yu, S., and Zak, E. The HITRAN2016 molecular spectroscopic database. Journal of Quantitative Spectroscopy and Radiative Transfer, 203:3–69, 2017. ISSN 0022-4073. doi: https://doi.org/10.1016/j.jqsrt.2017.06.038. URL https://www.sciencedirect.com/science/article/pii/S0022407317301073. HITRAN2016 Special Issue.

Grant, W. B. Effect of differential spectral reflectance on DIAL measurements using topographic targets. Appl. Opt., 21(13):2390–2394, Jul 1982. doi: 10.1364/AO.21.002390. URL https://opg.optica.org/ao/abstract.cfm?URI=ao-21-13-2390.

Grell, G. A., Peckham, S. E., Schmitz, R., McKeen, S. A., Frost, G., Skamarock, W. C., and Eder, B. Fully coupled "online" chemistry within the WRF model. Atmospheric Environment, 39(37):6957–6975, 2005. ISSN 1352-2310. doi: https://doi.org/10.1016/j.atmosenv.2005.04.027. URL https://www.sciencedirect.com/science/article/pii/S1352231005003560.

Grell, G. A. and Dévényi, D. A generalized approach to parameterizing convection combining ensemble and data assimilation techniques. Geophysical Research Letters, 29(14):38–1–38–4, 2002. doi: https://doi.org/10.1029/2002GL015311. URL https://agupubs.onlinelibrary.wiley.com/doi/abs/10.1029/2002GL015311.

Groß, S., Esselborn, M., Weinzierl, B., Wirth, M., Fix, A., and Petzold, A. Aerosol classification by airborne high spectral resolution lidar observations. Atmospheric Chemistry and Physics, 13(5):2487–2505, 2013. doi: 10.5194/acp-13-2487-2013. URL https://acp.copernicus.org/articles/13/2487/2013/.

Grudziński, Z. Wystarczalność zasobów węgla kamiennego w Polsce w świetle planu dostępu do zasobów oraz prognoz zapotrzebowania na węgiel. [The availability of hard coal resources in Poland in light of the access plan for resources and forecasts for coal demand]. Polityka Energetyczna, 8(2), 2005. ISSN 1429-6675. URL https://se.min-pan.krakow.pl/publikacje/05_30zg_pe.pdf. Accessed: 2025-07-13, in Polish.

Guanter, L., Irakulis-Loitxate, I., no, J. G., Sánchez-García, E., Cusworth, D. H., Varon, D. J., Cogliati, S., and Colombo, R. Mapping methane point emissions with the PRISMA spaceborne imaging spectrometer. Remote Sensing of Environment, 265:112671, 2021. ISSN 0034-4257. doi: https://doi.org/10.1016/j.rse.2021.112671. URL https://www.sciencedirect.com/science/article/pii/S0034425721003916.

Han, G., Huang, Y., Shi, T., Zhang, H., Li, S., Zhang, H., Chen, W., Liu, J., and Gong, W. Quantifying CO_2 emissions of power plants with Aerosols and Carbon Dioxide Lidar onboard DQ-1. Remote Sensing of Environment, 313:114368, 2024. ISSN 0034-4257. doi: https://doi.org/10.1016/j.rse.2024.114368. URL https://www.sciencedirect.com/science/article/pii/S0034425724003948.

Hancock, S. E., Jacob, D. J., Chen, Z., Nesser, H., Davitt, A., Varon, D. J., Sulprizio, M. P., Balasus, N., Estrada, L. A., Cazorla, M., Dawidowski, L., Diez, S., East, J. D., Penn, E., Randles, C. A., Worden, J., Aben, I., Parker, R. J., and Maasakkers, J. D. Satellite quantification of methane emissions from South American countries: a high-resolution inversion of TROPOMI and GOSAT observations. Atmospheric Chemistry and Physics, 25(2):797–817, 2025. doi: 10.5194/acp-25-797-2025. URL https://acp.copernicus.org/articles/25/797/2025/.

Hanfland, R., Brunner, D., Voigt, C., Fiehn, A., Roiger, A., and Pattantyús-Ábrahám, M. The Lagrangian Atmospheric Radionuclide Transport Model (ARTM) – sensitivity studies and evaluation using airborne measurements of power plant emissions. Atmospheric Chemistry and Physics, 24(4):2511–2534, 2024. doi: 10.5194/acp-24-2511-2024. URL https://acp.copernicus.org/articles/24/2511/2024/.

Henderson, H. V. and Searle, S. R. On Deriving the Inverse of a Sum of Matrices. SIAM Review, 23(1):53–60, 1981. doi: 10.1137/1023004. URL https://doi.org/10.1137/1023004.

Ho, D., Gałkowski, M., Reum, F., Botía, S., Marshall, J., Totsche, K. U., and Gerbig, C. Recommended coupling to global meteorological fields for long-term tracer simulations with WRF-GHG. Geoscientific Model Development, 17(20):7401–7422, 2024. doi: 10.5194/gmd-17-7401-2024. URL https://gmd.copernicus.org/articles/17/7401/2024/.

Houweling, S., Bergamaschi, P., Chevallier, F., Heimann, M., Kaminski, T., Krol, M., Michalak, A. M., and Patra, P. Global inverse modeling of CH_4 sources and sinks: an overview of methods. Atmospheric Chemistry and Physics, 17(1):235–256, 2017.

doi: 10.5194/acp-17-235-2017. URL https://acp.copernicus.org/articles/17/235/2017/.

Iacono, M. J., Delamere, J. S., Mlawer, E. J., Shephard, M. W., Clough, S. A., and Collins, W. D. Radiative forcing by long-lived greenhouse gases: Calculations with the AER radiative transfer models. Journal of Geophysical Research: Atmospheres, 113(D13), 2008. doi: https://doi.org/10.1029/2008JD009944. URL https://agupubs.onlinelibrary.wiley.com/doi/abs/10.1029/2008JD009944.

IPCC. 2006 IPCC Guidelines for National Greenhouse Gas Inventories. Edited by: H. S. Eggleston, L. Buendia, K. Miwa, T. Ngara and K. Tanabe. Institute for Global Environmental Strategies (IGES), Hayama, Japan, 2006. ISBN 4-88788-032-4. URL https://www.pcbs.gov.ps/Portals/_PCBS/Class/English/Geography/IPCC.pdf.

IPCC. Quality Assurance/Quality Control and Verification, 2019 Refinement to the 2006 IPCC Guidelines for National Greenhouse Gas Inventories. Intergovernmental Panel on Climate Change (IPCC). Authors: S. Maksyutov, S. Eggleston, J. H. Woo, S. Fang, J. Witi, M. Gillenwater, J. Goodwin and F. Tubiello, 2019. URL https://www.ipcc-nggip.iges.or.jp/public/2019rf/pdf/1_Volume1/19R_V1_Ch06_QA_QC.pdf. Chapter 6: QA/QC and Verification, last accessed: 2025-02-26.

IPCC. 2021: Summary for Policymakers. In Climate Change 2021: The Physical Science Basis. Contribution of Working Group I to the Sixth Assessment Report of the Intergovernmental Panel on Climate Change, pages 3–32. [V. Masson-Delmotte, P. Zhai, A. Pirani, S. L. Connors, C. Péan, S. Berger, N. Caud, Y. Chen, L. Goldfarb, M. I. Gomis, M. Huang, K. Leitzell, E. Lonnoy, J. B. R. Matthews, T. K. Maycock, T. Waterfield, O. Yelekçi, R. Yu and B. Zhou (eds.)]. Cambridge University Press, Cambridge, United Kingdom and New York, NY, USA, 2021. doi: 10.1017/9781009157896.001. URL https://www.cambridge.org/core/books/climate-change-2021-the-physical-science-basis/summary-for-policymakers/8E7A4E3AE6C364220F3B76A189CC4D4C.

Irakulis-Loitxate, I., Guanter, L., Liu, Y.-N., Varon, D. J., Maasakkers, J. D., Zhang, Y., Chulakadabba, A., Wofsy, S. C., Thorpe, A. K., Duren, R. M., Frankenberg, C., Lyon, D. R., Hmiel, B., Cusworth, D. H., Zhang, Y., Segl, K., no, J. G., Sánchez-García, E., Sulprizio, M. P., Cao, K., Zhu, H., Liang, J., Li, X., Aben, I., and Jacob, D. J. Satellite-based survey of extreme methane emissions in the Permian basin. Science Advances, 7(27):eabf4507, 2021. doi: 10.1126/sciadv.abf4507. URL https://www.science.org/doi/abs/10.1126/sciadv.abf4507.

Irakulis-Loitxate, I., Guanter, L., Maasakkers, J. D., Zavala-Araiza, D., and Aben, I. Satellites Detect Abatable Super-Emissions in One of the World's Largest Methane Hotspot Regions. Environmental Science & Technology, 56(4):2143–2152, 2022. doi: 10.1021/acs.est.1c04873. URL https://doi.org/10.1021/acs.est.1c04873. PMID: 35102741.

Jacob, D. J., Varon, D. J., Cusworth, D. H., Dennison, P. E., Frankenberg, C., Gautam, R., Guanter, L., Kelley, J., McKeever, J., Ott, L. E., Poulter, B., Qu, Z., Thorpe, A. K., Worden, J. R., and Duren, R. M. Quantifying methane emissions from the global scale down to point sources using satellite observations of atmospheric methane. Atmospheric Chemistry and Physics, 22(14):9617–9646, 2022. doi: 10.5194/acp-22-9617-2022. URL https://acp.copernicus.org/articles/22/9617/2022/.

Jacob, D. J. Lectures on Inverse Modeling. Harvard University, 2007. URL https://reef.atmos.colostate.edu/~odell/at652/t_project/jacob_lectures_inverse_modeling.pdf. last access: 2025-06-09.

Jervis, D., McKeever, J., Durak, B. O. A., Sloan, J. J., Gains, D., Varon, D. J., Ramier, A., Strupler, M., and Tarrant, E. The GHGSat-D imaging spectrometer. Atmospheric Measurement Techniques, 14(3):2127–2140, 2021. doi: 10.5194/amt-14-2127-2021. URL https://amt.copernicus.org/articles/14/2127/2021/.

Jiménez, P. A., Dudhia, J., González-Rouco, J. F., Navarro, J., Montávez, J. P., and García-Bustamante, E. A Revised Scheme for the WRF Surface Layer Formulation. Monthly Weather Review, 140(3):898 – 918, 2012. doi: 10.1175/MWR-D-11-00056.1. URL https://journals.ametsoc.org/view/journals/mwre/140/3/mwr-d-11-00056.1.xml.

Jiménez, P. A., Dudhia, J., González-Rouco, J. F., Montávez, J. P., García-Bustamante, E., Navarro, J., Arellano, J. V.-G. d, and Muñoz-Roldán, A. An evaluation of WRF's ability to reproduce the surface wind over complex terrain based on typical circulation patterns. Journal of Geophysical Research: Atmospheres, 118(14):7651–7669, 2013. doi: https://doi.org/10.1002/jgrd.50585. URL https://agupubs.onlinelibrary.wiley.com/doi/abs/10.1002/jgrd.50585.

Journal of Laws. Regulation of the Minister of Energy of 23 November 2016 on Detailed Requirements for Operating Underground Mining Plants. Journal of Laws 2017, Item 1118, Warsaw, June 2017. URL https://dziennikustaw.gov.pl/DU/rok/2017/pozycja/1118. Promulgated on 9 June 2017. (In Polish). Last accessed: 15 July 2025.

Kaifler, B. and Kaifler, N. A Compact Rayleigh Autonomous Lidar (CORAL) for the middle atmosphere. Atmospheric Measurement Techniques, 14(2):1715–1732, 2021. doi: 10.5194/amt-14-1715-2021. URL https://amt.copernicus.org/articles/14/1715/2021/.

Kerkweg, A. and Jöckel, P. The 1-way on-line coupled atmospheric chemistry model system MECO(n) – Part 2: On-line coupling with the Multi-Model-Driver (MMD). Geoscientific Model Development, 5(1):111–128, 2012. doi: 10.5194/gmd-5-111-2012. URL https://gmd.copernicus.org/articles/5/111/2012/.

Kiemle, C., Quatrevalet, M., Ehret, G., Amediek, A., Fix, A., and Wirth, M. Sensitivity studies for a space-based methane lidar mission. Atmospheric

Measurement Techniques, 4(10):2195–2211, 2011. doi: 10.5194/amt-4-2195-2011. URL https://amt.copernicus.org/articles/4/2195/2011/.

Kiemle, C., Ehret, G., Amediek, A., Fix, A., Quatrevalet, M., and Wirth, M. Potential of Spaceborne Lidar Measurements of Carbon Dioxide and Methane Emissions from Strong Point Sources. Remote Sensing, 9(11), 2017. ISSN 2072-4292. doi: 10.3390/rs9111137. URL https://www.mdpi.com/2072-4292/9/11/1137.

Kimutai, J., Barnes, C., Masambaya, F., Pinto, I., Mwai, Z., Wangari, H., Ogega, O. M., Kilavi, M., Vahlberg, M., Arrighi, J., Raju, E., Baumgart, N., Otto, F., Zachariah, M., Philip, S., Singh, R., Jjemba, E., and Mawanda, S. Urban planning at the heart of increasingly severe East African flood impacts in a warming world. Imperial College London, Faculty of Natural Sciences, May 2024. URL http://hdl.handle.net/10044/1/111671. Report, last accessed: 2025-02-25.

Klausner, T., Mertens, M., Huntrieser, H., Galkowski, M., Kuhlmann, G., Baumann, R., Fiehn, A., Jöckel, P., Pühl, M., and Roiger, A. Urban greenhouse gas emissions from the Berlin area: A case study using airborne CO_2 and CH_4 in situ observations in summer 2018. Elementa: Science of the Anthropocene, 8:15, 04 2020. ISSN 2325-1026. doi: 10.1525/elementa.411. URL https://doi.org/10.1525/elementa.411.

Knapp, M., Scheidweiler, L., Külheim, F., Kleinschek, R., Nęcki, J., Jagoda, P., and Butz, A. Spectrometric imaging of sub-hourly methane emission dynamics from coal mine ventilation. Environmental Research Letters, 18(4):044030, apr 2023. doi: 10.1088/1748-9326/acc346. URL https://dx.doi.org/10.1088/1748-9326/acc346.

Knutson, T., Camargo, S. J., Chan, J. C. L., Emanuel, K., Ho, C.-H., Kossin, J., Mohapatra, M., Satoh, M., Sugi, M., Walsh, K., and Wu, L. Tropical Cyclones and Climate Change Assessment: Part II: Projected Response to Anthropogenic Warming. Bulletin of the American Meteorological Society, 101(3):E303 – E322, 2020. doi: 10.1175/BAMS-D-18-0194.1. URL https://journals.ametsoc.org/view/journals/bams/101/3/bams-d-18-0194.1.xml.

Knutson, T. R., Chung, M. V., Vecchi, G., Sun, J., Hsieh, T.-L., and Smith, A. J. P. Climate change is probably increasing the intensity of tropical cyclones. Tyndall Centre for Climate Change Research, 2021. URL https://tyndall.ac.uk/wp-content/uploads/2023/10/ScienceBrief_Review_CYCLONES_Mar2021.pdf. ScienceBrief Review, part of a collection on Critical Issues in Climate Change Science for COP26. Eds: C. Le Quéré, P. Liss, P. Forster. Published 26 March 2021.

Kostinek, J., Roiger, A., Eckl, M., Fiehn, A., Luther, A., Wildmann, N., Klausner, T., Fix, A., Knote, C., Stohl, A., and Butz, A. Estimating Upper Silesian coal mine methane emissions from airborne in situ observations and dispersion modeling. Atmospheric Chemistry and Physics, 21(11):8791–8807, 2021. doi: 10.5194/acp-21-8791-2021. URL https://acp.copernicus.org/articles/21/8791/2021/.

Kotarba, M. J. Composition and origin of coalbed gases in the Upper Silesian and Lublin basins, Poland. Organic Geochemistry, 32(1):163–180, 2001. ISSN 0146-6380. doi: https://doi.org/10.1016/S0146-6380(00)00134-0. URL https://www.sciencedirect.com/science/article/pii/S0146638000001340.

Krautwurst, S., Gerilowski, K., Borchardt, J., Wildmann, N., Gałkowski, M., Swolkień, J., Marshall, J., Fiehn, A., Roiger, A., Ruhtz, T., Gerbig, C., Nęcki, J., Burrows, J. P., Fix, A., and Bovensmann, H. Quantification of CH_4 coal mining emissions in Upper Silesia by passive airborne remote sensing observations with the Methane Airborne MAPper (MAMAP) instrument during the CO_2 and Methane (CoMet) campaign. Atmospheric Chemistry and Physics, 21(23):17345–17371, 2021. doi: 10.5194/acp-21-17345-2021. URL https://acp.copernicus.org/articles/21/17345/2021/.

Krautwurst, S., Fruck, C., Wolff, S., Borchardt, J., Huhs, O., Gerilowski, K., Gałkowski, M., Kiemle, C., Quatrevalet, M., Wirth, M., Mallaun, C., Burrows, J. P., Gerbig, C., Fix, A., Bösch, H., and Bovensmann, H. Identification and Quantification of CH_4 Emissions from Madrid Landfills using Airborne Imaging Spectrometry and Greenhouse Gas Lidar. EGUsphere, 2024:1–52, 2024. doi: 10.5194/egusphere-2024-3182. URL https://egusphere.copernicus.org/preprints/2024/egusphere-2024-3182/.

Kreiner, K. and Żyła, M. Binarny charakter powierzchni węgla kamiennego. Górnictwo i Geoinżynieria, 30:19–34, 2006. URL https://www.infona.pl//resource/bwmeta1.element.baztech-article-AGH5-0015-0059. (Originally published in Polish. This English translation was generated using DeepL Translator and has not been officially verified.).

Krings, T., Gerilowski, K., Buchwitz, M., Reuter, M., Tretner, A., Erzinger, J., Heinze, D., Pflüger, U., Burrows, J. P., and Bovensmann, H. MAMAP – a new spectrometer system for column-averaged methane and carbon dioxide observations from aircraft: retrieval algorithm and first inversions for point source emission rates. Atmospheric Measurement Techniques, 4(9):1735–1758, 2011. doi: 10.5194/amt-4-1735-2011. URL https://amt.copernicus.org/articles/4/1735/2011/.

Krol, M., Houweling, S., Bregman, B., van den Broek, M., Segers, A., van Velthoven, P., Peters, W., Dentener, F., and Bergamaschi, P. The two-way nested global chemistry-transport zoom model TM5: algorithm and applications. Atmospheric Chemistry and Physics, 5(2):417–432, 2005. doi: 10.5194/acp-5-417-2005. URL https://acp.copernicus.org/articles/5/417/2005/.

Kuhlmann, G., Henne, S., Meijer, Y., and Brunner, D. Quantifying CO_2 Emissions of Power Plants With CO_2 and NO_2 Imaging Satellites. Frontiers in Remote Sensing, 2, 2021. ISSN 2673-6187. doi: 10.3389/frsen.2021.689838. URL https://www.frontiersin.org/journals/remote-sensing/articles/10.3389/frsen.2021.689838.

Kuhlmann, G., Stavropoulou, F., Schwietzke, S., Zavala-Araiza, D., Thorpe, A., Hueni, A., Emmenegger, L., Calcan, A., Röckmann, T., and Brunner, D. Evidence of successful methane mitigation in one of Europe's most important oil production region. Atmospheric Chemistry and Physics, 25(10):5371–5385, 2025. doi: 10.5194/acp-25-5371-2025. URL https://acp.copernicus.org/articles/25/5371/2025/.

Kędzior, S. and Dreger, M. Methane occurrence, emissions and hazards in the Upper Silesian Coal Basin, Poland. International Journal of Coal Geology, 211:103226, 2019. ISSN 0166-5162. doi: https://doi.org/10.1016/j.coal.2019.103226. URL https://www.sciencedirect.com/science/article/pii/S0166516218311492.

Lan, X., Tans, P., and Thoning, K. Trends in globally-averaged CO_2 determined from NOAA Global Monitoring Laboratory measurements, 2025a. URL https://doi.org/10.15138/9N0H-ZH07. last accessed: 2025-01-31.

Lan, X., Thoning, K., and Dlugokencky, E. Trends in globally-averaged CH_4, N_2O, and SF_6 determined from NOAA Global Monitoring Laboratory measurements, 2025b. URL https://doi.org/10.15138/P8XG-AA10. last accessed: 2025-01-31.

Lauvaux, T., Giron, C., Mazzolini, M., d'Aspremont, A., Duren, R., Cusworth, D., Shindell, D., and Ciais, P. Global assessment of oil and gas methane ultra-emitters. Science, 375(6580):557–561, 2022. doi: 10.1126/science.abj4351. URL https://www.science.org/doi/abs/10.1126/science.abj4351.

LEAG, L. Kraftwerk Jänschwalde. https://www.leag.de/de/geschaeftsfelder/kraftwerke/kraftwerk-jaenschwalde/, 2024. last access: 2024-05-15.

Levin, I., Karstens, U., Eritt, M., Maier, F., Arnold, S., Rzesanke, D., Hammer, S., Ramonet, M., Vítková, G., Conil, S., Heliasz, M., Kubistin, D., and Lindauer, M. A dedicated flask sampling strategy developed for Integrated Carbon Observation System (ICOS) stations based on CO_2 and CO measurements and Stochastic Time-Inverted Lagrangian Transport (STILT) footprint modelling. Atmospheric Chemistry and Physics, 20(18):11161–11180, 2020. doi: 10.5194/acp-20-11161-2020. URL https://acp.copernicus.org/articles/20/11161/2020/.

Lin, J. C., Gerbig, C., Wofsy, S. C., Andrews, A. E., Daube, B. C., Davis, K. J., and Grainger, C. A. A near-field tool for simulating the upstream influence of atmospheric observations: The Stochastic Time-Inverted Lagrangian Transport (STILT) model. Journal of Geophysical Research: Atmospheres, 108(D16), 2003. doi: https://doi.org/10.1029/2002JD003161. URL https://agupubs.onlinelibrary.wiley.com/doi/abs/10.1029/2002JD003161.

Luther, A., Kleinschek, R., Scheidweiler, L., Defratyka, S., Stanisavljević, M., Forstmaier, A., Dandocsi, A., Wolff, S., Dubravica, D., Wildmann, N., Kostinek, J., Jöckel, P., Nickl, A.-L., Klausner, T., Hase, F., Frey, M., Chen, J., Dietrich, F., Nęcki, J., Swolkień, J., Fix, A., Roiger, A., and Butz, A. Quantifying CH_4 emissions

from hard coal mines using mobile sun-viewing Fourier transform spectrometry. Atmospheric Measurement Techniques, 12(10):5217–5230, 2019. doi: 10.5194/amt-12-5217-2019. URL https://amt.copernicus.org/articles/12/5217/2019/.

Luther, A., Kostinek, J., Kleinschek, R., Defratyka, S., Stanisavljević, M., Forstmaier, A., Dandocsi, A., Scheidweiler, L., Dubravica, D., Wildmann, N., Hase, F., Frey, M. M., Chen, J., Dietrich, F., Nęcki, J., Swolkień, J., Knote, C., Vardag, S. N., Roiger, A., and Butz, A. Observational constraints on methane emissions from Polish coal mines using a ground-based remote sensing network. Atmospheric Chemistry and Physics, 22(9):5859–5876, 2022. doi: 10.5194/acp-22-5859-2022. URL https://acp.copernicus.org/articles/22/5859/2022/.

Lux, O., Lemmerz, C., Weiler, F., Marksteiner, U., Witschas, B., Rahm, S., Geiß, A., and Reitebuch, O. Intercomparison of wind observations from the European Space Agency's Aeolus satellite mission and the ALADIN Airborne Demonstrator. Atmospheric Measurement Techniques, 13(4):2075–2097, 2020. doi: 10.5194/amt-13-2075-2020. URL https://amt.copernicus.org/articles/13/2075/2020/.

Lynas, M., Houlton, B. Z., and Perry, S. Greater than 99% consensus on human caused climate change in the peer-reviewed scientific literature. Environmental Research Letters, 16(11):114005, oct 2021. doi: 10.1088/1748-9326/ac2966. URL https://dx.doi.org/10.1088/1748-9326/ac2966.

Maiman, T. H. Stimulated Optical Radiation in Ruby. Nature, 187(4736):493–494, 1960. doi: 10.1038/187493a0. URL https://doi.org/10.1038/187493a0.

Mao, J., Ramanathan, A., Abshire, J. B., Kawa, S. R., Riris, H., Allan, G. R., Rodriguez, M., Hasselbrack, W. E., Sun, X., Numata, K., Chen, J., Choi, Y., and Yang, M. Y. M. Measurement of atmospheric CO_2 column concentrations to cloud tops with a pulsed multi-wavelength airborne lidar. Atmospheric Measurement Techniques, 11(1):127–140, 2018. doi: 10.5194/amt-11-127-2018. URL https://amt.copernicus.org/articles/11/127/2018/.

Matsunaga, T. and Tanimoto, H. Greenhouse gas observation by TANSO-3 onboard GOSAT-GW. In Babu, S. R., Hélière, A., and Kimura, T., editors, Sensors, Systems, and Next-Generation Satellites XXVI, volume 12264, page 122640B. International Society for Optics and Photonics, SPIE, 2022. doi: 10.1117/12.2639221. URL https://doi.org/10.1117/12.2639221.

Meijer, Y., Bösch, H., Bombelli, A., Brunner, D., Buchwitz, M., Ciais, P., Crisp, D., Engelen, R., Holmund, K., Houweling, S., Janssen-Maenhout, G., Marshall, J., Nakajima, M., Pinty, B., Scholze, M., Bézy, J., Drinkwater, M., Fehr, T., Fernández, V., Löscher, A., Nett, H., Sierk, B., Dubovik, O., Landgraf, J., Lang, R., Lindqvist, H., Tamminen, J., and Veefkind, P. Copernicus CO_2 Monitoring Mission Requirements Document. Technical report, ESA Earth and Mission Science Division, 2020. URL https://esamultimedia.esa.int/docs/EarthObservation/CO2M_MRD_v3.0_20201001_Issued.pdf. last accessed: 2025-03-13.

Memish, Z., Zumla, A., and Parker, S. Heat-related deaths during the 2024 Hajj pilgrimage. Journal of Travel Medicine, 31(6):taae096, 07 2024. ISSN 1708-8305. doi: 10.1093/jtm/taae096. URL https://doi.org/10.1093/jtm/taae096.

Menoud, M., van der Veen, C., Nęcki, J., Bartyzel, J., Szénási, B., Stanisavljević, M., Pison, I., Bousquet, P., and Röckmann, T. Methane (CH_4) sources in Krakow, Poland: insights from isotope analysis. Atmospheric Chemistry and Physics, 21 (17):13167–13185, 2021. doi: 10.5194/acp-21-13167-2021. URL https://acp.copernicus.org/articles/21/13167/2021/.

Menzies, R. T. and Tratt, D. M. Differential Laser absorption spectrometry for global profiling of tropospheric carbon dioxide: selection of optimum sounding frequencies for high-precision measurements. Appl. Opt., 42(33):6569–6577, Nov 2003. doi: 10.1364/AO.42.006569. URL https://opg.optica.org/ao/abstract.cfm?URI=ao-42-33-6569.

Menzies, R. T., Spiers, G. D., and Jacob, J. Airborne Laser Absorption Spectrometer Measurements of Atmospheric CO_2 Column Mole Fractions: Source and Sink Detection and Environmental Impacts on Retrievals. Journal of Atmospheric and Oceanic Technology, 31(2):404 – 421, 2014. doi: 10.1175/JTECH-D-13-00128.1. URL https://journals.ametsoc.org/view/journals/atot/31/2/jtech-d-13-00128_1.xml.

Mertens, M., Kerkweg, A., Jöckel, P., Tost, H., and Hofmann, C. The 1-way on-line coupled model system MECO(n) – Part 4: Chemical evaluation (based on MESSy v2.52). Geoscientific Model Development, 9(10):3545–3567, 2016. doi: 10.5194/gmd-9-3545-2016. URL https://gmd.copernicus.org/articles/9/3545/2016/.

Moeini, O., Nassar, R., Mastrogiacomo, J.-P., Dawson, M., O'Dell, C. W., Nelson, R. R., and Chatterjee, A. Quantifying CO_2 Emissions From Smaller Anthropogenic Point Sources Using OCO-2 Target and OCO-3 Snapshot Area Mapping Mode Observations. Journal of Geophysical Research: Atmospheres, 130(2):e2024JD042333, 2025. doi: https://doi.org/10.1029/2024JD042333. URL https://agupubs.onlinelibrary.wiley.com/doi/abs/10.1029/2024JD042333. e2024JD042333 2024JD042333.

Moeng, C.-H., Dudhia, J., Klemp, J., and Sullivan, P. Examining Two-Way Grid Nesting for Large Eddy Simulation of the PBL Using the WRF Model. Monthly Weather Review, 135(6):2295 – 2311, 2007. doi: 10.1175/MWR3406.1. URL https://journals.ametsoc.org/view/journals/mwre/135/6/mwr3406.1.xml.

Morrison, H., Thompson, G., and Tatarskii, V. Impact of Cloud Microphysics on the Development of Trailing Stratiform Precipitation in a Simulated Squall Line: Comparison of One- and Two-Moment Schemes. Monthly Weather Review, 137 (3):991 – 1007, 2009. doi: 10.1175/2008MWR2556.1. URL https://journals.ametsoc.org/view/journals/mwre/137/3/2008mwr2556.1.xml.

Munich Re, N. Natural Disasters in 2024. Münchener Rückversicherungs-Gesellschaft, Königinstrasse 107, 80802 München, Germany, January 2025. URL https://www.munichre.com/content/dam/munichre/mrwebsitespressreleases/MunichRe-NatCAT-Stats2024-Full-Year-Factsheet.pdf/_jcr_content/renditions/original./MunichRe-NatCAT-Stats2024-Full-Year-Factsheet.pdf. last accessed: 2025-02-25.

Nakanishi, M. and Niino, H. Development of an Improved Turbulence Closure Model for the Atmospheric Boundary Layer. Journal of the Meteorological Society of Japan. Ser. II, 87(5):895–912, 2009. doi: 10.2151/jmsj.87.895. URL https://www.jstage.jst.go.jp/article/jmsj/87/5/87_5_895/_article.

Nassar, R., Mastrogiacomo, J.-P., Bateman-Hemphill, W., McCracken, C., MacDonald, C. G., Hill, T., O'Dell, C. W., Kiel, M., and Crisp, D. Advances in quantifying power plant CO2 emissions with OCO-2. Remote Sensing of Environment, 264:112579, 2021. ISSN 0034-4257. doi: https://doi.org/10.1016/j.rse.2021.112579. URL https://www.sciencedirect.com/science/article/pii/S0034425721002996.

Nickl, A.-L., Mertens, M., Roiger, A., Fix, A., Amediek, A., Fiehn, A., Gerbig, C., Gałkowski, M., Kerkweg, A., Klausner, T., Eckl, M., and Jöckel, P. Hindcasting and forecasting of regional methane from coal mine emissions in the Upper Silesian Coal Basin using the online nested global regional chemistry–climate model MECO(n) (MESSy v2.53). Geoscientific Model Development, 13(4):1925–1943, 2020. doi: 10.5194/gmd-13-1925-2020. URL https://gmd.copernicus.org/articles/13/1925/2020/.

Nisbet, E. G., Fisher, R. E., Lowry, D., France, J. L., Allen, G., Bakkaloglu, S., Broderick, T. J., Cain, M., Coleman, M., Fernandez, J., Forster, G., Griffiths, P. T., Iverach, C. P., Kelly, B. F. J., Manning, M. R., Nisbet-Jones, P. B. R., Pyle, J. A., Townsend-Small, A., Shalaan, A. a, Warwick, N., and Zazzeri, G. Methane Mitigation: Methods to Reduce Emissions, on the Path to the Paris Agreement. Reviews of Geophysics, 58(1):e2019RG000675, 2020. doi: https://doi.org/10.1029/2019RG000675. URL https://agupubs.onlinelibrary.wiley.com/doi/abs/10.1029/2019RG000675. e2019RG000675 2019RG000675.

Nottrott, A., Kleissl, J., and Keeling, R. Modeling passive scalar dispersion in the atmospheric boundary layer with WRF large-eddy simulation. Atmospheric Environment, 82:172–182, 2014. ISSN 1352-2310. doi: 10.1016/j.atmosenv.2013.10.026. URL https://www.sciencedirect.com/science/article/pii/S1352231013007796.

Nunalee, C. G., Kosović, B., and Bieringer, P. E. Eulerian dispersion modeling with WRF-LES of plume impingement in neutrally and stably stratified turbulent boundary layers. Atmospheric Environment, 99:571–581, 2014. ISSN 1352-2310. doi: 10.1016/j.atmosenv.2014.09.070. URL https://www.sciencedirect.com/science/article/pii/S1352231014007638.

O'Dell, C. W., Connor, B., Bösch, H., O'Brien, D., Frankenberg, C., Castano, R., Christi, M., Eldering, D., Fisher, B., Gunson, M., McDuffie, J., Miller, C. E., Natraj, V., Oyafuso, F., Polonsky, I., Smyth, M., Taylor, T., Toon, G. C., Wennberg, P. O., and Wunch, D. The ACOS CO_2 retrieval algorithm – Part 1: Description and validation against synthetic observations. Atmospheric Measurement Techniques, 5(1):99–121, 2012. doi: 10.5194/amt-5-99-2012. URL https://amt.copernicus.org/articles/5/99/2012/.

Parmesan, C., Morecroft, M. D., Trisurat, Y., Adrian, R., Anshari, G. Z., Arneth, A., Gao, Q., Gonzalez, P., Harris, R., Price, J., Stevens, N., and Talukdar, G. H. Terrestrial and Freshwater Ecosystems and Their Services. In Pörtner, H.-O., Roberts, D. C., Tignor, M., Poloczanska, E. S., Mintenbeck, K., Alegria, A., Craig, M., Langsdorf, S., Löschke, S., Möller, V., Okem, A., and Rama, B., editors, Climate Change 2022: Impacts, Adaptation and Vulnerability. Contribution of Working Group II to the Sixth Assessment Report of the Intergovernmental Panel on Climate Change, pages 197–377. Cambridge University Press, Cambridge, UK and New York, NY, USA, 2022. doi: 10.1017/9781009325844.004. URL https://www.cambridge.org/core/books/climate-change-2022-impacts-adaptation-and-vulnerability/terrestrial-and-freshwater-ecosystems-and-their-services/11743E866F800FF99CECE1CADF03F154.

Peters, W., Miller, J. B., Whitaker, J., Denning, A. S., Hirsch, A., Krol, M. C., Zupanski, D., Bruhwiler, L., and Tans, P. P. An ensemble data assimilation system to estimate CO2 surface fluxes from atmospheric trace gas observations. Journal of Geophysical Research: Atmospheres, 110(D24), 2005. doi: https://doi.org/10.1029/2005JD006157. URL https://agupubs.onlinelibrary.wiley.com/doi/abs/10.1029/2005JD006157.

Peters, W., Jacobson, A. R., Sweeney, C., Andrews, A. E., Conway, T. J., Masarie, K., Miller, J. B., Bruhwiler, L. M. P., Pétron, G., Hirsch, A. I., Worthy, D. E. J., Werf, G. R. v. d, Randerson, J. T., Wennberg, P. O., Krol, M. C., and Tans, P. P. An atmospheric perspective on North American carbon dioxide exchange: CarbonTracker. Proceedings of the National Academy of Sciences, 104(48):18925–18930, 2007. doi: 10.1073/pnas.0708986104. URL https://www.pnas.org/doi/abs/10.1073/pnas.0708986104.

Powers, J. G., Klemp, J. B., Skamarock, W. C., Davis, C. A., Dudhia, J., Gill, D. O., Coen, J. L., Gochis, D. J., Ahmadov, R., Peckham, S. E., Grell, G. A., Michalakes, J., Trahan, S., Benjamin, S. G., Alexander, C. R., Dimego, G. J., Wang, W., Schwartz, C. S., Romine, G. S., Liu, Z., Snyder, C., Chen, F., Barlage, M. J., Yu, W., and Duda, M. G. The Weather Research and Forecasting Model: Overview, System Efforts, and Future Directions. Bulletin of the American Meteorological Society, 98(8):1717 – 1737, 2017. doi: 10.1175/BAMS-D-15-00308.1. URL https://journals.ametsoc.org/view/journals/bams/98/8/bams-d-15-00308.1.xml.

Prather, M. J. and Zhu, L. Resetting tropospheric OH and CH_4 lifetime with

ultraviolet H_2O absorption. Science, 385(6705):201–204, 2024. doi: 10.1126/science.adn0415. URL https://www.science.org/doi/abs/10.1126/science.adn0415.

Qian, J. Generalization of the Kolmogorov -5/3 law of turbulence. Phys. Rev. E, 50:611–613, Jul 1994. doi: 10.1103/PhysRevE.50.611. URL https://link.aps.org/doi/10.1103/PhysRevE.50.611.

Rayleigh, L. XXXIV. On the transmission of light through an atmosphere containing small particles in suspension, and on the origin of the blue of the sky. The London, Edinburgh, and Dublin Philosophical Magazine and Journal of Science, 47(287):375–384, 1899. doi: 10.1080/14786449908621276. URL https://www.tandfonline.com/doi/abs/10.1080/14786449908621276.

Reitebuch, O., Lemmerz, C., Nagel, E., Paffrath, U., Durand, Y., Endemann, M., Fabre, F., and Chaloupy, M. The Airborne Demonstrator for the Direct-Detection Doppler Wind Lidar ALADIN on ADM-Aeolus. Part I: Instrument Design and Comparison to Satellite Instrument. Journal of Atmospheric and Oceanic Technology, 26(12):2501 – 2515, 2009. doi: 10.1175/2009JTECHA1309.1. URL https://journals.ametsoc.org/view/journals/atot/26/12/2009jtecha1309_1.xml.

Reum, F., Florentie, L., Peters, W., Dogniaux, M., Crevoisier, C., Sic, B., and Houweling, S. Performance of upcoming CO2 monitoring satellites in the new high-resolution inverse model CTDAS-WRF. In EGU General Assembly 2020. Copernicus Meetings, 2020. doi: 10.5194/egusphere-egu2020-19293. URL https://presentations.copernicus.org/EGU2020/EGU2020-19293_presentation.pdf. EGU2020-19293.

Reuter, M., Buchwitz, M., Schneising, O., Heymann, J., Bovensmann, H., and Burrows, J. P. A method for improved SCIAMACHY CO_2 retrieval in the presence of optically thin clouds. Atmospheric Measurement Techniques, 3(1):209–232, 2010. doi: 10.5194/amt-3-209-2010. URL https://amt.copernicus.org/articles/3/209/2010/.

Reuter, M., Buchwitz, M., Schneising, O., Krautwurst, S., O'Dell, C. W., Richter, A., Bovensmann, H., and Burrows, J. P. Towards monitoring localized CO_2 emissions from space: co-located regional CO_2 and NO_2 enhancements observed by the OCO-2 and S5P satellites. Atmospheric Chemistry and Physics, 19(14):9371–9383, 2019. doi: 10.5194/acp-19-9371-2019. URL https://acp.copernicus.org/articles/19/9371/2019/.

Reuter, M., Hilker, M., Noël, S., Di Noia, A., Weimer, M., Schneising, O., Buchwitz, M., Bovensmann, H., Burrows, J. P., Bösch, H., and Lang, R. Retrieving the atmospheric concentrations of carbon dioxide and methane from the European Copernicus CO2M satellite mission using artificial neural networks. Atmospheric Measurement Techniques, 18(1):241–264, 2025. doi: 10.5194/amt-18-241-2025. URL https://amt.copernicus.org/articles/18/241/2025/.

Reuters. Five dead, eight missing after methane explosion in Czech coal mine. Reuters, December 2018. URL https://www.reuters.com/article/idUSL8N1YP7KQ/. Last accessed: 15 July 2025.

Ripple, W. J., Wolf, C., Gregg, J. W., Rockström, J., Mann, M. E., Oreskes, N., Lenton, T. M., Rahmstorf, S., Newsome, T. M., Xu, C., Svenning, J.-C., Pereira, C. C., Law, B. E., and Crowther, T. W. The 2024 state of the climate report: Perilous times on planet Earth. BioScience, page biae087, 10 2024. ISSN 1525-3244. doi: 10.1093/biosci/biae087. URL https://doi.org/10.1093/biosci/biae087.

Rodgers, C. D. Inverse Methods for Atmospheric Sounding: Theory and Practice, volume 2 of Series on atmospheric, oceanic and planetary physics. World Scientific, 2000. ISBN 9789810227401. doi: 10.1142/3171. URL https://worldscientific.com/doi/abs/10.1142/3171.

Roger, J., Irakulis-Loitxate, I., Valverde, A., Gorroño, J., Chabrillat, S., Brell, M., and Guanter, L. High-Resolution Methane Mapping With the EnMAP Satellite Imaging Spectroscopy Mission. IEEE Transactions on Geoscience and Remote Sensing, 62:1–12, 2024. doi: 10.1109/TGRS.2024.3352403. URL https://ieeexplore.ieee.org/document/10387469.

Rubio, H., Kühn, M., and Gottschall, J. Evaluation of low-level jets in the southern Baltic Sea: a comparison between ship-based lidar observational data and numerical models. Wind Energy Science, 7(6):2433–2455, 2022. doi: 10.5194/wes-7-2433-2022. URL https://wes.copernicus.org/articles/7/2433/2022/.

Sánchez-García, E., Gorroño, J., Irakulis-Loitxate, I., Varon, D. J., and Guanter, L. Mapping methane plumes at very high spatial resolution with the WorldView-3 satellite. Atmospheric Measurement Techniques, 15(6):1657–1674, 2022. doi: 10.5194/amt-15-1657-2022. URL https://amt.copernicus.org/articles/15/1657/2022/.

Saunois, M., Martinez, A., Poulter, B., Zhang, Z., Raymond, P. A., Regnier, P., Canadell, J. G., Jackson, R. B., Patra, P. K., Bousquet, P., Ciais, P., Dlugokencky, E. J., Lan, X., Allen, G. H., Bastviken, D., Beerling, D. J., Belikov, D. A., Blake, D. R., Castaldi, S., Crippa, M., Deemer, B. R., Dennison, F., Etiope, G., Gedney, N., Höglund-Isaksson, L., Holgerson, M. A., Hopcroft, P. O., Hugelius, G., Ito, A., Jain, A. K., Janardanan, R., Johnson, M. S., Kleinen, T., Krummel, P. B., Lauerwald, R., Li, T., Liu, X., McDonald, K. C., Melton, J. R., Mühle, J., Müller, J., Murguia-Flores, F., Niwa, Y., Noce, S., Pan, S., Parker, R. J., Peng, C., Ramonet, M., Riley, W. J., Rocher-Ros, G., Rosentreter, J. A., Sasakawa, M., Segers, A., Smith, S. J., Stanley, E. H., Thanwerdas, J., Tian, H., Tsuruta, A., Tubiello, F. N., Weber, T. S., Werf, G. R. v. d, Worthy, D. E. J., Xi, Y., Yoshida, Y., Zhang, W., Zheng, B., Zhu, Q., Zhu, Q., and Zhuang, Q. Global Methane Budget 2000–2020. Earth System Science Data, 17(5):1873–1958, 2025. doi: 10.5194/essd-17-1873-2025. URL https://essd.copernicus.org/articles/17/1873/2025/.

Schmidt, H. and Schumann, U. Coherent Structure of the Convective Boundary Layer Derived from Large-Eddy Simulations. Journal of Fluid Mechanics, 200:511–562, 1989. doi: 10.1017/S0022112089000753. URL https://elib.dlr.de/53323/.

Schotland, R. M. The determination of the vertical profile of atmospheric gases by means of a ground based optical radar, proceedings of the 3rd symposium of remote sensing of the environment. Ann Arbor, Oct. 1964.

Schotland, R. M. Errors in the Lidar Measurement of Atmospheric Gases by Differential Absorption. Journal of Applied Meteorology (1962-1982), 13(1):71–77, 1974. ISSN 00218952, 2163534X. URL http://www.jstor.org/stable/26176876.

Schumann, U. Large-eddy simulation of turbulent diffusion with chemical reactions in the convective boundary layer. Atmospheric Environment (1967), 23(8):1713–1727, 1989. ISSN 0004-6981. doi: https://doi.org/10.1016/0004-6981(89)90056-5. URL https://www.sciencedirect.com/science/article/pii/0004698189900565.

Seinfeld, J. H. and Pandis, S. N. Atmospheric chemistry and physics: from air pollution to climate change. John Wiley & Sons, Inc., 605 Third Avenue, New York, N.Y. 10158-0012, 1st edition, 1997. ISBN 978-0-471-17816-3.

Sharan, M., Yadav, A. K., Singh, M. P., Agarwal, P., and Nigam, S. A mathematical model for the dispersion of air pollutants in low wind conditions. Atmospheric Environment, 30(8):1209–1220, 1996. ISSN 1352-2310. doi: https://doi.org/10.1016/1352-2310(95)00442-4. URL https://www.sciencedirect.com/science/article/pii/1352231095004424.

Sheng, J.-X., Jacob, D. J., Maasakkers, J. D., Zhang, Y., and Sulprizio, M. P. Comparative analysis of low-Earth orbit (TROPOMI) and geostationary (GeoCARB, GEO-CAPE) satellite instruments for constraining methane emissions on fine regional scales: application to the Southeast US. Atmospheric Measurement Techniques, 11(12):6379–6388, 2018. doi: 10.5194/amt-11-6379-2018. URL https://amt.copernicus.org/articles/11/6379/2018/.

Sherwin, E. D., Rutherford, J. S., Chen, Y., Aminfard, S., Kort, E. A., Jackson, R. B., and Brandt, A. R. Single-blind validation of space-based point-source detection and quantification of onshore methane emissions. Scientific Reports, 13(1):3836, 2023. ISSN 2045-2322. doi: 10.1038/s41598-023-30761-2. URL https://doi.org/10.1038/s41598-023-30761-2.

Sherwin, E. D., El Abbadi, S. H., Burdeau, P. M., Zhang, Z., Chen, Z., Rutherford, J. S., Chen, Y., and Brandt, A. R. Single-blind test of nine methane-sensing satellite systems from three continents. Atmospheric Measurement Techniques, 17(2):765–782, 2024. doi: 10.5194/amt-17-765-2024. URL https://amt.copernicus.org/articles/17/765/2024/.

Shi, T., Han, G., Ma, X., Pei, Z., Chen, W., Liu, J., Zhang, X., Li, S., and Gong, W. Quantifying strong point sources emissions of CO_2 using spaceborne LiDAR: Method development and potential analysis. Energy Conversion and Management, 292:117346, 2023. ISSN 0196-8904. doi: https://doi.org/10.1016/j.enconman.2023.117346. URL https://www.sciencedirect.com/science/article/pii/S0196890423006921.

Siegmund, P., Abermann, J., Baddour, O., Sparrow, M., Nitu, R., Tarasova, O., Canadell, P., Cazenave, A., Derksen, C., Mudryk, L., Howell, S., Garreau, A., Huss, M., Isensee, K., Schoo, K., Kennedy, J., Mottram, R., Ramasamy, S., Trewin, B., and Ziese, M. The Global Climate in 2015-2019. Policy document, World Meteorological Organization (WMO), Genf, Schweiz, 2020. URL https://oceanrep.geomar.de/id/eprint/57643/.

Sierk, B., Fernandez, V., Bézy, J.-L., Meijer, Y., Durand, Y., Courrèges-Lacoste, G. B., Pachot, C., Löscher, A., Nett, H., Minoglou, K., Boucher, L., Windpassinger, R., Pasquet, A., Serre, D., and Hennepe, F. t. The Copernicus CO2M mission for monitoring anthropogenic carbon dioxide emissions from space. In Cugny, B., Sodnik, Z., and Karafolas, N., editors, International Conference on Space Optics — ICSO 2020, volume 11852, page 118523M. International Society for Optics and Photonics, SPIE, 2021. doi: 10.1117/12.2599613. URL https://doi.org/10.1117/12.2599613.

Skamarock, W. C., Klemp, J. B., Dudhia, J., Gill, D. O., Barker, D. M., Duda, M. G., Huang, X.-Y., Wang, W., and Powers, J. G. A description of the advanced research WRF model version 3. University Corporation for Atmospheric Research, 2008. doi: 10.5065/D68S4MVH. URL https://www2.mmm.ucar.edu/wrf/users/docs/technote/v3_technote.pdf. Technical Note NCAR/TN–475+STR.

Skamarock, W. C., Klemp, J. B., Dudhia, J., Gill, D. O., Liu, Z., Berner, J., Wang, W., Powers, J. G., Duda, M. G., Barker, D. M., and Huang, X.-Y. A description of the advanced research WRF model version 4. University Corporation for Atmospheric Research, 2019. doi: 10.5065/1dfh-6p97. URL https://www2.mmm.ucar.edu/wrf/users/docs/technote/v4_technote.pdf. Technical Note NCAR/TN-556+STR.

Smagorinsky, J. GENERAL CIRCULATION EXPERIMENTS WITH THE PRIMITIVE EQUATIONS: I. THE BASIC EXPERIMENT. Monthly Weather Review, 91(3):99 – 164, 1963. doi: 10.1175/1520-0493(1963)091<0099:GCEWTP>2.3.CO;2. URL https://journals.ametsoc.org/view/journals/mwre/91/3/1520-0493_1963_091_0099_gcewtp_2_3_co_2.xml.

Spilling, D. and Thales, A. The Multi Angle Polarimeter (MAP) on board ESA's Copernicus Carbon Dioxide Monitoring mission (CO2M). In Cugny, B., Sodnik, Z., and Karafolas, N., editors, International Conference on Space Optics — ICSO 2020, volume 11852, page 118520R. International Society for Optics and Photonics, SPIE, 2021. doi: 10.1117/12.2599174. URL https://doi.org/10.1117/12.2599174.

Stauffer, R., Mayr, G. J., Dabernig, M., and Zeileis, A. Somewhere Over the Rainbow: How to Make Effective Use of Colors in Meteorological Visualizations. Bulletin of the American Meteorological Society, 96(2):203 – 216, 2015. doi: 10.1175/BAMS-D-13-00155.1. URL https://journals.ametsoc.org/view/journals/bams/96/2/bams-d-13-00155.1.xml.

Steiner, M., Cantarello, L., Henne, S., and Brunner, D. Flow-dependent observation errors for greenhouse gas inversions in an ensemble Kalman smoother. Atmospheric Chemistry and Physics, 24(21):12447–12463, 2024a. doi: 10.5194/acp-24-12447-2024. URL https://acp.copernicus.org/articles/24/12447/2024/.

Steiner, M., Peters, W., Luijkx, I., Henne, S., Chen, H., Hammer, S., and Brunner, D. European CH_4 inversions with ICON-ART coupled to the CarbonTracker Data Assimilation Shell. Atmospheric Chemistry and Physics, 24(4):2759–2782, 2024b. doi: 10.5194/acp-24-2759-2024. URL https://acp.copernicus.org/articles/24/2759/2024/.

Strandgren, J., Krutz, D., Wilzewski, J., Paproth, C., Sebastian, I., Gurney, K. R., Liang, J., Roiger, A., and Butz, A. Towards spaceborne monitoring of localized CO_2 emissions: an instrument concept and first performance assessment. Atmospheric Measurement Techniques, 13(6):2887–2904, 2020. doi: 10.5194/amt-13-2887-2020. URL https://amt.copernicus.org/articles/13/2887/2020/.

Stull, R. B. An introduction to boundary layer meteorology. Springer Science & Business Media, Dordrecht, the Netherlands, 1988. ISBN 978-94-009-3027-8.

Stull, R. B. Practical Meteorology: An Algebra-based Survey of Atmospheric Science. Univ. of British Columbia, 2020-2207 Main Mall, Vancouver, BC, Canada V6T 1Z4, 2017. ISBN 978-0-88865-283-6. URL https://www.eoas.ubc.ca/books/Practical_Meteorology/. Chapter 19 'POLLUTANT DISPERSION', version 1.02b.

Swolkień, J., Fix, A., and Gałkowski, M. Factors influencing the temporal variability of atmospheric methane emissions from Upper Silesia coal mines: a case study from the CoMet mission. Atmospheric Chemistry and Physics, 22(24):16031–16052, 2022. doi: 10.5194/acp-22-16031-2022. URL https://acp.copernicus.org/articles/22/16031/2022/.

Synge, E. XCI. A method of investigating the higher atmosphere. The London, Edinburgh, and Dublin Philosophical Magazine and Journal of Science, 9(60):1014–1020, 1930. doi: 10.1080/14786443008565070. URL https://doi.org/10.1080/14786443008565070.

Tanimoto, H., Matsunaga, T., Someya, Y., Fujinawa, T., Ohyama, H., Morino, I., Yashiro, H., Sugita, T., Inomata, S., Müller, A., Saeki, T., Yoshida, Y., Niwa, Y., Saito, M., Noda, H., Yamashita, Y., Ikeda, K., Saigusa, N., Machida, T., Frey, M. M., Lim, H., Srivastava, P., Jin, Y., Shimizu, A., Nishizawa, T., Kanaya, Y., Sekiya, T., Patra, P., Takigawa, M., Bisht, J., Kasai, Y., and Sato, T. O. The

greenhouse gas observation mission with Global Observing SATellite for Greenhouse gases and Water cycle (GOSAT-GW): objectives, conceptual framework and scientific contributions. Progress in Earth and Planetary Science, 12(1):8, 2025. doi: 10.1186/s40645-025-00684-9. URL https://doi.org/10.1186/s40645-025-00684-9.

Tewari, M., Chen, F., Wang, W., Dudhia, J., LeMone, M. A., Mitchell, K., Ek, M., Gayno, G., Wegiel, J., , and Cuenca, R. H. Implementation and verification of the unified NOAH land surface model in the WRF model. 20th conference on weather analysis and forecasting/16th conference on numerical weather prediction, 10–14 January 2004, 14.2a:2165–2170, 2004. URL https://ams.confex.com/ams/84Annual/webprogram/Paper69061.html. last access: 16 May 2024.

Thanwerdas, J., Berchet, A., Constantin, L., Tsuruta, A., Steiner, M., Reum, F., Henne, S., and Brunner, D. Improving the ensemble square root filter (EnSRF) in the Community Inversion Framework: a case study with ICON-ART 2024.01. Geoscientific Model Development, 18(5):1505–1544, 2025. doi: 10.5194/gmd-18-1505-2025. URL https://gmd.copernicus.org/articles/18/1505/2025/.

The New York Times, a. Czech Coal Mine Explosion Kills at Least 13. The New York Times, December 2018. URL https://www.nytimes.com/2018/12/21/world/europe/czech-republic-mine-explosion.html. Last accessed: 15 July 2025.

Tollefson, J. Earth breaches 1.5 °C climate limit for the first time: what does it mean? Nature News, 637:769–770, January 2025. doi: 10.1038/d41586-025-00010-9. URL https://doi.org/10.1038/d41586-025-00010-9. last accessed: 2025-02-19.

Tu, Q., Hase, F., Schneider, M., García, O., Blumenstock, T., Borsdorff, T., Frey, M., Khosrawi, F., Lorente, A., Alberti, C., Bustos, J. J., Butz, A., Carreño, V., Cuevas, E., Curcoll, R., Diekmann, C. J., Dubravica, D., Ertl, B., Estruch, C., León-Luis, S. F., Marrero, C., Morgui, J.-A., Ramos, R., Scharun, C., Schneider, C., Sepúlveda, E., Toledano, C., and Torres, C. Quantification of CH_4 emissions from waste disposal sites near the city of Madrid using ground- and space-based observations of COCCON, TROPOMI and IASI. Atmospheric Chemistry and Physics, 22(1):295–317, 2022a. doi: 10.5194/acp-22-295-2022. URL https://acp.copernicus.org/articles/22/295/2022/.

Tu, Q., Schneider, M., Hase, F., Khosrawi, F., Ertl, B., Nęcki, J., Dubravica, D., Diekmann, C. J., Blumenstock, T., and Fang, D. Quantifying CH_4 emissions in hard coal mines from TROPOMI and IASI observations using the wind-assigned anomaly method. Atmospheric Chemistry and Physics, 22(15):9747–9765, 2022b. doi: 10.5194/acp-22-9747-2022. URL https://acp.copernicus.org/articles/22/9747/2022/.

UNFCCC, U. The Paris Agreement, 2015. URL https://unfccc.int/sites/default/files/english_paris_agreement.pdf. last accessed: 2025-02-23.

Gon, H. D. v. d, Hendriks, C., Kuenen, J. J. P., Segers, A., and Visschedijk, A. J. H. Description of current temporal emission patterns and sensitivity of predicted AQ for temporal emission patterns. Eu fp7 macc deliverable report d_d-emis_1.3, TNO, Utrecht, The Netherlands, 2011. URL https://atmosphere.copernicus.eu/sites/default/files/2019-07/MACC_TNO_del_1_3_v2.pdf. Accessed July 1, 2025.

van der Laan-Luijkx, I. T., van der Velde, I. R., van der Veen, E., Tsuruta, A., Stanislawska, K., Babenhauserheide, A., Zhang, H. F., Liu, Y., He, W., Chen, H., Masarie, K. A., Krol, M. C., and Peters, W. The CarbonTracker Data Assimilation Shell (CTDAS) v1.0: implementation and global carbon balance 2001–2015. Geoscientific Model Development, 10(7):2785–2800, 2017. doi: 10.5194/gmd-10-2785-2017. URL https://gmd.copernicus.org/articles/10/2785/2017/.

Varon, D. J., Jacob, D. J., McKeever, J., Jervis, D., Durak, B. O. A., Xia, Y., and Huang, Y. Quantifying methane point sources from fine-scale satellite observations of atmospheric methane plumes. Atmospheric Measurement Techniques, 11(10): 5673–5686, 2018. doi: 10.5194/amt-11-5673-2018. URL https://amt.copernicus.org/articles/11/5673/2018/.

Varon, D. J., Jacob, D. J., Jervis, D., and McKeever, J. Quantifying Time-Averaged Methane Emissions from Individual Coal Mine Vents with GHGSat-D Satellite Observations. Environmental Science & Technology, 54(16):10246–10253, 2020. doi: 10.1021/acs.est.0c01213. URL https://doi.org/10.1021/acs.est.0c01213. PMID: 32672947.

Varon, D. J., Jervis, D., McKeever, J., Spence, I., Gains, D., and Jacob, D. J. High-frequency monitoring of anomalous methane point sources with multispectral Sentinel-2 satellite observations. Atmospheric Measurement Techniques, 14(4): 2771–2785, 2021. doi: 10.5194/amt-14-2771-2021. URL https://amt.copernicus.org/articles/14/2771/2021/.

Whitaker, J. S. and Hamill, T. M. Ensemble Data Assimilation without Perturbed Observations. Monthly Weather Review, 130(7):1913 – 1924, 2002. doi: 10.1175/1520-0493(2002)130<1913:EDAWPO>2.0.CO;2. URL https://journals.ametsoc.org/view/journals/mwre/130/7/1520-0493_2002_130_1913_edawpo_2.0.co_2.xml.

White, W. H., Anderson, J. A., Blumenthal, D. L., Husar, R. B., Gillani, N. V., Husar, J. D., and Wilson, W. E. Formation and Transport of Secondary Air Pollutants: Ozone and Aerosols in the St. Louis Urban Plume. Science, 194(4261): 187–189, 1976. doi: 10.1126/science.959846. URL https://www.science.org/doi/abs/10.1126/science.959846.

Wildmann, N., Vasiljevic, N., and Gerz, T. Wind turbine wake measurements with automatically adjusting scanning trajectories in a multi-Doppler lidar setup. Atmospheric Measurement Techniques, 11(6):3801–3814, 2018. doi: 10.5194/amt-11-3801-2018. URL https://amt.copernicus.org/articles/11/3801/2018/.

Wildmann, N., Päschke, E., Roiger, A., and Mallaun, C. Towards improved turbulence estimation with Doppler wind lidar velocity-azimuth display (VAD) scans. Atmospheric Measurement Techniques, 13(8):4141–4158, 2020. doi: 10.5194/amt-13-4141-2020. URL https://amt.copernicus.org/articles/13/4141/2020/.

Williams, J. P., Omara, M., Himmelberger, A., Zavala-Araiza, D., MacKay, K., Benmergui, J., Sargent, M., Wofsy, S. C., Hamburg, S. P., and Gautam, R. Small emission sources in aggregate disproportionately account for a large majority of total methane emissions from the US oil and gas sector. Atmospheric Chemistry and Physics, 25(3):1513–1532, 2025. doi: 10.5194/acp-25-1513-2025. URL https://acp.copernicus.org/articles/25/1513/2025/.

Wolff, S., Ehret, G., Kiemle, C., Amediek, A., Quatrevalet, M., Wirth, M., and Fix, A. Determination of the emission rates of CO_2 point sources with airborne lidar. Atmospheric Measurement Techniques, 14(4):2717–2736, 2021. doi: 10.5194/amt-14-2717-2021. URL https://amt.copernicus.org/articles/14/2717/2021/.

Wolff, S. Bestimmung der Emissionsraten von CH4- und CO2-Punktquellen mit flugzeuggetragenem Lidar. Master's thesis, LMU München, Dezember 2018. URL https://elib.dlr.de/123862/.

Wolff, S. Animated GIF of simulated plume and virtual flight tracks. Zenodo, November 2020. doi: 10.5281/zenodo.4266513. URL https://doi.org/10.5281/zenodo.4266513.

Worden, J. R., Pandey, S., Zhang, Y., Cusworth, D. H., Qu, Z., Bloom, A. A., Ma, S., Maasakkers, J. D., Byrne, B., Duren, R., Crisp, D., Gordon, D., and Jacob, D. J. Verifying Methane Inventories and Trends With Atmospheric Methane Data. AGU Advances, 4(4):e2023AV000871, 2023. doi: 10.1029/2023AV000871. URL https://agupubs.onlinelibrary.wiley.com/doi/abs/10.1029/2023AV000871. e2023AV000871 2023AV000871.

WUG, S. Assessment of Occupational Safety, Mining Rescue, and Public Safety in Connection with Mining and Geological Activities in 2018 (with comparison to 2014), 2019. URL https://www.wug.gov.pl/english/poland. Original title: *Ocena stanu bezpieczeństwa pracy, ratownictwa górniczego oraz bezpieczeństwa powszechnego w związku z działalnością górniczo-geologiczną w 2018 roku (porównanie od roku 2014)*. In Polish. Last accessed: 15 July 2025.

Wunch, D., Toon, G. C., Wennberg, P. O., Wofsy, S. C., Stephens, B. B., Fischer, M. L., Uchino, O., Abshire, J. B., Bernath, P., Biraud, S. C., Blavier, J.-F. L., Boone, C., Bowman, K. P., Browell, E. V., Campos, T., Connor, B. J., Daube, B. C., Deutscher, N. M., Diao, M., Elkins, J. W., Gerbig, C., Gottlieb, E., Griffith, D. W. T., Hurst, D. F., Jiménez, R., Keppel-Aleks, G., Kort, E. A., Macatangay, R., Machida, T., Matsueda, H., Moore, F., Morino, I., Park, S., Robinson, J., Roehl, C. M., Sawa, Y., Sherlock, V., Sweeney, C., Tanaka, T., and Zondlo, M. A. Calibration of the Total Carbon Column Observing Network using aircraft profile data. Atmospheric Measurement Techniques, 3(5):1351–1362, 2010.

doi: 10.5194/amt-3-1351-2010. URL https://amt.copernicus.org/articles/3/1351/2010/.

Yu, X., Millet, D. B., Henze, D. K., Turner, A. J., Delgado, A. L., Bloom, A. A., and Sheng, J. A high-resolution satellite-based map of global methane emissions reveals missing wetland, fossil fuel, and monsoon sources. Atmospheric Chemistry and Physics, 23(5):3325–3346, 2023. doi: 10.5194/acp-23-3325-2023. URL https://acp.copernicus.org/articles/23/3325/2023/.

Yver, C. E., Graven, H. D., Lucas, D. D., Cameron-Smith, P. J., Keeling, R. F., and Weiss, R. F. Evaluating transport in the WRF model along the California coast. Atmospheric Chemistry and Physics, 13(4):1837–1852, 2013. doi: 10.5194/acp-13-1837-2013. URL https://acp.copernicus.org/articles/13/1837/2013/.

Zhao, X., Marshall, J., Hachinger, S., Gerbig, C., Frey, M., Hase, F., and Chen, J. Analysis of total column CO_2 and CH_4 measurements in Berlin with WRF-GHG. Atmospheric Chemistry and Physics, 19(17):11279–11302, 2019. doi: 10.5194/acp-19-11279-2019. URL https://acp.copernicus.org/articles/19/11279/2019/.

Zhao, X., Chen, J., Marshall, J., Gałkowski, M., Hachinger, S., Dietrich, F., Shekhar, A., Gensheimer, J., Wenzel, A., and Gerbig, C. Understanding greenhouse gas (GHG) column concentrations in Munich using the Weather Research and Forecasting (WRF) model. Atmospheric Chemistry and Physics, 23(22):14325–14347, 2023. doi: 10.5194/acp-23-14325-2023. URL https://acp.copernicus.org/articles/23/14325/2023/.

Zhu, Y., Hu, Q., Gao, M., Zhao, C., Zhang, C., Liu, T., Tian, Y., Yan, L., Su, W., Hong, X., and Liu, C. Quantifying Contributions of Local Emissions and Regional Transport to NO_X in Beijing Using TROPOMI Constrained WRF-Chem Simulation. Remote Sensing, 13(9), 2021. ISSN 2072-4292. doi: 10.3390/rs13091798. URL https://www.mdpi.com/2072-4292/13/9/1798.

Acknowledgments

First and foremost, I would like to express my sincere gratitude to everyone who has contributed to the completion of this dissertation. Without their support and patience, this work would not have been possible.

I would like to thank **Prof. Dr. Markus Rapp** for the opportunity to conduct my PhD research at the Institute of Atmospheric Physics of DLR and at LMU Munich. I am grateful for his advice, for his constructive feedback on this manuscript, and for his continued interest in my work.

I would also like to thank **Prof. Dr. Sander Houweling** for serving as the second reviewer of this dissertation and for the scientific exchange during my research stay at SRON in Utrecht. My thanks also go to **Ilse Aben**, who kindly hosted me in her department and provided a welcoming environment during my time in the Netherlands.

My special thanks go to **Andreas Fix**, my group leader, for his excellent scientific supervision, the many discussions, and the constructive feedback throughout all stages of this work. His critical view and clear guidance have strongly shaped the direction of this dissertation.

I would like to thank **Christoph Kiemle** for his long-standing support. He has supervised me since my early days at DLR — first as an intern, later during my master's thesis, and finally as a PhD student. Over the years, he found an excellent balance between close supervision in the beginning and gradually giving me more freedom and confidence to pursue my own ideas. I have always appreciated his openness, his advice, and his willingness to take time for discussion.

I am especially thankful to **Julia Marshall** and **Friedemann Reum**. Without their help, I would probably still be struggling with cryptic error messages and WRF would never have run successfully on Levante. Friedemann especially devoted countless hours to explaining concepts, answering questions, and helping me find solutions. His patience and dedication have been invaluable, and much of this work would not have been possible without his help.

I also wish to thank the **CHARM-F team**: **Gerhard Ehret**, **Martin Wirth**, **Mathieu Quatrevalet**, **Christian Fruck** and **Sabrina Zechlau** as well as **Andreas Fix** and **Christoph Kiemle**. Their expertise in instrument operation, retrieval development, and data processing provided the foundation for this thesis. Without their work and the successful execution of the CoMet 1.0 campaign, the data used here would not exist.

I would like to thank my mates **Christopher Geach**, **Konstantin Krüger**, **Robert Reichert**, and **Manuel Gutleben**. We shared our office and coffee breaks for many years, and together we had countless good moments and a lot of laughter in and outside the office. Moreover, Christopher took the time to carefully proofread

the entire dissertation and helped me to improve my English throughout. I further wish to thank all colleagues from the **Lidar Department** at large. The atmosphere in the department makes every long commute worthwhile. I could not wish for better colleagues.

Finally, I would like to thank my family. To my parents, **Renate** and **Michael**, thank you for your unconditional support, for your trust, and for giving me the freedom to follow my own path. To my brother, **Christian**, thank you for your constant encouragement, your willingness to help, and for reminding me whenever necessary to uphold my own standards.

Dear **Anna**, I can't thank you enough for bearing me through the most difficult times. Words cannot express how much you have helped me. So instead, I'll take you out for ice cream!

I acknowledge financial support by BMBF (German Federal Ministry of Education and Research) through its AIRSPACE project (grant no. 01LK1701A/B/C) and the German Science Foundation (Deutsche Forschungsgemeinschaft, DFG) within DFG Priority Program SP 1294 "Atmospheric and Earth System Research with the Research Aircraft HALO (High Altitude and Long Range Research Aircraft)". The HALO flights also received support in the frame of DLR project "KliSAW" and from the Max Planck Society.

This work used resources of the Deutsches Klimarechenzentrum (DKRZ) granted by its Scientific Steering Committee (WLA) under project ID bd1231.

The simulation results in Chapter 4 were generated using Copernicus Atmosphere Monitoring Service (CAMS) information [2022] downloaded from CAMS Atmosphere Data Store (ADS). Neither the European Commission nor ECMWF is responsible for any use that may be made of the Copernicus information or data it contains.